Turbulence in partly vegetated channels: Experiments with complex morphology vegetation and rigid cylinders

Gerardo Caroppi

Dipartimento di Ingegneria Civile, Edile e Ambientale
Università degli Studi di Napoli Federico II

Thesis submitted for the degree of PhD in Civil Systems Engineering
Napoli, December 2018

PhD Candidate: Gerardo Caroppi
Supervisors: Prof. Maurizio Giugni, Prof. Paola Gualtieri

PhD Program Coordinator (XXXI Cycle): Prof. Andrea Papola

Reading Committee:
Prof. Roberto Gaudio, Università della Calabria
Dr. Monika Kalinowska, Instytut Geofizyki Polskiej Akademii Nauk
Prof. Michele Mossa, Politecnico di Bari
Dr. Kaisa Västilä, Aalto-yliopisto

alla mia Famiglia

Abstract

Vegetation is a fundamental feature of riverine ecosystems, playing a variety of valuable ecological and biological roles. Concurrently, the presence of vegetation and its interaction with the flow alter the mean and turbulent flow field, with implications on flow resistance, water conveyance and transport of mass and energy. The proper understanding of these vegetation-influenced processes is essential for solving the existing and future river management challenges, concerning both societal needs and ecosystem requirements.

The objective of this thesis is to provide new insight on the flow-vegetation hydrodynamic interaction with a specific focus on partly vegetated channels, a configuration representative of natural settings. Indeed, in natural watercourses, vegetation is generally found along river margins, partly obstructing the river cross-section and laterally interacting with the flow. Riparian vegetation presents a complex morphology and, owing to its flexibility, exhibits a dynamic and reconfiguring behavior under the flow forcing. In the analysis of flow in partly vegetated channels, these flow-influencing characteristics have been generally neglected, simulating vegetation with rigid cylinders.

In the current study, two main experimental campaigns were performed to investigate the turbulent structure of the flow in partly vegetated channels, simulating vegetation with natural-like plant stands (PN) and with rigid cylinders (PR). The PN tests aimed at investigating the effects of plant morphology, reconfiguration and dynamic motions on the turbulent flow field. Furthermore, the effects of seasonal variability of plants on flow structure were explored. Results showed that plant morphology and reconfiguration play a key role in the vegetated shear layer dynamics, significantly affecting the exchange processes across the vegetated interface. The PR test series was performed to investigate the effects of vegetation density on the turbulent flow structure. The results showed that, for rigid vegetation, the density directly affects the shear layer features, governing the onset of large-scale coherent structures. Finally, the impacts of embedding natural plant features in the simulation of partly vegetated flows were explored by comparing the shear layers induced by complex morphology vegetation (PN) and by rigid cylinders (PR). In addition, an existing model for velocity prediction was tested against the experimental results, showing the need to improve existing models for taking into account the peculiar hydrodynamic behavior of natural vegetation.

Keywords: turbulence; vegetation; partly vegetated channels; reconfiguration; shear layer; ADV

Abstract

La vegetazione rappresenta una componente fondamentale degli ecosistemi fluviali, rivestendo una serie di fondamentali ruoli ecologici e biologici. Tuttavia, la presenza di vegetazione e la sua interazione con la corrente altera le caratteristiche idrodinamiche del moto, le resistenze idrauliche e i livelli idrici, con conseguenze sulla capacità di trasporto di materia ed energia. Pertanto, la corretta comprensione dei processi idrodinamici che coinvolgono la vegetazione è essenziale per la gestione sostenibile dei corsi d'acqua, alla ricerca di soluzioni di compromesso tra esigenze di natura tecnico-idraulica ed ambientale.

Nel presente elaborato di tesi, l'interazione idrodinamica tra corrente e vegetazione è stata approfondita con specifico riferimento ai canali parzialmente vegetati, configurazione ritenuta particolarmente rappresentativa dei corsi d'acqua naturali. Infatti, nei contesti naturali, la vegetazione si presenta generalmente lungo i margini fluviali, parzialmente ostruendo la sezione trasversale e interagendo lateralmente con la corrente. La vegetazione ripariale presenta tipicamente una morfologia complessa e, a causa della sua flessibilità, sotto l'azione idrodinamica della corrente, esibisce un complesso comportamento dinamico e deformativo (riconfigurazione). Nello studio delle correnti in alveo parzialmente vegetato tali caratteristiche sono generalmente trascurate, simulando la vegetazione con dei cilindri rigidi.

Nell'ambito del presente lavoro di tesi, due campagne sperimentali sono state condotte allo scopo di investigare le caratteristiche idrodinamiche di una corrente defluente in un alveo parzialmente vegetato con vegetazione flessibile morfologicamente complessa (PN) e con cilindri rigidi (PR). La serie sperimentale PN è stata condotta allo scopo di esplorare gli effetti della presenza di piante dalla morfologia complessa e della riconfigurazione sullo *shear layer* in alveo vegetato, con riferimento anche agli effetti della variazione stagionale della morfologia vegetale. I risultati hanno dimostrato come tali aspetti influenzino profondamente le interazioni laterali tra la corrente e la vegetazione. La serie sperimentale PR è stata condotta per investigare gli effetti della densità sulle caratteristiche dello *shear layer* vegetato. Lo scambio di quantità di moto all'interfaccia è risultato direttamente legato alla densità. Infine, lo *shear layer* indotto da vegetazione morfologicamente complessa è stato confrontato con quello indotto da cilindri rigidi, esplorando gli effetti legati al modello di vegetazione impiegato. Infine, un modello di letteratura per la previsione della velocità è stato applicato ai casi investigati, mettendo in luce la necessità di adeguare i modelli esistenti per tenere in debita considerazione il caratteristico comportamento idrodinamico della vegetazione naturale.

Acknowledgements

I have enjoyed conducting this doctoral research over the past three years, having had the chance to meet many great people to whom I am grateful.

I sincerely thank my tutors Prof. Maurizio Giugni and Prof. Paola Gualtieri.

Prof. Maurizio Giugni gave me the invaluable chance to join the PhD program and his research group, introducing me into scientific research. He encouraged me to work freely, giving me the chance to develop my research topic following my inclinations.

Prof. Paola Gualtieri has been a point of reference during these three years, directing my steps into experimental hydraulics. I want to thank her for having supported me and believed in my capabilities.

I am profoundly thankful to Dr. Juha Järvelä and Dr. Kaisa Västilä for having accepted me at the Environmental Hydraulics Lab of the Aalto University and for having taught me how to conduct good research. I am sincerely grateful to them for having shared their expertise and network in environmental hydraulics.

I sincerely thank the reading committee for the time spent reviewing this thesis and for the insightful comments they provided.

I wish to thank Prof. Nicola Fontana, for having inspired me as a student. I am thankful to him and to Prof. Gustavo Marini, for their support during these years.

An acknowledgement goes to Prof. Francesco De Paola for having enriched these years with various stimulating academic activities.

Many thanks go to Antti Louhio for his help with experiments at the Environmental Hydraulics Lab and to Antonio Fusco and Domenico Palmiero for their continuous help with the experimental setup at the Laboratory of Hydraulics at DICEA.

Special greetings to Walter, for our discussions during the long-lasting laboratory sessions. Affectionately thanks go to Giuseppe, with whom I shared the office during part of my research stay at Aalto University.

Thanks to Vittorio, for his unconditional and friendly support during the initial stage of my PhD.

I thank my colleagues at DICEA. Inevitable thanks go to Diana, Maria Cristina and Ivo. I am particularly thankful to Francesco, who guided me throughout these years, representing an example of dedication to work, and to Andrea, for the inspiring discussions, for his invaluable support, for having believed in me.

I am most grateful to my family, for stimulating me to go always further with enthusiasm, love and laughter. Thanks to Arianna.

Napoli, December 2018
Gerardo

Table of Contents

1 Introduction

Aquatic and riparian vegetation is a fundamental feature of riverine ecosystems playing a variety of valuable ecological and biological roles (Gregory et al., 1991; Naiman et al., 1993; Naiman and Decamps, 1997; Nilsson and Svedmark, 2002). Vegetation in rivers, riparian areas and wetlands has numerous interconnected functions. It provides habitat to a variety of different animal species, creating favorable conditions for several aquatic and terrestrial species, including macroinvertebrates (Milner and Gloyne-Phillips, 2005; Rios and Bailey, 2006), fishes (Meehan et al., 1977; Wesche et al., 1987) and mammals (Doyle, 1990). Riparian vegetation regulates light availability, preventing adverse water temperature fluctuations and mediating concentrations of oxygen, carbon, and nutrients (Carpenter and Lodge, 1986; Tabacchi et al., 1998). Aquatic and riparian vegetation importantly affects the water quality (Connolly et al., 2015; Osborne and Kovacic, 1993). Vegetation reduces the near bed velocities and stresses reinforcing soils against erosion (Ortiz et al., 2013), and provides a stabilizing effects on the soil substrate and on the river banks (Micheli and Kirchner, 2002; Simon and Collison, 2013). Concurrently, the presence of vegetation and its interaction with the flow introduces additional flow resistance, and additional drag forces that notably affect the flow field. Consequently, the presence of vegetation alters hydraulic resistance and water levels, mean and turbulent flow field (Aberle and Järvelä, 2013; Bal et al., 2011; Folkard, 2011; Nepf, 2012a; Nepf et al., 2013; Nezu and Sanjou, 2008; Västilä and Järvelä, 2014), with implications on water conveyance and transport of sediments, contaminants and energy (Gurnell, 2013; Sonnenwald et al., 2015; Vargas-Luna et al., 2015; Zong and Nepf, 2010). In addition, from a river management viewpoint, vegetation presents unused potential to obtain large-scale positive environmental impacts in rivers and streams experiencing anthropogenic pressures. Indeed, vegetation can be used as a nature-based solution for tackling river management problems such as resilience to flooding, transport of substances and improvement of ecological status (Rowiński et al., 2018b).

As a consequence, the hydrodynamics of vegetated channels and the flow-vegetation interaction has been in the focus of several scientific disciplines ranging from aquatic ecology to hydraulic engineering (Aberle and Järvelä, 2015). Specifically, the new interfacial discipline bridging aquatic ecology, biomechanics and environmental fluid dynamics is referred to as *hydrodynamics of aquatic ecosystems* (Nikora, 2010; Nikora et al., 2012). The interest in the characterization of the flow-biota interaction is driven by a variety of applications, ranging from civil and environmental engineering (Escarameia et al., 2002; Kouwen, 1992; Salama and Bakry, 1992) to aquaculture (Folkard and Gascoigne, 2009).

The general objective of this thesis is to improve the understanding of the hydrodynamic interaction between flow and vegetation at the scale of the cross-section and the vegetation patch in partly vegetated channels, with a specific focus on experimental models for vegetation representation.

1.1 Aquatic and riparian vegetation

Vegetation growing in riverine areas presents a variety of characteristics in terms of species, morphology, biomechanical properties and position with respect to the flow. Following the classical submergence-based distinction, depending on the relative height and position of the vegetation with respect to the water depth, it is possible to identify submerged, emergent and floating vegetation. Submerged and floating vegetation is mainly composed by macrophytes occurring in the aquatic zone (Janauer et al., 2013), as schematized in Figure 1. Emergent vegetation, generally found along river margins, is composed by sedges and grasses. Moving further toward the riparian zone, the interfacial zone between aquatic and terrestrial ecosystems interested by the elevated water tables (Naiman et al., 1993), vegetation species are different and prevalently made by woody deciduous trees, shrubs and bushes (Richardson et al., 2007).
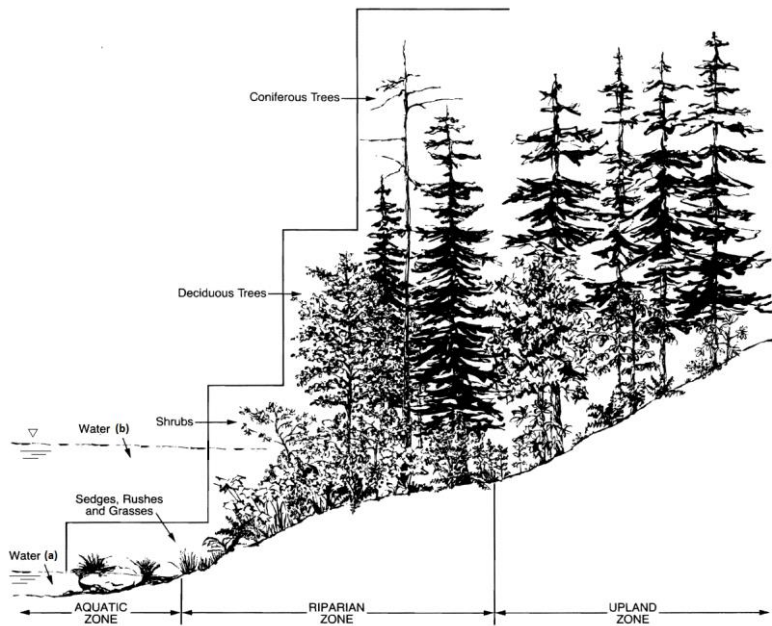
Figure 1 – Example of typical watercourse cross-section with specification of vegetative strata (delimited by black lines). Low- (a) and high-water marks (b) are indicated (Oakley et al., 1985).

This distinction does not take into account the different morphology and bio-mechanical properties (Miler et al., 2012; Niklas, 1997) exhibited by the different species belonging to the various vegetative strata observed in the riparian areas

(Figure 1). In Figure 2 some common riparian and aquatic European vegetation species are indicated. The wide variety of vegetation morphology and biomechanical properties found in riverine areas ranges from blade shaped, highly flexible, submerged vegetation (Figure 2, f) to cylindrical flexible and semi-rigid reeds (Figure 2, e, b), to more complex vegetation, like woody branched and foliated shrubs and trees (Figure 2, a, c, d).

Figure 2 – Common European species of riparian and aquatic vegetation: (a) Salix viminalis; (b) Phragmites australis; (c) Populus alba; (d) riparian forest of Alnus glustinosa; (e) Carex acutiformis; (f) Vallisneria spiralis.

The vegetation response to the flow depends on three types of plant characteristics (Aberle and Järvelä, 2015; Nikora, 2010; Västilä, 2015): biomechanical properties, morphological characteristics and flow-vegetation interaction characteristics. While the characteristics of the flow-vegetation interaction are discussed in more detail in Section 1.3, in this Section some basic concepts about plant morphology and biomechanical properties are provided.

As defined by Aberle and Järvelä (2015), plant morphology describes the visible structure of vegetation and vegetation communities, and is described by linear, areal, volumetric and density parameters. These parameters include e.g. the stem diameter, the canopy height, the frontal projected area, the leaf one sided area, the frontal area per canopy volume, the solid volume fraction etc. The vegetation morphology plays a fundamental role in determining the characteristics of the flow-vegetation interaction, directly affecting the drag forces and the obstruction provided to the flow.

Plant biomechanical properties refers to the material properties of the different plant tissues (Niklas, 1993). The most important plant biomechanical properties are the plant density, the Young's modulus and the second moment of cross-sectional area. These parameters, even if in a simplified way, allow describing the structural response of vegetation to the flow forcing. Indeed, plants can be seen from an engineering point of view, as composite, anisotropic, viscoelastic, highly heterogeneous structures onto which the flow exerts complex loads via tension, compression, bending, torsion and shear (Nikora, 2010). It is possible to classify plants in two categories: (1) tensile plants, presenting a very high flexibility (e.g. Figure 2, f); (2) bending plants, with a relatively high flexural rigidity. Clearly, this definition should take into account the flow characteristics and can be made considering the Cauchy number, i.e. the ratio between the restoring force due to the blade rigidity (proportional to the Young's modulus and the second moment of cross-sectional area) and the drag force (Ghisalberti and Nepf, 2002).

Bending plants, like shrubs and trees found in the riparian areas, remain fairly erect in flow and experience mainly form drag. Form drag arises from differences in pressure between the upstream and downstream sides of plant surfaces. By contrast, tensile plants, including many macrophytes, follow the flow resulting in a prone position. Their flow resistance is thus mainly generated by viscous drag (Miler et al., 2012). Viscous drag results from skin friction and is dominating for plant surfaces having close to a parallel orientation with respect to the main flow direction.

Plant flexibility and biomechanical properties play a fundamental role in the flow-vegetation interaction (Ghisalberti and Nepf, 2006; Ortiz et al., 2013; Västilä et al., 2013). Specifically, aquatic, grassy and woody vegetation exhibit a modification of their shape, frontal projected area and hydraulic behavior under the flow forcing. These processes, described in more detail in Section 1.2.1, are indicated as reconfiguration (Västilä and Järvelä, 2014; Vogel, 1994) and are associated with a reduction in pressure drag and hence form drag, affecting the overall flow structure, hydraulic resistance and the mixing processes within the flow domain.

The morphological and biomechanical properties of plants and plant parts show a high variability with regard to environment, species, and scales (Albayrak et al., 2014; Miler et al., 2014; Niklas, 1993). Additionally, riparian vegetation experiences periodic variability of morphological and biomechanical characteristics, driven by annual and seasonal variation in e.g. temperature, light availability and precipitation (Laine, 2011) and is further influenced by fluvial and hydrologic processes (Naiman and Decamps, 1997).

The most apparent examples of morphological seasonal variability include foliation and leaf shedding, and senescence (Lim et al., 2007; Łoboda et al., 2018). In Figure 3 an example of the effects of seasonal variability is shown with reference to a two-stage channel with vegetated floodplain.
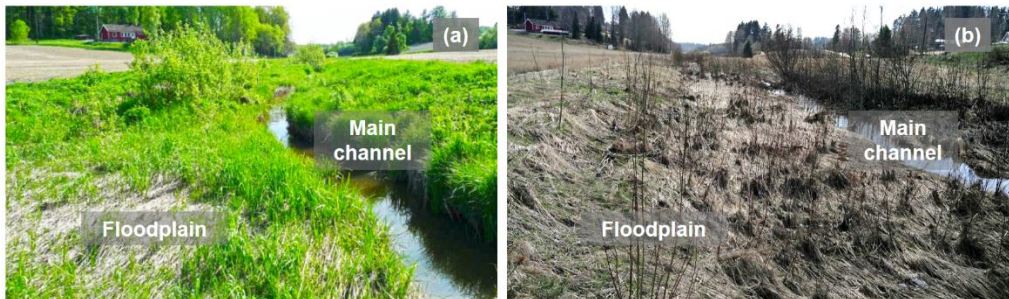
Figure 3 – Seasonal variability of floodplain vegetation morphology: summer (a) and winter (b) conditions. Ritobäcken Brook (Sipoo, Finland). Left photo taken from Rowiński et al. (2018a), right photo by the author.

This seasonal variability of vegetative conditions deeply affects the flow with implications on e.g. hydraulic resistance, flow structure, sediment transport and erosion (Cotton et al., 2006; Shih and Rahi, 1982; Västilä et al., 2016). While the effects of the presence of vegetative obstructions are widely studied, no literature deals with the hydrodynamic effects of the seasonal variability of vegetative obstructions, even though the effects of seasonality can dramatically alter the riparian vegetation morphology.

1.2   Representation of vegetation in laboratory experiments

The need to characterize the flow-vegetation interaction leads to the necessity of defining suitable models for representing vegetation in experimental and numerical studies. The simplest way to describe an individual plant element in hydraulic engineering has been to reduce the plant to a cylindrical shape. In this case, the parameters needed for the morphological description are the stem diameter d and plant height k (Figure 4).

Most of the research on the flow-vegetation interaction has been carried out simulating plants as array of rigid cylinders or rigid prismatic elements (Lopez and Garcia, 2001; Nezu and Sanjou, 2008; Poggi et al., 2004). The results of these studies, partially illustrated throughout this chapter, provided fundamental knowledge in the individuation of the main processes influencing the interaction in terms of turbulent coherent structures and transport of mass and momentum.

Even though the rigid cylinder model allows describing the main effects of the presence of an obstruction in the flow, it neglects a variety of flow-influencing mechanism exhibited by real vegetation. Specifically, rigid cylinders do not allow properly taking into account the complex morphology exhibited by natural

vegetation and its reconfiguration behavior. Moreover, rigid cylinders present a uniform distribution of properties along the elevation, while natural vegetation generally exhibits a heterogeneous distribution of masses and biomechanical properties over the height (Jalonen et al., 2012; Kubrak et al., 2008; Siniscalchi et al., 2012).
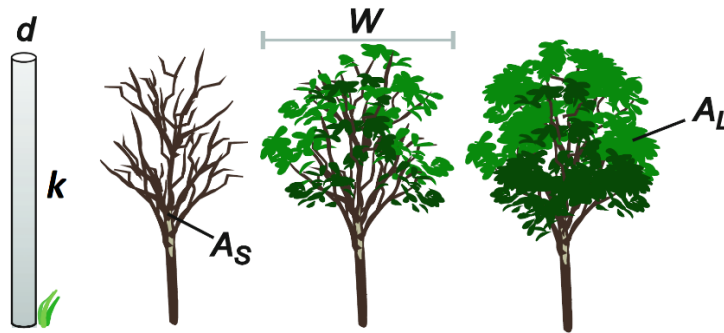
Figure 4 – Definition of parameters for hydraulic description of rigid cylinders and natural vegetation (Aberle and Järvelä, 2015).

As schematically shown in Figure 4, the description of natural riparian vegetation cannot be done with just a characteristic diameter and height. Indeed, complex morphology vegetation is generally composed by different constituents, such as stems, branches, leaves, and therefore a more complete description of areal and volumetric characteristic is needed. To this purpose the frontal projected area of stem A_S and one-sided leaf area A_L can provide a synthetic description of plant morphology. From these parameters, the frontal projected area per canopy volume of stems and leaves (a_S and a_L, respectively) can be derived. Another broadly adopted parameter for the description of natural vegetation is the leaf area index (*LAI*), defined as the one-sided leaf area per unit bed area.

The interaction between simple morphology vegetation (blade shaped tensile aquatic vegetation) and flow has been investigated using prototype or real vegetation (Abdolahpour et al., 2018; Ghisalberti and Nepf, 2002; Nepf et al., 2007; Sukhodolov and Sukhodolova, 2012). These studies highlighted the major differences between rigid and natural vegetation, represented by the dynamic motion exhibited by real vegetative obstructions. The periodical waving, such as the *monami* (Ackerman and Okubo, 1993), has been found to affect the drag discontinuity between the submerged vegetation and overflow, with effects on the coherence of large-scale turbulent structures and, in turn, on the cross-section exchange of mass and momentum (Ghisalberti and Nepf, 2006). These studies demonstrated that embedding realism in model vegetation can profoundly impact the structure of the flow, altering the rate of mixing in current and wave dominated flows (Abdolahpour et al., 2018; Ghisalberti and Nepf, 2006).

Riparian vegetation, made of deciduous trees and shrubs, generally presenting branches and foliation, exhibits a much higher complex morphology (see Figure 2) with direct implications on the complexity of the flow-vegetation interaction. Investigation of flow-vegetation interaction with complex morphology vegetation are much rarer (Järvelä, 2002; Rubol et al., 2018; Västilä et al., 2013) and only few of them focus in deep on the effects ingenerated by riparian vegetation on the turbulent flow field (Siniscalchi et al., 2012).

1.2.1   Drag force and reconfiguration

In order to clarify how the realism in vegetation models can deeply alter the flow-vegetation interaction it is possible to focus briefly on the drag forces exerted on the immersed vegetation. Indeed, the impact of vegetation is largely determined by the additional drag it provides. In presence of relative motion between a flowing fluid and an immersed body, the fluid exerts a force on the object called drag force (Hoerner, 1965). The total force acting on the body is due to two different contributions: (1) the skin drag force, due to the shear stress caused by the viscous interaction between the fluid and the surfaces of the body; and (2) the pressure or form drag, arising from change in pressure over the body surface. The total drag force F can be expressed as:

$$F = \frac{1}{2}\rho C_D A U^2, \tag{1.1}$$

where ρ represents the fluid density, A a reference area of the body, U a reference approach velocity and C_D the dimensionless drag coefficient. The drag coefficient C_D is a function of the object Reynolds number ($Re=UL/\nu$, where L and ν are the characteristic length of the object and the fluid kinematic viscosity, respectively).

For rigid isolated emergent cylinders, C_D is fairly constant at the Re range relevant for practical applications, and can be assumed $C_D\approx1$. In this case the frontal projected area $A_P=dk$ can be assumed as a reference area (Hoerner, 1965).

Although the variation of the drag coefficient with the Reynolds number for isolated cylinders is well understood, the flow pattern around multiple cylinders quickly becomes very difficult to predict as the number of elements increases. The drag coefficient for a single cylinder in an array of cylinders could differ from that for a single cylinder (Blevins, 2003; Nepf, 1999). Moreover, array of rigid cylinders have been used for simulating rigid submerged vegetation, in this configuration the drag coefficient is different (Poggi et al., 2004; Wu et al., 1999).

Dealing with natural riparian vegetation, generally presenting a complex, dynamically varying morphology, the definition of the drag force becomes a difficult task (Luhar and Nepf, 2013).

For natural grassy and woody vegetation, the flexibility induces various changes in the plant shape (and hence in the frontal projected area) and hydraulic behavior under the flow forcing. Because of these processes, considered as a whole and referred to as reconfiguration (de Langre et al., 2012; Vogel, 1989), both the projected area and the drag coefficient decrease with increasing flow velocity (Figure 5), reflecting the effort of the plant to minimize pressure drag (Nikora, 2010; Västilä et al., 2013; Vogel, 1994).
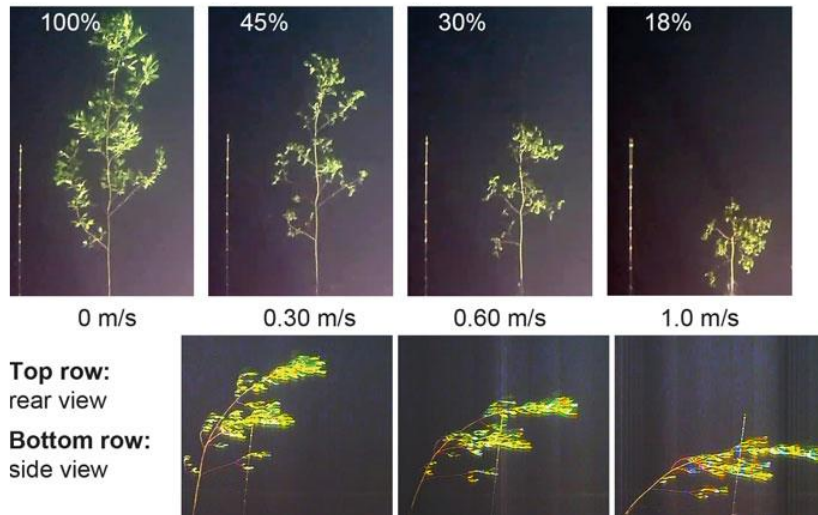
Figure 5 – Reconfiguration of a 1.8 m tall Goat Willow (Salix caprea) exposed to different flow velocities. The percentages indicate the share of the projected area compared to the no-flow case (specimen SC7 from Jalonen and Järvelä (2014), image from Aberle and Järvelä (2015)).

To take reconfiguration into consideration, Equation 1.2, can be modified including the Vogel exponent χ (Vogel, 1989), as:

$$F = \frac{1}{2}\rho C_D A U^{2+\chi}. \tag{1.2}$$

The χ exponent is introduced for describing the non-quadratic relationship between the drag force and the flow velocity resulting from the flexibility-induced reconfiguration. Differently from rigid cylinders, for which $\chi=0$, for natural woody vegetation χ assumes values between -0.7 and -0.9 for foliated conditions and between -0.2 and -0.5 for leafless conditions (for approach velocity <1 m/s) (Jalonen and Järvelä, 2014; Västilä and Järvelä, 2014; Whittaker et al., 2015). Based on Equation 1.2, different models taking into account the reconfiguration have been presented for the prediction of the drag and the flow resistance of woody vegetation (Kouwen and Fathi-Moghadam, 2000; Västilä and Järvelä, 2014; Whittaker et al., 2015).

1.2.2 Uniformly, partly and patchy vegetated channels

Vegetation in aquatic ecosystems generally forms colonies commonly arranged into spatially complex configurations composed by vegetation patches and vegetation-free areas (Sukhodolova and Sukhodolov, 2012). Therefore, another simplification generally introduced in the analysis of flow-vegetation interaction is the spatial representation of vegetation. The problem, from two different perspectives, concerns both aquatic tensile vegetation and riparian complex morphology plants.

The effects on the flow of a uniformly distributed canopy of submerged aquatic vegetation have been widely studied using both rigid and flexible vegetation models (Ghisalberti and Nepf, 2002; Maltese et al., 2007; Nezu and Sanjou, 2008; Poggi et al., 2004; Raupach et al., 1996). Nevertheless, in riverine aquatic ecosystems vegetation generally aggregates forming densely populated communities arranged into spatially complex mosaics comprising vegetation patches and vegetation-free areas (Nikora, 2010; Schoelynck et al., 2012; Sukhodolova and Sukhodolov, 2012). Even though biomechanical properties of individual vegetation elements characterize the response of a patch to the flow (Luhar and Nepf, 2011; Niklas, 1993; Sukhodolova and Sukhodolov, 2012), most relevant interactions between turbulent flow and aquatic vegetation are reported on a scale of patches (Ghisalberti and Nepf, 2002; Ortiz et al., 2013; Zong and Nepf, 2010).
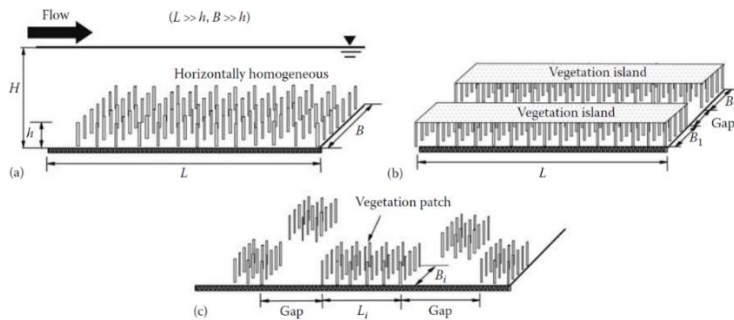
Figure 6 – Schematization of uniformly (a), partly (b) and patchy (c) vegetated channels (Nezu and Okamoto, 2012).

Riparian vegetation, generally made of complex morphology shrubs and trees, emerging from the water table, is observed to occur along river banks, margins and floodplains, in lateral zones approximately parallel to the flow. In these configurations, referred to as channel-vegetated-bank systems (White and Nepf, 2008), the main feature of the flow-vegetation interaction is represented by the mutual interactions between the flow evolving in the main channel and the flow within the adjacent vegetated area. The exchange of mass and momentum between the main channel and the vegetated floodplain is of fundamental importance for the

characterization of the mixing at the cross-section-scale, with implications on sediment and pollutant transport.

The features of the flow in a uniformly vegetated channel through a canopy of emergent vegetation has been widely investigated, mainly simulating vegetation using rigid cylinders (Liu et al., 2008; Nepf, 1999; Stoesser et al., 2010; Tanino and Nepf, 2008). Simple reed-like vegetation has been used (Li et al., 2015; Nepf and Vivoni, 2000) but only few studies with complex morphology vegetation are available (Järvelä, 2002; Siniscalchi et al., 2012) and none of them refers to a spatial configuration of partly vegetated channel, more effective for simulating the presence of riparian vegetation. The characteristics of the flow in partly vegetated channels have been commonly investigated by simulating plants as rigid cylinders (Ben Meftah et al., 2014; Choi and Kang, 2006; Naot et al., 1996; Tsujimoto and Kitamura, 1992; White and Nepf, 2008) and the effects of plant morphology are not yet explored.

1.3 Flow-vegetation interaction: a multi-scale process

A characteristic feature of flow-vegetation interaction is represented by the variety of temporal and spatial scales at which the process takes place (Luhar and Nepf, 2013), depending on how characteristic physical scales of the aquatic ecosystem match the vegetation scales (like leaves, stems, vegetation or vegetation patches dimensions) (Nikora et al., 2012). Flow variability in watercourses, as illustrated by Nikora et al. (2012), covers a wide range of temporal and spatial scales, ranging from milliseconds to many years and from sub-millimeters to tens of kilometers. In Figure 7 the flow scales variability is summarized by schematic velocity spectra, showing how the energy of fluctuations is distributed across the scales.
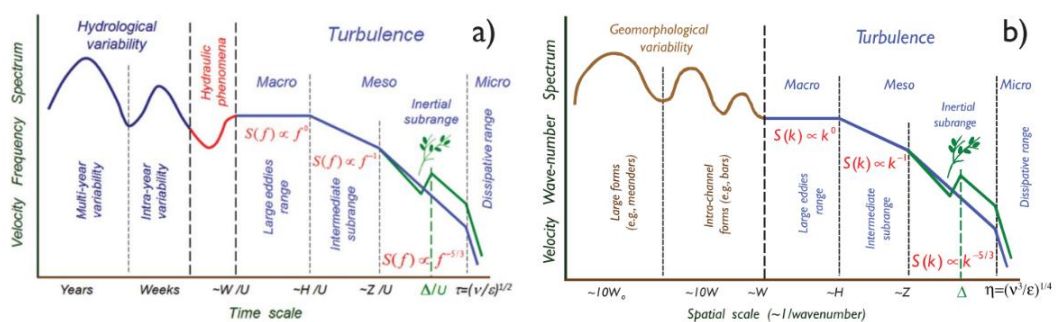
Figure 7 – Schematized velocity spectra in rivers: (a) frequency spectrum; and (b) wave-number spectrum (W_0 and W represent the river valley and river channel width, H the water depth, Z the distance from the bed, Δ represents the plant scale, U the flow velocity and η the turbulence micro-scale) (Nikora et al., 2012).

The low frequency and wavenumber flow variability is driven by abiotic factors and triggers hydrogeological and morphological variability, respectively. At smaller

spatial and temporal scales (comparable to and less than the flow characteristic scales), velocity fluctuations are due to turbulence. This range of scales is most relevant to vegetation since plants scales (Δ) generally fall into this range. This is the range of frequency at which the presence of vegetation mainly alters the velocity spectra (green line in Figure 7) interacting with the flow.

Focusing on vegetation and vegetation communities, it is possible to identify four different characteristic scales at which the flow-vegetation interaction takes place (Aberle and Järvelä, 2015; Nikora et al., 2012), schematized in Figure 8:

- sub-organism scale (leaf and stem scale);
- canopy and patch scale;
- mosaic patch scale;
- reach scale.
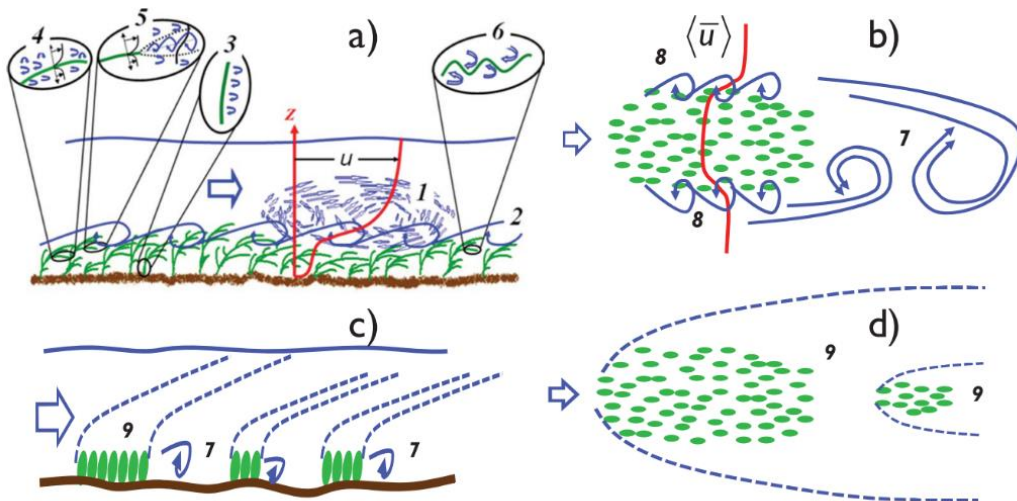
Figure 8 – Conceptual schematization of the flow patterns in vegetated channels: side view at a patch scale (a); plan view at a patch scale (b); side view at a patch mosaic scale (c); and plan view at a patch mosaic scale (d). Depth-scale shear-generated turbulence (1); canopy-height-scale turbulence (2); flow separation generated turbulence (3); small-scale boundary layer turbulence (4); small-scale mixing layer turbulence (5); plant waviness-generated turbulence (6); large-scale structures (7, 8, 9) (Nikora et al., 2012).

Of the abovementioned processes, the sub-organism and canopy scale effects are briefly introduced in Section 1.3.1 and 1.3.2. Further information about the processes at the patch, patch mosaic and reach scale can be found in Aberle and Järvelä (2015), Nepf (2012a, 2012c) and Nikora et al. (2012).

1.3.1 Processes at the sub-organism scale (leaves and stems)

At the scale of individual blades and leaves, the hydrodynamic response is dominated by the boundary-layer (BL) formation on the plant element surfaces (Nepf, 2012c; Nikora et al., 2012). A flat plate BL has often been used as a model for

flow adjacent to leaves oriented in the streamwise (x) direction (Figure 9). A viscous BL forms at the leading edge (x=0), and its thickness, $\delta(x)$, grows with the streamwise distance $\delta(x)=5\sqrt{vx/U}$, with U being the cross-sectional mean velocity and v the kinematic viscosity (Pope, 2000). As the viscous BL grows, it becomes sensitive to perturbations caused by turbulent oscillations in the outer flow or by irregularities in surface texture. At some point along the blade, the BL transitions to a turbulent BL with a viscous sub-layer, δ_S. The transition occurs near $Re_x= xU/v \approx 5 \cdot 10^5$, but this can be modified by surface roughness (White, 2010). If the blade length is less than the transition length, the BL is laminar over the entire blade. If the BL becomes turbulent, the viscous sub-layer has a constant thickness set by the friction velocity on the blade, u_{b*}. Within this layer, the flow is essentially laminar.
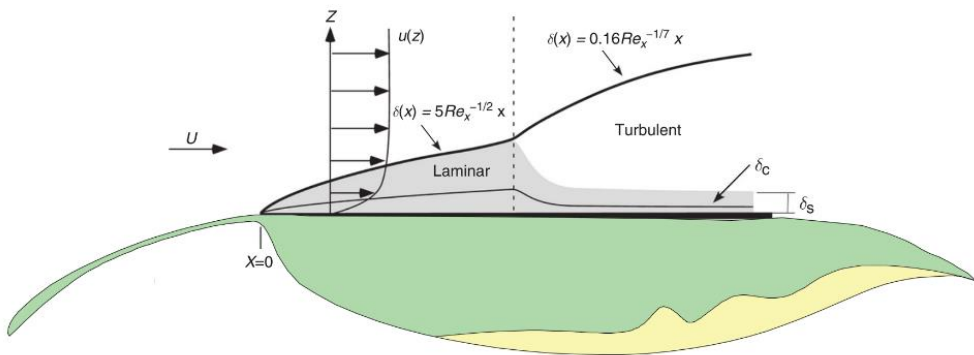
Figure 9 – Evolution of a boundary layer on a leaf. The vertical coordinate is exaggerated. The momentum boundary layer δ grows with the distance from the leading edge x=0. Initially the boundary layer is laminar (shaded grey). At distance x corresponding to $Re_x= xU/v \approx 5 \cdot 10^5$, the boundary layer becomes turbulent, except for a thin layer near the surface that remains laminar, called the viscous sub-layer δ_S (Modified from Nepf, 2012b).

At this scale the flow-vegetation interaction governs the nutrient uptakes (Nepf, 2012c; Thomas et al., 2000). The introduced behavior assumes that the BL is static in time. Some authors have suggested that outer turbulence, waves, and blade motion may periodically disturb the sublayer, replacing the fluid next to the surface with fluid from outside the BL, altering the BL characteristics (Nepf, 2012b and reference therein).

Because of their approximately cylindrical geometry (Figure 10), branches and stems of many aquatic and riparian species can generate turbulence. The cross-section has diameter d. When the branch-scale Reynolds number, $Re_d=Ud/v$, is large enough, the branch sheds a continuous street of vortices of scale d. Von Kármán type vortex shedding is common behind all bluff cross-sections, that is, sections for which the width is comparable to or greater than the thickness. For an isolated cylinder, vortex shedding is initiated at around Re_d=50.

However, within a canopy, the wakes generated by upstream stems can delay the onset of vortex shedding to higher Re_d (Dybbs and Edwards, 1984). For canopies of solid volume fraction between 1% and 7%, vortex shedding is not initiated until Re_d=150-200 (Nepf et al., 1997). Vortex generation drains energy from the mean flow (expressed in form drag) and feeds it into the turbulent kinetic energy (TKE) at the scale of the individual elements.

Laminar wake   Turbulent wake
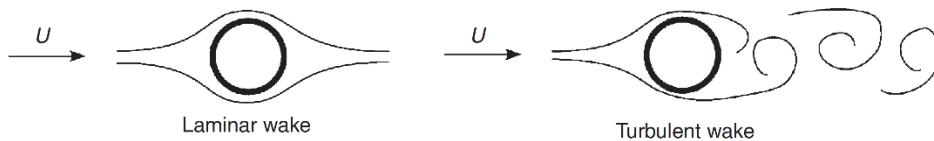
Figure 10 – Streamlines around a cylinder with diameter d. For Re_d=Ud/ν<5, there is no vortex shedding and the wake is laminar (a). For Re_d>50, flow separates from the cylinder surface, and a street of alternating vortices is shed from the cylinder (b). The shed vortices contribute turbulence at scale d to the ambient flow (Nepf, 2012c)

In addition to the small scale turbulence associated with flow separation from stems, and the local small scale BL attached to leaf and stem surfaces (respectively patterns 3 and 4 in Figure 8), leaves and stems generate small scales mixing layers (ML). Leaves act as small splitter plates generating small scale ML and associated turbulence through Kelvin-Helmholtz (KH) type instabilities (pattern 5 of Figure 8). Finally, as schematized in pattern 6 of Figure 8, leaf and stem waviness generates turbulence at a range of scales.

1.3.2   Processes at the canopy scale

Depending on the vegetation spatial arrangement and the relative submergence of the canopy (i.e. the water depth h to canopy height k ratio, indicated as submergence ratio), the flow-vegetation interaction assumes different features.

1.3.2.1   *Uniform canopies of submerged vegetation*

For submerged conditions, the flow depth exceeds the (deflected) canopy height, h/k>1. In this condition, the flow within the submerged canopy is driven by the turbulent stress at the canopy top and by gravity (Nepf, 2012b). Depending on h/k, it is possible to distinguish: deeply submerged canopies (h/k>10) and shallow submerged canopies (1<h/k<5) (Nepf and Vivoni, 2000). The flow over deeply submerged canopies resembles unconfined terrestrial flows (Finnigan, 2000; Raupach et al., 1996). In this conditions, the contribution of pressure gradients (gravity) in driving the flow within the canopy is negligible. In the context of vegetated flows, owing to the constraint of light, deeply submerged conditions are rare.

Following the schematization of Nepf (2012b), depending on the relative importance of the bed drag and the canopy drag, it is possible to define two different limit behaviors. When the canopy drag is small compared to the bed drag, like for

sparse canopies or leafless canopies, the velocity follows a turbulent BL (Figure 11, a). On the other hand, when the canopy drag is large, like for dense canopies or foliated vegetation, the discontinuity in drag at the canopy top generates a region of shear, resembling a free shear layer with an inflection point approximately located at the top of the canopy. Quantitative indications are provided by the drag-area parameter $C_D ak$ (Belcher et al., 2003; Nepf et al., 2007), product between the drag coefficient of the canopy C_D, the frontal area per canopy volume a and the canopy height k, as indicated in Figure 11.

For dense canopies, Raupach et al. (1996) demonstrated the analogy between the canopy shear layers and free shear layers. In such flows, the inflection point observed in the velocity profile due to the high momentum absorption of the canopy, triggers KH type instabilities that in turn lead to the generation of KH vortices (Ash and Khorrami, 1995). These vortices are often referred to as canopy-scale vortices (Nepf, 2012b; Poggi et al., 2004). The presence of these turbulent structures deeply affects the transport of mass and momentum across the vegetative interface (Finnigan, 2000; Ghisalberti and Nepf, 2002).
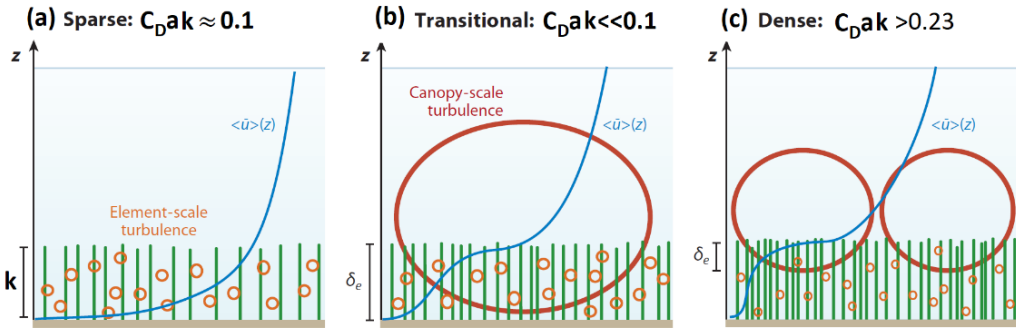
Figure 11 – Vertical profiles of longitudinal velocity and specification of dominant turbulent structures shown for sparse canopy (a), transitional canopy (b) and dense canopy (c) (Nepf, 2012b).

In Figure 11 the dominant turbulent structures are indicated for sparse (a), transitional (b) and dense canopies (c), respectively. With increasing density, concurrently with the modification of the velocity profile, the flow, firstly dominated by stem-scale turbulence, turns to be dominated by canopy-scale large turbulent structures. The canopy density also regulates the penetration of the canopy-scale structures into the vegetation.

The vortex penetration length scale δ_e, in the fully developed region, scales as (Nepf et al., 2007):

$$\delta_e = \frac{0.23 \pm 0.06}{C_D a}. \tag{1.3}$$

It is worth observing that the word density refers to the traditional schematization of vegetation by rigid cylinders. For complex morphology vegetation, such as riparian vegetation, the concept of density, in terms of number of stems per unit bed area, can be misleading. Indeed, also considering the same number of stems per unit bed area, the presence of foliation can completely alter the canopy drag.

The penetration of large-scale turbulent structures set the turbulence intensities within the vegetation and the bed, with important implications on erosion, ventilation and forces acting on vegetation (Nikora, 2010).

In contrast to canonical free shear layers, vegetated shear layers attain stabilization at a certain distance from the origin of the layer. This is due to the equilibrium between the production of shear layer-scale TKE and its dissipation within the canopy (Ghisalberti and Nepf, 2004; Sukhodolova and Sukhodolov, 2012).

The submergence ratio h/k can also affect the penetration length scale. For $h/k<2$, δ_e diminishes, as the interaction with the water surface diminishes the strength and scale of the vortices (Nepf and Vivoni, 2000; Okamoto and Nezu, 2009).

Okamoto and Nezu (Okamoto and Nezu, 2009) observed increased momentum absorption by flexible canopies, since larger penetration depth was observed for rigid canopies. Flexible canopies show often a waving motion, known as *monami* (Ackerman and Okubo, 1993; Nepf, 2012b; Okamoto and Nezu, 2013). This motion, which is the effect of the passage of canopy-scale structures (Ghisalberti and Nepf, 2002; Okamoto and Nezu, 2009), generates turbulence. The periodical waving of vegetation has been found to affect the drag discontinuity between the submerged vegetation and overflow, with implication on coherent structures and, in turn, on cross-section exchange of mass and momentum (Ghisalberti and Nepf, 2006). Depending also on biomechanical properties, it remains to be investigated to what extent these properties affect mixing layer eddies and the *monami* (Aberle and Järvelä, 2015; Nikora, 2010).

The introduced hydrodynamic processes for submerged vegetation are schematized in Figure 8 (a), by flow patterns 1 and 2. Specifically, pattern 1 represents the conventional depth-scale shear generated turbulence associated with perturbed BLs in the region above the canopy. Pattern 2 represents the canopy-scale structures associated with the KH instabilities at the upper boundary of the vegetation canopy.

1.3.2.2   *Uniform canopies of emergent vegetation*
Emergent canopies pierce the water surface filling the entire water depth $h/k<1$. The flow through the canopy is driven by the pressure gradients (gravity). This type of canopy is representative of riparian and floodplain shrubby vegetation. The flow is

dominated by sub-organism small-scale turbulent structures associated with flow separation at the scale of the stems (see previous Section 1.3.1).

Specifically, the canopy dissipates turbulence with scales greater than those of the spacing among elements and the stem diameter, while generating supplementary turbulent energy at these scales. As a result, the dominant turbulent length scale within a canopy is determined by the stem diameter or the stem spacing, regardless of the water depth (Tanino and Nepf, 2008). If the stem diameter d is smaller than the spacing among elements, turbulence is generated within stem wakes. Inversely, turbulence is generated within the pore channels at the scale of the spacing (Nepf, 2012b).

Vortex generation by stem wakes and/or in pore channels drains energy from the mean flow (expressed in terms of canopy drag) and feeds it into the TKE. If this conversion is 100% efficient, then the rate at which TKE per unit mass is produced by wakes, P_w, is equal to the rate at which mean flow energy is extracted, i.e., the rate of work done by the flow against canopy drag (Nepf and Vivoni, 2000):

$$P_w = \frac{1}{2} C_D a U^3, \tag{1.4}$$

where U represents a reference velocity. In fact, only the form drag is converted into TKE. The viscous drag component is immediately dissipated to heat. For rigid canopies and $Re_d > \approx 200$, the majority of the drag is form drag, and Equation 1.4 is a reasonable approximation (Tanino & Nepf 2008a,b). In contrast, for highly flexible canopies the drag is predominantly viscous, and Equation 1.4 would overestimate the stem-scale turbulence production. For complex morphology vegetation both the components are important, and the relative contributions of viscous drag and form drag depend on the morphology and alignment (streamlined versus bluff) of leaves and stems within the canopy.

For emergent vegetation, additional TKE per unit mass is produced at rate P_S by the shear at the bed:

$$P_s = -\overline{u_i' u_j'} \frac{\partial \overline{u_i}}{\partial y}, \tag{1.5}$$

where u_i' is the velocity fluctuation in the i direction, y is the vertical coordinate with origin at the boundary and the overbars indicate a temporal average. For submerged vegetation, the shear layer at the open-water vegetation interface represents another mechanism of TKE production.

1.3.2.3   *Emergent canopies of finite width*
As introduced in the previous Section 1.1, in many environmental settings vegetation occurs in lateral zones approximately parallel to the flow, creating

vegetated areas of finite width B_V along the bank (Figure 12). Owing to the obstruction provided by vegetation, much of the approaching flow is deflected laterally in the main channel. The flow deflection was observed to begin upstream to the patch, over a distance scaling with B_V, and extends up to a distance x_D into the vegetation (Nepf, 2012a; Zong and Nepf, 2010). With reference to an array of rigid cylinders, x_D was found to scale with the larger between B_V and $2(C_D a)^{-1}$ (Rominger and Nepf, 2011). For $x > x_D$ the deflection is complete and the shear layer develops along the main-channel-vegetation interface.
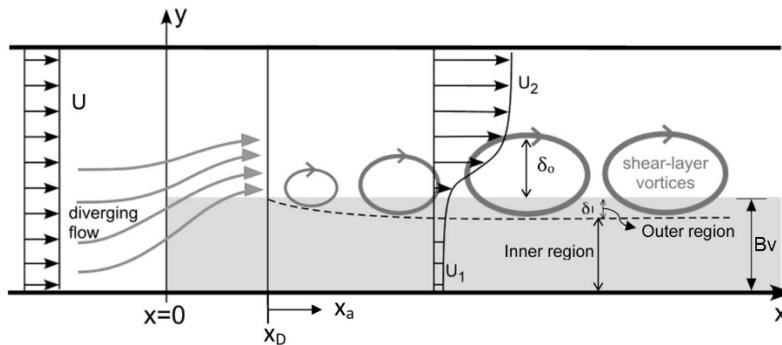
Figure 12 – Conceptual picture of flow field in presence of an emergent vegetative obstruction (grey shaded area) of finite width (top view). The width of the vegetated zone is B_V. The flow approaching the from upstream has uniform velocity U. The ambient flow in the vegetated area is U_1, in the main channel is U_2. The flow begins to deflect at x_D (Zong and Nepf, 2011).

In such channel-vegetated-bank systems, the different drag conditions between the lateral vegetated area and the main channel lead to the formation of two nearly parallel streams of different velocity, U_1 and U_2 in Figure 12. The consequent typical streamwise velocity lateral distribution is characterized by a strong inflectional nature that gives rise to KH type instability (Ash and Khorrami, 1995). The KH vortices at the interface govern the interaction between the two areas of the channel, regulating the mass and momentum exchange between the vegetation and the adjacent open flow (White and Nepf, 2007).

The horizontal shear layer occurring at the interface, as seen for the vertical shear layer generated by submerged vegetation, attains stabilization at a certain distance from the origin of the layer (Dupuis et al., 2017; White and Nepf, 2008). This is due to the equilibrium between the production of shear layer-scale TKE and its dissipation within the canopy (Ghisalberti and Nepf, 2004; Sukhodolova and Sukhodolov, 2012). Moreover, the stabilization of the mixing layer growth is also controlled by the vertical and lateral confinement of the flow produced by the lateral boundaries of the channel and the free surface, and is also influenced by bed friction (Chu and Babarutsi, 1988; Uijttewaal and Booij, 2000).

The vortices extend into the open channel over a length $\delta_0 \approx h/C_f$, where C_f is the bed friction (White and Nepf, 2007)

When fully developed, the canopy scale turbulent structures penetrate the vegetation of δ_I, segregating the canopy in an outer layer, interested by higher turbulence intensities, and an inner layer, sheltered from the shear layer-related turbulence. Based on studies on rigid cylinders, White and Nepf (2008, 2007) found the following scaling:

$$\delta_I = \frac{0.5 \pm 0.1}{C_D a}. \tag{1.6}$$

Based on the results of their experiments, the scale factor for the penetration of canopy-scale vortices for horizontal shear layer was observed to be approximately twice that observed for vertical shear layers above submerged canopies.

Depending on the penetration of vortices, the balance between the two effects in driving the flow within the canopy can change. Indeed, the flow within the lateral vegetated area is driven by pressure gradients and turbulent stress at the interface. If the patch width is greater than the penetration distance, turbulent stress does not penetrate to the centerline of the patch, and the velocity within the patch U_1 is set by a balance of potential gradient (bed and/or water surface slope) and vegetation drag (Nepf, 2012a).

In order to effectively model velocity and other quantities of practical interest, the flow in channel-vegetated-bank systems has been generally considered as canonical mixing-layer (White and Nepf, 2008) or boundary-layer (Ben Meftah et al., 2014) and, even though the occurrence of these flow types in aquatic ecosystems generally deviates from their canonical forms (Nikora et al., 2012), it remains important to define which type of behavior is more suitable for describing the overall flow structure.

Even though the configuration of partly vegetated channels is particularly relevant for the simulation of the effects of riparian vegetation in natural conditions, most of the research on flow-vegetation interaction in partly vegetated channels has been carried out simulating vegetation as arrays of rigid cylinders (Ben Meftah et al., 2014; White and Nepf, 2008, 2007). As illustrated in Section 1.1, in the riparian areas vegetation generally exhibits more complex morphology that, together with the flexibility-induced reconfiguration, is expected to significantly affect the flow structure and associated mixing processes.

1.4 Objectives

As emerged from the literature review, important gaps exist in the knowledge of the hydrodynamic processes related to the presence of riparian vegetation in natural ecosystems and its modelling in experimental studies. The impact of plant dynamic motion and reconfiguration on hydrodynamic processes in vegetated channel are poorly investigated, especially for riparian environments, where vegetation exhibits more complex morphologies.

The specific research questions are referred to the impact of flexibility-induced reconfiguration of plants on the turbulent flow structure in partly vegetated channels, with a specific focus on the lateral distribution of velocity and the transport of momentum. Moreover, the current knowledge of hydrodynamic processes in partly vegetated channels is based on the typical rigid cylinder representation of vegetation. The representativeness of this assumption for the simulation of flow in partly vegetated channels is yet unexplored.

In the framework of this thesis three different experimental investigations were performed in order to improve the understanding of the flow-vegetation interaction in different contexts, considering uniformly and partly vegetated channels. Moreover, with reference to the indications of Section 1.2, the effects of simulating vegetation with rigid cylinders in the context of partly vegetated channels were experimentally investigated.

In terms of spatial distribution of vegetation, two different configurations were investigated: uniformly and partly vegetated channel. Furthermore, two different vegetation models were considered, simulating vegetation with arrays of rigid cylinders (submerged and emergent) and with natural-like plant stands (emerging). The two different spatial configurations (uniformly and partly vegetated channel) and the two different vegetation models (rigid cylinders and natural-like foliated plant stands) resulted altogether in three experimental series:
1. flow over an array of rigid submerged cylinders in a uniformly vegetated channel (indicated in the following as Uniformly Rigid, UR);
2. flow in a partly vegetated channel with natural-like complex morphology plant stands and grassy bed (indicated in the following as Partly Natural-like, PN);
3. flow in a partly vegetated channel with an array of emergent rigid cylinders (indicated in the following as Partly Rigid, PR).

The general information of each test series is reported in Table 1.

Table 1 – Specification of spatial arrangement of vegetation and vegetation model for each test series.

Test series	Configuration	Vegetation model
Uniformly rigid vegetated channel – UR		Rigid cylinders (submerged)
Partly vegetated channel with natural-like plant stands and grassy bed – PN		Natural-like emergent foliated plants and grassy bed
Partly vegetated channel with rigid cylinders – PR		Rigid cylinders (emergent)
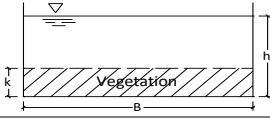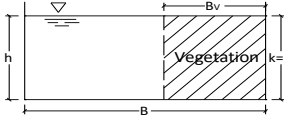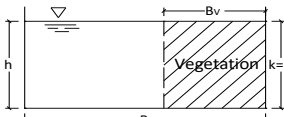
The main objective of the UR test series was to transfer the technique of the anisotropy analysis and the invariant maps to vegetated flows, in order to focus on the turbulence anisotropy at the rigid vegetation-flow interface. In the framework of this thesis, the UR series was performed as to provide a tool for the interpretation of anisotropy patterns at vegetated interfaces performed in the experiments of flow in partly vegetated channels.

The objectives of PN test series was to characterize the effects of morphologically complex vegetation and its seasonal variability on lateral mixing and turbulent flow pattern in a partly vegetated channel. A specific focus was set on the effects of foliation and reconfiguration on the overall flow structure (lateral distributions of velocity statistics), on large coherent turbulent structures (presence and strength), and on the turbulence anisotropy (degree and nature) across the vegetated interface.

PR test series was carried out in order to investigate the conditions, in term of vegetated density shear layer characteristics, for the onset of coherent large-scale structures. Furthermore, these experiments were designed as to provide a data set for benchmarking the rigid vegetation model against the natural-like vegetation model adopted in the PN test series. The PN and PR series were designed with the aim of investigating the suitability of the rigid cylinder model for the reproduction of the effects of natural vegetation in natural watercourses, highlighting the effects of embedding realism in flow-vegetation interaction analysis.

1.5 Publications related to this thesis and author's contribution

The journal papers and proceedings related to this thesis are listed below.

I. Caroppi, G., Gualtieri, P., Fontana, N., Giugni, M., 2018. Vegetated channel flows: turbulence anisotropy at flow-rigid canopy interface. Geosciences 259. doi:10.3390/geosciences8070259.

II. Caroppi, G., Västilä, K., Järvelä, J., Rowiński, P.M., Giugni, M., submitted. Turbulence at water-vegetation interface in open channel flow: experiments with natural-like plants. Submitted to Adv. Water Resour. on 6 August 2018, under revision.

III. Caroppi, G., Västilä, K., Järvelä, J., Rowiński, P.M., 2018. Experimental investigation of turbulent flow structure in a partly vegetated channel with natural-like flexible plant stands, in: Armanini, A., Nucci, E. (Eds.), Proc. of the 5th IAHR Europe Congress - New Challenges in Hydraulic Research and Engineering. Trento, Italy, pp. 615–616. doi:10.3850/978-981-11-2731-1_118-cd.

IV. Caroppi, G., Fontana, N., Giugni, M., Gualtieri, P., 2018. Use of acoustic Doppler velocimetry in vegetated flows, in Proc. of the XXXVI Convegno Nazionale di Idraulica e Costruzioni Idrauliche, Ancona 12-14 September, Italy.

Publication I and IV. The author was mainly responsible for designing the research and the measurements jointly with Prof. Gualtieri. The author was responsible for collecting the data and conducting the analysis. The author was responsible for interpreting the data and writing of the paper. Prof. Gualtieri participated in the interpretation of the results. Prof. Gualtieri, Prof. Fontana and Prof. Giugni participated in the writing of the paper.

Publication II and III. The author designed the measurements jointly with Dr. Västilä and Dr. Järvelä based on the original idea and experimental setup developed by Dr. Västilä and Dr. Järvelä at Aalto University, Finland. The author was responsible for collecting the data and conducting the analyses. The author was mainly responsible for interpreting the results and writing of the paper. Dr. Västilä and Dr. Järvelä participated in the interpretation of the results and writing of the paper. Prof. Rowiński participated in the research design, interpretation of the results and writing of the paper. Prof. Giugni provided comments on the paper.

Chapter 3 is directly based on publication I. Chapter 4 is directly based on publication II.

References

Abdolahpour, M., Ghisalberti, M., Mcmahon, K., Lavery, P.S., 2018. The impact of flexibility on flow , turbulence , and vertical mixing in coastal canopies. doi:10.1002/lno.11008

Aberle, J., Järvelä, J., 2015. Hydrodynamics of Vegetated Channels, in: Rivers-Physical, Fluvial and Environmental Processess. pp. 255–277. doi:10.1007/978-3-319-17719-9

Aberle, J., Järvelä, J., 2013. Flow resistance of emergent rigid and flexible floodplain vegetation. J. Hydraul. Res. 51, 33–45. doi:10.1080/00221686.2012.754795

Ackerman, J.D., Okubo, A., 1993. Reduced Mixing in a Marine Macrophyte Canopy. Funct. Ecol. 7, 305–309. doi:10.2307/2390209

Albayrak, I., Nikora, V.I., Miler, O., O'Hare, M.T., 2014. Flow-plant interactions at leaf, stem and shoot scales: Drag, turbulence, and biomechanics. Aquat. Sci. 76, 269–294. doi:10.1007/s00027-013-0335-2

Ash, R.L., Khorrami, M.R., 1995. Fluid Vortices, Fluid Vor. doi:10.1007/978-94-011-0249-0

Bal, K., Struyf, E., Vereecken, H., Viaene, P., De Doncker, L., de Deckere, E., Mostaert, F., Meire, P., 2011. How do macrophyte distribution patterns affect hydraulic resistances? Ecol. Eng. 37, 529–533. doi:10.1016/j.ecoleng.2010.12.018

Belcher, S.E., Jerram, N., Hunt, J.C.R., 2003. Adjustment of a turbulent boundary layer to a canopy of roughness elements. J. Fluid Mech. 488, S0022112003005019. doi:10.1017/S0022112003005019

Ben Meftah, M., De Serio, F., Mossa, M., 2014. Hydrodynamic behavior in the outer shear layer of partly obstructed open channels. Phys. Fluids 26. doi:10.1063/1.4881425

Blevins, R.D., 2003. Applied Fluid Dynamics Handbook. Krieger Pub.

Carpenter, S.R., Lodge, D.M., 1986. Effects of submersed macrophytes on ecosystem processes. Aquat. Bot. 26, 341–370. doi:10.1016/0304-3770(86)90031-8

Choi, S.U., Kang, H., 2006. Numerical investigations of mean flow and turbulence structures of partly-vegetated open-channel flows using the Reynolds stress model. J. Hydraul. Res. 44, 203–217. doi:10.1080/00221686.2006.9521676

Chu, V.H., Babarutsi, S., 1988. Confinement and bed-friction effects in shallow turbulent mixing layers. J. Hydraul. Eng. 114, 1257–1274.

Connolly, N.M., Pearson, R.G., Loong, D., Maughan, M., Brodie, J., 2015. Water quality variation along streams with similar agricultural development but contrasting riparian vegetation. Agric. Ecosyst. Environ. 213, 11–20. doi:10.1016/j.agee.2015.07.007

Cotton, J.A., Wharton, G., Bass, J.A.B., Heppell, C.M., Wotton, R.S., 2006. The effects of seasonal changes to in-stream vegetation cover on patterns of flow and accumulation of sediment. Geomorphology 77, 320–334. doi:10.1016/j.geomorph.2006.01.010

de Langre, E., Gutierrez, A., Cossé, J., 2012. On the scaling of drag reduction by reconfiguration in plants. Comptes Rendus - Mec. 340, 35–40. doi:10.1016/j.crme.2011.11.005

Doyle, A.T., 1990. Use of riparian and upland habitat by small mammals. J. Mammal. 71, 14–23.

Dupuis, V., Proust, S., Berni, C., Paquier, A., 2017. Mixing layer development in compound channel flows with submerged and emergent rigid vegetation over the floodplains. Exp. Fluids 58, 0. doi:10.1007/s00348-017-2319-9

Dybbs, A., Edwards, R. V, 1984. A New Look at Porous Media Fluid Mechanics --- Darcy to Turbulent, in: Bear, J., Corapcioglu, M.Y. (Eds.), Fundamentals of Transport Phenomena in Porous Media. Springer Netherlands, Dordrecht, pp. 199–256. doi:10.1007/978-94-009-6175-3_4

Escarameia, M., Gasowski, Y., May, R., 2002. Grassed drainage channels—hydraullic resistance characteristic. Proc. ICE - Water Marit. Eng. 154, 333–341. doi:10.1680/wame.2002.154.4.333

Finnigan, J.J., 2000. Turbulence in plant canopies 519–571.

Folkard, A.M., 2011. Flow regimes in gaps within stands of flexible vegetation: Laboratory flume simulations. Environ. Fluid Mech. 11, 289–306. doi:10.1007/s10652-010-9197-5

Folkard, A.M., Gascoigne, J.C., 2009. Hydrodynamics of discontinuous mussel beds: Laboratory flume

simulations. J. Sea Res. 62, 250–257. doi:10.1016/j.seares.2009.06.001

Ghisalberti, M., Nepf, H.M., 2006. The structure of the shear layer in flows over rigid and flexible canopies. Environ. Fluid Mech. 6, 277–301. doi:10.1007/s10652-006-0002-4

Ghisalberti, M., Nepf, H.M., 2004. The limited growth of vegetated shear layers. Water Resour. Res. 40, 1–12. doi:10.1029/2003WR002776

Ghisalberti, M., Nepf, H.M., 2002. Mixing layers and coherent structures in vegetated aquatic flows. J. Geophys. Res. 107, 1–11. doi:10.1029/2001JC000871

Gregory, S. V, Swanson, F.J., Mckee, W.A., Kenneth, W., Swanson, J., Cummins, K.W., 1991. An Ecosystem Perspective of Riparian Zones Focus on links between land and water. Bioscience 41, 540–551. doi:10.2307/1311607

Gurnell, A., 2013. Plants as river system engineers. Earth Surf. Process. Landforms 40, 135–137. doi:10.1002/esp.3671

Hoerner, S.F., 1965. Fluid Dynamic Drag. Hoerner Fluid Dynamics, Bakersfield.

Jalonen, J., Järvelä, J., 2014. Estimation of drag forces caused by natural woody vegetation of different scales. J. Hydrodyn. 26, 608–623. doi:10.1016/S1001-6058(14)60068-8

Jalonen, J., Järvelä, J., Aberle, J., 2012. Vegetated flows: Drag force and velocity profiles for foliated plant stands, in: Taylor & Francis, L. (Ed.), Proceedings of River Flow 2012, International Conference on Fluvial Hydraulics. San José.

Janauer, G.A., Schmidt-mumm, U., Reckendorfer, W., 2013. Ecohydraulics and Aquatic Macrophytes : Assessing 245–259.

Järvelä, J., 2002. Flow resistance of flexible and stiff vegetation: A flume study with natural plants. J. Hydrol. 269, 44–54. doi:10.1016/S0022-1694(02)00193-2

Kouwen, N., 1992. Modern Approach to Design of Grassed Channels. J. Irrig. Drain. Eng. 118, 733–743. doi:10.1061/(ASCE)0733-9437(1992)118:5(733)

Kouwen, N., Fathi-Moghadam, M., 2000. Friction factors for coniferous trees along rivers. J. Hydraul. Eng. 126, 732–740.

Kubrak, E., Kubrak, J., Rowinski, P.M., 2008. Vertical velocity distributions through and above submerged, flexible vegetation. Hydrol. Sci. Journal-Journal Des Sci. Hydrol. 53, 905–920. doi:10.1623/hysj.53.4.905

Laine, C.M., 2011. An Assessment of Vegetation Metrics and Plot Types to Measure Seasonal Variation and Grazing Effects on Riparian Plant Communities 75, 1–49. doi:10.3398/064.075.0111

Li, Y., Du, W., Yu, Z., Tang, C., Wang, Y., Anim, D.O., Ni, L., Lau, J., Chew, S.A., Acharya, K., 2015. Impact of flexible emergent vegetation on the flow turbulence and kinetic energy characteristics in a flume experiment. J. Hydro-Environment Res. 9, 354–367. doi:10.1016/j.jher.2014.01.006

Lim, P.O., Kim, H.J., Gil Nam, H., 2007. Leaf Senescence. Annu. Rev. Plant Biol. 58, 115–136. doi:10.1146/annurev.arplant.57.032905.105316

Liu, D., Diplas, P., Fairbanks, J.D., Hodges, C.C., 2008. An experimental study of flow through rigid vegetation. J. Geophys. Res. Earth Surf. 113, 1–16. doi:10.1029/2008JF001042

Łoboda, A.M., Przyborowski, Karpiński, M., Bialik, R.J., Nikora, V.I., 2018. Biomechanical properties of aquatic plants: The effect of test conditions. Limnol. Oceanogr. Methods 222–236. doi:10.1002/lom3.10239

Lopez, F., Garcia, M.H., 2001. Mean Flow and Turbulence Structure of Open-Channel Flow Through Non-Emergent Vegetation. J. Hydraul. Eng. 127, 392–402. doi:10.1061/(ASCE)0733-9429(2001)127:5(392)

Luhar, M., Nepf, H.M., 2013. From the blade scale to the reach scale: A characterization of aquatic vegetative drag. Adv. Water Resour. 51, 305–316. doi:10.1016/j.advwatres.2012.02.002

Luhar, M., Nepf, H.M., 2011. Flow-induced reconfiguration of buoyant and flexible aquatic vegetation. Limnol. Oceanogr. 56, 2003–2017. doi:10.4319/lo.2011.56.6.2003

Maltese, A., Cox, E., Folkard, A.M., Ciraolo, G., La Loggia, G., Lombardo, G., 2007. Laboratory

measurements of flow and turbulence in discontinuous distributions of Ligulate seagrass. J. Hydraul. Eng. 133, 750–760.

Meehan, W.R., Swanson, F.J., Sedell, J.R., 1977. Influences of Riparian Vegetation on Aquatic Ecosystems with Particular Reference to Salmonid Fishes and Their Food Supply. USDA For. Serv. Gen. … 137–145.

Micheli, E.R., Kirchner, J.W., 2002. Effects of wet meadow riparian vegetation on streambank erosion. 2. Measurements of vegetated bank strength and consequences for failure mechanics. Earth Surf. Process. Landforms 27, 687–697. doi:10.1002/esp.340

Miler, O., Albayrak, I., Nikora, V.I., O'Hare, M., 2014. Biomechanical properties and morphological characteristics of lake and river plants: implications for adaptations to flow conditions. Aquat. Sci. 76, 465–481. doi:10.1007/s00027-014-0347-6

Miler, O., Albayrak, I., Nikora, V.I., O'Hare, M.T., 2012. Biomechanical properties of aquatic plants and their effects on plant – flow interactions in streams and rivers 31–44. doi:10.1007/s00027-011-0188-5

Milner, A.M., Gloyne-Phillips, I.T., 2005. The role of riparian vegetation and woody debris in the development of macroinvertebrate assemblages in streams. River Res. Appl. 21, 403–420. doi:10.1002/rra.815

Naiman, R.J., Decamps, H., 1997. The ecology of interfases: Riparian Zones. Annu. Rev. Ecol. Evol. Syst. 28, 621–658. doi:10.1146/annurev.ecolsys.28.1.621

Naiman, R.J., Decamps, H., Pollock, M., 1993. The Role of Riparian Corridors in Maintaining Regional Biodiversity. Ecol. Appl. 3, 209–212. doi:10.2307/1941822

Naot, D., Nezu, I., Nakagawa, H., 1996. Hydrodynamic Behavior of Partly Vegetated Open Channels. J. Hydraul. Eng. 122, 625–633. doi:10.1061/(ASCE)0733-9429(1996)122:11(625)

Nepf, H.M., 2012a. Hydrodynamics of vegetated channels. J. Hydraul. Res. 50, 262–279. doi:10.1080/00221686.2012.696559

Nepf, H.M., 2012b. Flow and Transport in Regions with Aquatic Vegetation. Annu. Rev. Fluid Mech. 44, 123–142. doi:10.1146/annurev-fluid-120710-101048

Nepf, H.M., 2012c. Flow Over and Through Biota, Treatise on Estuarine and Coastal Science. Elsevier Inc. doi:10.1016/B978-0-12-374711-2.00213-8

Nepf, H.M., 1999. Drag, turbulence, and diffusion in flow through emergent vegetation. Water Resour. Res. 35, 479–489. doi:10.1029/1998WR900069

Nepf, H.M., Ghisalberti, M., White, B.L., Murphy, E., 2007. Retention time and dispersion associated with submerged aquatic canopies 43, 1–10. doi:10.1029/2006WR005362

Nepf, H.M., Rominger, J., Zong, L., 2013. Coherent Flow Structures in Vegetated Channels i, 135–147.

Nepf, H.M., Sullivan, J. a., Zavistoski, R. a., 1997. A model for diffusion within emergent vegetation. Limnol. Oceanogr. 42, 1735–1745. doi:10.4319/lo.1997.42.8.1735

Nepf, H.M., Vivoni, E.R., 2000. Flow structure in depth-Iimited, vegetated flow. J. Geophys. Res. 105, 28547–28557.

Nezu, I., Okamoto, T., 2012. Hydraulics of Vegetated Canopies, in: Handbook of Environmental Fluid Dynamics, Volume One. pp. 285–309. doi:doi:10.1201/b14241-27\r10.1201/b14241-27

Nezu, I., Sanjou, M., 2008. Turburence structure and coherent motion in vegetated canopy open-channel flows. J. Hydro-Environment Res. 2, 62–90. doi:10.1016/j.jher.2008.05.003

Niklas, K.J., 1997. Mechanical properties of black locust (Robinia pseudoacacia L) wood. Size and age-dependent variations in sap and heartwood. Ann. Bot. 79, 265–272. doi:DOI 10.1006/anbo.1996.0340

Niklas, K.J., 1993. Plant biomechanics: An engineering approach to plant form and function, Trends in Ecology & Evolution. doi:10.1016/0169-5347(93)90072-W

Nikora, V.I., 2010. Hydrodynamics of aquatic ecosystems: an interface between ecology, biomechanics and environmental fluid mechanics. River Res. Appl. 26, 367–384. doi:10.1002/rra.1291

Nikora, V.I., Cameron, S., Albayrak, I., Miler, O., Nikora, N., Siniscalchi, F., Stewart, M., 2012. Flow-biota interactions in aquatic systems : Scales, mechanisms, and challenges, in: Environmental Fluid Mechanics. pp. 217–235.

Nilsson, C., Svedmark, M., 2002. Basic principles and ecological consequences of changing water regimes: Riparian plant communities. Environ. Manage. 30, 468–480. doi:10.1007/s00267-002-2735-2

Oakley, A.L., Collins, J.A., Everson, L.B., Heller, D.A., Howerton, J.C., Vincent, R.E., 1985. Riparian zones and freshwater wetlands. Manag. Wildl. fish habitats For. West. Oregon Washington. USDA For. Serv. Portland, Oregon, Publ. No. R 6, 57–80.

Okamoto, T. aki, Nezu, I., 2013. Spatial evolution of coherent motions in finite-length vegetation patch flow. Environ. Fluid Mech. 13, 417–434. doi:10.1007/s10652-013-9275-6

Okamoto, T.A., Nezu, I., 2009. Turbulence structure and "Monami" phenomena in flexible vegetated open-channel flows. J. Hydraul. Res. 47, 798–810. doi:10.3826/jhr.2009.3536

Ortiz, A.C., Ashton, A., Nepf, H.M., 2013. Mean and turbulent velocity fields near rigid and flexible plants and the implications for deposition. J. Geophys. Res. Earth Surf. 118, 2585–2599. doi:10.1002/2013JF002858

Osborne, L.L., Kovacic, D.A., 1993. Riparian vegetated buffer strips in water-quality restoration and stream management. Freshw. Biol. 29, 243–258. doi:10.1111/j.1365-2427.1993.tb00761.x

Poggi, D., Porporato, A., Ridolfi, L., Albertson, J.D., Katul, G.G., 2004. The effect of vegetation density on canopy sub-layer turbulence. Boundary-Layer Meteorol. 111, 565–587. doi:10.1023/B:BOUN.0000016576.05621.73

Pope, S.B., 2000. Turbulent Flows. Cambridge University Press. doi:10.1017/CBO9780511840531

Raupach, M.R., Finnigan, J.J., Brunei, Y., 1996. Coherent eddies and turbulence in vegetation canopies: The mixing-layer analogy. Boundary-Layer Meteorol. 78, 351–382. doi:10.1007/BF00120941

Richardson, D.M., Holmes, P.M., Esler, K.J., Galatowitsch, S.M., Stromberg, J.C., Kirkman, S.P., Pysek, P., Hobbs, R.J., 2007. Riparian vegetation: degradation, alien plant invasions, and restoration prospects RID A-1495-2008 RID F-5883-2010. Divers. Distrib. 13, 126–139. doi:10.1111/j.1472-4642.2006.00314.x

Rios, S.L., Bailey, R.C., 2006. Relationship between riparian vegetation and stream benthic communities at three spatial scales. Hydrobiologia 553, 153–160. doi:10.1007/s10750-005-0868-z

Rominger, J.T., Nepf, H.M., 2011. Flow adjustment and interior flow associated with a rectangular porous obstruction. J. Fluid Mech. 680, 636–659. doi:10.1017/jfm.2011.199

Rowiński, P.M., Aberle, J., Järvelä, J., Kalinowska, M.B., Västilä, K., 2018a. How vegetation can aid in coping with river management challenges: a brief review. Ecohydrol. Hydrobiol.

Rowiński, P.M., Västilä, K., Aberle, J., Järvelä, J., Kalinowska, M.B., 2018b. How vegetation can aid in coping with river management challenges: A brief review. Ecohydrol. Hydrobiol. 1–10. doi:10.1016/j.ecohyd.2018.07.003

Rubol, S., Ling, B., Battiato, I., 2018. Universal scaling-law for flow resistance over canopies with complex morphology. Sci. Rep. 8, 4430. doi:10.1038/s41598-018-22346-1

Salama, M.M., Bakry, M.F., 1992. Design of earthen vegetated open channels. Water Resour. Manag. 6, 149–159. doi:10.1007/BF00872209

Schoelynck, J., De Groote, T., Bal, K., Vandenbruwaene, W., Meire, P., Temmerman, S., 2012. Self-organised patchiness and scale-dependent bio-geomorphic feedbacks in aquatic river vegetation. Ecography (Cop.). 35, 760–768. doi:10.1111/j.1600-0587.2011.07177.x

Shih, S.F., Rahi, G.S., 1982. Seasonal Variation of Manning's Roughness Coefficient in A Subtropical Marsh. Am. Soc. Agric. Eng. 25, 116–119. doi:10.13031/2013.33488

Simon, A., Collison, A.J.C., 2013. Advances in Assessing the Mechanical and Hydrologic Effects of Riparian Vegetation on Streambank Stability. Riparian Veg. Fluv. Geomorphol. 546, 125–139. doi:10.1029/008WSA10

Siniscalchi, F., Nikora, V.I., Aberle, J., 2012. Plant patch hydrodynamics in streams: Mean flow, turbulence, and drag forces. Water Resour. Res. 48, 1–14. doi:10.1029/2011WR011050

Sonnenwald, F., Hart, J.R., Stovin, V.R., Guymer, I., 2015. Transverse and longitudinalmixing in real emergent vegetation at low velocities. Water Resour. Res. 51, 4815–4822. doi:10.1002/2014WR016085

Stoesser, T., Kim, S.J., Diplas, P., 2010. Turbulent Flow through Idealized Emergent Vegetation. J. Hydraul. Eng. 136, 1003–1017. doi:Doi 10.1061/(Asce)Hy.1943-7900.0000153

Sukhodolov, A.N., Sukhodolova, T.A., 2012. Vegetated mixing layer around a finite-size patch of submerged plants: Part 2. Turbulence statistics and structures. Water Resour. Res. 48, 1–16. doi:10.1029/2011WR011804

Sukhodolova, T.A., Sukhodolov, A.N., 2012. Vegetated mixing layer around a finite-size patch of submerged plants: Part 1. Theory and field experiments. Water Resour. Res. 48, 1–16. doi:10.1029/2011WR011804

Tabacchi, E., Correll, D.L., Hauer, R., Pinay, G., Planty-Tabacchi, A.M., Wissmar, R.C., 1998. Development, maintenance and role of riparian vegetation in the river landscape. Freshw. Biol. 40, 497–516. doi:10.1046/j.1365-2427.1998.00381.x

Tanino, Y., Nepf, H.M., 2008. Laboratory Investigation of Mean Drag in a Random Array of Rigid, Emergent Cylinders. ReCALL 34–41.

Thomas, F.I.M., Cornelisen, C.D., Zande, J.M., 2000. Effects of Water Velocity and Canopy Morphology on Ammonium Uptake by Seagress Communities. Ecol. Soc. Am. 1, 2704–2713. doi:10.1017/CBO9781107415324.004

Tsujimoto, T., Kitamura, I., 1992. Appearance of Organized Fluctuations in Open-channel Flow with Vegetated Zone. KHL Progress. Rep. '92 21–35.

Uijttewaal, W.S.J., Booij, R., 2000. Effects of shallowness on the development of free-surface mixing layers. Phys. Fluids 12, 392–402. doi:10.1063/1.870317

Vargas-Luna, A., Crosato, A., Uijttewaal, W.S.J., 2015. Effects of vegetation on flow and sediment transport: Comparative analyses and validation of predicting models. Earth Surf. Process. Landforms 40, 157–176. doi:10.1002/esp.3633

Västilä, K., 2015. Flow–plant–sediment interactions: Vegetative resistance modeling and cohesive sediment processes.

Västilä, K., Järvelä, J., 2014. Modeling the flow resistance of woody vegetation using physically based properties of the foliage and stem. Water Resour. Res. 50, 229–245. doi:10.1002/2013WR013819

Västilä, K., Järvelä, J., Aberle, J., 2013. Characteristic reference areas for estimating flow resistance of natural foliated vegetation 492, 49–60. doi:10.1016/j.jhydrol.2013.04.015

Västilä, K., Järvelä, J., Koivusalo, H., 2016. Flow-Vegetation-Sediment Interaction in a Cohesive Compound Channel. J. Hydraul. Eng. 142, 1--1. doi:10.1061/(ASCE)HY.1943-7900.0001058.

Vogel, S., 1994. Life in Moving Fluids The Physical Biology of Flow, 2nd ed. Princeton University Press.

Vogel, S., 1989. Drag and Reconfiguration of Broad Leaves in High Winds. J. Exp. Bot. 40, 941–948. doi:10.1093/jxb/40.8.941

Wesche, T.A., Goertler, C.M., Frye, C.B., 1987. Contribution of Riparian Vegetation to Trout Cover in Small Streams. North Am. J. Fish. Manag. 7, 151–153. doi:10.1577/1548-8659(1987)7<151:CORVTT>2.0.CO;2

White, B.L., Nepf, H.M., 2008. A vortex-based model of velocity and shear stress in a partially vegetated shallow channel. Water Resour. Res. 44, 1–15. doi:10.1029/2006WR005651

White, B.L., Nepf, H.M., 2007. Shear instability and coherent structures in shallow flow adjacent to a porous layer. J. Fluid Mech. 593, 1–32. doi:10.1017/S0022112007008415

White, F., 2010. Fluid Mechanics. McGraw-Hill,New York 862. doi:10.1111/j.1549-8719.2009.00016.x.Mechanobiology

Whittaker, P., Wilson, C.A.M.E., Aberle, J., 2015. An improved Cauchy number approach for

predicting the drag and reconfiguration of flexible vegetation. Adv. Water Resour. 83, 28–35. doi:10.1016/j.advwatres.2015.05.005

Wu, F.-C., Shen, H.W., Chou, Y.-J., 1999. Variation of roughness coefficients for unsubmerged and submerged vegetation. J. Hydraul. Eng. 934–942.

Zong, L., Nepf, H.M., 2011. Spatial distribution of deposition within a patch of vegetation. Water Resour. Res. 47. doi:10.1029/2010WR009516

Zong, L., Nepf, H.M., 2010. Flow and deposition in and around a finite patch of vegetation. Geomorphology 116, 363–372. doi:10.1016/j.geomorph.2009.11.020

2 Experimental investigation of turbulence

The description of the flow-vegetation interaction presented in the framework of this thesis is based on the statistical analysis of the flow velocity detected with acoustic Doppler velocimetry techniques. In this Section, the basic concepts of turbulence, the physical meaning of the considered velocity statistics, and the analyses performed for the flow structure interpretation are briefly introduced.

The information provided in this Chapter is deduced from the lecture notes of Prof. V. Armenio (Armenio, 2017) and from two main manuals (Pope, 2000; Tennekes and Lumley, 1972). The introduced parameters and analyses are discussed with specific reference to the research activity described in the thesis.

Before introducing the statistical description of turbulence, the basic concepts of canonical mixing layer (ML), are described. Indeed, strong similarity exists between the shear layer observed in partly vegetated channels and canonical ML (White and Nepf, 2008), in terms of large-scale coherent structures and overall distribution of flow velocity. Therefore, the basic quantities and concepts of canonical ML, widely used within this thesis for the description of the vegetated shear layers, are here briefly introduced.

2.1 The plane mixing layer

The ML is the turbulent flow that forms between two uniform, nearly parallel streams of different velocities U_1 and U_2, with $U_1 < U_2$, as sketched in Figure 13 (Pope, 2000). In canonical mixing layer studies, U_1 generally indicates the highest velocity, while, in vegetated shear layer studies, U_1 refers to the lowest velocity, observed within the vegetation.

The consequent typical streamwise mean velocity lateral distribution $U(y)$ is characterized by a strong inflectional nature that gives rise to Kelvin-Helmholtz type instability (Ash and Khorrami, 1995). The flow depends on two characteristic velocities: (1) the convection velocity $U_C = (U_1 + U_2)/2$ and (2) the velocity difference or differential velocity $\Delta U = U_2 - U_1$.

A third fundamental parameter which controls the spatially growing characteristic of the plane MLs (Brown and Roshko, 1974), is represented by the normalized differential velocity or velocity ratio $\lambda = (U_2 - U_1)/(U_1 + U_2) = \Delta U / 2U_C$, which measures the relative magnitude of the total shear compared to the convection velocity (Ho and Huerre, 1984).

A characteristic length scale is represented by the ML width δ defined as the cross-flow distance between positions $y_{0.1}$ and $y_{0.9}$, where velocity reaches the $U_1+0.1\Delta U$ and $U_1+0.9\Delta U$. A second characteristic length of the plane ML is the momentum thickness θ, defined as:

$$\theta = \int_{-\infty}^{+\infty} \left\{ \frac{1}{4} - \left[\frac{U(y) - U_c}{\Delta U} \right]^2 \right\} dy. \tag{2.1}$$

The ML width δ and the momentum thickness θ are theoretically related for a canonical mixing layer by the geometrical relationship $\delta = 4\sqrt{\pi}\theta$.
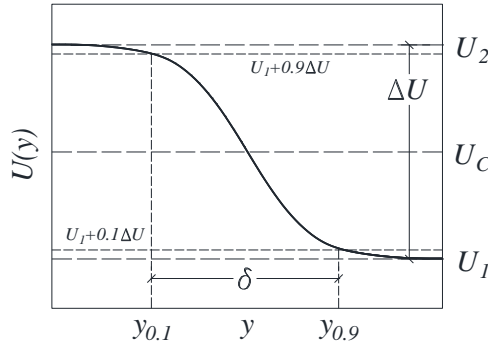
Figure 13 – Sketch of mean velocity U against lateral coordinate y, showing the definitions of $y_{0.1}$, $y_{0.9}$ and δ. The characteristic velocities U_1, U_2, U_C and ΔU are specified.

Because of the inflection point in the velocity profile, MLs are characterized by the formation of large coherent vortices resulting from a Kelvin-Helmholtz (KH) type instability, also indicated as KH vortices. These coherent structures, generated with a characteristic frequency f_{ML} corresponding to Strouhal number St equals to 0.032 (Ho and Huerre, 1984), strongly enhance the lateral transport of momentum and mass across the layer.

$$St = f_{ML} \frac{\theta}{U_C} = 0.032. \tag{2.2}$$

2.2   Statistical description of turbulence

2.2.1   Probability density function and central moments

The generic velocity component at a given location within the turbulent flow domain presents the features of a rapidly varying random function of time and space. In Figure 14 the temporal velocity signal at a given point of the flow domain is shown as an example. Following the Reynolds decomposition, the instantaneous velocity field $u(t)$ can be expressed as the superposition of the mean velocity field U and the turbulent contribution of the fluctuating velocity field $u'(t)$. The same decomposition can be operated for homogeneous turbulent velocity fields

considering the space instead of the time and, in some circumstances, considering both space and time.
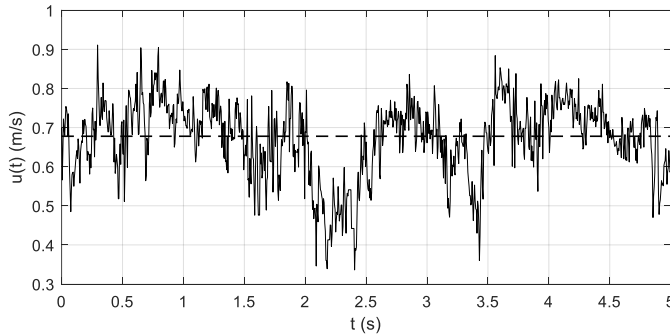
Figure 14 – Example of turbulent velocity time series. Solid line indicates the instantaneous velocity and dashed line the mean velocity.

This approach, applicable for the generic turbulent quantity describing the flow (e.g. pressure, temperature), is the basic consideration for the statistical description of turbulence. A complete description of a turbulent variable, e.g. the velocity component u, is given by its probability density function (PDF) $P(u)$, which satisfies the equation:

$$\int_{-\infty}^{+\infty} P(u)\, du = 1. \tag{2.3}$$

The PDF helps to exploit features of the turbulent field, showing how fluctuations are distributed about the mean value. The nth moment of $P(u)$ is defined as:

$$m^n(u) = \int_{-\infty}^{+\infty} u^n P(u)\, du. \tag{2.4}$$

The first order moment (n=1) is the mean value. With reference to the velocity field, this represents the mean velocity. Considering the perturbation quantity $u'=u-U$, it is possible to calculate the nth central moments:

$$m^n(u') = \int_{-\infty}^{+\infty} u'^n P(u')\, du'. \tag{2.5}$$

By definition the first central moment of u' is equal to zero. The higher order moments of u' can provide both qualitative and quantitative description of the fluctuating field. The variance $\sigma_u{}^2$ is the second order moment of the perturbation and describes the level of variability about the mean:

$$\sigma_u{}^2 = \int_{-\infty}^{+\infty} u'^2 P(u')\, du'. \tag{2.6}$$

The square root of $\sigma_u{}^2$ is the root mean square, indicated with u_{rms}. This quantity provides a measure of the amount (not the quality) of fluctuations in the turbulent field. When normalized by the mean velocity this quantity is the turbulent intensity.

The third order central moment of u' normalized by the variance is the skewness or skewness factor Sk_u and provides information about the asymmetry in the fluctuating field. It is defined as:

$$Sk_u = \frac{m^3}{(\sigma_u{}^2)^{\frac{3}{2}}}.$$

(2.7)

Positive skewness indicates that the PDF has a longer tail for $u'>0$ than for $u'<0$. Hence a positive skewness means that variable u' is more likely to take on large positive values than large negative ones. The skewness factor is zero in isotropic or homogeneous turbulence.

The fourth order central moment of the PDF of u' is a measure if the quality of the fluctuation field. Specifically, the kurtosis Ku_u is the fourth order moment of u', normalized by the variance:

$$Ku_u = \frac{m^4}{(\sigma_u{}^2)^2}.$$

(2.8)

A turbulent field with most measurements clustered around the mean has low kurtosis, whereas a turbulent field dominated by intermittent extreme events has high kurtosis. Therefore, the flatness factor increases in regions characterized by large spotty turbulent events.

Considering that in practice the above mentioned statistical moments are evaluated using a finite series of velocity measurements, made of a discrete number n of equi-spaced points, the Equations 2.4-2.8 are substituted by the expressions of Table 2.

Table 2 – Statistical turbulence descriptors for a discrete equi-spaced velocity time series.

Parameter	Units	Symbol	Formula
Mean velocity	(m/s)	U	$\frac{1}{n}\sum_{i=1}^{n} u'_i$
Root mean square	(m/s)	u_{rms}	$\sqrt{\frac{1}{n}\sum_{i=1}^{n} u'_i{}^2}$

Skewness	(–)	Sk_u	$\dfrac{\frac{1}{n}\sum_{i=1}^{n}u'^{3}_{i}}{\left(\frac{1}{n}\sum_{i=1}^{n}u'^{2}_{i}\right)^{3/2}}$
Kurtosis	(–)	Ku_u	$\dfrac{\frac{1}{n}\sum_{i=1}^{n}u'^{4}_{i}}{\left(\frac{1}{n}\sum_{i=1}^{n}u'^{2}_{i}\right)^{2}}$

In the current thesis the formulas of Table 2 were adopted.

2.2.2   Joint probability density function

In the analysis of a turbulent field, the degree of correlation between two variables, like for example the velocity along two directions, can provide additional information. Therefore, it is necessary to define joint probability density functions (JPDF). Considering as an example the two velocity components u and v, the JPDF $P_J(u, v)$ is defined as to satisfy the equation:

$$\int_{-\infty}^{+\infty} \int_{-\infty}^{+\infty} P_J(u, v)\, du\, dv = 1. \tag{2.9}$$

Integrating $P_J(u, v)$ over all values of u (or v) it returns $P(u)$ (or $P(v)$). The joint first moment of u and v, $\overline{uv}$, is defined as:

$$\overline{uv} = \int_{-\infty}^{+\infty} \int_{-\infty}^{+\infty} uv P_J(u, v)\, du\, dv. \tag{2.10}$$

The covariance of u and v, cov_{uv} is defined as:

$$cov_{uv} = \overline{uv} - \bar{u}\bar{v} = \overline{u'v'}. \tag{2.11}$$

The velocity fluctuations covariance coincides with the Reynolds shear stress. The covariance of u and v normalized by the root mean square of u and v is called correlation function r_{uv} and provides information about the degree of correlation between the two variables:

$$r_{uv} = \overline{u'v'}/u_{rms}v_{rms}. \tag{2.12}$$

For perfectly correlated variables, the correlation function is ±1. The covariance is a measure of the asymmetry of the JPDF.

In Table 3 the formulas for the evaluation of the joint variability descriptors for two discrete equi-spaced samples of n values are reported.

Table 3 – Statistical turbulence descriptors for joint variability for discrete equi-spaced velocity time series.

Parameter	Units	Symbol	Formula
Covariance	(m²/s²)	cov_{uv}	$\dfrac{1}{n-1}\displaystyle\sum_{i=1}^{n} u'_i v'_i$
Correlation coefficient	(−)	r_{uv}	$\dfrac{\frac{1}{n-1}\sum_{i=1}^{n} u'_i v'_i}{\sqrt{\frac{1}{n}\sum_{i=1}^{n} u'^{\,2}_i}\,\sqrt{\frac{1}{n}\sum_{i=1}^{n} v'^{\,2}_i}}$

2.3   Autocorrelation functions

The characterization of length and time scales of turbulent flows can be performed calculating the Eulerian integral time scales by integrating the velocity autocorrelation functions. Considering for example the fluctuating velocity signal $u'(t)$, the normalized autocorrelation function $R(\tau)$ is defined as:

$$R(\tau) = \frac{\overline{u'(t)u'(t+\tau)}}{\overline{u'u'}}, \tag{2.13}$$

where τ represents the time lag for which the autocorrelation of the velocity signal is evaluated. A typical autocorrelation plot is shown in Figure 15.
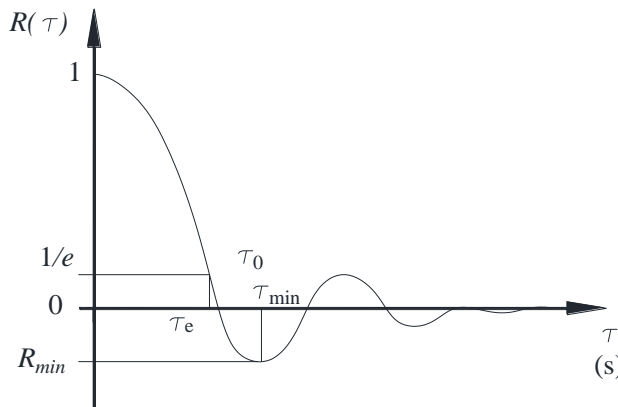
Figure 15 – Typical autocorrelation function and specification of integration domain for time scale calculation. Value of τ corresponding to $R=1/e^n$, $R=0$ and $R=R_{min}$ are indicated as $\tau_{e,n}$, τ_0 and τ_{min}, respectively.

For the time lag $\tau=0$, the autocorrelation is trivially unity, and it decays with increasing time lag. For the limit of very large time lags the autocorrelation function converges to zero, since turbulence is a random phenomenon.

This allows for the definition of an integral time scale T of turbulence defined as:

$$T = \int_0^\tau R(\tau)d\tau. \qquad (2.14)$$

The Eulerian integral time scale T represents the time over which the process $u'(t)$ is highly correlated to itself. Specifically, an integral time scale is a measure of the memory effect in the flow field of the persistence of a large-scale eddy at a fixed Eulerian point and, therefore, can provide useful information about the presence and coherence of turbulent structures.

The integration domain for the determination of the integral scale of the turbulence can be specified in a number of ways (O'Neill et al., 2004). In the current study, depending on the features of the fluctuating velocity field (and the corresponding shape of the autocorrelation functions) and the sampling rate of the velocity acquisition, three different methods were considered, integrating up to (Figure 15):

- the first zero crossing, where $\tau=\tau_0$ such that $R(\tau_0)$=0;
- the value $\tau=\tau_e$ where the autocorrelation function falls to $1/e$, $R(\tau_e)$=1/e;
- the first minimum of the autocorrelation function, where $\tau=\tau_{min}$ such that $R(\tau_{min})$= R_{min}.

In the analysis of flow over rigid submerged vegetation, for which lower frequency velocity measurements were performed, the integration domain ranged from 0 up to the value of τ at which the autocorrelation function falls to 1/e (Beckett, 1991; O'Neill et al., 2004), as to define an integration domain independent of the shape of the autocorrelation function (Gualtieri et al., 2015). For oscillating autocorrelation functions (like the ones of Figure 43), the time scales where evaluated integrating up to the first minimum.

So far, only correlation in time has been considered. However, correlation in space can be treated in an analogue way. Referring to the fluctuating velocity field $u'(x,t)$, it is possible evaluating, considering homogeneous turbulence, the Eulerian integral length scales L by integrating the spatial autocorrelation function. In this case the temporal lag is substituted by a spatial lag. The integral length scales provide information about the length of the average spatial extent or coherence of the fluctuations. It is also the length scale of the largest eddy of the flow.

In the present work, considering that velocity measurements were performed with a single stationary probe fixed at a given position (hence Eulerian), the integral length scales were deduced from the time scales by applying the Taylor hypothesis of the frozen turbulence:

$$L = UT, \qquad (2.15)$$

where U represents a characteristic local convective velocity of the flow, usually assumed to be the local mean velocity of the flow. The accuracy of this assumption

depends upon the properties of the flow and can be considered sufficiently accurate for low values of turbulence intensity $u_{rms}/U \ll 1$ (Pope, 2000).

2.4 Turbulence spectra

Turbulence is characterized by a range of different scales, both spatial and temporal, and, therefore, it is frequently convenient to consider the Fourier transform of the velocity field in order to analyze the Fourier components of different frequency and wavenumber. The Fourier transform of a function $f(t)$ can be written as:

$$g(\omega) = \frac{1}{2\pi} \int f(t)e^{-i\omega t}\, dt, \qquad (2.16)$$

with the angular frequency ω equal to $2\pi f$, where f is the frequency. The inverse transformation is given by:

$$f(t) = \int g(\omega)e^{i\omega t}\, d\omega. \qquad (2.17)$$

By examining the transform $g(\omega)$ it is possible to identify what frequencies are present in the original function $f(t)$, and identify which are the dominant ones (or corresponding time periods). If $f(t)$ is a function of space, the Fourier transform gives information on the wavelengths present in it. The pair of functions $f(t)$ and $g(t)$ defines a Fourier transform pair.

It is possible to define the turbulent velocity spectrum $S(\omega)$ as the Fourier transform of the autocorrelation function $R(\tau)$ in its dimensional form:

$$S(\omega) = \frac{1}{2\pi} \int R(\tau)e^{-i\omega\tau}\, d\tau. \qquad (2.18)$$

The autocorrelation function and the velocity spectrum define a Fourier transform pair:

$$R(\tau) = \int S(\omega)e^{i\omega\tau}\, d\omega. \qquad (2.19)$$

For τ=0 it is possible to note that the integral of Equation 2.19 defines the TKE K_u for the considered direction:

$$R(0) = \overline{u'(t)^2} = \int S(\omega)\, d\omega, \qquad K_u = 0.5\overline{u'(t)^2} = 0.5 \int S(\omega)\, d\omega. \qquad (2.20)$$

Therefore, the quantity $S(\omega)d\omega$ defines the TKE in a frequency band $d\omega$ centered at ω; $S(\omega)$ is thus the (one-dimensional) energy spectrum, showing how kinetic energy (power spectral density) is distributed as a function of frequency.

A typical power spectral density distribution for a sufficiently large *Re* turbulent velocity field is shown in Figure 16.
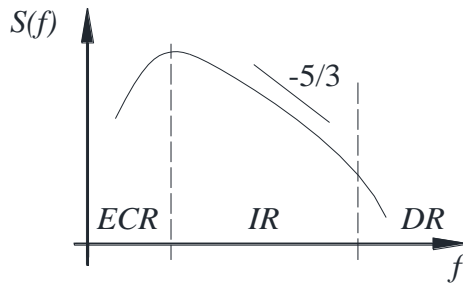

Figure 16 – Typical energy spectrum on a log-log plane. Individuation of the energy containing range (ECR), inertial subrange (IR) and dissipation range (DR). The -5/3 slope of the inertial subrange is also indicated.

2.4.1 Energy cascade and Kolmogorov's -5/3 spectrum

Following the Kolmogorov theory and the energy cascade concept, it is possible to identify three different ranges in the energy spectrum (Figure 16), characterized by different scales. The energy containing range (ECR), at the low frequency side of the spectrum, is the range of modes at which turbulence is generated at large scales through generation of large-scale eddies. An eddy can be considered as a patch of fluid in motion with some coherence. The largest scale eddies have a length scale comparable to the flow scale. Large scales are anisotropic and affected by boundary conditions (geometrical constraints). The energy spectrum typically shows a maximum for some frequency, corresponding to the larger energy-containing eddies. These eddies contain most of energy and are unstable, generating smaller size eddies through non-linear inviscid mechanisms. The spectrum decays at higher frequencies (smaller eddies) and energy is transferred to progressively smaller size structures through the so called energy cascade. As soon as smaller and smaller scales are generated, they lose memory and directionality, and small scales tend to become independent on the kind of turbulent field responsible of their generation. Small scales tend to exhibit universal behavior.

In a sufficiently large *Re* number turbulent flow, there exists an inertial range (IR) where energy is neither produced nor dissipated. In this range the Reynolds number is large enough to make dissipation negligible, meaning that these scales do not dissipate energy. In the IR, transfer of energy from large scales to small scales (on average) takes place.

Finally, energy is dissipated at the dissipation range (DR) by viscous mechanisms at a rate ε, the dissipation rate. The statistics of the small scale motions have a universal form and are determined by ε and the viscosity ν. If we define $T(IR)$ the rate at which energy is transferred from large to smaller eddies, the conservation of energy leads to $T(IR)=\varepsilon$.

Summarizing, the Kolmogorov theory considers the large anisotropic eddies as the sources of energy, which is transferred down to progressively smaller scales. At some point the eddies lose all structure; they become homogeneous and isotropic, i.e., similar. In this region, their energy is determined only by the rate of transfer from the larger eddies and the rate of dissipation by the smaller ones. Kolmogorov stated the following two similarity hypotheses:

1. at large *Re* the local average properties of the small-scale components of any turbulent motion are determined entirely by kinematic viscosity and average rate of dissipation per unit mass;

2. there is an upper subrange (the inertial subrange) in this bandwidth of small eddies in which the local average properties are determined only by the rate of dissipation per unit mass.

These hypotheses lead to a universal form for the energy spectrum in the inertial subrange:

$$S(k) = C\varepsilon^{2/3}k_s^{-5/3}, \tag{2.21}$$

where k_s is the wavenumber and C is a universal constant. Equation 2.21 is the so called Kolmogorov -5/3 spectrum.

In the current study, as done by Nepf and Vivoni (2000), the rate of turbulent dissipation ε was evaluated by fitting the spectra from the streamwise and spanwise velocity components to the inertial subrange fit of Equation 2.21, written in terms of frequency by considering the Taylor hypothesis:

$$S_{uu} = A\frac{18}{55}\varepsilon^{2/3}(U/2\pi)^{2/3}f^{-5/3}, \quad S_{vv} = \frac{4}{3}S_{uu}, \tag{2.22}$$

where $A\approx1.5$ is an experimentally determined, universal constant for turbulent flows (Kundu et al., 2002). In regions of high turbulent intensity, this technique overestimates the true dissipation rate owing to aliasing of energy between adjacent wave numbers (Lumley, 1965).

2.4.2   Shear-stress spectrum (velocity cross-spectrum)

Given the prominent role played by the shear stress both in momentum transport and in production of turbulence energy, it is important to ascertain the contributions to the turbulent shear stress from the various scales of motion. To this aim, starting from the cross-correlation function $R_{uv}(\tau)$ evaluated, for example, considering the two fluctuating velocity fields u' and v', it is possible to define the energy cross-spectrum S_{uv}. In the current study the lateral-longitudinal velocity cross-spectra were evaluated to identify the dominant mechanisms in the momentum transport.

2.5 Quadrant analysis

Quadrant analysis is a simple conditional-sampling technique that can provide useful information for the interpretation and the detection of organized coherent structures in the flow. Considering for example a turbulent BL, characterized by velocity fluctuations in the longitudinal and vertical directions u' and w', respectively, the quadrant analysis allows understanding the nature of contributions to the Reynolds stress $\overline{u'w'}$ from different structures and events (Lu and Willmarth, 1973; Pope, 2000). In the quadrant analysis (Lu and Willmarth, 1973; Nakagawa and Nezu, 1977; Wallace and Brodkey, 1977) the velocity fluctuations components are plotted on a u'-w' plane (Figure 17).
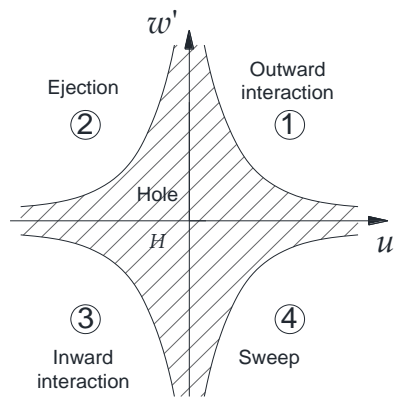
Figure 17 – Velocity fluctuations plane and sketch of hole region.

The plane, as sketched in Figure 17, is divided into four quadrants, each one is characteristic of a different event:

- quadrant 1, outward interaction (u'>0, w'>0);
- quadrant 2, ejection (u'<0, w'>0);
- quadrant 3, inward interaction (u'<0, w'<0);
- quadrant 4, sweep (u'>0, w'<0).

Ejection (or burst) refers to the rapid migration of low-speed patches of fluid away from the wall. With fluid moving away from the wall in ejections, continuity demands a flow toward the wall in some other regions, with high-speed fluid moving toward the wall in events called sweeps (Pope, 2000 and reference therein). Inward and outward interactions occur when low-speed patches of fluid move toward the wall and when high-speed patches of fluid arise far from the wall, respectively. An important issue is the significance of ejections and sweeps in turbulence production. Indeed, in quadrants 2 and 4 the product $u'w'$ is negative, and consequently events in these regions correspond to positive production of TKE (see Equation 1.5).

In order to highlight the contribution of extreme events to the overall Reynolds stress, a hyperbolic threshold can be introduced, defined by the expression $|u'w'| = H u'_{rms} w'_{rms}$ (Lu and Willmarth, 1973; Nezu and Sanjou, 2008; Poggi et al., 2004), which defines on the u'-w' plane a hyperbolic hole. At any point in the flow domain, the total contribution of each quadrant to the Reynolds stress can be calculated as (Raupach and Thom, 1981):

$$S_i = \frac{1}{\overline{u'w'}} \lim_{T \to \infty} \frac{1}{T} \int_0^T u'(t)w'(t)I_i dt, \tag{2.23}$$

where the subscript i refers to the ith quadrant and I_i is a dummy variable equal to 1 if $u'(t)w'(t)$ belongs to the ith quadrant, 0 otherwise. Clearly, $S_1 + S_2 + S_3 + S_4 = 1$.

The contribution of the extreme events of each quadrant, instead, can be calculated as (Lu and Willmarth, 1973):

$$S_{i,H} = \frac{1}{\overline{u'w'}} \lim_{T \to \infty} \frac{1}{T} \int_0^T u'(t)w'(t)I_{i,H} dt, \tag{2.24}$$

where H is the threshold level defining the size of the hyperbolic hole region, and the subscript i refers to the ith quadrant. $I_{i,H}$ is a dummy variable equal to 1 if $u'(t)w'(t)$ belongs to the ith quadrant and $|u'(t)w'(t)| > H u'_{rms} w'_{rms}$, 0 otherwise.

When analyzing vegetated shear layers, the quadrant analysis technique can be conveniently applied as to characterize the momentum transport at the interface, both for horizontal and vertical shear layers.

2.6 Turbulence anisotropy

The Reynolds stresses, which stem from the momentum transfer by the fluctuating velocity fields, are the components of a second-order tensor. Using conveniently the matrix notation, the components of the Reynolds stress tensor are defined as $\overline{u'_i u'_j}$. The Reynolds stress tensor is symmetric. The diagonal components $\overline{u'_i}^2$ are normal stresses, while the off diagonal components are the shear stresses. The TKE K is defined as half the trace of the Reynolds stress tensor:

$$K = \frac{1}{2}\overline{u'_i u'_i} = \frac{1}{2}\left(\overline{u'_1}^2 + \overline{u'_2}^2 + \overline{u'_3}^2\right). \tag{2.25}$$

It is the mean kinetic energy per unit mass in the fluctuating velocity field. In the principal axes of the Reynolds stress tensor, the shear stresses are zero, and the normal stresses are the eigenvalues, which are non-negative. In general, all eigenvalues are strictly positive; in special circumstances, one or more of the

eigenvalues can be zero. This distinction between shear and normal stresses is dependent on the choice of the coordinate system. An intrinsic distinction can be made between isotropic and anisotropic stresses. The isotropic stress is $\frac{2}{3}K\delta_{ij}$ and, consequently, the deviatoric anisotropic part is:

$$a_{ij} = \overline{u'_i u'_j} - \frac{2}{3}K\delta_{ij}, \tag{2.26}$$

where δ_{ij} is the Kronecker delta function. The normalized anisotropy tensor is defined by:

$$b_{ij} = \frac{\overline{u'_i u'_j}}{2K} - \frac{1}{3}\delta_{ij}. \tag{2.27}$$

Considering that only the anisotropic component b_{ij} is effective in transporting momentum, the normalized anisotropic stress tensor can provide useful information about the amount and type of anisotropy of a specific flow.

2.6.1 Invariant maps and anisotropy visualization

In order to deduce information from the anisotropy stress tensor different visualization techniques for second-order tensor fields can be applied, e.g. glyphs or hyper-streamlines (Hashash et al., 2003). Owing to their complex construction and interpretation, none of these technique is broadly used in fluid dynamics. On the contrary, a variety of derived quantities, which distill the relevant information contained in b_{ij} to either scalar or vector metrics, is used to investigate anisotropic behavior (Emory and Iaccarino, 2014).

One of the most popular visualization technique is represented by the anisotropy invariant map. Originally introduced by Lumley & Newman (1977), this technique is based on the construction of two-dimensional domains based on invariant properties of b_{ij}. Specifically, the eigenvalues of the anisotropic stress tensor (λ_1, λ_2, λ_3 with $\lambda_1 \geq \lambda_2 \geq \lambda_3$) provide information about the relative strengths of the fluctuating velocity components, i.e. the componentality of the turbulence field (Helgeland et al., 2004). The invariant map considered in the current study is the so called turbulence triangle (Choi and Lumley, 2001), depicted in Figure 18.

The turbulence triangle is a domain based on the second (*II*) and third (*III*) invariants of b_{ij} defined using the coordinates ξ and η:

$$\xi = \sqrt[3]{III/2}, \quad \eta = \sqrt{II/3}, \tag{2.28}$$

where $II=\lambda_1{}^2+\lambda_1\lambda_2+\lambda_2{}^2$ and $III=\lambda_1\lambda_2(\lambda_1+\lambda_2)$ are the quadratic and cubic invariant of the Reynolds stress anisotropic tensor, respectively.

It has been demonstrated (Lumley, 1978) that all the possible states of turbulence must occur within the triangular shaped domain delimited by borders corresponding to special states of turbulence, as indicated in Figure 18.

There are three limiting states of componentality which define the boundaries of the invariant maps. All other states of b_{ij} (other locations within the map) can be represented as a convex combination of these limiting states.
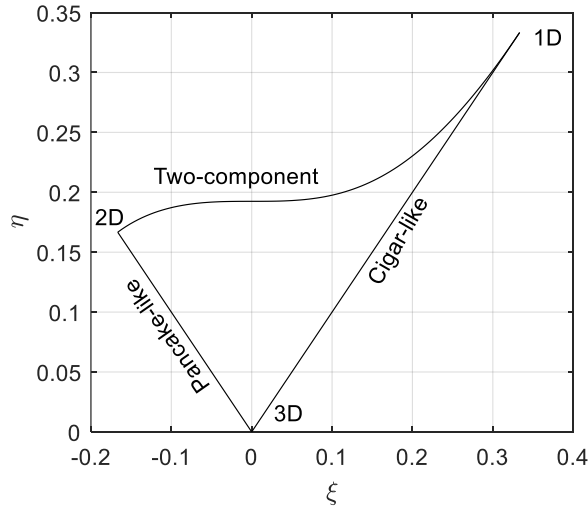
Figure 18 – Turbulence triangle and specification of special states of turbulence

The lower vertex ($\xi=\eta=0$) is representative of isotropic turbulence (3D), while the vertices $\xi=1/3$, $\eta=1/3$ (1D) and $\xi=-1/6$, $\eta=1/6$ (2D) are representative of one-component and two-component axisymmetric turbulence, respectively. The upper boundary corresponds to two-component turbulence and the lateral edges are representative of specific turbulent processes: axisymmetric expansion (from 2D to 3D) and axisymmetric contraction (from 1D to 3D). While the η coordinate defines the degree of anisotropy, points closer to the upper boundary are characterized by higher degree of anisotropy; the ξ coordinate defines the type of anisotropy:

- points on the left-hand side of the triangle are representative of axisymmetric turbulence, with one component of the TKE being smaller than the other two (indicated as pancake-like turbulence);
- points on the right-hand side of the triangle represents the other type of axisymmetric turbulence, where one component of the TKE is greater than the other two (indicated as cigar-like turbulence) (Choi and Lumley, 2001).

It should be noted that the anisotropy invariants do not define the shape of any particular coherent turbulent structure, but rather provide a description of the eigenvalues of the stress tensor (Simonsen and Krogstad, 2005). A wealth of

physical understanding and insight is provided by visualizing the proximity of turbulent anisotropy to these different behaviors (Emory and Iaccarino, 2014).

This technique allows analyzing the turbulence independently from the specific reference systems adopted for the flow feature investigation. Thus, it is mostly effective for the description of turbulence in highly tridimensional flows and, moreover, it is particularly suitable when dealing with ADV measurements. Indeed, ADV probe orientation represents a critical aspect of the experimental measurements (see Appendix A) that can lead to significant error in the Reynolds stress estimation. With the turbulence triangles it is possible to investigate the turbulence independently from possible ADV probe misorientation.

References

Armenio, V., 2017. Notes of PhD Course on Turbulence. University of Trieste, Italy.

Ash, R.L., Khorrami, M.R., 1995. Fluid Vortices, Fluid Vor. doi:10.1007/978-94-011-0249-0

Beckett, P.M., 1991. Physical Fluid Dynamics By D. J. Tritton, Oxford University Press, Oxford, 1988, pp. 519, price: £35.00 (hardback), $16.95 (paperback). ISBN 0–19–854489-8 (hardback); 0–19–854493-6 (paperback). J. Chem. Technol. Biotechnol. 50, 144. doi:10.1002/jctb.280500121

Brown, G.L., Roshko, A., 1974. On density effects and large structure in turbulent mixing layers. J. Fluid Mech. 64, 775–816. doi:10.1017/S002211207400190X

Choi, K.-S., Lumley, J.L., 2001. The return to isotropy of homogeneous turbulence. J. Fluid Mech. 436, 161. doi:10.1017/S002211200100386X

Emory, M., Iaccarino, G., 2014. Visualizing turbulence anisotropy in the spatial domain with componentality contours. Cent. Turbul. Res. Annu. Res. Briefs 123–138.

Gualtieri, P., De Felice, S., Pasquino, V., Pulci Doria, G., 2015. Evaluation of integral length scale from experimental data in a flow through submerged vegetation. In Proceedings of the XXXVI IAHR Congress, Delft–The Hague, The Netherlands, 28 June–3 July 2015; pp. 1–9.

Hashash, Y.M.A., Yao, J.I.C., Wotring, D.C., 2003. Glyph and hyperstreamline representation of stress and strain tensors and material constitutive response. Int. J. Numer. Anal. Methods Geomech. 27, 603–626. doi:10.1002/nag.288

Helgeland, A., Andreassen, O., Ommundsen, A., Reif, B.A.P., Werne, J., Gaarder, T., 2004. Visualization of the Energy-Containing Turbulent Scales. Proc. {IEEE} Symp. Vol. Vis. '04 Vi, 103–109. doi:10.1109/SVVG.2004.15

Ho, C., Huerre, P., 1984. Perturbed free shear layers. Annu. Rev. Fluid Mech. 16, 365–422. doi:10.1146/annurev.fl.16.010184.002053

Kundu, P.K., Cohen, I.M., Hu, H.H., 2002. Fluid mechanics, Second. ed. doi:978-0-12-381399-2

Lu, S.S., Willmarth, W.W., 1973. Measurements of the structure of the Reynolds stress in a turbulent boundary layer 60, 481–511.

Lumley, J.L., 1978. Computational Modeling of Turbulent Flows. Adv. Appl. Mech. 18.

Lumley, J.L., 1965. Interpretation of Time Spectra Measured in High-Intensity Shear Flows. Phys. Fluids 8, 1056–1062. doi:10.1063/1.1761355

Lumley, J.L., Newman, G.R., 1977. The return to isotropy of homogeneous turbulence. J. Fluid Mech. 82, 161–178. doi:10.1017/S0022112077000585

Nakagawa, H., Nezu, I., 1977. Prediction of the contributions to the Reynolds stress from bursting events in open-channel flows. J. Fluid Mech. 80, 99. doi:10.1017/S0022112077001554

Nepf, H.M., Vivoni, E.R., 2000. Flow structure in depth-Iimited, vegetated flow. J. Geophys. Res. 105, 28547–28557.

Nezu, I., Sanjou, M., 2008. Turburence structure and coherent motion in vegetated canopy open-channel flows. J. Hydro-Environment Res. 2, 62–90. doi:10.1016/j.jher.2008.05.003

O'Neill, P.L., Nicolaides, D., Honnery, D.R., Soria, J., 2004. Autocorrelation Functions and the Determination of Integral Length with Reference to Experimental and Numerical Data. 15th Australas. Fluid Mech. Conf. 1, 1–4.

Poggi, D., Porporato, A., Ridolfi, L., Albertson, J.D., Katul, G.G., 2004. The effect of vegetation density on canopy sub-layer turbulence. Boundary-Layer Meteorol. 111, 565–587. doi:10.1023/B:BOUN.0000016576.05621.73

Pope, S.B., 2000. Turbulent Flows. Cambridge University Press. doi:10.1017/CBO9780511840531

Raupach, M.R., Thom, A.S., 1981. Turbulence in and above Plant Canopies. Annu. Rev. Fluid Mech. 13, 97–129. doi:10.1146/annurev.fl.13.010181.000525

Simonsen, A.J., Krogstad, P.Å., 2005. Turbulent stress invariant analysis: Clarification of existing terminology. Phys. Fluids 17, 1–4. doi:10.1063/1.2009008

Tennekes, H., Lumley, J.L., 1972. A First Course In Turbulence, Mit. doi:10.1088/1751-8113/44/8/085201

Wallace, J.M., Brodkey, R.S., 1977. Reynolds stress and joint probability density distributions in the u-v plane of a turbulent channel flow. Phys. Fluids 20, 351–355. doi:10.1063/1.861897

3 Flow over uniformly vegetated bed

The presence of a submerged macro-roughness represented by a vegetative obstruction deeply alters the mean and turbulent structure of the flow with implications on mass and momentum exchange across the flow-vegetation interface. In this Chapter, the features of the flow over a submerged rigid canopy are experimentally investigated considering different submergence ratios.

The hydrodynamic structure of the flow over a submerged canopy has been investigated, as illustrated in Section 1.3.2.1, with reference to two main vegetation models: (1) rigid vegetation, in which the vegetative obstruction is generally represented by an array of rigid cylinders or prismatic elements (Nezu and Sanjou, 2008; Poggi et al., 2004; Rowiński and Kubrak, 2002); (2) flexible vegetation, generally simulated by blade shaped vegetation (Ghisalberti and Nepf, 2002; Sukhodolova and Sukhodolov, 2012). The rigid cylinder model is not able to reproduce a variety of flow-influencing mechanisms exhibited by natural vegetation, generally presenting a wide range of different bio-mechanical properties (Aberle and Järvelä, 2013) and velocity dependent drag characteristics (Västilä and Järvelä, 2014). Nevertheless, rigid cylinder models can be considered qualitatively effective for simulating the cross-section scale effects on turbulence structure and describing morphodynamic processes of channels with vegetated floodplains (Vargas-Luna et al., 2016). Owing to the practical importance of modeling turbulence in natural watercourses and coastal wetlands, an increasing interest in describing the turbulent flow structure in vegetated flows (Devi and Kumar, 2016; Peruzzo et al., 2018; Viero et al., 2017), highly rough bed and obstructed flows (Coscarella et al., 2017), is registered.

The flow over rigid submerged vegetation has been widely investigated in order to assess the effects of vegetation (density and submergence) on flow structure and the implication on hydraulic resistance, turbulent structures, mixing processes and sediment transport (Ghannam et al., 2018, 2015; Gualtieri et al., 2018; Nezu and Sanjou, 2008; Poggi et al., 2004; Raupach and Thom, 1981). A distinctive feature of such vegetated shear flows is represented by the anisotropy of Reynolds stresses, which reflects, to a large extent, the presence of organized motions. Indeed, the anisotropic Reynolds stress component is the only part of the total stress responsible for the momentum transport (Pope, 2000) and, therefore, its study is crucial for the understanding and modeling of turbulence in vegetated flows.

The anisotropy pattern within the flow domain can be investigated using the technique of the anisotropy invariants proposed by Lumley and Newman (Lumley and Newman, 1977). This technique, fairly less common for the analysis of vegetated flows, allows the characterization of spatial distribution of anisotropy degree and nature (see Section 2.6). Only few examples of the application of this methodology are available in literature and mainly referred to numerical and experimental analysis of flows over highly rough bed (Bomminayuni and Stoesser, 2011; Smalley et al., 2002).

In this Chapter, the results of the experimental investigation of the turbulent structure of the flow over a submerged array of rigid cylinders (UR) are described and discussed coupling the traditional approach based on the spatial distributions of velocity statistics and spectral analysis (Ghisalberti and Nepf, 2006; Nezu and Sanjou, 2008; Poggi et al., 2004), with a new methodology adopted for providing the overall description of the turbulence anisotropy, represented by the turbulence triangles (Choi and Lumley, 2001). Specifically, the effects of the variability of the submergence, i.e. the ratio between uniform flow depth and the cylinders height, on the mean velocity profiles, the distributions of higher order velocity statistics, quadrant analysis, distribution of integral time and length scales, were analyzed with reference to the anisotropy pattern resulting from the invariant maps.

3.1 Materials and Methods

3.1.1 Laboratory Flume

The experiments were carried out in an 8 m long, 0.4 m wide, and 0.4 m high Plexiglas-walled recirculating flume in the Laboratory of Hydraulics at the University of Naples Federico II (Figure 19).
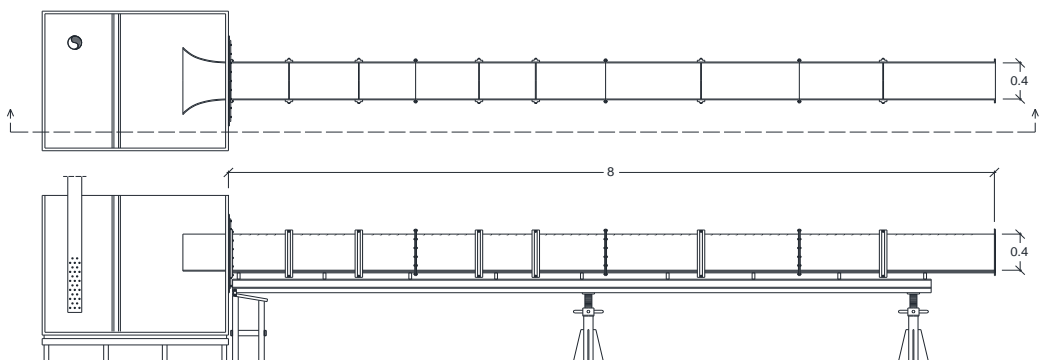

Figure 19 - Experimental facility. The laboratory flume was 8 m long with a 0.4 m wide and 0.4 m deep rectangular cross-section. The bed of the flume was uniformly covered by an array of rigid cylinders.

The channel was supplied by a 4.5 m³ tank in which water was led into through the water supply system of the laboratory from a water tower. Specifically, in order to

stabilize flow rates in the channel, water was not directly pumped in the flume but, from the recirculating system reservoir, was led to a water tower with a pumping station. The discharge was measured by a magnetic flow meter (with accuracy of ±0.1 l/s) installed on the feeding pipeline of the channel. The discharge ranged up to 30 l/s. The channel slope was set to 1%. At the inlet section, a parabolic transition from the feeding tank to the experimental channel was placed in order to reduce the disturbance at the inlet and to damp the related turbulence. The x, y and z flume coordinate system axes refer to the longitudinal, lateral, and vertical (normal to the flume bottom) directions, respectively.

All the tests were carried out in uniform flow conditions with different cylinders submergences. In the range of considered flow rates, the uniform flow reach was identified analyzing the backwater profiles (Figure 20), experimentally determined using a gauging needle (with accuracy of ±0.1 mm). For all the test runs, uniform flow conditions were observed to be restored approximately at 4.5 m from the outlet section. Measurements were taken between $x \approx 2.5$ and 3.5 m from the channel inlet, within the uniform flow section of the flume and sufficiently downstream of the inlet.
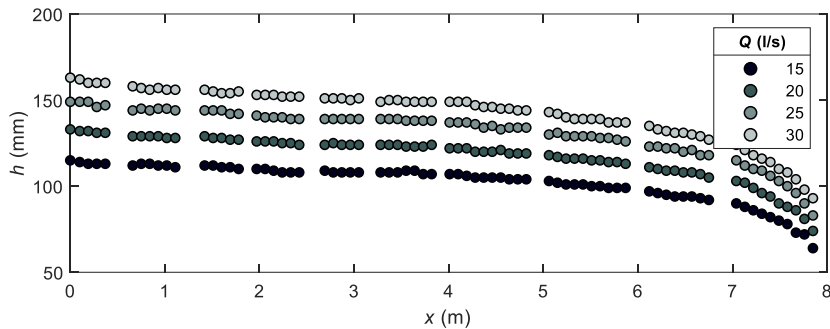
Figure 20 – Backwater profiles for the investigated test runs. Vertical coordinate is exaggerated.

3.1.2 Rigid Vegetation Model

This experimental analysis was performed considering a uniformly vegetated channel bed, in which metallic cylinders were used to simulate rigid, submerged vegetation (Figure 21). The 45 mm long rods of 4 mm diameter, installed in holes bored into the bed Plexiglas panels, were arranged in an aligned pattern with constant density covering the entire channel bed. The space between cylinders, in the streamwise L_x and spanwise L_y directions, was equal to 25 mm (Figure 21).

Consequently, the number of cylinders per unit bed area n was equal to 1600 m^{-2}. Vegetation density was described by three other parameters:
- the frontal area per canopy volume $a = d/(L_x L_y)$, equal to 6.4 m^{-1};
- the frontal area per bed area λ_V, also known as density roughness, computable as ak for vertically uniform vegetation, equal to 0.288;

- the solid volume fraction occupied by the canopy elements ϕ, evaluable as $(\pi/4)ad$ for cylindrical elements, equal to 0.020.

Figure 21 – Geometry of the array of aligned cylinders and specification of diameter (d), spacing (L_x and L_y), and cylinder height (k).

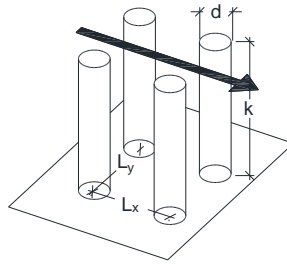The considered vegetation geometry and density, typical of dense canopies (Nepf, 2012), was comparable to those commonly exhibited by aquatic submerged vegetation, reported in Table 4.

Table 4 – Comparison between the current vegetation model and aquatic vegetation (Nepf, 2012).

Vegetation type	d (mm)	ϕ (-)	a (m⁻¹)
Current vegetation model	4	0.02	6.4
Marsh grasses	1-10	0.001-0.01	1-7
Mangroves	40-90	≤0.45	≤2
Seagrasses	-	0.01-0.1	1-100

3.1.3 Test Cases and Velocity Measurements

The effects of submergence ratio on flow structure were experimentally investigated for the hydraulic conditions reported in Table 5.

Table 5 – Details of experimental conditions.

Q (l/s)	h (mm)	h/k (-)	U_k (cm/s)	U^* (cm/s)	U_m (cm/s)	Re_k (-)	Re_h (-)	Re_d (-)	Fr (-)
15	109	2.4	29.2	5.4	34.56	13121	37500	218	0.34
20	125	2.8	32.3	6.3	40.00	14517	50000	254	0.36
25	139	3.1	35.4	7.2	44.96	15916	62500	290	0.39
30	151	3.4	37.2	7.9	49.54	16747	75000	316	0.41

Specifically, four different submergence ratios were considered: 2.4, 2.8, 3.1, and 3.4. For each condition, the canopy edge velocity (U_k), the measured friction velocity at

the canopy edge ($U^*=\sqrt{-\overline{u'w'}}$), and the cross-sectional mean velocity ($U_m=Q/Bh$) were evaluated. Furthermore, the relevant Reynolds numbers (the roughness $Re_k=kU^*/\nu$, flow $Re_h=hU_m/\nu$, and vegetation element $Re_d=dU^*/\nu$) and the flow Froude number are indicated (Table 5).

In the considered conditions of shallow submerged canopies (Augustijn et al., 2008; Nepf, 2012), with $h/k<5$, both turbulent stress and potential gradients drive the flow within the canopy (Nepf and Vivoni, 2000).
Instantaneous velocity measurements were performed with SonTek 16-MHz MicroADV, a three-axis acoustic Doppler velocimeter (ADV) with down looking probe. In order to describe the turbulence structure within and above the canopy, the maximum available sampling frequency of the instrument was adopted, i.e. 50 Hz. In order to achieve well converging higher order moments (Appendix A), a sample size of more than 50000 values was assumed (Chanson et al., 2005).

ADV data were filtered assuming a threshold correlation and signal to noise ratio level of 70% and 30 dB respectively. Finally, data were de-spiked using the phase-space thresholding method (Goring and Nikora, 2002) as modified by Wahl (2003). Velocity measurements were performed in the uniform flow reach, along a vertical line in the channel midline (Figure 22). The sampling volume (SV) was approximately cylindrical with 4 mm diameter and 4.5 mm height (Figure 22, a), therefore, the distance between each acquisition point was selected equal to 10 mm, in order to avoid overlapping the sampling volumes of each measurement point.
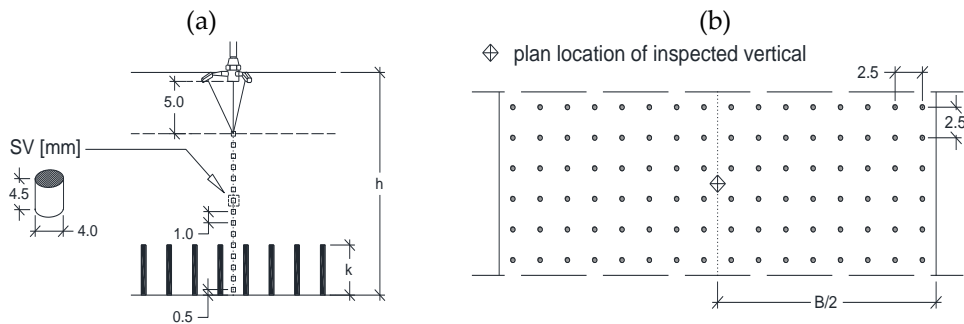
Figure 22 – Position of measurement stations and geometry of sampling volume (SV) (a). Location of inspected vertical within the cylinder array (b).

Considering the distance between the center of the sampling volume and the acoustic transmitter of the probe (50 mm), the flow was investigated up to 50 mm from the water surface (Figure 22, a). The orientation of the probe was defined to identify the streamwise axis of the channel with the x axis of the probe; y is the spanwise direction (positive leftwards) and z the vertical one (positive upwards).

The good alignment and the verticality of the instrument were addressed with a laser cross-level and a 3D bubble level.

3.2 Results and Discussion

3.2.1 Mean Velocity Profiles

In Figure 23 the mean velocity profiles of U, V and W (for the x, y and z directions, respectively) are shown. Velocity and distance from the bed are made dimensionless with the streamwise mean velocity at the canopy top and the vegetation height, respectively.
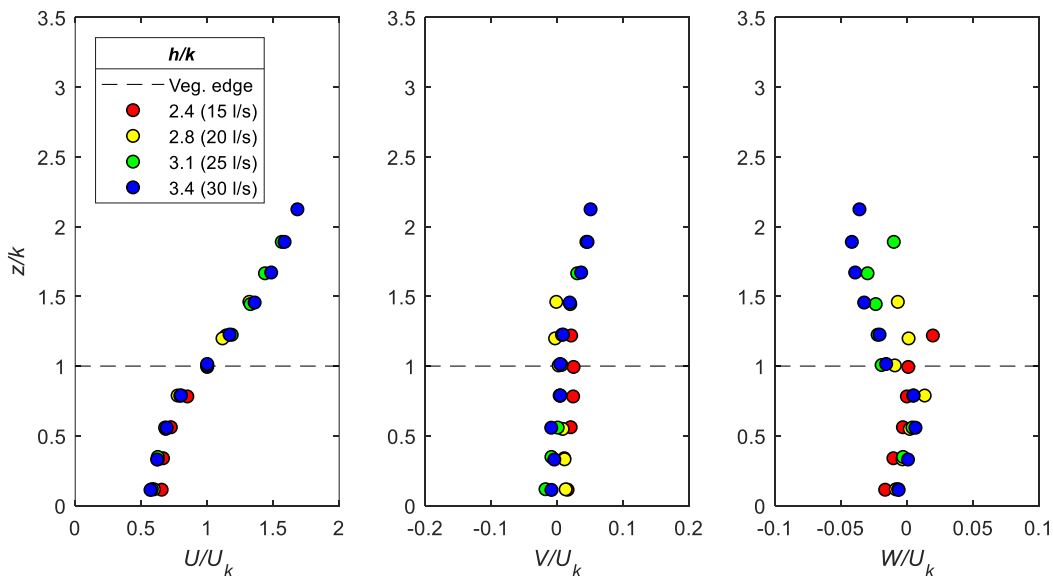
Figure 23 – Dimensionless mean velocity profiles for U, V and W. Dashed line indicates the canopy top.

The discontinuity in drag at the vegetation top modified the longitudinal velocity profile, characterized by an inflection point at the top of the canopy, resembling a canonical ML (Nepf, 2012). Specifically, the drag exerted by the canopy decelerates the flow in the vegetated layer: as firstly addressed by Raupach et al. (1996), this effect dominates the transfer of momentum across the flow-vegetation interface. The profile deflection, slightly more pronounced for the higher values of h/k, is characteristic of dense canopies and, specifically, for canopies with $ak>\approx0.23$ (Nepf, 2012). The large interfacial coherent structures, also called canopy-scale vortices, occupy the surface layer and partly penetrate the vegetation layer, depending on the canopy density (see Section 1.3.2.1). The penetration depth δ_e can be evaluated using Equation 1.3, defined by Nepf et al. (Nepf et al., 2007). In this study, for C_D=1, δ_e varied between 27 and 45 mm and δ_e/k between 0.6 and 1.

The turbulent flow in the investigated region of the channel was fully developed and, considering that the leading edge of the canopy was located approximately 2.5 m upstream to the measurement section, the canopy-scale vortices and the penetration depth reached a stable condition.

3.2.2   Turbulent Intensities

In Figure 24, the turbulent intensities u_{rms}, v_{rms} and w_{rms} in the three directions, defined as the root mean square values for the three velocity components, made dimensionless with the measured friction velocity at the canopy top, are shown.
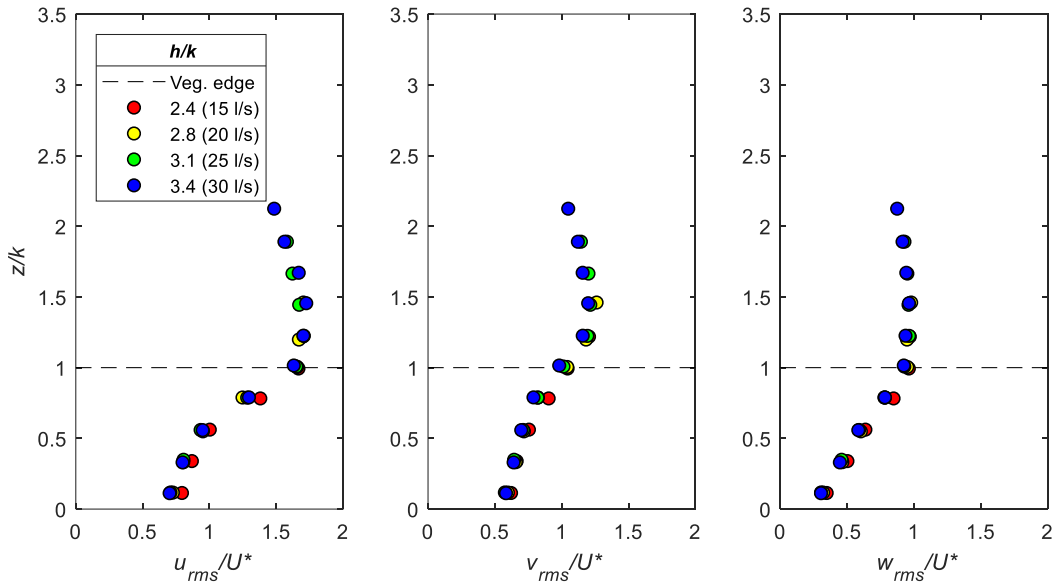
Figure 24 – Turbulent intensities in the three directions x, y and z.

The profiles showed a similar trend, collapsing together along the same curve. Maximum longitudinal turbulent intensities occurred at the top and directly above the canopy. The turbulent intensity decreased within the vegetation layer and towards the free surface. Indeed, the vegetation damped the turbulence and this effect was observed to be slightly more pronounced for higher submergence ratios. At the canopy top, the normalized vertical fluctuating velocity component was ≈1 for each submergence. For dense canopies, the characteristic value is about 1.1, which is typical for mixing layers, in agreement with Raupach et al. (1996) and Poggi et al. (2004). Larger values, up to 1.3, are typical for sparse canopies. At the canopy top, the normalized streamwise and vertical fluctuating velocity components attained values in agreement with Raupach et al. (1996), Poggi et al. (2004) and Nezu and Sanjou (2008), for dense canopy.

3.2.3 Skewness and Kurtosis

The skewness Sk_u, Sk_v and Sk_w of velocity fluctuations, as defined in Section 2.2.1, are shown in Figure 25. A non-zero skewness indicates an asymmetric probability density function of the considered variable, which means that larger excursions in one direction are more probable than in the other one, depending on the sign of the statistics. The profiles of Figure 25 describe a clear trend for skewness in u to take positive values inside the canopy and negative ones outside and, complementarily, for the skewness in w to take negative values inside the canopy and positive ones outside. This trend indicates the dominant role of sweep events inside the cylinders array and the ejection events above the canopy, in agreement with the results of other experimental analyses (Devi and Kumar, 2016; Nezu and Sanjou, 2008; Poggi et al., 2004). The intensity of these effects, as confirmed by the quadrant analysis, increased with the submergence ratio owing to the increasing momentum transfer between vegetated and non-vegetated zone. A normal distribution can be assumed for the fluctuations in the spanwise direction.
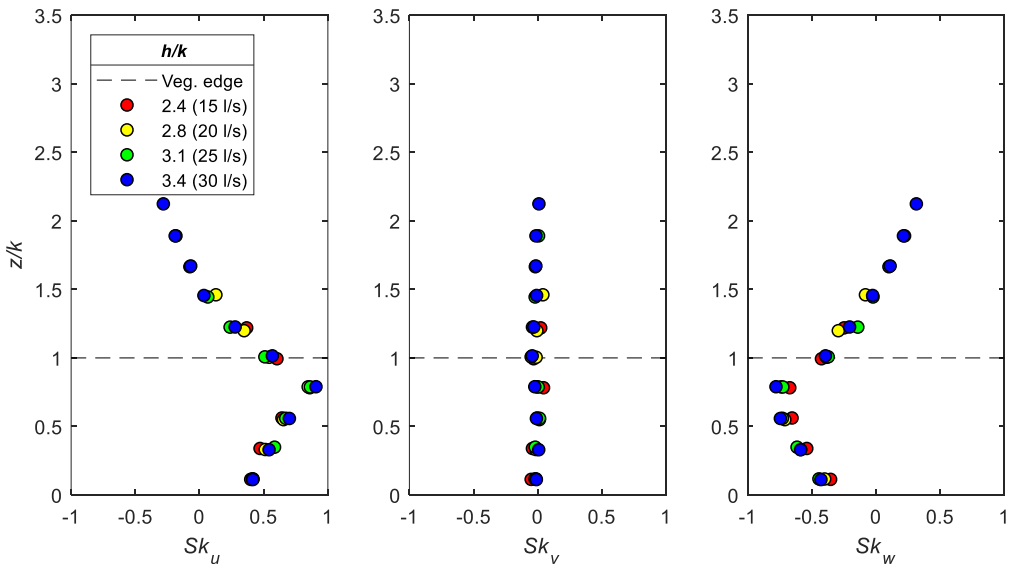
Figure 25 – Skewness of the fluctuation velocity components in the three directions x, y and z.

The kurtosis Ku_u, Ku_v and Ku_w profiles, shown in Figure 26, were observed to assume higher values in the regions immediately around the canopy top, consistently with the results of Poggi et al. (2004) for dense canopies. This effect, as confirmed by the quadrant analysis illustrated in the next Section, confirms the dominant role of sweep and ejection events for the Reynolds shear stress production and the momentum transport at the canopy top.

Within the canopy, Ku_v was observed to attain values >0, consistently with the lateral fluctuations related to the von Kármán vortex shedding process induced by the presence of cylinders.
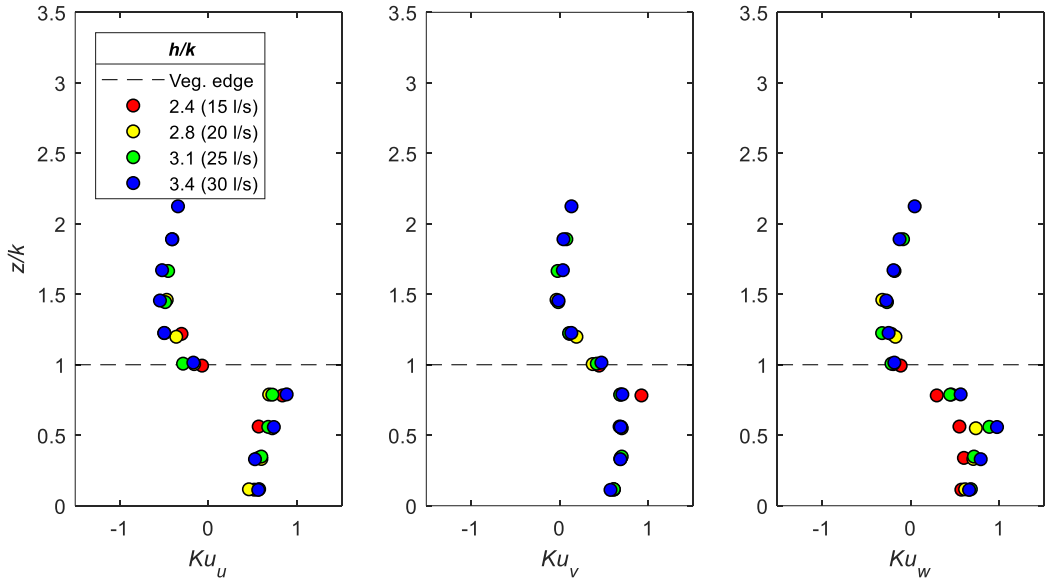
Figure 26 – Kurtosis of the fluctuation velocity components in the three directions x, y and z.

3.2.4 Reynolds Shear Stress

In Figure 27, the Reynolds shear stresses $-\overline{u'_i u'_j}$ (expressed in terms of covariances $-cov_{ij}$), normalized with the squared friction velocity at the canopy top, are plotted along the inspected vertical for the four different submergences.
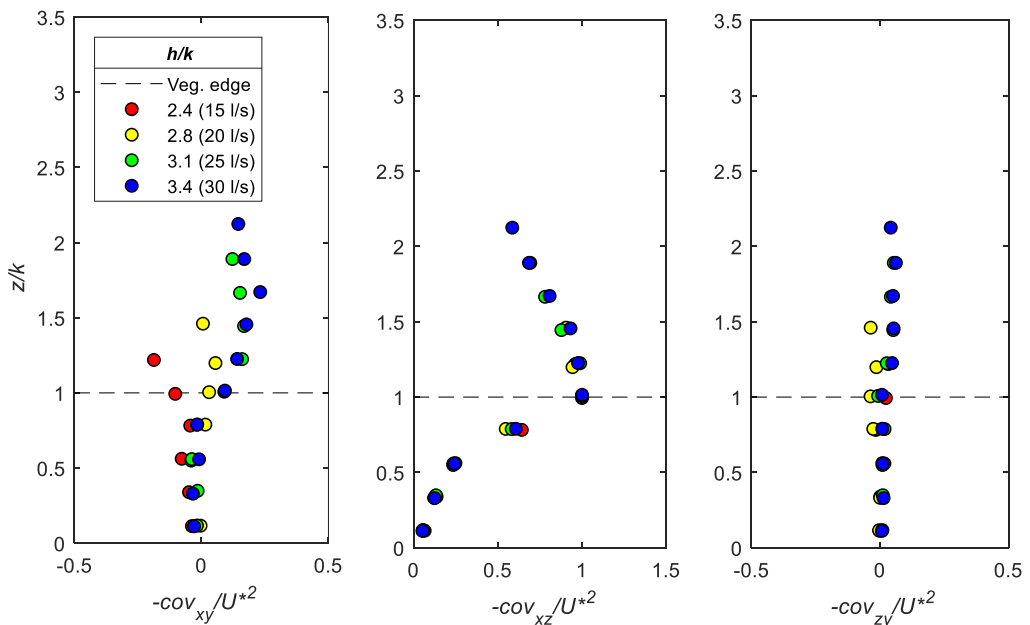
Figure 27 – Reynolds stress profiles. The quantities are normalized with the square of the friction velocity at the canopy top U^*.

The Reynolds stress $-\overline{u'w'}$ profile attained a peak at the canopy top (z/k=1) and exhibited a sharp decrease within the canopy. This effect, as observed by other authors (Nepf and Vivoni, 2000; Nezu and Sanjou, 2008), is due to the presence of the canopy elements which inhibits the momentum transfer between the surface layer and the underlying vegetated one.

The penetration depth (Table 6), estimated as the elevation at which the Reynolds stress $-\overline{u'w'}$ decays to 10% of its maximum value (Nepf and Vivoni, 2000), was evaluated from Figure 27 for the different submergence ratios, showing a good agreement with the estimation of the scaling of Equation 3.1. Depending only on the vegetation density, an approximately constant value was observed for all the test runs.

Table 6 – Penetration depth.

h/k	δ_e
(-)	(mm)
2.4	35
2.8	33
3.1	34
3.4	33

As the submergence increased, the shape of the normalized xy shear stress profile changed exhibiting higher values. These effects were ascribable to the growing effects of the secondary currents inside the experimental channel (Nezu and Sanjou, 2008), considering that the aspect ratio of the channel ($B/(h-k)$) ranged from 3.8 to 6.2.

3.2.5 Quadrant Analysis

The trend emerging from the skewness and kurtosis distributions was confirmed by the results of the quadrant analysis (see Section 2.5). In Figure 28, the contribution of each quadrant to the Reynolds stress is plotted as a function of the normalized distance from the bed.
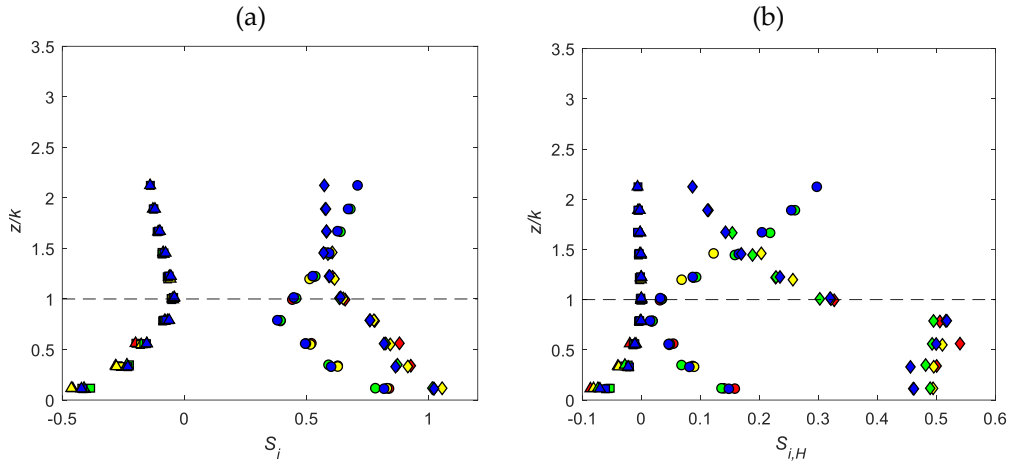
Figure 28 - Contribution of each quadrant to the overall Reynolds stress: (a) evaluated with Equation 2.23 considering all the events; (b) evaluated with Equation 2.24 considering only the extreme events, assuming the H parameter equal to 2. Inward S_1 and outward S_3 interaction are represented by solid squares (■) and triangles (▲), respectively, sweep S_2 and ejection S_4 by diamonds (♦) and circles (●). The different colors are referred to the four different considered conditions: blue 30 l/s, green 25 l/s, yellow 20 l/s and red 15 l/s.

The contributions of the different events were firstly evaluated considering H equal to 0 (S_i, Equation 2.23) and, secondly, considering H equal to 2 ($S_{i,H}$, Equation 2.24) (Figure 28, b), to make more evident the role played by the sweep and ejection events in the Reynolds stress production (Lu and Willmarth, 1973).

The quadrant analysis confirmed the central role of sweep within the canopy and, complementarily, the dominant role of ejection events in the region above the canopy, only slightly affected by the submergence. Inward and outward interaction event contributions were almost equal and negligible. At $z/k{\approx}1.5$, the contributions of sweep and ejection were approximately equal.

3.2.6 Turbulence Anisotropy

In order to provide an overall description of turbulence in the flow over rigid vegetated bed, the time mean invariants analysis was performed using the turbulence triangle (Choi and Lumley, 2001; Lumley and Newman, 1977), an anisotropy invariant map (Section 2.6). In Figure 29, the anisotropy invariant maps for the investigated test cases are reported.

The pattern defined by the points of the invariant map, in the range of the considered Reynolds number and submergences, was clear and approximately equal for all the considered conditions.
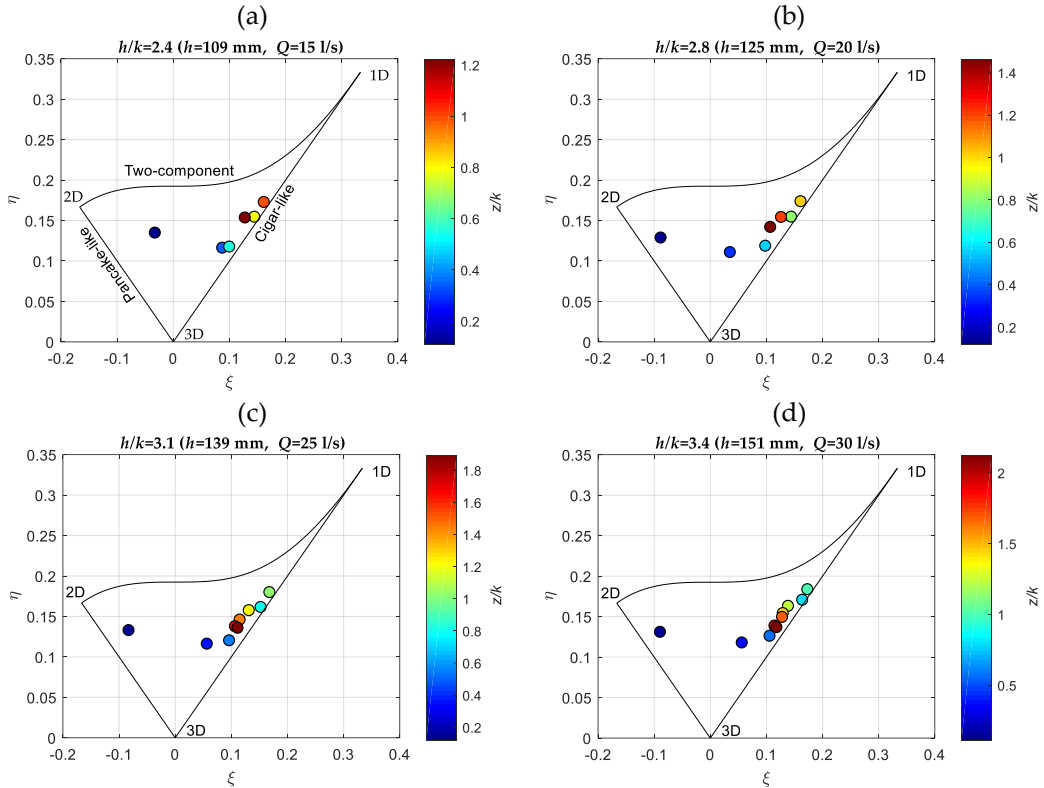
Figure 29 – Invariant maps for the different submergences: 2.4 (a), 2.8 (b), 3.1 (c), 3.4 (d).

Moving from the bed toward the water surface, the points of the invariants of the Reynolds stress tensor described a peculiar path. Near the channel bed, at z/k approximately equal to 0.1, the turbulence approached a 2D state. Moving upward, the turbulence reached, at the top of the canopy (z/k=1), a quasi-one-dimensional state, the fluctuation in the streamwise direction was dominant owing to the presence of the large-scale coherent structures, the shape of the turbulence was cigar-like. Specifically, for all the investigated conditions, the one-dimensional characteristic and the degree of anisotropy was maximum at z/k=1. Above the canopy (z/k>1), the path described by the points of the invariants moved through the axisymmetric expansion tending to an isotropic state. Owing to the dimension of the ADV sampling volume, for each submergence ratio, the last measurement point was 50 mm far from the surface (for the highest flow condition the last point is at z/k equal to 2.1, the water surface is at z/k equal to 3.4), therefore, the evolution of the path to the water surface is not shown. Anyway, owing to the presence of the

water surface which inhibits the vertical fluctuations, the turbulence structure is expected to become two-dimensional (Bomminayuni and Stoesser, 2011).

The two-dimensional state of the turbulence inside the canopy, and, specifically, in the lower part of the vegetated layer, indicates the growing importance of the lateral fluctuations due to the von Kármán vortex shedding process triggered by the cylinder array, as shown also by the plots of Figure 29. The onset of this process was ensured by the local high stem Reynolds number $Ud/v{\approx}850{>}150{-}200$ (Nepf et al., 1997).

In Figure 30, the dimensionless power density spectra of the lateral velocity fluctuations, evaluated at $z/k{=}0.1$ for all the investigated conditions, are shown together. The spectral density was normalized dividing by the product between the root mean square level of the local longitudinal velocity and the stem diameter. The frequency is given in terms of Strouhal number ($St{=}fd/U$). A concentration of energy in the range of Strouhal number equal to 0.2 and 0.1 was observed, in agreement with the frequency of the vortex shedding process observed by Poggi et al. (2004) and Zong et al. (2012) for a cylinder array. The von Karman vortex shedding peak in the power density spectra was only slightly visible owing to the deep penetration of the canopy scale structures within the array (Table 6).
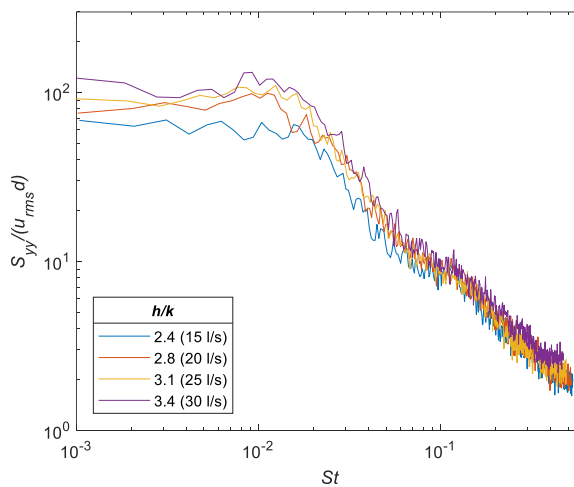
Figure 30 – Power density spectra at z=5 mm for the different runs. The ordinates are made dimensionless dividing by the local root mean square level of longitudinal velocity fluctuations multiplied by the diameter of the rods.

In order to highlight the effects of the rigid cylinders on the turbulent structure, a comparison between the anisotropy invariant maps deduced for the flow over rigid vegetated bed (Figure 29, d) and for the flow over a smooth bed (Figure 31) can be established.

The map of Figure 31 was resulted from the large eddy simulation of a flow over smooth bed at Re=13680 (Bomminayuni and Stoesser, 2011).
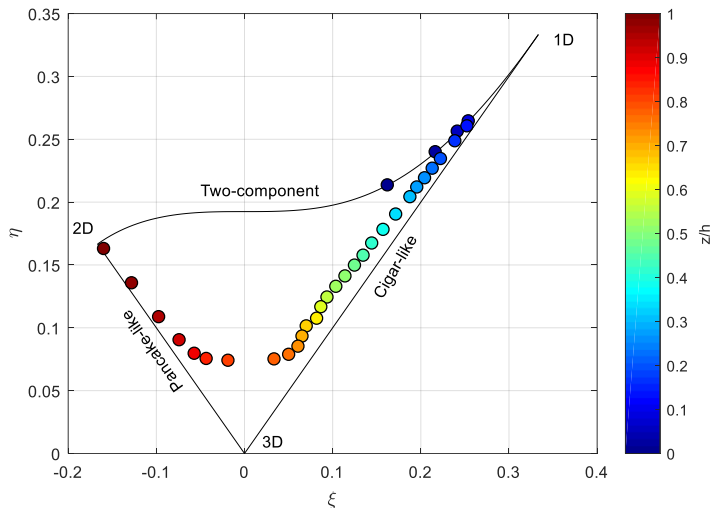
Figure 31 – Turbulence triangle for the smooth bed case, (Re_h=13680) (Bomminayuni and Stoesser, 2011).

Even though the two plots refer to flows with different Reynolds (13680 and 75000 for the smooth and uniformly vegetated bed, respectively), the comparison allows spotting the main differences in terms of turbulence anisotropy pattern. While in the viscous sublayer, directly above the flume bed, a two-component isotropic turbulence is expected for both the conditions, at z/k=0.1 (z/h≈0.04) the behavior is different and the turbulence in the vegetated case presented a 2D structure. On the contrary, in the smooth bed, as expected for a canonical BL, the turbulence is highly anisotropic and one-dimensional. Moving upwards, the evolution of the pattern is still different and, while for the vegetated bed anisotropy progressively increases and a one-dimensional characteristic was observed, for the smooth bed, turbulence gradually returns to isotropy via an axisymmetric expansion process. For the vegetated bed, turbulence at z/k≈2 (z/h≈0.6) still presented a high degree of anisotropy and a cigar-like shape, because this area of the flow was dominated by the canopy-scale coherent structures. For the smooth bed, turbulence becomes quasi-isotropic at z/h≈0.7 and then presents, approaching the free surface, a tendency to a 2D structure.

3.2.7 Integral Scales

In order to investigate the time and spatial extent of the coherent structures dominating the flow, the calculation of Eulerian integral time scales T_i and length scales L_i was performed (as described in Section 2.3). In Figure 32, integral time scales evaluated by means of Equation 2.14, for the three directions, along the inspected vertical and for the different considered conditions are shown.
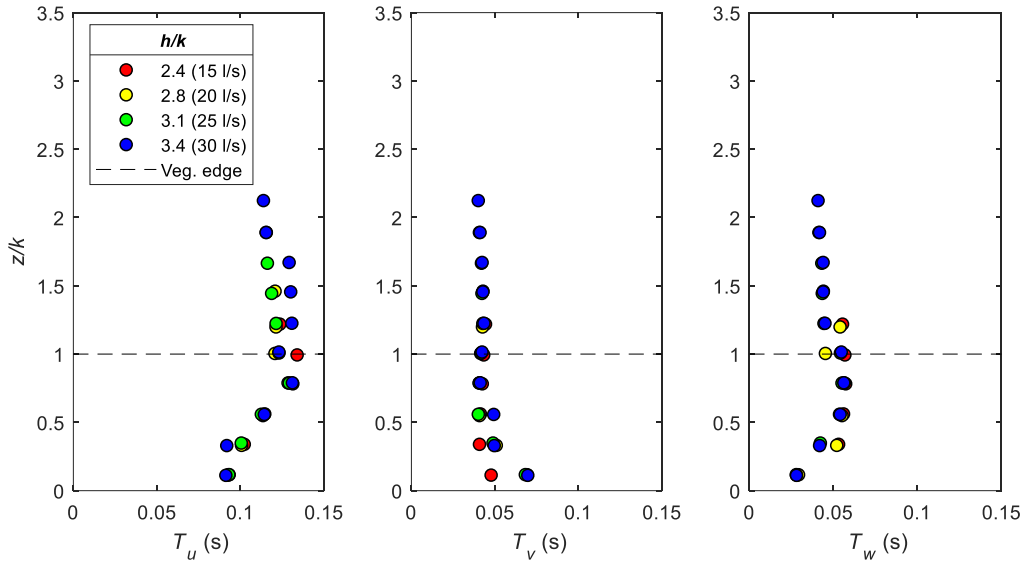
Figure 32 – Profiles of Eulerian integral time scales for the different investigated conditions.

The integration domain for the determination of the integral time scale ranged from 0 up to the value where the autocorrelation function fell to $1/e$ (Beckett, 1991; O'Neill et al., 2004), as to define an integration domain independent of the shape of the autocorrelation function (Gualtieri et al., 2015).

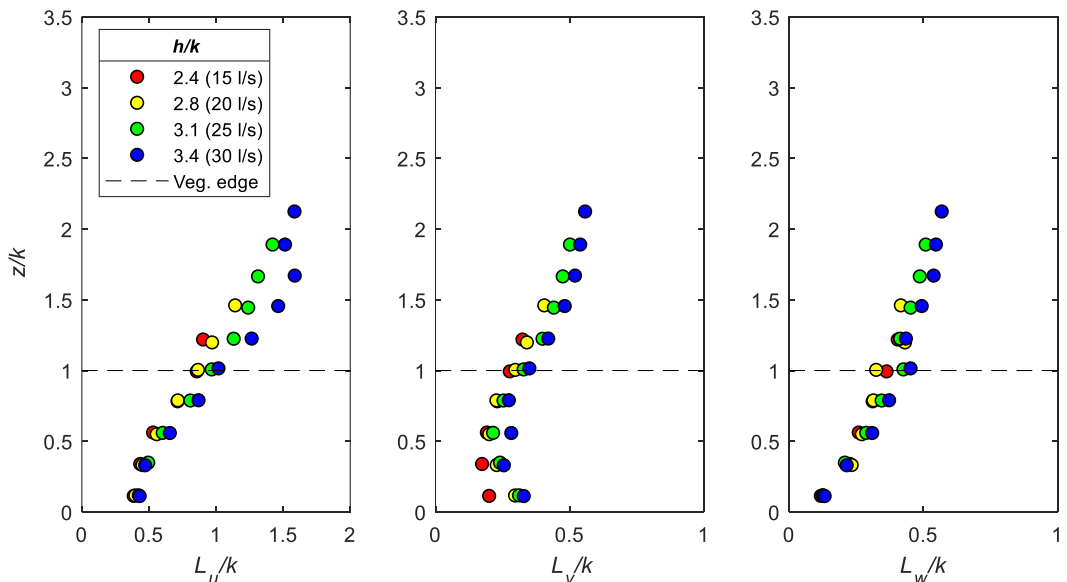*Figure 33 – Profiles of Eulerian integral length scales for the different investigated conditions.*

The Eulerian integral length scales can be estimated from the single-point integral time scales applying Taylor's frozen-turbulence hypothesis and assuming the mean local longitudinal velocity U as the convection velocity U_c of the mean eddies, using

the equation $L_i = UT_i$. The highest turbulence intensity, locally evaluated as u_{rms}/U was equal to 0.3. The integral length scales evaluated for the four different conditions are shown in Figure 33. The results confirmed the interpretation of the flow structure drawn by the anisotropy analysis. Turbulence exhibited a quasi-two-dimensional structure near the channel bed, within the vegetation layer, owing to the dominant effects of stem scale turbulence and von Kármán vortices. Moving toward the vegetation top, while L_v tended to decrease, L_u and L_w showed a progressively increasing trend, confirming the axisymmetric expansion process shown by the invariant maps. Specifically, at the canopy top, L_u and L_w were approximately equal to k and $0.4k$, showing that in the upper vegetated layer the dominant eddy size is in the order of k, consistently with the results of Raupach et al. (1996) and Nezu and Sanjou (2008). Over the canopy, the three integral length scales became larger, in this region the flow was dominated by the canopy scale turbulence. In Figure 34, the good agreement between the integral length scales relative to runs 3 and 4, and the results for dense canopies of Nezu and Sanjou (2008) is shown.
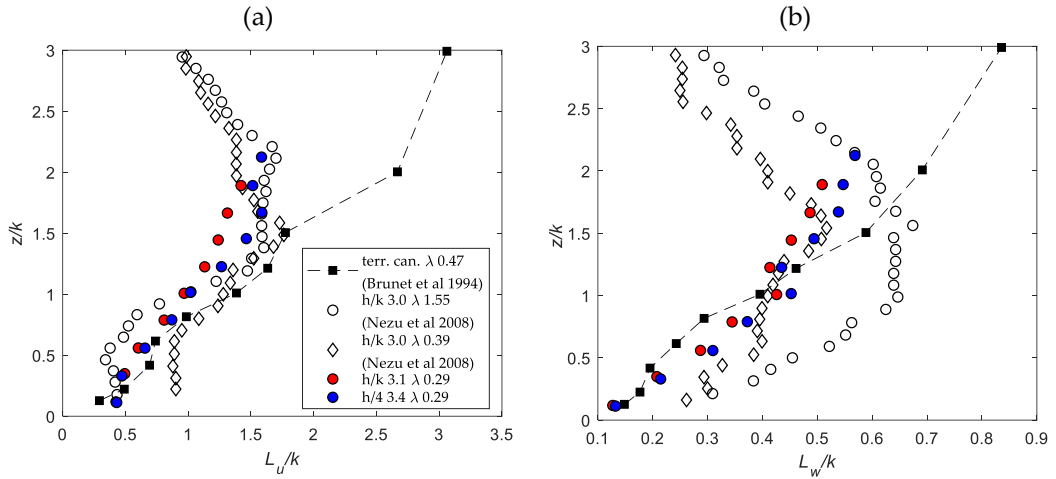
Figure 34 - Comparison with analogous literature calculation of integral length scales (Brunet et al., 1994; Nezu and Sanjou, 2008): (a) integral length scale profile along the vertical direction for the x component; (b) integral length scale profile along the vertical direction for the z component. In the plot only the profiles evaluated for the two highest submergence conditions are reported.

In Figure 34 the integral length scales evaluated for terrestrial canopies are also reported (Brunet et al., 1994). Owing to the effect of the confinement induced by the free surface, significant difference was observed between aquatic and terrestrial canopies. These results confirm how, in aquatic canopy, eddies are influenced by submergence.

3.3   Conclusions

The results of this experimental analysis provided an exhaustive picture of the effects of increasing submergence on the mean and turbulent structure of the flow over an array of submerged rigid cylinders, modeling dense vegetation. Specifically, rigid cylinders were arranged in an aligned pattern, modeling submerged rigid vegetation. Different submergence ratios were investigated.

The effects of a variation of approximately 50% of h/k was observed not to significantly affect the flow structure, indicating that, in the range of the tested submergences, the stem density plays a major role on the hydrodynamic structure of the flow, as reported by Nezu and Sanjou (2008) and Poggi et al. (2004). The mean velocity profiles presented a characteristic inflected shape due to the different flow velocity within and above the vegetation, slightly more pronounced for the higher values of submergence. This effect, related to the high density of the cylinder array, was the main feature of the considered obstructed flow, and the consequent KH type instability dominated the momentum exchange across the vegetated interface.

The higher order moments and the quadrant analysis allowed characterizing the Reynolds stress production process and distribution throughout the water depth, confirming the dominant role of the sweep and ejection bursting events. The maximum Reynolds stress was observed at the top of the canopy. The sudden decay of τ_{zx} within the vegetation, owing to the significant contribute of the drag force to the momentum balance, was observed. The integral length scales showed a trend characteristic of dense aquatic canopy, allowing characterizing eddies of the flow field.

The invariant maps, generally used for verification of numerical models results, and here applied for the interpretation of the componentality of the turbulence in vegetated flows, gave interesting results, showing that they can be useful for the interpretation of the turbulent structure of vegetated flows. In particular, the flow structure picture emerging from the anisotropy analysis was consistent with the traditional statistical analysis of turbulence, providing a complete description of the flow field. Specifically, the method can be easily transferred to more complex vegetation models and configurations and, together with traditional analysis, can contribute to the understanding of turbulence in vegetated contexts.

References

Aberle, J., Järvelä, J., 2013. Flow resistance of emergent rigid and flexible floodplain vegetation. J. Hydraul. Res. 51, 33–45. doi:10.1080/00221686.2012.754795

Augustijn, D.C.M., Huthoff, F., Van Velzen, E.H., 2008. Comparison of vegetation roughness descriptions. Proc. River Flow 2008 - Fourth Int. Conf. Fluv. Hydraul. 3-5 Sept. 2008 Cesme, Turkey 9.

Beckett, P.M., 1991. Physical Fluid Dynamics By D. J. Tritton, Oxford University Press, Oxford, 1988, pp. 519, price: £35.00 (hardback), $16.95 (paperback). ISBN 0–19–854489-8 (hardback); 0–19–854493-6 (paperback). J. Chem. Technol. Biotechnol. 50, 144. doi:10.1002/jctb.280500121

Bomminayuni, S., Stoesser, T., 2011. Turbulence Statistics in an Open-Channel Flow over a Rough Bed. J. Hydraul. Eng. 137, 1347–1358. doi:10.1061/(ASCE)HY.1943-7900.0000454

Brunet, Y., Finnigan, J.J., Raupach, M.R., 1994. A wind tunnel study of air flow in waving wheat: Single-point velocity statistics. Boundary-Layer Meteorol. 70, 95–132. doi:10.1007/BF00712525

Chanson, H., Trevethan, M., Koch, C., 2005. Discussion of "Turbulence Measurements with Acoustic Doppler Velocimeters" by Carlos M. Garcia, Mariano I. Cantero, Yarko Nino, and Marcelo H. Garcia. J. Hydraul. Eng. 131, 1062–1073. doi:10.1061/(ASCE)0733-9429(2005)131:12(1062)

Choi, K.-S., Lumley, J.L., 2001. The return to isotropy of homogeneous turbulence. J. Fluid Mech. 436, 161. doi:10.1017/S002211200100386X

Coscarella, F., Servidio, S., Ferraro, D., Carbone, V., Gaudio, R., 2017. Turbulent energy dissipation rate in a tilting flume with a highly rough bed. Phys. Fluids 29. doi:10.1063/1.4996773

Devi, T.B., Kumar, B., 2016. Experimentation on submerged flow over flexible vegetation patches with downward seepage. Ecol. Eng. 91, 158–168. doi:10.1016/j.ecoleng.2016.02.045

Ghannam, K., Katul, G.G., Bou-Zeid, E., Gerken, T., Chamecki, M., 2018. Scaling and similarity of the anisotropic coherent eddies in near-surface atmospheric turbulence. J. Atmos. Sci. JAS-D-17-0246.1. doi:10.1175/JAS-D-17-0246.1

Ghannam, K., Poggi, D., Porporato, A., Katul, G.G., 2015. The Spatio-temporal Statistical Structure and Ergodic Behaviour of Scalar Turbulence Within a Rod Canopy. Boundary-Layer Meteorol. 157, 447–460. doi:10.1007/s10546-015-0073-1

Ghisalberti, M., Nepf, H.M., 2006. The structure of the shear layer in flows over rigid and flexible canopies. Environ. Fluid Mech. 6, 277–301. doi:10.1007/s10652-006-0002-4

Ghisalberti, M., Nepf, H.M., 2002. Mixing layers and coherent structures in vegetated aquatic flows. J. Geophys. Res. 107, 1–11. doi:10.1029/2001JC000871

Goring, D.G., Nikora, V.I., 2002. Despiking Acoustic Doppler Velocimeter Data. J. Hydraul. Eng. 128, 117–126. doi:10.1061/(ASCE)0733-9429(2002)128:1(117)

Gualtieri, P., De Felice, S., Pasquino, V., Pulci Doria, G., 2015. Evaluation of integral length scale from experimental data in a flow through submerged vegetation. In Proceedings of the XXXVI IAHR Congress, Delft–The Hague, The Netherlands, 28 June–3 July 2015; pp. 1–9.

Gualtieri, P., Felice, S. De, Pasquino, V., Doria, G.P., 2018. Use of conventional flow resistance equations and a model for the Nikuradse roughness in vegetated flows at high submergence. J. Hydrol. Hydromechanics 66, 107–120. doi:10.1515/johh-2017-0028

Lu, S.S., Willmarth, W.W., 1973. Measurements of the structure of the Reynolds stress in a turbulent boundary layer 60, 481–511.

Lumley, J.L., Newman, G.R., 1977. The return to isotropy of homogeneous turbulence. J. Fluid Mech. 82, 161–178. doi:10.1017/S0022112077000585

Nakagawa, H., Nezu, I., 1977. Prediction of the contributions to the Reynolds stress from bursting events in open-channel flows. J. Fluid Mech. 80, 99. doi:10.1017/S0022112077001554

Nepf, H.M., 2012. Hydrodynamics of vegetated channels. J. Hydraul. Res. 50, 262–279. doi:10.1080/00221686.2012.696559

Nepf, H.M., Ghisalberti, M., White, B.L., Murphy, E., 2007. Retention time and dispersion associated

with submerged aquatic canopies 43, 1–10. doi:10.1029/2006WR005362

Nepf, H.M., Sullivan, J. a., Zavistoski, R. a., 1997. A model for diffusion within emergent vegetation. Limnol. Oceanogr. 42, 1735–1745. doi:10.4319/lo.1997.42.8.1735

Nepf, H.M., Vivoni, E.R., 2000. Flow structure in depth-Iimited, vegetated flow. J. Geophys. Res. 105, 28547–28557.

Nezu, I., Sanjou, M., 2008. Turburence structure and coherent motion in vegetated canopy open-channel flows. J. Hydro-Environment Res. 2, 62–90. doi:10.1016/j.jher.2008.05.003

O'Neill, P.L., Nicolaides, D., Honnery, D.R., Soria, J., 2004. Autocorrelation Functions and the Determination of Integral Length with Reference to Experimental and Numerical Data. 15th Australas. Fluid Mech. Conf. 1, 1–4.

Peruzzo, P., de Serio, F., Defina, A., Mossa, M., 2018. Wave height attenuation and flow resistance due to emergent or near-emergent vegetation. Water (Switzerland) 10, 1–13. doi:10.3390/w10040402

Poggi, D., Porporato, A., Ridolfi, L., Albertson, J.D., Katul, G.G., 2004. The effect of vegetation density on canopy sub-layer turbulence. Boundary-Layer Meteorol. 111, 565–587. doi:10.1023/B:BOUN.0000016576.05621.73

Pope, S.B., 2000. Turbulent Flows. Cambridge University Press. doi:10.1017/CBO9780511840531

Raupach, M.R., Finnigan, J.J., Brunei, Y., 1996. Coherent eddies and turbulence in vegetation canopies: The mixing-layer analogy. Boundary-Layer Meteorol. 78, 351–382. doi:10.1007/BF00120941

Raupach, M.R., Thom, A.S., 1981. Turbulence in and above Plant Canopies. Annu. Rev. Fluid Mech. 13, 97–129. doi:10.1146/annurev.fl.13.010181.000525

Rowiński, P.M., Kubrak, J., 2002. A mixing-length model for predicting vertical velocity distribution in flows through emergent vegetation. Hydrol. Sci. J. 47, 893–904. doi:10.1080/02626660209492998

Smalley, R., Leonardi, S., Antonia, R.A., Djenidi, L., Orlandi, P., 2002. Reynolds stress anisotropy of turbulent rough wall layers. Exp. Fluids 33, 31–37. doi:10.1007/s00348-002-0466-z

Sukhodolova, T.A., Sukhodolov, A.N., 2012. Vegetated mixing layer around a finite-size patch of submerged plants: Part 1. Theory and field experiments. Water Resour. Res. 48, 1–16. doi:10.1029/2011WR011804

Vargas-Luna, A., Crosato, A., Calvani, G., Uijttewaal, W.S.J., 2016. Representing plants as rigid cylinders in experiments and models. Adv. Water Resour. 93, 205–222. doi:10.1016/j.advwatres.2015.10.004

Västilä, K., Järvelä, J., 2014. Modeling the flow resistance of woody vegetation using physically based properties of the foliage and stem. Water Resour. Res. 50, 229–245. doi:10.1002/2013WR013819

Viero, D.P., Pradella, I., Defina, A., 2017. Free surface waves induced by vortex shedding in cylinder arrays. J. Hydraul. Res. 55, 16–26. doi:10.1080/00221686.2016.1217948

Wahl, T.L., 2003. Discussion of '"Despiking Acoustic Doppler Velocimeter Data"' by Derek G. Goring and Vladimir I. Nikora January. J. Eng. Mech. 128, 2002–2003. doi:10.1061/(ASCE)0733-9372(2003)129

Wallace, J.M., Brodkey, R.S., 1977. Reynolds stress and joint probability density distributions in the u-v plane of a turbulent channel flow. Phys. Fluids 20, 351–355. doi:10.1063/1.861897

Zong, L., Nepf, H.M., 2012. Vortex development behind a finite porous obstruction in a channel. J. Fluid Mech. 691, 368–391. doi:10.1017/jfm.2011.479

4 Flow in partly vegetated channel with complex morphology vegetation

In a variety of natural settings, vegetation communities occur along rivers in lateral zones approximately parallel to the flow. Examples include vegetated channel banks, floodplains and patches of aquatic vegetation that typically extend in elongated shape in the downstream direction (e.g. Dupuis et al., 2017; Hu et al., 2018; Liu et al., 2017; Ortiz et al., 2013; White and Nepf, 2008). This consideration led to focus the research interest toward the so-called channel-vegetated-bank systems. In these systems, the mutual interactions between the lateral vegetated areas and the adjacent main channel deeply affect the hydrodynamic structure of the flow, influencing the lateral exchange of mass and momentum across the river section (Ben Meftah et al., 2014; Rowiński et al., 2018; White and Nepf, 2008). The lateral exchange controls the efficiency of cross-sectional mixing (White and Nepf, 2008), governing the fate of dissolved and particulate substances (Gacia and Duarte, 2001; Hu et al., 2010).

In partly vegetated channels (as introduced in Section 1.3.2.3), owing to the different drag conditions between the lateral vegetated area and the main channel, a region of shear is formed between two approximately parallel streams of different velocity U_1 and U_2, with $U_1 < U_2$. Thus, the resulting flow field is characterized by a strong inflectional nature that gives rise to KH type instability (Ash and Khorrami, 1995). Such vegetated shear layers have been generally patterned on canonical MLs (White and Nepf, 2008) or BLs (Ben Meftah et al., 2014), as to effectively model velocity and other quantities of practical interest. Nevertheless, the effects of natural vegetation properties are still unexplored, since previous investigation simulated vegetation with rigid cylinders. Indeed, in the analysis of flow in partly vegetated channels the vegetation characteristics should be adequately taken into account.

Floodplain and riparian vegetation generally presents a complex morphology with highly heterogeneous geometric and bio-mechanical properties distribution along the elevation (Niklas, 1997; Weissteiner et al., 2015). In response to the flow forcing, the different parts of the plants assume a streamlined configuration, undergoing a process called reconfiguration (Västilä and Järvelä, 2017; Vogel, 1994), as introduced in Section 1.2.1.

Additionally, as introduced in Section 1.1, riparian vegetation experiences periodic seasonal morphological variability that deeply affects the flow with implications on e.g. hydraulic resistance, flow structure, sediment transport and erosion (Cotton et al., 2006; Shih and Rahi, 1982; Västilä et al., 2016).

While the effects of complex plant morphology and reconfiguration on hydraulic resistance and hydrodynamic flow structure in uniformly vegetated flows have been widely investigated (Järvelä, 2002; Rowiński and Kubrak, 2002; Rubol et al., 2018; Siniscalchi et al., 2012; Västilä and Järvelä, 2014), the effects of complex plant morphology in partly vegetated flows are still poorly explored. The characteristics of the flow in partly vegetated channels have been commonly investigated by simulating plants as rigid cylinders (Ben Meftah et al., 2014; Choi and Kang, 2006; Naot et al., 1996; Tsujimoto and Kitamura, 1992; White and Nepf, 2008) neglecting a variety of flow influencing mechanisms exhibited by real vegetation (Ghisalberti and Nepf, 2006). A major difference between rigid and natural vegetation is the dynamic motion exhibited by real vegetative obstructions. The periodical waving, such as the *monami* (Ackerman and Okubo, 1993), has been found to affect the drag discontinuity between the submerged vegetation and overflow, influencing the coherence of large-scale turbulent structures and, in turn, on cross-section exchange of mass and momentum (Ghisalberti and Nepf, 2006). In this context, the effects of seasonality which produce strong morphological modification on vegetation, and consequently deeply alter the flow structure, are generally neglected.

A characteristic feature of shear flows in channel-vegetated-bank systems is the anisotropy of the Reynolds stresses, which reflects the presence of organized motions. Indeed, turbulence anisotropy enhances and maintains the coherence of turbulent structures, governing the mutual interactions at the vegetated interface. The anisotropic component of the stress is the only effective in transporting momentum (Pope, 2000) and, therefore, the study of turbulence anisotropy is of fundamental importance to understand the interface dynamics in partly vegetated channels. Additionally, most Reynolds-averaged Navier-Stokes models for the simulation of vegetated flows have been developed with turbulence closure strategies that assume isotropic turbulence over the flow domain (e.g. Li and Yu, 2010; Shimizu and Tsujimoto, 1994) and, therefore, it is important to identify and quantify turbulence anisotropy. In presence of a morphologically complex vegetative obstruction, for which the instantaneously variable drag conditions at the interface and the reconfiguration behavior deeply affect the flow structure, these considerations assume even more relevance. The degree and type of departure from isotropy within the flow can be investigated using the technique of the anisotropy invariants (Lumley and Newman, 1977), introduced in Section 2.5. This technique has been applied for the analysis of turbulence anisotropy in a variety of different

contexts, including meandering channels (Mera et al., 2015) and flows over highly rough beds (Bomminayuni and Stoesser, 2011) or over non-cohesive sediment beds (Sarkar and Dey, 2015). In Section 3.2.6 the anisotropy invariant map has been applied to flow over submerged rigid vegetation, showing that this technique is effective for the interpretation of the turbulence in vegetated flows.

A crucial aspect of the experimental investigation of obstructed flows or in presence of macro-bed roughness is the representativeness of punctual velocity measurements owing to the high local heterogeneity of flow characteristics. To address this local spatial variability, the flow characteristics are generally double averaged both temporally and spatially across the direction of homogeneity of the flow, following the so-called double-averaging methodology (Nikora et al., 2007; Nikora and Rowiński, 2008). The experimental applicability of this procedure clearly depends on the measurement technique and the type of obstruction. For not-moving boundaries like macro-bed roughness (Coscarella et al., 2017; Ferraro et al., 2016), rigid cylinders (Nezu and Sanjou, 2008; Poggi et al., 2004) or simple vegetation models (Nepf and Vivoni, 2000; Righetti and Armanini, 2002) this task has been accomplished. In contrast, for a complex dynamically moving and dense vegetative obstruction, the double-averaging is generally more complex. In earlier studies of flow through complex vegetative morphologies, the local spatial variability of flow characteristics due to vegetation heterogeneity has been mostly neglected. In the present work, the flow spatial variability was partially addressed averaging the measurements obtained along two different transects, carefully positioned within the flow domain. This procedure, although not comparable to the double-averaging method, was considered to provide representative flow characteristics.

The goal of this Chapter is to characterize the effects of morphologically complex vegetation and its seasonal variability on lateral mixing and turbulent flow pattern in a partly vegetated channel. The effects of foliation and reconfiguration on the overall flow structure (lateral distributions of velocity statistics), on large coherent turbulent structures (presence and strength), and on the turbulence anisotropy (degree and nature) across the vegetated interface were explored. In order to provide a contribution to the understanding of shear layer type flows in channel-vegetated-bank systems with reference to real riparian vegetation, the fully developed flow in a partly vegetated channel with natural-like emergent plant stands was experimentally investigated. Natural-like vegetation morphology was reproduced designing branched foliated plant stands exhibiting a natural reconfiguration behavior, with leaf to stem area ratios comparable to those of real riparian vegetation. In addition, the vegetation density was accurately adjusted to

mimic actual riparian conditions, while improving the representation of natural settings by placing the emergent plant stands on a grassy bed.

4.1 Materials and methods

Experiments were carried out in a partly vegetated channel using the same emergent vegetation under foliated and leafless conditions (Figure 35). To improve the representativeness of natural conditions, where low grasses typically grow beneath shrubs and trees, the bed roughness of the vegetated part of the flume consisted of 20 mm tall dense artificial grasses. Two different vegetative conditions: grasses with emergent foliated vegetation (F), and grasses with emergent leafless vegetation (L) were investigated. The third vegetative condition, where only grasses were present (G), and which results are not intended to be analyzed separately, was also tested. To evaluate the influence of the flexibility-induced reconfiguration, the lateral structure of the flow was determined at three different flow rates (low, medium and high) for each of the three vegetative conditions, resulting in altogether nine test runs. All runs were conducted under uniform flow conditions (in a spatially-averaged sense) with the water depth h of 0.17 m. The experimental conditions are described in detail in the following Sections.

4.1.1 Experimental facility

Experiments were carried out in a 20 m long, 0.6 m wide, and 0.8 m deep tilting glass-walled recirculating flume in the Environmental Hydraulics Lab of Aalto University. The x, y, and z flume coordinate system axes (Figure 35, a) refer to the longitudinal, lateral, and vertical (normal to the flume bottom) directions, respectively. The coordinate system origin was defined as $x=0$ at the inlet cross-section, positive downstream; $y=0$ at the edge of the grassy bed (see Figure 35, a) and positive toward the main channel; and $z=0$ at the channel bottom and positive upwards. In the defined right-handed rectangular Cartesian coordinate system, velocity components were denoted as u, v and w, in the x (longitudinal), y (lateral) and z (vertical) direction. The flume bottom from $x=4$ m to $x=14$ m was covered with a 600 mm wide PVC base plate, onto which vegetation elements were installed in 2.5 mm diameter holes. The vertical coordinate was defined as to have the origin at the top of the bed plate.

The flow into the experimental facility was driven and recirculated with a centrifugal pumping system. The centrifugal pumps, separated from the experimental section, were connected to the feeding pipe of the flume via a hose, ensuring the vibration isolation of the experimental section. The flow entered the flume via an inlet element, a limited capacity reservoir, provided with a dissipation plate and a flow straightener to reduce inlet related turbulence and possible flow surface instabilities. The discharge was measured with a magnetic flow-meter (with

accuracy of 0.5% of reading ±0.035 l/s) and recorded at 80 Hz for the entire duration of the tests. The flow rate resulted highly stable with a coefficient of variation <0.5%.

The free surface elevation along the partly vegetated reach was measured with 6 pressure transducers (with accuracy of ±1.8 mbar +0.2% FS) tapped at the centerline of the flume and located at x=5, 6.5, 8, 9.5, 11.5 and 13 m respectively, and sampled at 80 Hz for the entire duration of the tests. The slope of the flume and the position of a downstream tailgate were adjusted to achieve the desired spatially averaged uniform flow conditions, with the water depth of 170 mm through the 10 m long vegetated reach for all examined cases. The plants were just submerged at all runs, with a negligible change in the submerged leaf area at different flow rates.

4.1.2 Vegetation models, flow rates and test cases

Approximately 40% of the flume bottom was covered by an array of emergent artificial foliated plant stands Figure 35 (a). In order to reproduce representative near-bed flow conditions, a 20 mm tall and 230 mm wide artificial grass lining was selected as bed roughness from y=0 to y=-230 mm (Figure 35, a). The natural-like complex vertical distribution of mass and mechanical characteristics, together with the pronounced variability of plant geometry along the depth, made the selected artificial plants suitable for simulating the flexibility and reconfiguration behavior of natural riparian bushes and shrubs (Västilä and Järvelä, 2014). Moreover, the selected plants allowed reproducing and observing the central effects of the vegetation spatial morphologic variability on the flow structure (Defina and Bixio, 2005; Nepf and Vivoni, 2000).
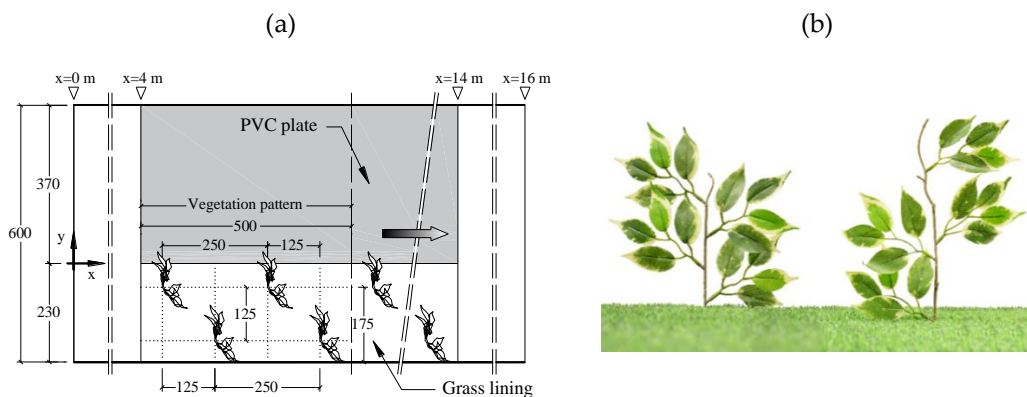
Figure 35 – Top view of the experimental flume with the repetitive vegetation pattern and flume coordinate system. All units are in millimeters unless otherwise indicated (a). The modular vegetation elements were built starting from two different types of stems (270 and 205 mm tall with 3 mm average diameter) and leaf clusters (each of them was made of 4 opposite aristate-like leaves with entire margin connected to a short stem) (b).

Because a nearly uniform distribution of longitudinal mean velocity along the water depth is typically observed in flows with emergent vegetation (Kubrak et al., 2008;

Liu et al., 2008), the plant stand was designed aiming at achieving as close to a uniform vertical distribution of the leaf area as possible for all flows, considering that the shape and orientation of leaves varied at each investigated flow velocity. Therefore, the vegetation model was made of four different plants composed of a vertical stem (with an average diameter of approximately 3 mm) and 4-5 lateral foliated branches, each one having 4 leaves (two plants are shown in Figure 35, b). Specifically, a 0.5 m long repetitive pattern composed by the four different plants was used for covering the 10 m long vegetated section of the flume (Figure 35, a). The plants (Figure 35, b) were arranged in a staggered pattern with a longitudinal (L_x) and lateral (L_y) spacing of 250 and 125 mm, respectively. The number n of stems per m² of bed area was equal to 35. Taking into account both the main stem and the side-twigs, the characteristic diameter d of the non-foliated plants was approximately equal to 3.8 mm and the solid volume fraction ($\phi=\pi d^2 n/4$) to 0.039%.

The bulk one-sided leaf area per unit volume (a_L) and the frontal projected area of the stems per unit volume ($a_S= d/(L_x L_y)$) were equal to 4.1 and 0.13 m⁻¹ respectively, falling into the range of a_S=0.01-0.13 m⁻¹ observed for natural riparian shrubs and bushes (Zinke, 2011), but regarded as very sparse vegetation by Nepf (Nepf, 2012). The leaf area to stem area ratio (A_L/A_S) (Västilä et al., 2013) was approximately equal to 31, comparable to the leaf to stem area ratios of common woody riparian species (Västilä and Järvelä, 2014). For the investigation under the leafless conditions, the leaves were de-attached from the plants.

Table 7 – Test cases and relevant mixing layer quantities. Q is the flow rate, U_m the cross-sectional mean velocity, i the flume slope, U_1 the low speed stream velocity (in the vegetated area), U_2 the high speed stream velocity (in the main channel), U_c the convection velocity ((U_1+U_2)/2), ΔU the differential velocity, δ the mixing layer width, θ the momentum thickness, λ the velocity ratio, and $C_D a$ the drag-density parameter. For all the test runs, uniform flow conditions with h=170 mm were considered

Run	Q (l/s)	U_m (m/s)	i (%)	U_1 (m/s)	U_2 (m/s)	U_c (m/s)	ΔU (m/s)	δ (mm)	θ (mm)	λ (-)	$C_D a$ (m⁻¹)
Foliated plant stands and grasses
F1	22.2	0.22	0.107	0.042	0.364	0.203	0.323	175.0	40.1	0.795	12.154
F2	50.0	0.49	0.336	0.216	0.787	0.501	0.571	170.0	37.1	0.569	1.432
F3	83.3	0.82	0.707	0.532	1.274	0.903	0.742	155.0	33.5	0.411	0.485
Leafless plant stands and grasses
L1	22.2	0.22	0.064	0.180	0.303	0.241	0.123	135.0	22.2	0.255	0.425
L2	50.0	0.49	0.168	0.403	0.672	0.538	0.268	135.0	24.7	0.250	0.205
L3	83.3	0.82	0.414	0.666	1.128	0.897	0.463	122.5	24.9	0.258	0.181
Grasses only
G1	22.2	0.22	0.050	0.241	0.276	0.259	0.035	67.5	15.8	0.068	0.169
G2	50.0	0.49	0.150	0.527	0.615	0.571	0.089	75.0	11.9	0.078	0.106
G3	83.3	0.82	0.286	0.865	1.010	0.937	0.145	67.5	16.1	0.077	0.076

The combination of two vegetative conditions (F and L, foliated and leafless vegetation, respectively) and three flow rates (low, medium and high) resulted in 6 different test cases, whose details are indicated in Table 7. The third vegetative condition (G), where only the grassy bed roughness was present and which results are not intended to be analyzed separately, was also investigated.

The drag-density parameter $C_D a$, i.e. the vegetation drag coefficient C_D multiplied by the total projected area per unit canopy volume a, was used to describe the overall vegetative drag per unit water volume, which takes into account also the plants reconfiguration effects. The $C_D a$ parameter was estimated from the data as in White and Nepf (2008), assuming the equilibrium between the overall vegetative drag and the pressure gradient and neglecting the contribution of the interface turbulence stress in driving the flow within the vegetation:

$$\frac{1}{2} C_D a U_1{}^2 = -g \frac{dh}{dx}. \tag{4.1}$$

4.1.3 Determination of flow structure

The flow in the partly vegetated channel was investigated measuring instantaneous three dimensional velocity components along two lateral transects with acoustic Doppler velocimetry.

The z=95 mm position was selected as the most representative measurement location for the depth-averaged velocity. Differently from studies with rigid cylinders (e.g. White and Nepf, 2008), the within-vegetation vertical profiles exhibited a much higher variability caused by the complex velocity-dependent streamlining and reconfiguration of the foliage: a difference between the mid-depth longitudinal velocity $U(z$=95 mm) and the depth-averaged velocity as high as 23% (23% for the verticals within the vegetation and 19% for all the verticals including the main channel ones) was observed. This higher variability is consistent with the observation of Kubrak et al. (2008) about longitudinal velocity profiles within flexible vegetation. Furthermore, as observed from the longitudinal and lateral velocity spectra along the investigated verticals (not shown), the turbulent structure in the mid-depth region of the flow resulted to be weakly affected by the bed roughness and free surface.

On the basis of lateral profiles of longitudinal mean velocity recorded along the experimental flume, the reach of the flume between x=11 and 12 m (7 m downstream of the leading edge of the vegetation) was selected as an appropriate measurement section as the flow was fully developed.

In order to address the local spatial variability of the flow due to the heterogeneity of the vegetation characteristics within the pattern, the two transects were measured

at the same relative position with respect to the location of the stems (shifted 250 mm longitudinally), see Figure 36. The lateral distributions of velocity statistics were successively obtained by averaging the two investigated transects. The measurement positions were selected to obtain high-quality ADV data under all the examined conditions, by ensuring that the moving parts of the plants (which exhibited strong dynamic motions) did not enter the paths of the acoustic beams of the ADV and that no leaves had to be removed during the measurements.

The investigated transects were located approximately 40 mm upstream and 210 mm downstream of the closest plants (Figure 36, a); at these longitudinal positions the lateral velocities within the stands were the lowest. As is shown in Figure 36 (a), owing to the obstruction provided by the foliated plants, each transect was composed by two segments: a first one in the vegetated area covering the points from y=-230 to y=-130 mm and a second segment, shifted upstream of 125 mm, covering the remaining part of the cross-section. This ensured that the flow properties at different lateral positions could be directly compared. In the leafless runs, the continuous transect along the cross-section, depicted in Figure 36 (b), were longitudinally shifted of 125 mm.
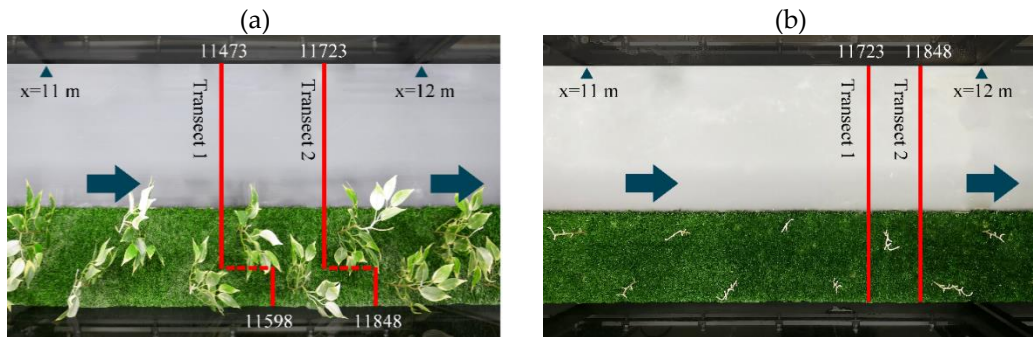
Figure 36 – Plan view of the investigated transects for the foliated (a) and leafless (b) case.

For each transect, a total of 45 and 39 velocity measurement points, for the foliated and the leafless test cases respectively, were considered. The spacing ranged from 5 to 20 mm, sampling location were more densely placed at the interface where strong gradient in mean velocity and Reynolds stress profiles were observed.

The variability of flow characteristics along z was investigated by measuring flow velocity along 5 verticals distributed across the shear layer. Specifically, the five lateral positions y=220, 70, 0, -60 and -180 mm were considered.

Three-dimensional instantaneous velocity components were measured at 200 Hz with an ADV Nortek Vectrino+ with a 4-beam side looking probe, with accuracy of ±1%. The sampling volume was 7 mm long with a 6 mm diameter (≈198 mm³) and the lowest velocity range of the instrument was appropriately selected depending

on the flow characteristics (mean velocity and turbulence intensity). The flow was constantly seeded with solid glass micro-spheres (average particles diameter of 7-10 μm) in order to achieve and maintain good operational conditions for the entire duration of the tests. A recording time of 120 s (24000 samples) was found to be sufficiently large to achieve statistically time-independent averaged velocity and turbulence parameters (see Appendix A).

The ADV raw data were pre-filtered discarding the values with signal to noise ratio and correlation lower than 15 dB and 70%, respectively, and despiked with the Velocity Signal Analyser software (v1.5.64) (Jesson et al., 2015). The modified phase-space thresholding method (Parsheh et al., 2010) with $C_1=C_2=1.48$ (Parsheh et al., 2010; Wahl, 2003) and the standard deviation as characteristic scalar was adopted. Based on the analyses of the effects of the software available spike replacement methods on the velocity statistics and spectral analysis, the last good value method was selected, as also recommended by Jesson et al. (2013) (Appendix A). The overall average percentage of good data was greater than 95%.

4.1.4 Characterization of the dynamic plant motions

Organized plant motions caused by the downstream advection of large-scale coherent structures was observed and video recorded for the foliated vegetation test runs. Specifically, the lateral position of the outermost plant element was tracked (using the software Tracker 5.0 – Video Analysis and Modeling Tool) from 25 s video recordings at 25 Hz. Five different plants spanning over the entire 1 m long measurement section were monitored in order to define a temporal and spatial average position of the main channel-vegetation interface y_0 and to explore the dynamic plant motions in response to the flow.
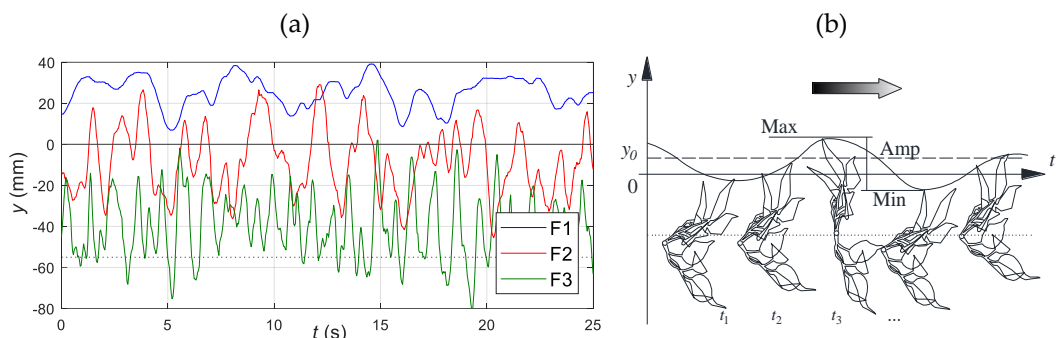

Figure 37 – Time series of the lateral displacement of the outermost element of a selected plant. The position of the edge of the grassy bed and the interfacial plant row are denoted with a solid and a dotted line, respectively (a). Scheme for the detection of lateral position of the outermost plant element (b).

In Figure 37 (a), the lateral position of the outermost element of a selected plant is shown for the 3 foliated test cases. The amplitude of the lateral displacement of vegetation was defined and estimated referring to previous study on *monami* effect in submerged canopies (Ghisalberti and Nepf, 2002) as indicated, together with the schematic picture of the generic plant motion, in Figure 37 (b). The waving amplitude and the mean lateral position of the interface y_0 taken from the video recordings are reported in Table 8. The foliated tests recordings allowed estimating the lateral vegetation motion frequency f_V. Specifically, the values reported in Table 10 are spatially averaged between the five observed plants within the measurement section, which the f_V variability is referred to. For the F2 and F3 cases the values are referred to 4 and 3 plants respectively.

Table 8 – Amplitude of plants waving motion and y_0 coordinate of mean position of main channel-vegetation interface. The reported values are temporally and spatially averaged considering 5 plants spanning along the measurement section (>1 m). Values are ±5 mm.

Run	Amplitude (mm)	Interface lateral position, y_0 (mm)
F1	46	16
F2	70	-8
F3	78	-38

For the leafless vegetation scenarios, where the erected plant stems exhibited a quasi-rigid behavior, the interface position was assumed to coincide with the grassy bed roughness edge, at y=0 mm. The y=0 mm location was adopted as a reference position for the analysis of interfacial coherent structures and the general turbulence pattern of the flow in both the vegetative conditions.

4.1.5 Theoretical framework for flow structure investigation

Mixing layer characteristic parameters and coherent structure scaling

In channel-vegetated-bank systems, the different drag conditions between the lateral vegetated area and the main channel lead to the formation of two nearly parallel streams of different ambient velocity, namely U_1 within the vegetation and U_2 in the main channel, with $U_1<U_2$. The consequent typical streamwise mean velocity lateral distribution $U(y)$ is characterized by a strong inflectional nature that gives rise to KH type instability (Ash and Khorrami, 1995). In the following, the investigated vegetated shear layers in partly vegetated channel are described referring to characteristic lengths and velocity defined leaning on the theory of canonical plane MLs (see section 2.1). Specifically, the flow was described with reference to the following characteristic velocities and lengths (defined in Section 2.2): (1) the convection velocity U_C=$(U_1+U_2)/2$; (2) the velocity difference or differential velocity ΔU=U_2-U_1; (3) the normalized differential velocity or velocity

ratio $\lambda=(U_2-U_1)/(U_1+U_2)=\Delta U/2U_C$; (4) the mixing layer width δ; (5) the momentum thickness θ (Eq. 2.1).

For the current conditions, the momentum thickness was evaluated integrating the velocity profile between the lateral positions where U attained the ambient value U_1 and U_2. In the main channel the velocity approached an approximately constant value U_2 for all the tests. The ambient velocity within the vegetation U_1 was evaluated by laterally averaging the velocity within the vegetated area of the channel, considering that for leafless (L) and highly reconfigured vegetation (F3) the velocity did not approach a constant value owing to the local effects of the stems.

In canonical MLs, the large-scale coherent structures due to the presence of an inflection point into the velocity profile are shed with a characteristic frequency corresponding to a Strouhal number $St=f_{ML}\theta/U_C=0.032$ (Ho and Huerre, 1984). These structures play a key role in the lateral transport of momentum and mass.

In contrast to plane MLs, vegetated shear layers attain stabilization at a certain distance from the origin of the layer. This is due to the equilibrium between the production of shear layer-scale TKE and its dissipation within the canopy (Ghisalberti and Nepf, 2004; Sukhodolova and Sukhodolov, 2012). Moreover, the stabilization of the mixing layer growth is also controlled by the vertical and lateral confinement of the flow produced by the channel walls and the free surface together with the bed friction (Chu and Babarutsi, 1988; Uijttewaal and Booij, 2000).

The validity of $St=f_{ML}\theta/U_C=0.032$ for vegetated flows and the suitability of the mixing layer analogy for the description of vegetated shear layer has been studied for rigid and blade-shaped submerged vegetation (Ghisalberti and Nepf, 2006; Jahadi et al., 2019; Poggi et al., 2004; Sukhodolov and Sukhodolova, 2012) and in partly vegetated channels with an array of rigid cylinders (White and Nepf, 2008).

Considering the shear layer around a finite-size patch of submerged filamentous flexible blades of *Sagittaria sagittifolia*, Sukhodolov and Sukhodolova (2012) proposed a scaling for the frequency of the coherent structures that explicitly takes into account the vegetation characteristics:

$$f_S \approx \frac{U_C}{\delta}\left(\frac{2U_C}{c_f\Delta U}\right)^{-\frac{1}{3}},\tag{4.2}$$

where c_f represents a bulk friction factor evaluated using the turbulent shear stress at the centreline of the mixing layer and the convective velocity: $\tau_c=0.5\rho c_f U_C{}^2$. The mixing layer width in Equation 4.2 is evaluated as $2\Delta U/(dU/dy)_{max}$. Equation 4.2 was derived assuming the validity of the Taylor's frozen turbulence hypothesis with the

assumption of local equilibrium between dissipation and mean turbulence production.

Selected turbulent statistics and spectral analysis

The general description of the turbulent structure of the flow presented in the next Sections is based on the analysis of the lateral distribution of temporally and spatially averaged velocity statistics. Specifically, each point value of the generic analyzed parameter is the result of the average between the two investigated transects as to address the variability of flow characteristics due to the heterogeneity of the vegetation. The following velocity statistics, as defined in Section 2.2.1, were analyzed: (1) mean longitudinal velocity; (2) lateral-longitudinal fluctuating velocities covariance (Reynolds stress); (3) root mean square (turbulence intensities); (4) skewness in the three directions; (5) lateral-longitudinal velocity correlation coefficient (efficiency of lateral transport of momentum).

Spectral analysis was employed to detect coherent turbulent structures, using the Welch method for the estimation of the power spectral density. In order to quantify the coherence of the large-scale interfacial turbulent structures, the autocorrelation function of the lateral velocity fluctuations R_{ii} (Equation 2.13), and the integral Eulerian time scale T_i (Equation 2.14) for the x and y velocity fluctuations, were computed at the interfacial position $y=0$.

Anisotropy analysis

The anisotropy of turbulence was investigated using the anisotropy invariant maps (Lumley, 1978; Lumley and Newman, 1977). In this study, the anisotropy of turbulence across the main channel-vegetation interface was described using the turbulence triangles (Choi and Lumley, 2001), introduced in Section 2.6.1.

4.2   Results and discussion

4.2.1   General description of the flow

Lateral profiles of transect-averaged mean longitudinal velocity are shown in Figure 38, for the foliated (F) and leafless (L) test runs. Both conditions exhibited a characteristic shear layer profile with an inflection point at the interface, where the horizontal Reynolds stress reached the maximum (Figure 39). The local deceleration (Figure 38) and the change in the sign of the Reynolds stress close to the locations of the leafless stems (Figure 39) indicated that the leafless vegetation had a marked local effect on the flow. The leafy vegetation, on the other hand, introduced a global effect on the flow, affecting the profile all over the vegetated area, with an increasing importance as the drag-density parameter increases.

For the foliated runs, the maximum shear was located in the vegetated area of the flow. Only for the high flow rate case (F3), in which strong reconfiguration was observed, the maximum was located on the left-hand side of the mean lateral position of the vegetation interface.

The position of the inflection point, owing to the increasing importance of the grassy bed roughness in comparison with the plant stands form drag, was shifted toward the main channel for the leafless conditions.
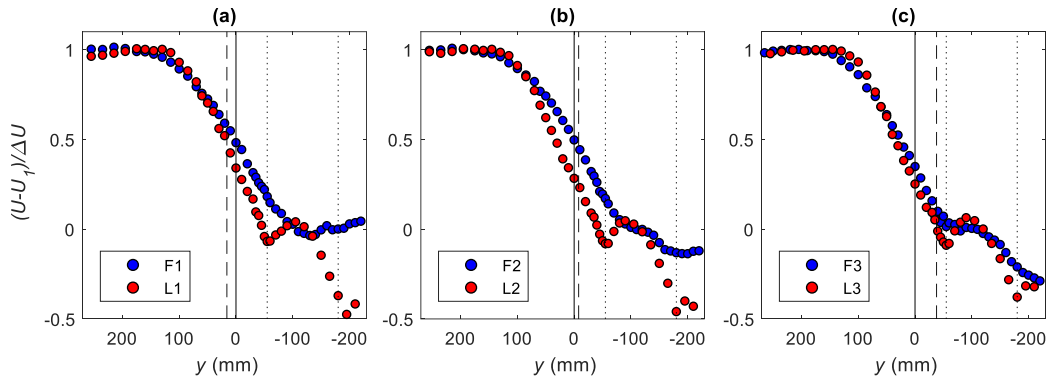
Figure 38 – Lateral distribution of transect averaged streamwise mean velocity for foliated and leafless conditions with (a) low, (b) medium and (c) high flow rate. Emergent plants were in a staggered pattern with the stems positioned along the dotted lines. Solid line indicates the edge of the grassy bed (y=0) and dashed line the foliated vegetation interface (y_0).

Figure 39 – Lateral profiles of transect averaged lateral Reynolds stress for foliated and leafless conditions with (a) low, (b) medium and (c) high flow rate. Vertical bars indicate the between-transect variability. Emergent plants were in a staggered pattern with the stems positioned along the dotted lines. Solid line indicates the edge of the grassy bed (y=0) and dashed line the foliated vegetation interface (y_0).
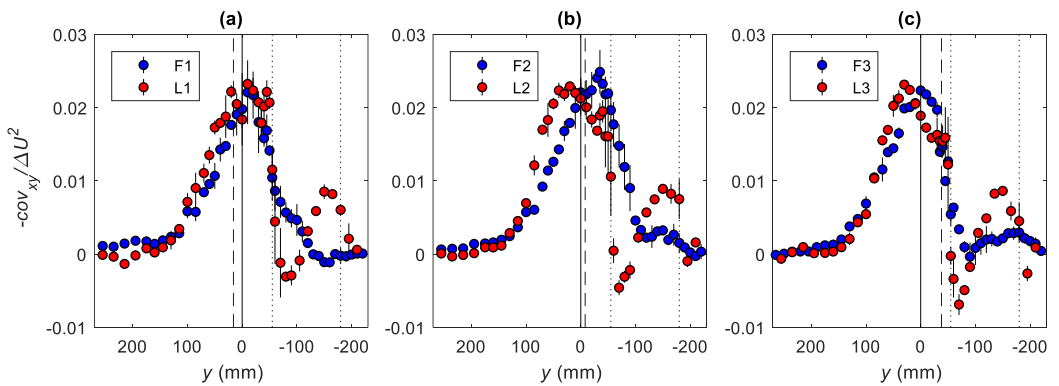
A preliminary picture of the pattern of the turbulent flow structure is provided by the lateral distribution of u_{rms} and v_{rms}, respectively the turbulence intensities of the longitudinal and lateral velocity fluctuations, normalized with the differential velocity ΔU (Figure 40). All the turbulence intensity profiles presented a peak in the interfacial region. A clear peak, located on the vegetated side of the moving flow-vegetation interface, was observed in the profiles of u_{rms} and v_{rms} for the foliated vegetation cases. The turbulence intensity was observed to decrease asymmetrically toward the main channel and, with stronger gradients, within the vegetation. These observations are consistent with the turbulence intensity pattern observed for submerged vegetation (Ghisalberti and Nepf, 2006; Nepf and Vivoni, 2000; Nezu and Sanjou, 2008), showing the analogy between the mixing layer in flow over dense submerged canopies and in channels partly covered by emergent vegetation.
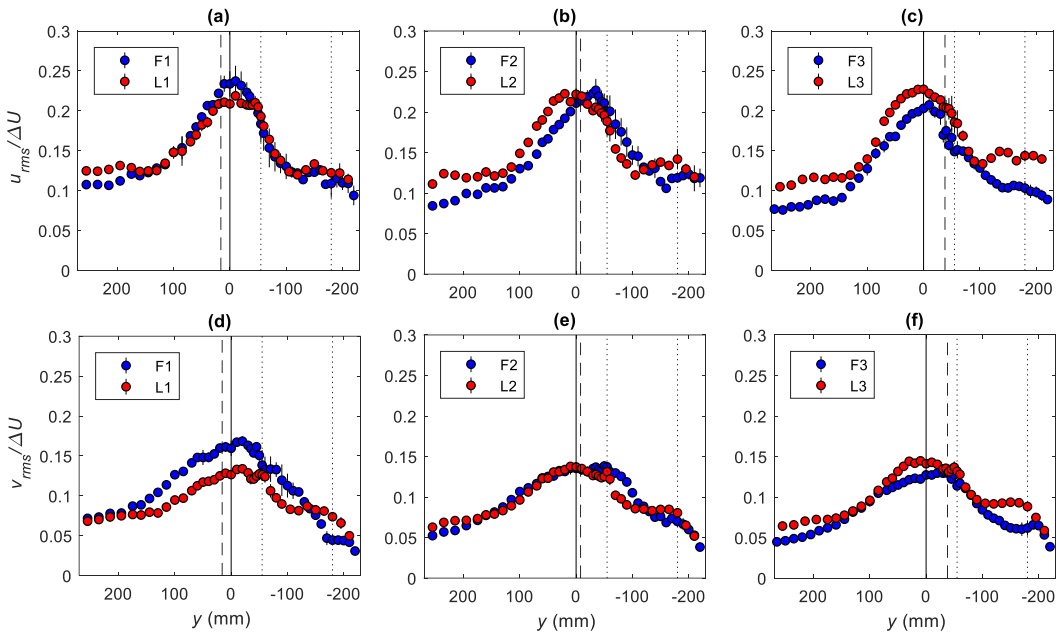
Figure 40 – Lateral distribution of longitudinal (a, b, c) and lateral (d, e, f) turbulence intensities for foliated and leafless conditions with (a, d) low, (b, e) medium and (c, f) high flow rate. Vertical bars indicate the between-transect variability. Emergent plants were in a staggered pattern with the stems positioned along the dotted lines. Solid line indicates the edge of the grassy bed (y=0) and dashed line the foliated vegetation interface (y_0).

For the leafless cases, the peak in the turbulent intensity, for the longitudinal and lateral velocity, was approximately located at y=0, the lateral position corresponding to the grasses edge. A local peak in turbulence intensity was observed at the stems lateral position y=-55 mm.

The lateral distributions of skewness of the longitudinal (Sk_u) and lateral (Sk_v) velocity fluctuations were almost symmetric about the x axis for the foliated vegetation and this characteristic resulted to be increasingly less pronounced with the flow rate and vegetation reconfiguration (Figure 41, a, b, c).
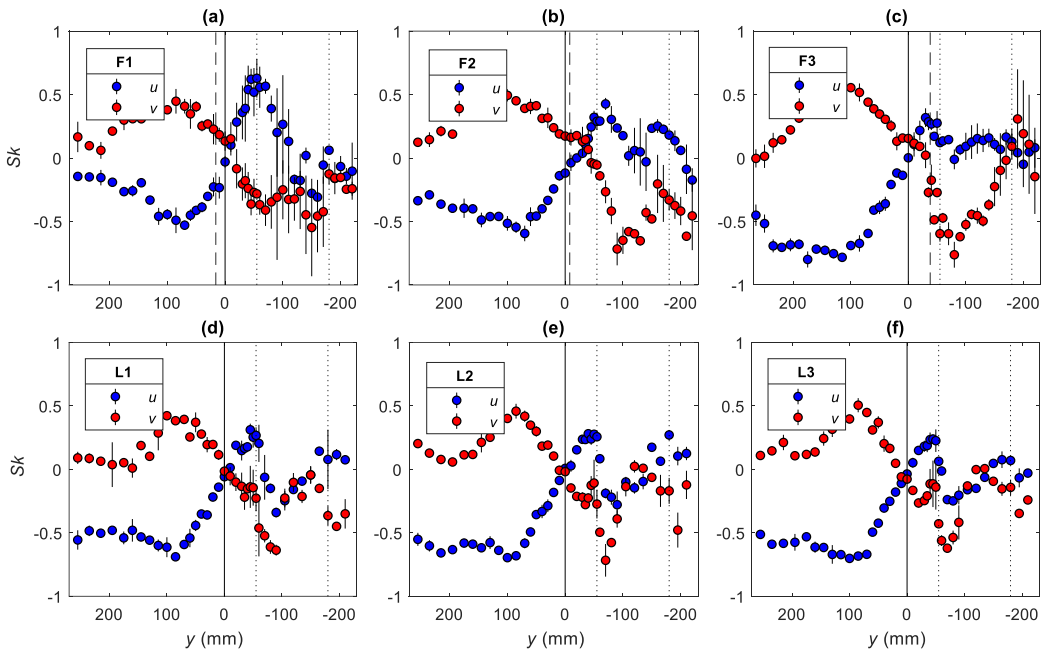

Figure 41 – Lateral distributions of skewness of longitudinal Sk_u and lateral Sk_v velocity fluctuations for foliated (a, b, c) and leafless (d, e, f) conditions with (a, d) low, (b, e) medium and (c, f) high flow rate. Vertical bars indicate the between-transect variability. Emergent plants were in a staggered pattern with the stems positioned along the dotted lines. Solid line indicates the edge of the grassy bed (y=0) and dashed line the foliated vegetation interface (y_0).

Two different regions were clearly distinguishable: a sweep dominated region (where Sk_u>0 and Sk_v<0) on the vegetated side of the interface, and, complementarily, an ejection dominated region on the other side (where Sk_u<0 and Sk_v>0). The lateral position where the skewness factor changed sign, coinciding for Sk_u and Sk_v, was variable between the 3 foliated test cases and only for the high flow rate case, where vegetation exhibited strong reconfiguration, the point was located on the left-hand side of y_0. Stronger Sk_u values within the vegetated area were observed for the F1 case and resulted to be progressively decreasing with the $C_D a$. This observation is consistent with the results of Nezu and Sanjou (2008) and

Poggi et al. (2004) for different density of submerged rigid vegetation, where the skewness was observed to be higher for the higher density cases, highlighting the key role played by reconfiguration for real vegetation.

In the leafless case, for which only a little stem reconfiguration was observed (as shown by the almost constant $C_D a$ value in Table 7), no notable differences were visible in the lateral distribution of skewness between the three different cases L1, L2 and L3. Also for the leafless case it is possible to identify the sweep and ejection dominated regions, but, differently from the leafy vegetation case, the lateral position where the skewness sign changed coincided always with the edge of the grassy bed, suggesting a dominant role of the lateral bed roughness discontinuity in the shear layer dynamics.

As observed from the lateral distributions of Figures 38-41, since the foliated vegetation progressively reconfigured with the increasing U_1 velocity, the lateral distributions of velocity statistics tended to resemble those of leafless vegetation. Because of the decreasing $C_D a$ value, the vegetation stopped affecting globally the flow across the channel acting as a whole, and the local effect of each plant stand became increasingly important.

This similitude between the strongly reconfigured foliated plants (F3) and leafless stems (L) was reflected also in the role of the bed roughness on the velocity statistics distributions. As the vegetation reconfigured, the role of the bed roughness became increasingly important, as shown by the relative position of y_0 (the lateral position of the foliated vegetation) with respect to y=0 (the grasses edge).

For the leafless cases and for the highly reconfigured vegetation case (F3), the shear layer resulted to be generated mainly by the bed roughness lateral variability. Indeed, lateral heterogeneity of bed roughness can actually generate strong shear layer, as described by Vermaas et al. (2011).

A high variability of flow statistics was observed across the foliated vegetated area of the channel (Figures 38-41). This between-transect variability was more pronounced for the low flow rate case (F1) and progressively decreased with the flow rate, affecting a progressively smaller area of the cross-section. This can be reasonably explained by the reconfiguration of foliated vegetation and the drag-density parameter: for higher $C_D a$ the flow had to adapt to the blockage conditions locally faced by the current; conversely, with streamlined plants, the flow is channelized in the gaps defined by the reconfigured morphology of the vegetation. In the leafless vegetation scenario only the local variability due to the presence of the stems was observed.

4.2.2 Coherent structures at the interface

This Section mainly focuses on the large coherent structures occurring in the interface region, generated by the drag discontinuity between the vegetated area and the adjacent main channel. Specifically, the results discussed herein were derived from the upstream transect (where not diversely specified), since no significant local between-transect variability was observed in the coherent structures characteristics.

The foliated cases showed coherent, quasi-periodic fluctuations of the longitudinal and lateral velocity (Figure 42, F1), manifestation of the passage of large coherent structures. The u' and v' velocity fluctuations were in opposite phase and contributed preponderantly to the overall Reynolds stress with strong sweep ($u'>0$, $v'<0$) and ejection events ($u'>0$, $v'<0$).
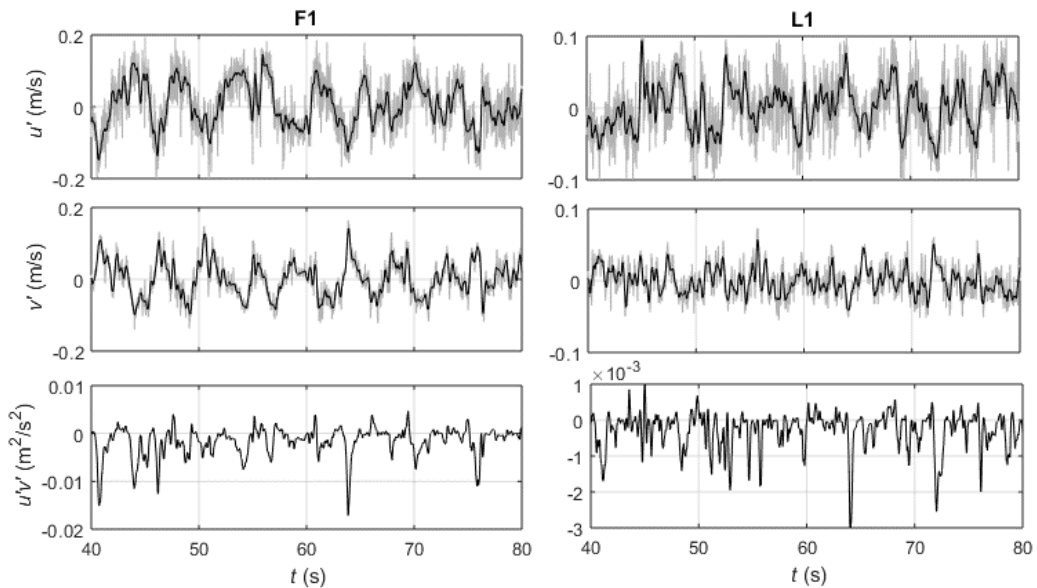
Figure 42 – Comparison between the longitudinal and lateral velocity fluctuations, and the instantaneous Reynolds stress measured at the interface position y=0 for the foliated case F1 and the leafless case.L1 From the 40 s window shown it is possible to notice the strong sweep and ejection events that dominate the interfacial region, visible in the u′v′ time series for the F1 case. The solid black line is the low pass filtered signal and the grey line is the actual velocity fluctuation time series.

This periodic signature of the velocity fluctuations was not observed for the leafless case. The shear layer characteristics between the leafless and foliated cases were deeply different because of the completely dissimilar behavior of the foliated vegetation and its blockage effect compared with the leafless stems. Indeed, the foliation and its reconfiguration affected the differential velocity (Table 9) with a direct effect on the mixing layer structures and the lateral momentum transport. The autocorrelation functions (Figure 43) and the integral time scales (Table 9),

respectively evaluated with Equations 2.13 and 2.14, revealed that the turbulent structures of the foliated test cases were coherent over a much longer duration (Figure 43, a) than those of the leafless cases (Figure 43, b). This difference is related to the magnitude of the drag-density parameter that directly affects the differential velocity ratio and the coherence of KH structures.
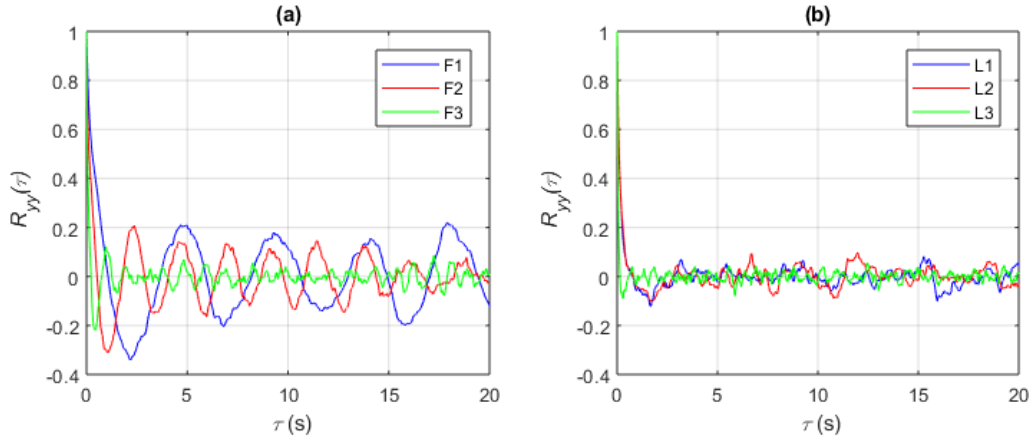

Figure 43 – Autocorrelation functions at the interface for the foliated (a) and leafless (b) test cases.

Table 9 – Eulerian integral time scales at the interface and characteristic Reynolds numbers.

Run	T_u (s)	T_v (s)	$C_D a$ (m^{-1})	λ	Re_θ	Re_h	Re_θ/Re_h
Foliated plant stands and grasses							
F1	0.677	0.624	12.154	0.795	12952	61880	0.209
F2	0.303	0.307	1.432	0.569	21184	133790	0.158
F3	0.129	0.109	0.485	0.411	24857	216580	0.115
Leafless plant stands and grasses							
L1	0.333	0.211	0.425	0.255	2731	51510	0.053
L2	0.139	0.095	0.205	0.250	6620	114240	0.058
L3	0.097	0.051	0.181	0.258	11529	191760	0.060

For both the vegetation scenarios, as the Reynolds number in the main channel ($Re_h = U_2 h/\nu$) increased, compared with the mixing layer one ($Re_\theta = \Delta U \theta/\nu$) (Table 9), a progressive loss of coherence was observed, as a consequence of the growth of three-dimensional instabilities and the increasing number of small scale structures.

For foliated vegetation, the progressive loss of coherence of the interfacial coherent structures with increasing flow rate (and the corresponding λ and $C_D a$ reduction) can be considered ascribable also to the dynamic lateral motion of the vegetation interface. For foliated vegetation, the lateral plant motion (described in Section 4.1.4) induced instantaneously variable interface drag conditions that can strain the vortex structure and induce a loss of coherence. This circumstance, firstly addressed

by Ghisalberti and Nepf (2006) considering the flow over rigid and flexible submerged vegetation, is evident looking at the progressively increasing amplitude of the plants lateral motion and the instantaneous position of the outermost plant elements (Figure 37 and Table 8).

The quantity $v_{rms}/\Delta U$ (Figure 40), interpretable as the relative speed of vortex rotation (Ghisalberti and Nepf, 2006), can provide an indirect measurement of the coherence of the interfacial large-scale structures. Among the F cases, a higher $v_{rms}/\Delta U$ at the interface was observed (0.17) for the F1 case, where the amplitude of lateral plant motion was less pronounced (46 mm) and the plant motion was observed to be more organized. For the F2 and F3 cases, for which the amplitudes reached 70 and 78 mm respectively, lower values of $v_{rms}/\Delta U$ were observed (≈0.12). Maximum values of the turbulence intensity found for rigid and flexible submerged vegetation were 0.15 and 0.11, respectively (Ghisalberti and Nepf, 2006). This suggests that the lateral motion caused by the presence of foliation and its complex distribution along the plant stands strongly affect the interface large-scale structure coherence with implications on the lateral transport of momentum.

Velocity spectra

Velocity spectra were analyzed for the detection and characterization of the large mixing layer coherent structures (where present), in order to compare the measured frequency of vortex shedding f with the predictions of the two scalings of Equations 2.2 and 4.2, together with the observed frequency of plant motions f_V. Spectra of the lateral velocity component at the interface $y=0$ are reported in Figure 44.

Figure 44 – Lateral velocity power spectra for foliated and leafless conditions with (a) low, (b) medium and (c) high flow rate. To make the spectra comparable the abscissae were normalized in terms of Strouhal numbers as $f\theta/U_c$. The natural frequency of a canonical mixing ($f\theta/U_c=0.032$) is shown by a dashed line. The -3 slope corresponding to 2D structures is also illustrated.

In all the foliated test cases, the presence of large coherent structures was visible as a clear peak in the power spectral density located in the energy containing range of

frequencies. At the high frequency side of the peaks a slope of approximately -3 was observed, indicating that the coherent structures were largely two-dimensional (Proust et al., 2017; Uijttewaal and Booij, 2000). The concentration of energy at the frequency of the 2D vortices was observed all along the cross-section with a progressively decreasing energy content moving away from the interfacial region (not shown).

Moreover, a peak was observed at the same frequency in the $u'v'$ cross spectra (Figure 45), proving that the detected coherent structures were responsible for the lateral momentum transport across the vegetation-main channel interface. In the leafless test cases, even though an increased energy content at the Strouhal numbers corresponding to the mixing layer structures frequencies was registered, the relative magnitude of the energy associated to this mode was notably lower.
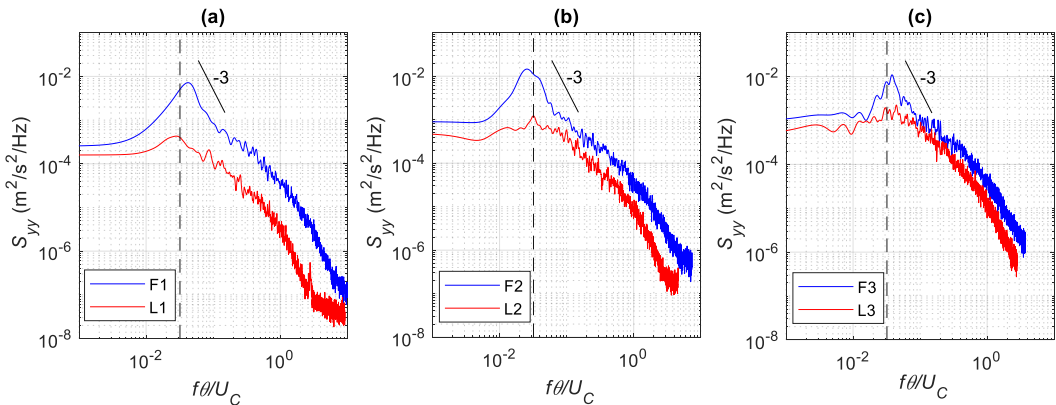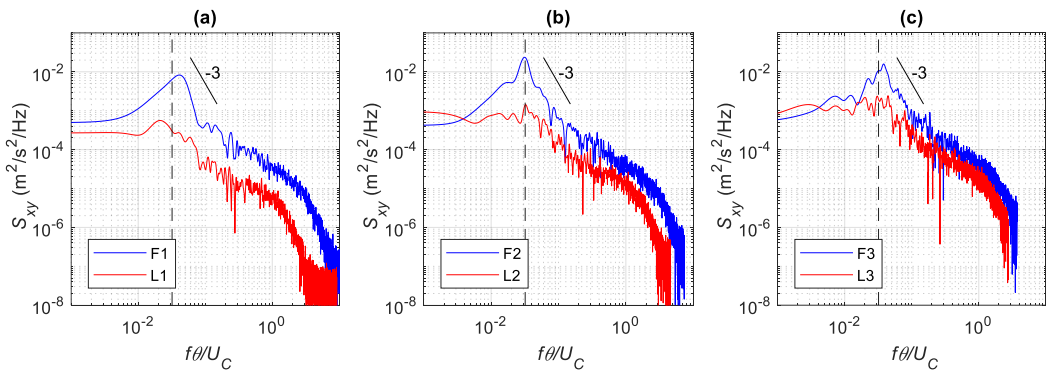

Figure 45 – Lateral-longitudinal velocity power cross-spectra for foliated and leafless conditions with (a) low, (b) medium and (c) high flow rate. To make the spectra comparable the abscissae were normalized in terms of Strouhal numbers as $f\theta/U_c$. The natural frequency of a canonical mixing ($f\theta/U_c$=0.032) is shown by a dashed line. The -3 slope corresponding to 2D structures is also illustrated.

The presence of KH vortices was observed only for the foliated vegetation, all characterized by differential velocity ratio λ>0.3. According to Proust et al. (Proust et al., 2017) and Dupuis et al. (2016), based on studies on mixing layer in compound channels, λ>0.3 represents the condition for the onset of KH coherent structures.

Furthermore, correspondingly to the progressive increase of the bulk flow velocity (from F1 to F3, Table 7), the progressive reconfiguration of vegetation produced a progressively decreasing differential velocity ratio, which resulted in a loss of coherence of the interfacial structures. This observation suggests the key role played by foliage and, considering flexible vegetation, by the reconfiguration. As the vegetation progressively reconfigures, the favorable conditions for the onset of KH structures can disappear with direct implications on the efficiency of the lateral mixing.

The blockage provided by the leafless vegetation was not sufficient to establish favorable conditions for the onset of KH vortices. Moreover, the differential velocity ratio did not depend on the flow condition. For such non-reconfiguring plants, the density of the stems clearly plays the most important role on the shear layer characteristics (White and Nepf, 2007), as further investigated in Chapter 5.

In Table 10, the frequency of the large coherent 2D structures detected from the lateral velocity spectra is reported together with the predictions of the scalings of Equations 2.2 and 4.2, and the frequency of the lateral plant motions (as deduced from the video recordings). The frequency deduced from the spectra were spatially averaged over the main channel mixing layer width (between y=0 and 270 mm) and between the two investigated transects, congruently to the estimation of the scaling based on the temporal and spatial mean quantities of Table 7.

Table 10 – Frequency of coherent structures and comparison with predicted values of Equations 2.2 and 4.2, and dominant frequency of lateral motions of plants. The variability of f is referred to the variability of the between-transect average along the lateral direction.

Run	f (Hz)	σ_f (Hz)	f_{ML} (Hz)	c_f (-)	$|dU/dy|_{max}$ (m/s/m)	δ (mm)	f_S (Hz)	f_V (Hz)	σ_{fV} (Hz)
F1	0.195	0.018	0.162	0.091	2.56	252	0.336	0.161	0.005
F2	0.379	0.032	0.432	0.057	4.00	286	0.558	0.330	0.058
F3	0.860	0.091	0.863	0.027	5.18	287	0.699	0.770	0.338

The peak frequency of the lateral velocity spectra f, the predicted KH frequency f_{ML}, and the observed frequency of vegetation lateral movement f_V were in good agreement (within the 17% of f), while the f_S values presented higher difference with respect to f (up to 72%). Owing to the high turbulence intensities, the assumptions on which Equation 4.2 is derived were not strictly satisfied for our case. In addition, Equation 4.2 is referred to the vertical shear layer generated by submerged blade-like vegetation, in contrast to the horizontal shear layer of the present study generated by complex morphology emergent vegetation.

The variability of frequency of plant motion increased with the flow rate (Table 10). As observed during the tests, when the frequency of the vortex shedding was higher, the plant stands were not able to adapt quickly to the rapidly changing flow conditions, resulting in a less organized motion. Moreover, owing to the variability of plant stands morphology along the elevation, asynchronous motion was observed for the parts of the same plant stand.

4.2.3 Turbulence anisotropy in the interfacial region

The anisotropy of turbulence across the interface is here investigated in order to define the mechanism responsible for the momentum transport between the

vegetated area and the main channel. It is related to the detected large interfacial coherent structures.

The invariant maps reported in Figure 46 provide an overall description of the anisotropic pattern along the interface between the main channel and the vegetated area. Specifically, only the points between y=130 (main channel) and -80 mm (within the vegetated area) were considered. This range was defined with reference to the lateral distribution of $v_{rms}/\Delta U$ (Figure 40), as to investigate the area of the cross-section with higher lateral interactions.
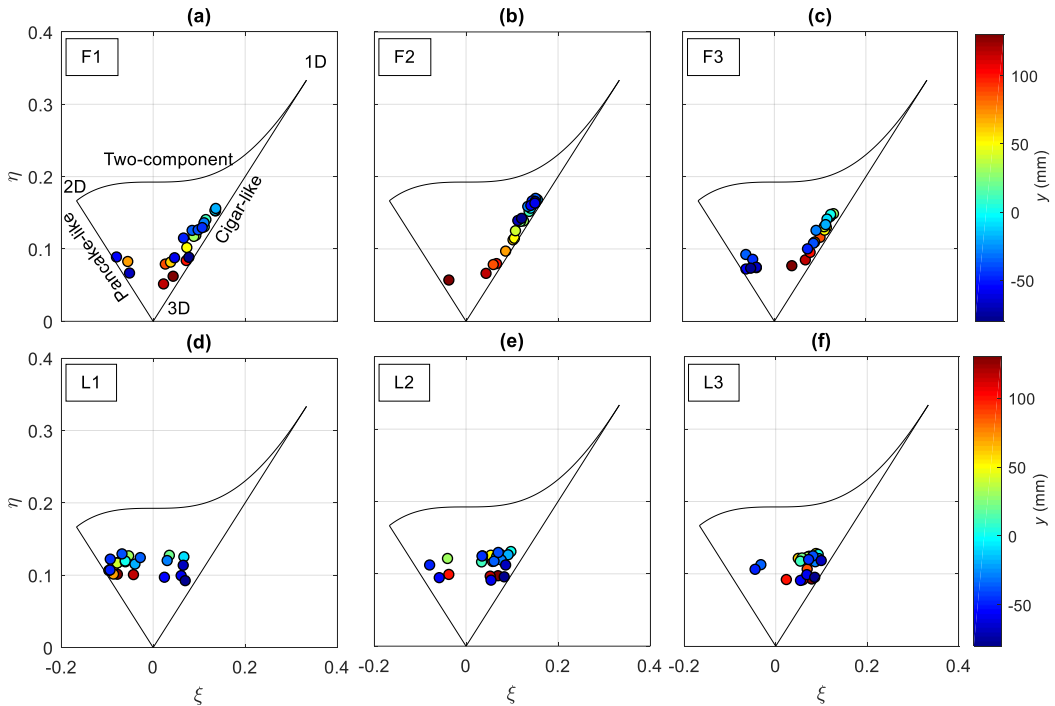

Figure 46 – Anisotropy pattern across the interface for foliated (a, b, c) and leafless (d, e, f) vegetation conditions with (a, d) low, (b, e) medium and (c, f) high flow rate.

The points of the invariant maps for the foliated cases (F1, F2 and F3) defined a clear and qualitatively similar pattern for all the flow rate (and qualitatively independent from the transect). Moving from the main channel (y=120 mm), where the turbulence presented a general tendency to isotropy, toward the interface (y=0 mm), a progressively increasing trend in the degree of anisotropy was observed. Approaching the interface, the turbulence acquired a gradually increasing one-component characteristic due to the dominant effect of the longitudinal fluctuations as a consequence of the passage of the coherent structures. This gradual axisymmetric contraction process reached a maximum in terms of degree of anisotropy and mono-dimensionality at the positions y=10, -30 and -10 mm for F1, F2 and F3, respectively.

Moving further within the foliated vegetation (up to y=-80 mm), an opposite trend was observed: an axisymmetric expansion process brought the state of the turbulence to a quasi-isotropic behavior. The deepest points into the vegetated area (y<-80; not shown) were characterized by a high spatial heterogeneity in terms of type of anisotropy.
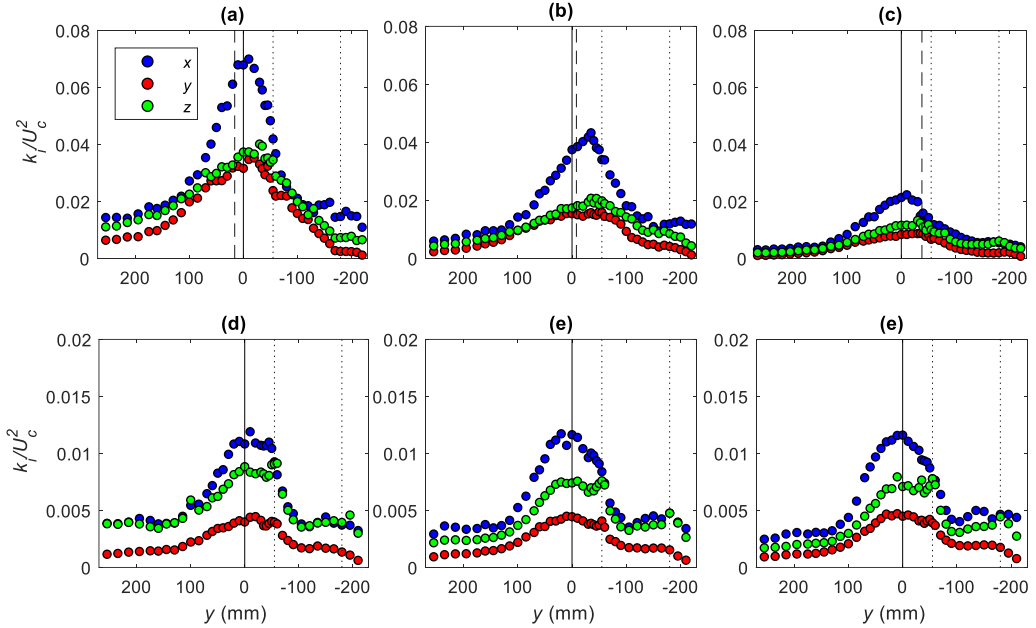

Figure 47 – Lateral distributions of TKE components for foliated (a, b, c) and leafless (d, e, f) conditions with (a, d) low, (b, e) medium and (c, f) high flow rate. Emergent plants were in a staggered pattern with the stems positioned along the dotted lines. Solid line indicates the edge of the grassy bed (y=0) and dashed line the foliated vegetation interface (y_0).

For the leafless vegetation, a largely different anisotropy pattern was observed, highlighting the profound difference between the two vegetation scenarios in terms of turbulent flow structure. Going from L1 to L3, the patterns exhibited a highly flow rate dependent characteristic. For the L1 case, a trend toward the pancake-like turbulence was observed in the main channel while, approaching the interface, a trend to cigar-like turbulence prevailed. With the increase of the flow rate, a majority of cigar-like shaped turbulence was observed, with the predominant effect of the longitudinal component of TKE (Figure 47). In the leafless scenario the degree of anisotropy was limited and independent from the flow rate. In this condition, as a consequence of the increasing importance of the vertical BL effects, the vertical fluctuations of velocity assumed a relatively greater importance.

4.2.4 Momentum transport across the interface

The global picture of the flow emerging from the previous analyses can be discussed with reference to the lateral distributions of $-r_{uv}$, the longitudinal and lateral velocity correlation coefficient, shown in Figure 48. This parameter quantifies the efficiency of the turbulent lateral transport of streamwise momentum and can provide information about location, size and strength of the detected interfacial vortices.
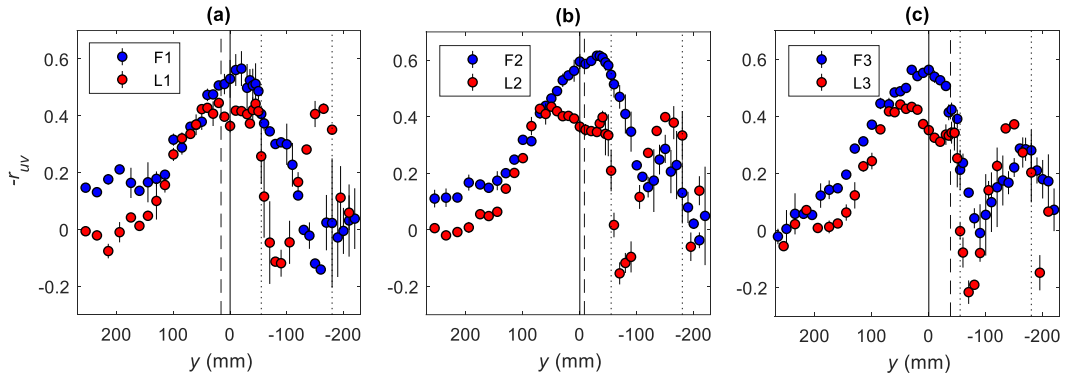

Figure 48 – Lateral distribution of correlation coefficient for foliated and leafless conditions with (a) low, (b) medium and (c) high flow rate. Vertical bars indicate the between-transect variability. Emergent plants were in a staggered pattern with the stems positioned along the dotted lines. Solid line indicates the edge of the grassy bed (y=0) and dashed line the foliated vegetation interface (y_0).

Foliated vegetation cases presented a peak in the interfacial region where $-r_{uv}$ attained a maximum value approximately equal to 0.6. For the leafless vegetation scenarios, the correlation coefficient attained a maximum value approximately equal to 0.44 at the main-channel side of the interface, remaining stably high across the interface with additional peaks observed at the lateral positions of the stems. This difference highlights the effects of foliation on the flow: in the F cases, large, highly coherent turbulent structures were detected at the interface and, correspondingly, the efficiency of the lateral transport of streamwise momentum was observed to be notably higher while the leafless vegetation induced strong local mixing, that was of the same order as the shear layer-scale mixing.

Looking at the position of the maximum value with respect to the mean position of the vegetation interface (y_0), a different penetration of the coherent structures was observed depending on the reconfiguration. Specifically, the region of high lateral mixing efficiency was located on the vegetated side of the interface for the F1 and F2 cases.

In BL flows and canonical MLs, typical values of the correlation between longitudinal and lateral velocities are approximately 0.32 and 0.44 respectively (Ghisalberti and Nepf, 2002). For terrestrial canopies (Raupach et al., 1996) and

aquatic flexible stripe-like submerged canopy (Ghisalberti and Nepf, 2002) values of 0.5 were observed. The $-r_{uv}$ values observed in the current work suggest a specific property of the lateral mixing layer in partly vegetated channels with complex morphology plants, characterized by a stronger mixing in comparison with analogous flows with less complex vegetation morphology.

4.3   Conclusions

The experimental arrangement was novel in that the combination of the plant properties (emergent reconfiguring plants with grassy bed roughness) and the vegetation densities (volumetric leaf area a_L=4 m^{-1}, volumetric stem area a_S=0.13 m^{-1}) closely presented conditions found along natural river margins. In the partly vegetated channel, different foliation and flow forcing conditions for the same natural-like plant stands profoundly affected the interface flow characteristics, as summarized in Figure 49.
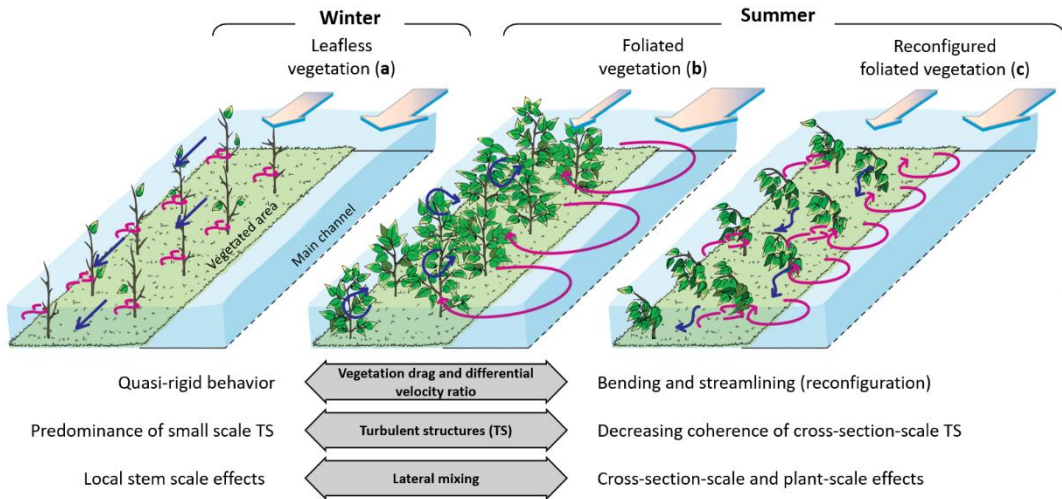

Figure 49 – Conceptualization of differences in flow and mixing at the vegetation-main channel interface. Grey arrows show the main effects of foliation (case a vs. b) and reconfiguration (case c vs. b). The thick arrows indicate the share of the flow in the vegetated and unvegetated parts of the cross-section, the blue arrows show the flow paths within vegetation, and the magenta arrows describe the dominant turbulent structures. Reconfiguration and lateral motions of vegetation have implications on the coherence of turbulent structures and lateral mixing by affecting the differential velocity ratio and the drag discontinuity at the interface. Presence of foliation (winter vs. summer) alters the flow dynamics at the interface, directly affecting the drag-density parameter ($C_D a$) and the differential velocity ratio (λ). In winter, with leafless vegetation, bed roughness heterogeneity plays a key role in the shear layer dynamics, and the flow is governed by small-scale turbulent structures. In summer, the higher differential velocity ratio and vegetation drag-density trigger the onset of large coherent turbulent structures that enhance the mixing at the cross-section-scale.

The presence of leaves markedly influenced the flow distribution, resulting in higher velocity difference (λ) between the open and vegetated parts of the cross-section. In the leafless stage representing the winter condition (a), vegetation

exhibited a quasi-rigid behavior, analogous to rigid cylinders. In this condition, the cross-section-scale lateral shear layer was mainly generated by the bed roughness heterogeneity between the vegetated area and the open water, and was coupled with the local-scale mixing induced by the stems. For the foliated vegetation (b and c in Figure 49), the flow was dominated by large coherent interfacial structures, which governed and enhanced the lateral interaction between the vegetated and unvegetated areas of the channel. In addition, foliation generated higher three-dimensionality and isotropy of turbulence with major seasonal differences in flow paths within vegetation (blue arrows in Figure 49).

The results highlighted that foliated vegetation reconfigured by adapting its morphology to the increased hydrodynamic forcing (increasing the flow rate from b to c in Figure 49), reinforcing that complex shrub-like vegetation undergoes drag reduction caused by both the seasonal shedding of leaves and the reconfiguration. This marked drag reduction (the drag-density parameter $C_D a$ varied in the ranges 0.5-12 and 0.18-0.4 for foliated and leafless vegetation, respectively) was associated with less strong and coherent interfacial shear layer-scale flow structures, resulting in notably lower lateral transport of longitudinal momentum (Figure 48) for leafless (a) compared to the foliated cases (b and c). The dominant frequency of the large coherent structures matched the lateral dynamic motions of the plants. These frequencies were consistent with the canonical mixing layer scaling (with the applicability of the classical Strouhal number $St \approx 0.032$), indicating that they can be reliably predicted from the basic flow characteristics for dynamically moving natural-like shrubs and bushes (Eq. 3). Overall, the presence of leaves directly induced and enhanced mixing mechanisms at the cross-section-scale, in contrast with the local scale effects induced by the leafless plants.

References

Ackerman, J.D., Okubo, A., 1993. Reduced Mixing in a Marine Macrophyte Canopy. Funct. Ecol. 7, 305–309. doi:10.2307/2390209

Ash, R.L., Khorrami, M.R., 1995. Fluid Vortices, Fluid Vor. doi:10.1007/978-94-011-0249-0

Ben Meftah, M., De Serio, F., Mossa, M., 2014. Hydrodynamic behavior in the outer shear layer of partly obstructed open channels. Phys. Fluids 26. doi:10.1063/1.4881425

Bomminayuni, S., Stoesser, T., 2011. Turbulence Statistics in an Open-Channel Flow over a Rough Bed. J. Hydraul. Eng. 137, 1347–1358. doi:10.1061/(ASCE)HY.1943-7900.0000454

Choi, K.-S., Lumley, J.L., 2001. The return to isotropy of homogeneous turbulence. J. Fluid Mech. 436, 161. doi:10.1017/S002211200100386X

Choi, S.U., Kang, H., 2006. Numerical investigations of mean flow and turbulence structures of partly-vegetated open-channel flows using the Reynolds stress model. J. Hydraul. Res. 44, 203–217. doi:10.1080/00221686.2006.9521676

Chu, V.H., Babarutsi, S., 1988. Confinement and bed-friction effects in shallow turbulent mixing layers. J. Hydraul. Eng. 114, 1257–1274.

Coscarella, F., Servidio, S., Ferraro, D., Carbone, V., Gaudio, R., 2017. Turbulent energy dissipation rate in a tilting flume with a highly rough bed. Phys. Fluids 29. doi:10.1063/1.4996773

Cotton, J.A., Wharton, G., Bass, J.A.B., Heppell, C.M., Wotton, R.S., 2006. The effects of seasonal changes to in-stream vegetation cover on patterns of flow and accumulation of sediment. Geomorphology 77, 320–334. doi:10.1016/j.geomorph.2006.01.010

Defina, A., Bixio, A.C., 2005. Mean flow and turbulence in vegetated open channel flow. Water Resour. Res. 41, 1–12. doi:10.1029/2004WR003475

Dupuis, V., Proust, S., Berni, C., Paquier, A., 2017. Mixing layer development in compound channel flows with submerged and emergent rigid vegetation over the floodplains. Exp. Fluids 58, 0. doi:10.1007/s00348-017-2319-9

Dupuis, V., Proust, S., Berni, C., Paquier, A., 2016. Combined effects of bed friction and emergent cylinder drag in open channel flow. Environ. Fluid Mech. 16, 1173–1193. doi:10.1007/s10652-016-9471-2

Ferraro, D., Servidio, S., Carbone, V., Dey, S., Gaudio, R., 2016. Turbulence laws in natural bed flows. J. Fluid Mech. 798, 540–571. doi:10.1017/jfm.2016.334

Gacia, E., Duarte, C.M., 2001. Sediment retention by a Mediterranean Posidonia oceanica meadow: The balance between deposition and resuspension. Estuar. Coast. Shelf Sci. 52, 505–514. doi:10.1006/ecss.2000.0753

Ghisalberti, M., Nepf, H.M., 2006. The structure of the shear layer in flows over rigid and flexible canopies. Environ. Fluid Mech. 6, 277–301. doi:10.1007/s10652-006-0002-4

Ghisalberti, M., Nepf, H.M., 2004. The limited growth of vegetated shear layers. Water Resour. Res. 40, 1–12. doi:10.1029/2003WR002776

Ghisalberti, M., Nepf, H.M., 2002. Mixing layers and coherent structures in vegetated aquatic flows. J. Geophys. Res. 107, 1–11. doi:10.1029/2001JC000871

Ho, C., Huerre, P., 1984. Perturbed free shear layers. Annu. Rev. Fluid Mech. 16, 365–422. doi:10.1146/annurev.fl.16.010184.002053

Hu, C., Ji, Z., Guo, Q., 2010. Flow movement and sediment transport in compound channels. J. Hydraul. Res. 48, 23–32. doi:10.1080/00221680903568600

Hu, Z., Lei, J., Liu, C., Nepf, H.M., 2018. Wake structure and sediment deposition behind models of submerged vegetation with and without flexible leaves. Adv. Water Resour. 118, 28–38. doi:10.1016/j.advwatres.2018.06.001

Jahadi, M., Afzalimehr, H., Rowiński, P.M., 2019. Flow structure within a vegetation patch in a gravel-bed river. J. Hydrol. Hydromechanics.

Järvelä, J., 2002. Flow resistance of flexible and stiff vegetation: A flume study with natural plants. J.

Hydrol. 269, 44–54. doi:10.1016/S0022-1694(02)00193-2

Jesson, M.A., Bridgeman, J., Sterling, M., 2015. Novel software developments for the automated post-processing of high volumes of velocity time-series. Adv. Eng. Softw. 89, 36–42. doi:10.1016/j.advengsoft.2015.06.007

Jesson, M.A., Sterling, M., Bridgeman, J., 2013. Despiking velocity time-series-Optimisation through the combination of spike detection and replacementmethods. Flow Meas. Instrum. 30, 45–51. doi:10.1016/j.flowmeasinst.2013.01.007

Kubrak, E., Kubrak, J., Rowinski, P.M., 2008. Vertical velocity distributions through and above submerged, flexible vegetation. Hydrol. Sci. Journal-Journal Des Sci. Hydrol. 53, 905–920. doi:10.1623/hysj.53.4.905

Li, C.W., Yu, L.H., 2010. Hybrid LES/RANS modelling of free surface flow through vegetation. Comput. Fluids 39, 1722–1732. doi:10.1016/j.compfluid.2010.06.009

Liu, D., Diplas, P., Fairbanks, J.D., Hodges, C.C., 2008. An experimental study of flow through rigid vegetation. J. Geophys. Res. Earth Surf. 113, 1–16. doi:10.1029/2008JF001042

Liu, D., Valyrakis, M., Williams, R., 2017. Flow Hydrodynamics across Open Channel Flows with Riparian Zones : Implications for riverbank stability. Water 9, 1–19. doi:10.3390/w9090720

Lumley, J.L., 1978. Computational Modeling of Turbulent Flows. Adv. Appl. Mech. 18.

Lumley, J.L., Newman, G.R., 1977. The return to isotropy of homogeneous turbulence. J. Fluid Mech. 82, 161–178. doi:10.1017/S0022112077000585

Mera, I., Franca, M.J., Anta, J., Peña, E., 2015. Turbulence anisotropy in a compound meandering channel with different submergence conditions. Adv. Water Resour. 81, 142–151. doi:10.1016/j.advwatres.2014.10.012

Naot, D., Nezu, I., Nakagawa, H., 1996. Hydrodynamic Behavior of Partly Vegetated Open Channels. J. Hydraul. Eng. 122, 625–633. doi:10.1061/(ASCE)0733-9429(1996)122:11(625)

Nepf, H.M., 2012. Flow and Transport in Regions with Aquatic Vegetation. Annu. Rev. Fluid Mech. 44, 123–142. doi:10.1146/annurev-fluid-120710-101048

Nepf, H.M., Vivoni, E.R., 2000. Flow structure in depth-Iimited, vegetated flow. J. Geophys. Res. 105, 28547–28557.

Nezu, I., Sanjou, M., 2008. Turburence structure and coherent motion in vegetated canopy open-channel flows. J. Hydro-Environment Res. 2, 62–90. doi:10.1016/j.jher.2008.05.003

Niklas, K.J., 1997. Mechanical properties of black locust (Robinia pseudoacacia L) wood. Size and age-dependent variations in sap and heartwood. Ann. Bot. 79, 265–272. doi:DOI 10.1006/anbo.1996.0340

Nikora, V.I., McLean, S., Coleman, S., Pokrajac, D., McEwan, I., Campbell, L., Aberle, J., Clunie, D., Koll, K., 2007. Double-Averaging Concept for Rough-Bed Open-Channel and Overland Flows: Applications. J. Hydraul. Eng. 133, 884–895. doi:10.1061/(ASCE)0733-9429(2007)133:8(884)

Nikora, V.I., Rowiński, P.M., 2008. Rough-bed flows in geophysical, environmental, and engineering systems: Double-Averaging Approach and its applications. Acta Geophys. 56, 529–533. doi:10.2478/s11600-008-0037-7

Ortiz, A.C., Ashton, A., Nepf, H.M., 2013. Mean and turbulent velocity fields near rigid and flexible plants and the implications for deposition. J. Geophys. Res. Earth Surf. 118, 2585–2599. doi:10.1002/2013JF002858

Parsheh, M., Sotiropoulos, F., Porté-Agel, F., 2010. Estimation of Power Spectra of Acoustic-Doppler Velocimetry Data Contaminated with Intermittent Spikes. J. Hydraul. Eng. 136, 368–378. doi:10.1061/(ASCE)HY.1943-7900.0000202

Poggi, D., Porporato, A., Ridolfi, L., Albertson, J.D., Katul, G.G., 2004. The effect of vegetation density on canopy sub-layer turbulence. Boundary-Layer Meteorol. 111, 565–587. doi:10.1023/B:BOUN.0000016576.05621.73

Pope, S.B., 2000. Turbulent Flows. Cambridge University Press. doi:10.1017/CBO9780511840531

Proust, S., Fernandes, J.N., Leal, J.B., Rivière, N., Peltier, Y., 2017. Mixing layer and coherent structures in compound channel flows: Effects of transverse flow, velocity ratio, and vertical confinement. Water Resour. Res. 53, 3387–3406. doi:10.1002/2016WR019873

Raupach, M.R., Finnigan, J.J., Brunei, Y., 1996. Coherent eddies and turbulence in vegetation canopies: The mixing-layer analogy. Boundary-Layer Meteorol. 78, 351–382. doi:10.1007/BF00120941

Righetti, M., Armanini, A., 2002. Flow resistance in open channel flows with sparsely distributed bushes. J. Hydrol. 269, 55–64. doi:10.1016/S0022-1694(02)00194-4

Rowiński, P.M., Aberle, J., Järvelä, J., Kalinowska, M.B., Västilä, K., 2018. How vegetation can aid in coping with river management challenges: a brief review. Ecohydrol. Hydrobiol.

Rowiński, P.M., Kubrak, J., 2002. A mixing-length model for predicting vertical velocity distribution in flows through emergent vegetation. Hydrol. Sci. J. 47, 893–904. doi:10.1080/02626660209492998

Rubol, S., Ling, B., Battiato, I., 2018. Universal scaling-law for flow resistance over canopies with complex morphology. Sci. Rep. 8, 4430. doi:10.1038/s41598-018-22346-1

Sarkar, S., Dey, S., 2015. Turbulence Anisotropy in Flow at an Entrainment Threshold of Sediment. J. Hydraul. Eng. 141, 1–4. doi:10.1061/(ASCE)HY.1943-7900.0001026.

Shih, S.F., Rahi, G.S., 1982. Seasonal Variation of Manning's Roughness Coefficient in A Subtropical Marsh. Am. Soc. Agric. Eng. 25, 116–119. doi:10.13031/2013.33488

Shimizu, Y., Tsujimoto, T., 1994. Numerical analysis of turbulent open-channel flow over vegetation layer using a k-εturbulence model. J. Hydrosci. Hydraul. Eng. 2, 57–67.

Siniscalchi, F., Nikora, V.I., Aberle, J., 2012. Plant patch hydrodynamics in streams: Mean flow, turbulence, and drag forces. Water Resour. Res. 48, 1–14. doi:10.1029/2011WR011050

Sukhodolov, A.N., Sukhodolova, T.A., 2012. Vegetated mixing layer around a finite-size patch of submerged plants: Part 2. Turbulence statistics and structures. Water Resour. Res. 48, 1–16. doi:10.1029/2011WR011804

Sukhodolova, T.A., Sukhodolov, A.N., 2012. Vegetated mixing layer around a finite-size patch of submerged plants: Part 1. Theory and field experiments. Water Resour. Res. 48, 1–16. doi:10.1029/2011WR011804

Tsujimoto, T., Kitamura, I., 1992. Appearance of Organized Fluctuations in Open-channel Flow with Vegetated Zone. KHL Progress. Rep. '92 21–35.

Uijttewaal, W.S.J., Booij, R., 2000. Effects of shallowness on the development of free-surface mixing layers. Phys. Fluids 12, 392–402. doi:10.1063/1.870317

Västilä, K., Järvelä, J., 2017. Characterizing natural riparian vegetation for modeling of flow and suspended sediment transport. J. Soils Sediments 1–2. doi:10.1007/s11368-017-1848-4

Västilä, K., Järvelä, J., 2014. Modeling the flow resistance of woody vegetation using physically based properties of the foliage and stem. Water Resour. Res. 50, 229–245. doi:10.1002/2013WR013819

Västilä, K., Järvelä, J., Aberle, J., 2013. Characteristic reference areas for estimating flow resistance of natural foliated vegetation 492, 49–60. doi:10.1016/j.jhydrol.2013.04.015

Västilä, K., Järvelä, J., Koivusalo, H., 2016. Flow-Vegetation-Sediment Interaction in a Cohesive Compound Channel. J. Hydraul. Eng. 142, 1--1. doi:10.1061/(ASCE)HY.1943-7900.0001058.

Vermaas, D.A., Uijttewaal, W.S.J., Hoitink, A.J.F., 2011. Lateral transfer of streamwise momentum caused by a roughness transition across a shallow channel. Water Resour. Res. 47, 1–12. doi:10.1029/2010WR010138

Vogel, S., 1994. Life in Moving Fluids The Physical Biology of Flow, 2nd ed. Princeton University Press.

Wahl, T.L., 2003. Discussion of '"Despiking Acoustic Doppler Velocimeter Data"' by Derek G. Goring and Vladimir I. Nikora January. J. Eng. Mech. 128, 2002–2003. doi:10.1061/(ASCE)0733-9372(2003)129

Weissteiner, C., Jalonen, J., Järvelä, J., Rauch, H.P., 2015. Spatial-structural properties of woody riparian vegetation with a view to reconfiguration under hydrodynamic loading. Ecol. Eng. 85,

85–94. doi:10.1016/j.ecoleng.2015.09.053

White, B.L., Nepf, H.M., 2008. A vortex-based model of velocity and shear stress in a partially vegetated shallow channel. Water Resour. Res. 44, 1–15. doi:10.1029/2006WR005651

White, B.L., Nepf, H.M., 2007. Shear instability and coherent structures in shallow flow adjacent to a porous layer. J. Fluid Mech. 593, 1–32. doi:10.1017/S0022112007008415

Zinke, P., 2011. Modelling of Flow and Levee Depositions in a Freshwater Delta with Natural Vegetation 252.

5 Flow in partly vegetated channels with an array of rigid cylinders

As emerged from the previous analysis of partly vegetated channels, the presence of a vegetative obstruction alters the flow features, with implication on lateral transport of mass and momentum across the two areas of the channels. As resulted from the experiments with natural-like plant stands (Chapter 4) and in previous studies with rigid cylinders (Poggi et al., 2004; White and Nepf, 2008; Zong and Nepf, 2012), the presence of an inflection point in the velocity profiles gives rise to KH type instabilities that governs the hydrodynamic processes at the vegetated interface.

Considering the importance of the large-scale interfacial structures on the cross-section-scale processes, a second experimental campaign was designed and carried out as to explore the effects of vegetation density and shear-layer features on the onset on KH type instabilities in partly vegetated channels. About the condition for the onset of large-scale coherent structures in shear layers in compound channels, Proust et al. (2017) and Dupuis et al. (2017) found in $\lambda > 0.3$ the condition on the velocity ratio for the onset of KH type vortices. For partly vegetated channels the conditions for the onset of KH type instabilities are still unexplored.

Thus, an open channel partially filled with an array of rigid cylinders, simulating emergent rigid vegetation, was considered for investigating the effects of vegetation density and vegetated shear layer characteristics on the onset of KH vortices and the lateral transport of momentum. Specifically, in order to obtain vegetated shear layers with a wide range of different characteristics (including velocity ratio, velocity within the vegetated area and mixing layer Reynolds number), different cylinder packing densities and flow rates were tested.

The tests with rigid cylinders described in this Chapter were also designed and carried out in order to provide a set of experiments for benchmarking the tests performed with natural-like vegetation, as to compare the different vegetation models. This is expected to aid in the understanding of the effects of vegetation model in the study of flow in channel-vegetated-bank systems, as described in detail in Chapter 6.

In this Chapter the concepts introduced in Chapters 2 and 4 are extensively used.

5.1 Materials and methods

Experiments were carried out at the Laboratory of Hydraulics at the University of Naples Federico II in the experimental facility described in detail in Chapter 2. The x, y, and z flume coordinate system axes refer to the longitudinal, lateral, and vertical (normal to the flume bottom) directions, respectively (Figure 50). The coordinate system origin was defined as $x=0$ at the inlet cross-section, positive downstream; $y=0$ at the edge of the vegetated area and positive toward the main channel; and $z=0$ at the channel bottom and positive upwards. In the defined right-handed rectangular Cartesian coordinate system, velocity components were denoted as u, v and w, in the x (longitudinal), y (lateral) and z (vertical) direction.
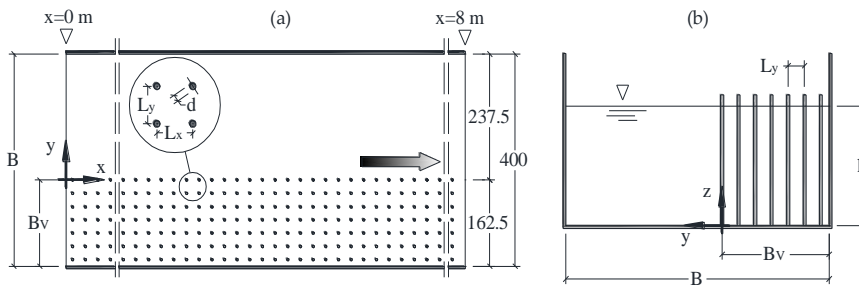

Figure 50 – Top (a) and frontal (b) view of the experimental flume. For all the tests, the vegetation was simulated by an array of aligned emergent cylinders with diameter d=4.5 mm covering the entire length of the flume. L_x and L_y are the spacing along the x and y directions, respectively. B is the channel width, B_v is the width of the vegetated area, which was kept constant for all the runs. The flume coordinate system is also specified. All units are in millimeters unless otherwise indicated.

The discharge was varied in the range 15-30 l/s. The channel slope was set to 1%. All the tests were carried out in uniform flow conditions, considering different flow rates as to achieve different velocity ratios. In the range of considered flow rates, the uniform flow reach was identified analyzing the backwater profiles, experimentally determined along the channel midline using a gauging needle (with accuracy of ±0.1 mm). The cross-section distribution of flow depth was measured at different locations observing a negligible variability. For all the test runs, uniform flow conditions, in a spatially averaged sense, were observed to be restored approximately at 3.5 m from the outlet section. Velocity measurements were taken approximately at 3.5 m from the channel inlet, within the uniform flow section of the flume.

5.1.1 Vegetation models and test cases

Approximately 40% of the flume width was covered by an array of emergent cylinders. The vegetation model properties are described by the cylinder diameter d, the solid volume fraction $\phi=(\pi/4)d^2 n$, where n is the number of cylinders per unit bottom area, the spacing between cylinders L_x and L_y in the x and y directions, respectively, and the frontal projected area per unit volume $a=nd$. Seven different

cylinder spatial distributions were considered, resulting in six different packing densities, indicated in the following as D1, D2, D3, D4, D5 and D6, from the densest to the sparsest. For the density D2, two different spatial distributions of cylinders were considered, indicated with D2x and D2y (Figure 56). The densities D1, D2x and D2y were tested under three different flow rates (≈15, 20 and 30 l/s). The combination of density and flow rate resulted in 13 test runs, as specified in Table 11.

Table 11 – Test cases and relevant mixing layer quantities. Q is the flow rate, h the water depth, U_m the cross-sectional mean velocity, U_1 the low speed stream velocity (in the vegetated area), U_2 the high speed stream velocity (in the main channel), U_c the convection velocity ((U_1+U_2)/2), ΔU the differential velocity, δ the mixing layer width, θ the momentum thickness, λ the differential velocity ratio, $C_D a$ the drag-density parameter, Re_θ and Re_h the momentum thickness and flow depth based Reynolds number, respectively. The slope of the flume was set to 1%.

Run	I	II	III	IV	V	VI	VII	VIII	IX	X	XI	XII	XIII
Density	D1	D1	D1	D2x	D2x	D2x	D2y	D2y	D2y	D3	D4	D5	D6
L_x (mm)	25	25	25	50	50	50	25	25	25	50	100	200	400
L_y (mm)	25	25	25	25	25	25	50	50	50	50	50	50	50
ϕ (-)	0.0254	0.0254	0.0254	0.0127	0.0127	0.0127	0.0127	0.0127	0.0127	0.0064	0.0032	0.0016	0.0008
a (m^{-1})	7.20	7.20	7.20	3.60	3.60	3.60	3.60	3.60	3.60	1.80	0.90	0.45	0.23
Q (l/s)	15.2	19.5	29.4	17.3	21.7	31.8	17.3	21.7	31.7	31.7	31.7	31.7	31.7
h (mm)	84	102	135	85	106	136	88	106	135	133	122	111	88
U_m (m/s)	0.452	0.478	0.544	0.509	0.512	0.585	0.491	0.512	0.587	0.596	0.650	0.714	0.901
U_1 (m/s)	0.095	0.101	0.119	0.142	0.153	0.169	0.195	0.210	0.238	0.311	0.397	0.517	0.6551
U_2 (m/s)	0.842	0.912	1.007	0.870	0.904	0.996	0.819	0.849	0.975	0.934	0.921	0.940	0.988
U_C (m/s)	0.468	0.507	0.563	0.506	0.528	0.583	0.507	0.529	0.607	0.622	0.659	0.728	0.822
ΔU (m/s)	0.747	0.811	0.888	0.728	0.751	0.828	0.624	0.639	0.737	0.623	0.524	0.423	0.333
δ (mm)	102	99	111	95	104	112	94	88	104	106	104	82	82
θ (mm)	21.0	21.4	24.2	21.3	22.6	24.4	19.3	18.8	22.0	23.1	22.0	15.7	12.2
λ (-)	0.80	0.80	0.79	0.72	0.71	0.71	0.61	0.60	0.61	0.50	0.40	0.29	0.20
$C_D a$ (m^{-1})	21.88	19.20	13.85	9.68	8.43	6.89	5.14	4.45	3.46	2.03	1.24	0.73	0.46
Re_θ (-)	15673	17340	21468	15506	16965	20167	11359	12012	16189	11347	11519	6655	4072
Re_θ/Re_h (-)	0.22	0.19	0.16	0.21	0.18	0.15	0.16	0.13	0.12	0.09	0.10	0.06	0.05

The position of the main channel-vegetation interface was kept constant for all the runs. The different combinations of density and flow rate provided a wide range of different vegetated shear layers. The water depth to width ratio (h/B) of the flow ranged between 0.2 and 0.3. The drag-density parameter, consistently with the PN test series, was evaluated using Equation 4.1.

5.1.2   Determination of flow structure

The flow in the partly vegetated channel was investigated by measuring instantaneous three dimensional velocity components with ADV. The fully developed flow was investigated by acquiring a transversal mid-depth ($h/2$) transect. The $z=h/2$ position was selected as a representative measurement location for the depth-averaged velocity, as done in previous analogous investigations (Ben

Meftah et al., 2014; White and Nepf, 2008). The mid-depth measurements were within 5% of the depth-averaged velocity, confirmed by vertical velocity profiles taken at five different lateral positions (as specified in Section 0) for the III and VI test cases (with the highest aspect ratio). Therefore, the flow was reasonably considerable as one dimensional (along y). The investigated transects were located at a distance equal to L_x/2 downstream of the closest row of cylinders. Considering the interest in the characterization of large-scale coherent structures and the cross-section-scale variability of velocity, the stem-scale spatial variability of flow was not investigated in the current experiments.

On the basis of lateral profiles of longitudinal mean velocity recorded at different x positions, the cross-section at $x{\approx}3.5$ m was selected as an appropriate measurement location as the flow was fully developed. The flume and the cylinder array were wide enough to ensure that the shear layer for all cases was unaffected by the channel side walls.

Two rows of cylinders for the D1 and D2y cases and one row for the D2x and D3 cases, equivalent respectively to $2L_x$ and L_x, were removed to allow the ADV probe access within the array. As shown in previous investigation with rigid cylinders and flexible vegetation (Ghisalberti and Nepf, 2004; Ikeda and Kanazawa, 1996), the removal of canopy elements over a length $<3L_x$ has negligible impact upon the measured velocity statistics. Owing to the configuration of the ADV probe, the uppermost ${\approx}40$ mm of the flow could not be sampled.

Three-dimensional instantaneous velocity components were measured at 100 Hz with an ADV Nortek Vectrino II with a 4-beam down looking probe, with accuracy of ±1%. The sampling volume, 40 mm far from the probe tip, was 4 mm long with a 6 mm diameter (${\approx}113$ mm^3). The lowest velocity range of the instrument was appropriately selected depending on the flow characteristics (mean velocity and turbulence intensity). A recording time of 240 s (24000 samples) was found to be sufficiently large to achieve statistically time-independent averaged velocity and turbulence parameters (see Appendix A).

The ADV raw data were pre-filtered discarding the values with signal to noise ratio and correlation lower than 30 dB and 70%, respectively, and despiked with the Velocity Signal Analyser software (v1.5.64) (Jesson et al., 2015). The modified phase-space thresholding method (Parsheh et al., 2010) with $C_1{=}C_2{=}1.48$ (Parsheh et al., 2010; Wahl, 2003) and the standard deviation as characteristic scalar were adopted. Based on the analyses of the effects of the software available spike replacement methods on the velocity statistics and spectral analysis (Appendix A), the last good value method was selected, as recommended by Jesson et al. (2013).

5.2   Results and discussion

5.2.1   General description of the flow

The lateral distribution of mean longitudinal velocity for test cases III, VI, IX-XIII (all presenting flow rate approximately equal to 30 l/s) are shown in Figure 51. Following White and Nepf (2008), the mean velocity within the vegetation was spatially averaged over the vegetation lateral spacing L_y, in order to remove stem-scale heterogeneity.
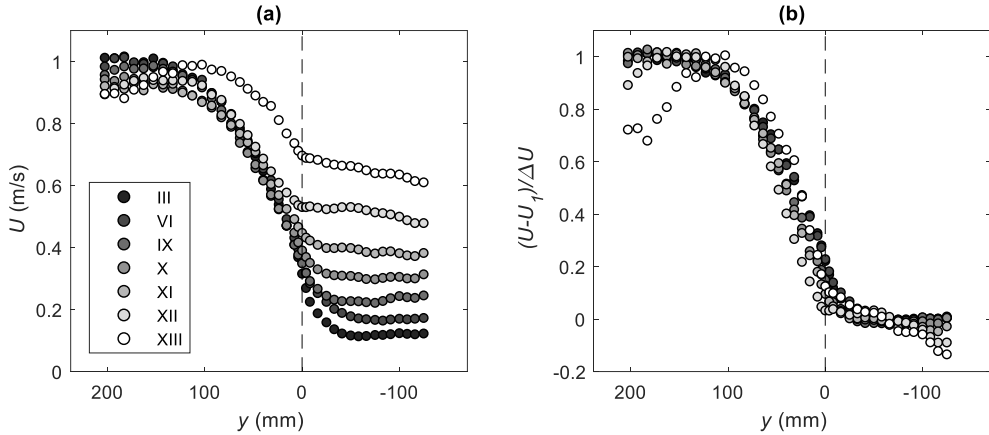

Figure 51 – Lateral distribution of dimensional (a) and normalized (b) longitudinal mean velocity for test cases III, VI, IX-XIII (from the densest to the sparsest). Dashed line indicates the edge of the cylinder array.

For each test case the velocity reached a constant value within the vegetation and in the open main channel, presenting a characteristic shear layer profile in between. With decreasing packing density, a progressively decreasing differential velocity was observed (Table 11), resulting in velocity ratios λ ranging from 0.80 down to 0.20.
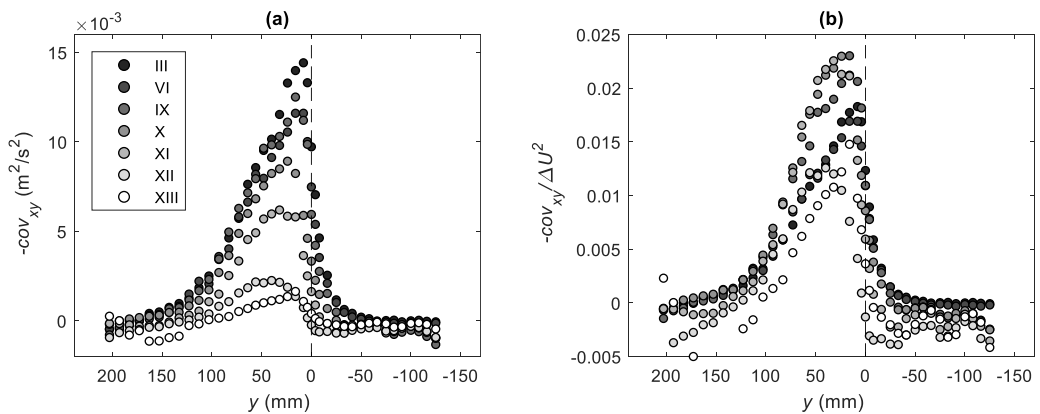

Figure 52 – Lateral distribution of dimensional (a) and normalized (b) Reynolds stress in the lateral-longitudinal direction (expressed in terms of covariance) for test cases III, VI, IX-XIII (from the densest to the sparsest). Dashed line indicates the edge of the cylinder array.

With decreasing density the penetration of the shear within the vegetation was observed to progressively decrease, as shown in Figure 51 (a). The lateral position where $U= 1.1U_1$ was progressively shifted toward the vegetation edge (for the XII case on the main channel side of the interface).

In Figure 52 the lateral distributions of lateral-longitudinal Reynolds stresses is shown. The lateral position of the maximum Reynolds stress resulted to be shifted toward the main channel with decreasing density. Moreover, the penetration of the Reynolds stresses was observed to decrease with the density. In vegetated shear layers, with decreasing density, a progressively larger penetration of coherent structures is generally observed (Nezu and Sanjou, 2008; Poggi et al., 2004; White and Nepf, 2008). Owing to the lesser momentum absorption from the canopy, the Reynolds stresses can penetrate deeper. This was experimentally verified for partly vegetated channels by White and Nepf (2008), who considered vegetated shear layers all characterized by velocity ratios λ greater than ≈0.8.

In the current experiments, the slope of the flume and the flow rate were kept constant while decreasing the vegetation density. As a consequence, the observed shear layers were characterized by progressively decreasing velocity ratios, resulting in progressively weaker interfacial coherent structures and, in turn, smaller shear penetration within the canopy, as discussed in the next.

The flow field at the interface was characterized by sweep and ejection events governing the mass and momentum exchanges across the interface, as shown in Figure 53 in which test cases III, X and XIII (with λ equal to 0.8, 0.5 and 0.2, respectively) are considered.
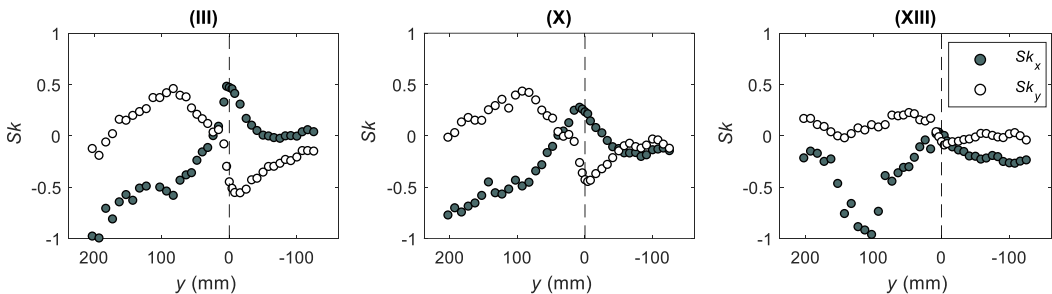

Figure 53 – Lateral distribution of skewness of the longitudinal and lateral velocity fluctuating velocities for test cases III, X and XII, with λ equal to 0.8, 0.5 and 0.2 respectively. Dashed line indicates the edge of the cylinder array.

With decreasing density (and, correspondingly, velocity ratio), the skewness of the longitudinal and lateral fluctuating velocity progressively decreased, indicating a weaker interaction across the interface between the two areas of the flume.

The effects of the density is also evident when looking at the lateral distributions of turbulence intensities (Figure 54). With decreasing density the turbulence of the shear layer, described using the root mean square of the lateral fluctuating velocity v_{rms}, progressively decreased.
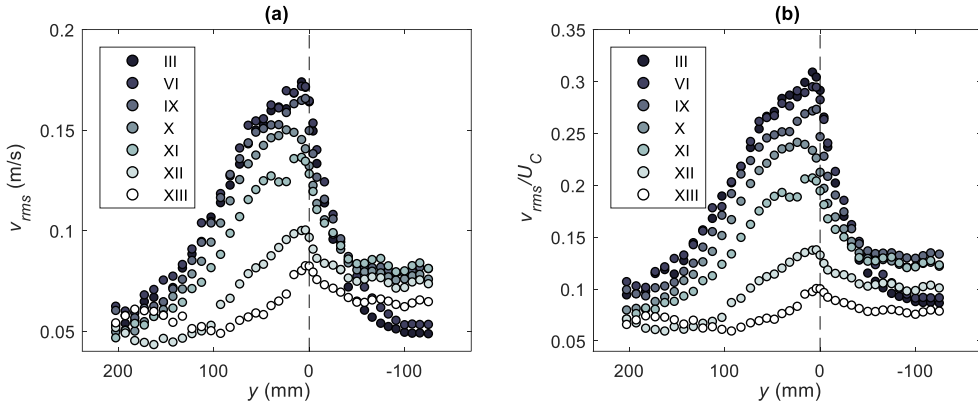

Figure 54 – Lateral distribution of dimensional (a) and normalized (b) turbulence intensities of the lateral fluctuating velocity for test cases III, VI, IX-XIII (from the densest to the sparsest). Dashed line indicates the edge of the cylinder array.

The v_{rms} peaked directly on the main channel side of the interface and, for the highest density cases (III and VI), rapidly decreased within the vegetation. The dense array of cylinders sheltered the inner vegetated area from the turbulence induced by the shear layer. Moreover, the turbulence intensity within the vegetation was observed to be lower than that of the shear layer generated turbulence. With decreasing density (and increasing lateral spacing between cylinders), the level of the turbulence intensity within the vegetation was of the same order as that of the shear layer generated turbulence.

The D1, D2x and D2y configurations were tested under three different flow rates: 15, 20 and 30 l/s. An approximately constant velocity ratio λ was observed for each density (Table 11) in the range of investigated flow rates, suggesting that the stem density is a key parameter governing the velocity ratio of vegetated shear layer induced by rigid vegetation. In Figure 55 (a), the relation between the velocity ratio λ and the drag-density parameter $C_D a$ is shown for all the test runs. For a given spatial distribution (density and spatial distribution of cylinders), the velocity ratio of the vegetated shear layer was observed to be constant, decreasing with the density. The drag-density parameter takes into account the velocity within the

vegetation and, therefore, the frontal area per canopy volume can be more effective in describing the relation between λ and the array geometry (Figure 55, b).
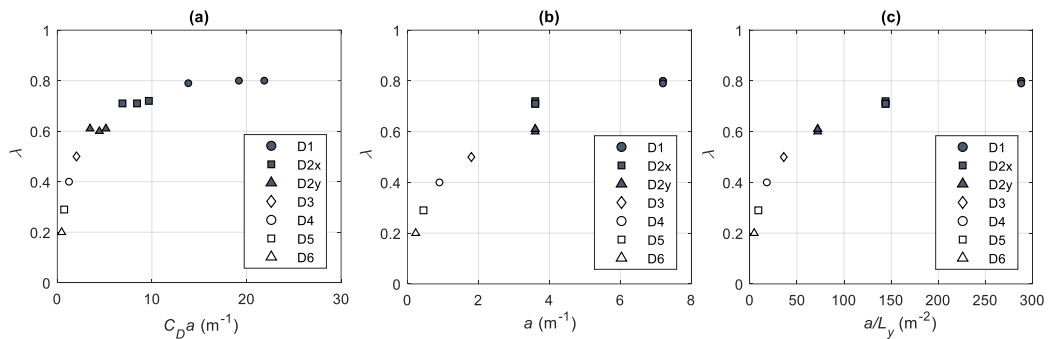

Figure 55 – Relation between velocity ratio λ and drag-density parameter $C_D a$ (a), frontal area per canopy volume a (b), and a/L_y (c).

Even though the cylinder spatial distribution in the D2x and D2y cases led to equivalent a values, two different velocity ratios were observed. This difference can be still considered ascribable to a different geometric feature of the rigid vegetation pattern. Indeed, D2x and D2y refer to two different spatial distributions of cylinders, differing for orientation of the spacing with respect to the flow, as schematized in the following Figure 56.
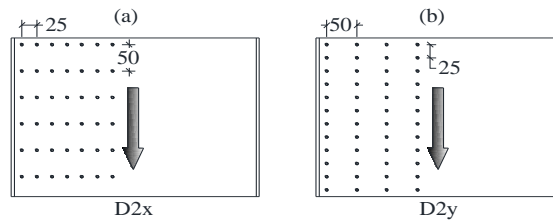

Figure 56 – Specification of cylinder array geometry for the D2x (a) and D2y (b) cases.

In order to take into account the difference in the spatial distribution, as a first approximation, the frontal area per canopy volume was divided by the lateral spacing L_y, considering that the lateral spacing sets the number of cylinders faced by the flow. The velocity ratio plotted against a/L_y is illustrated in Figure 55 (c), showing the dependence of λ on purely geometric features of the vegetation. Thus, differently from shear layers induced by flexible reconfiguring vegetation (Chapter 4), the velocity ratio was observed to depend mainly on the geometric characteristics of the array of cylinders, with very low influence of the flow rate.

5.2.2   Spectral analysis

The lateral interaction across the interface, as observed from the penetration of shear within the canopy (Figure 52) and from the turbulence intensities (Figure 54), resulted to be highly dependent on the velocity ratio, set by the density and spatial distribution of cylinders within the array. Previous studies of vegetated shear layers above submerged vegetation have shown how the vegetation density governs the shape of the velocity profile (Aberle and Järvelä, 2015; White and Nepf, 2008). The presence of large-scale structures (also known as canopy-scale structures) can be directly related to the shape of the velocity profile and, specifically, it is due to the presence of an inflection point in the velocity profile (Finnigan, 2000; White and Nepf, 2007). Thus, the qualitative prediction of the velocity profile shape and, in turn, the presence of large-scale coherent structures, is typically performed referring to the density of the canopy, generally expressed in terms of drag-density parameter or equivalent parameters (Aberle and Järvelä, 2015; Nepf, 2012). In the present study a more general condition based on the velocity ratio is sought.

Therefore, in order to investigate the condition for the onset of large-scale structures (and the related processes regarding the lateral transport of momentum across the interface and its variability with the velocity ratio, and vegetation density), the distribution of the lateral-longitudinal fluctuating velocities correlation coefficient was evaluated (Figure 57, a). Considering that in BLs r_{uv} reaches a maximum of approximately -0.32 and in pure mixing layers -0.44, this parameter can provide information about size, location, and strength characteristics of the generated vortices (Ghisalberti and Nepf, 2002).
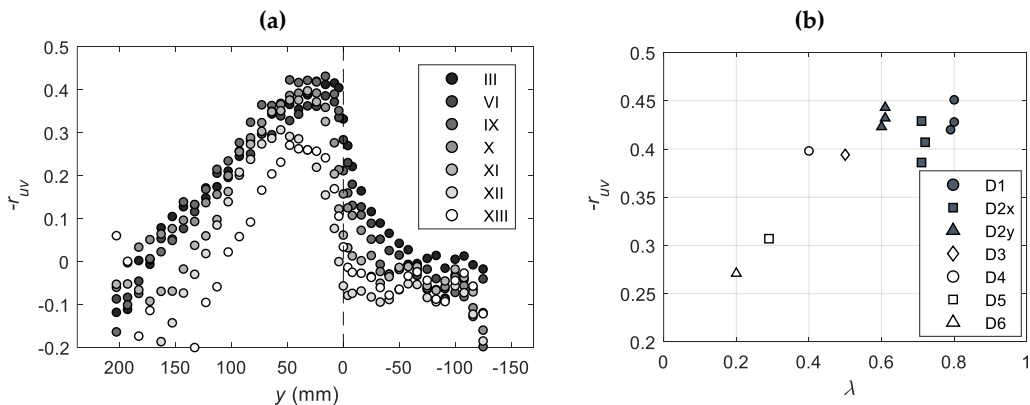

Figure 57 – Lateral distribution of correlation coefficient for test cases III, VI, IX-XIII (from the densest to the sparsest). Dashed line indicates the edge of the cylinder array (a). Maximum lateral transport efficiency (-r_{uv}) plotted versus velocity ratio λ for all the test runs (b).

As shown in Figure 57 (a and b), for the test cases with density D1, D2x, D2y, D3, and D4, all characterized by velocity ratios ≥0.40, -r_{uv} peaked approximately on the

main channel side of the interface reaching values in the range 0.40-0.45, indicating a strong correlation between u' and v' associated with coherent vortical motion. For the sparsest vegetation, with shear layer characterized by velocity ratios ≤0.29, the maximum correlation was equal to 0.31-0.27.

To further investigate the presence of large-scale coherent structures, the spectral analysis of the velocity signal along the investigated transects was performed. In Figure 58, the lateral fluctuating velocity spectra and the lateral-longitudinal fluctuating velocities cross-spectra are shown. The spectra are referred to the lateral location where $-r_{uv}$ reached its maximum. For all the cases with velocity ratios equal or greater than 0.4, the spectra and the cross-spectra exhibited a clear peak at the frequency f corresponding to the Strouhal number $St=f\theta/U_C$=0.032. This value corresponds to the natural frequency of KH vortices in a plane ML and has been observed in shear layers in partly vegetated flows with both rigid cylinders (White and Nepf, 2008) and complex morphology flexible vegetation (Chapter 3).
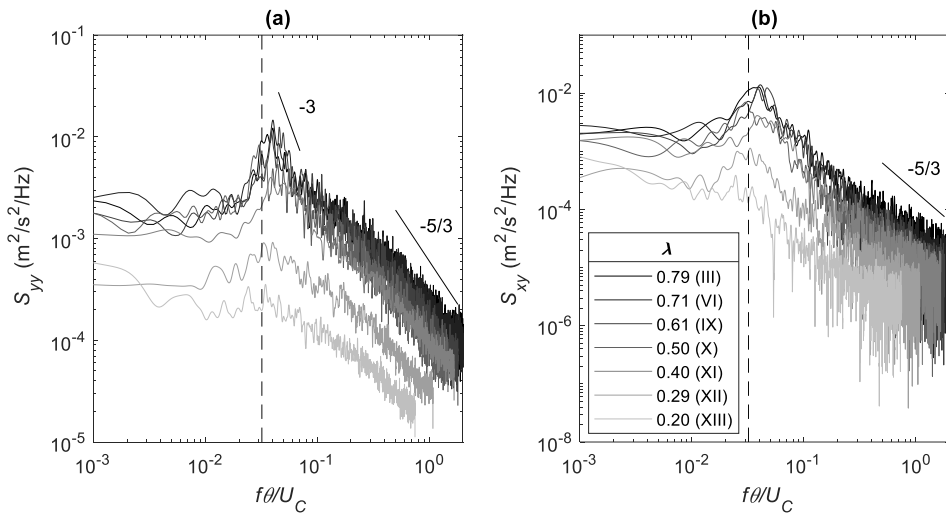

Figure 58 – Spectra of the lateral fluctuating velocity (a) and cross-spectra of the lateral-longitudinal fluctuation velocities (b) for test cases III, VI, IX-XIII (from the densest to the sparsest). The corresponding velocity ratio is indicated in the legend. To make the spectra comparable the abscissae were normalized in terms of Strouhal numbers as $f\theta/U_C$. The natural frequency of a canonical mixing ($f\theta/U_c$=0.032) is shown by a dashed line. The -3 and -5/3 slopes are also illustrated.

For the shear layers with velocity ratios ≤0.29 (test cases XII and XIII), no energy concentration at St=0.032 was observed, indicating that no large-scale structures were present. Indeed, the cross-spectra for case XII exhibited a slight energy concentration at St=0.032.

To further clarify and investigate the presence of coherent structures, the frequency at the peak of the cross-spectra calculated at all the lateral positions with $-r_{uv} \geq 0.32$ was evaluated, as to identify its variability across the shear layer (Table 12).

Table 12 – Frequency f at peak of the lateral-longitudinal cross-spectra; σ_f is the standard deviation of f, and f_{ML} the canonical frequency of coherent structures in a plane mixing layer.

Run	I	II	III	IV	V	VI	VII	VIII	IX	X	XI	XII	XIII
λ (-)	0.80	0.80	0.79	0.72	0.71	0.71	0.61	0.60	0.61	0.50	0.40	0.29	0.20
f (Hz)	0.78	0.85	0.91	0.88	0.87	0.90	1.01	1.04	1.21	1.03	1.45	1.57	0.27
σ_f (Hz)	0.061	0.074	0.067	0.070	0.078	0.106	0.062	0.094	0.132	0.076	0.205	0.513	0.142
f_{ML} (Hz)	0.71	0.76	0.75	0.76	0.75	0.77	0.89	0.90	0.88	1.09	0.96	1.48	2.15

A progressively increasing difference between f and f_{ML} was observed with decreasing velocity ratio. Furthermore, an increased variability of the frequency at the peak was observed across the shear layer.

In Figure 59 the spectra of v' at the lateral position where $-r_{uv} \geq 0.2$ are reported, as to show how the peak indicating the presence of large-scale coherent structures was not observable for the case with velocity ratio equal to 0.20 and only slightly visible for 0.29.
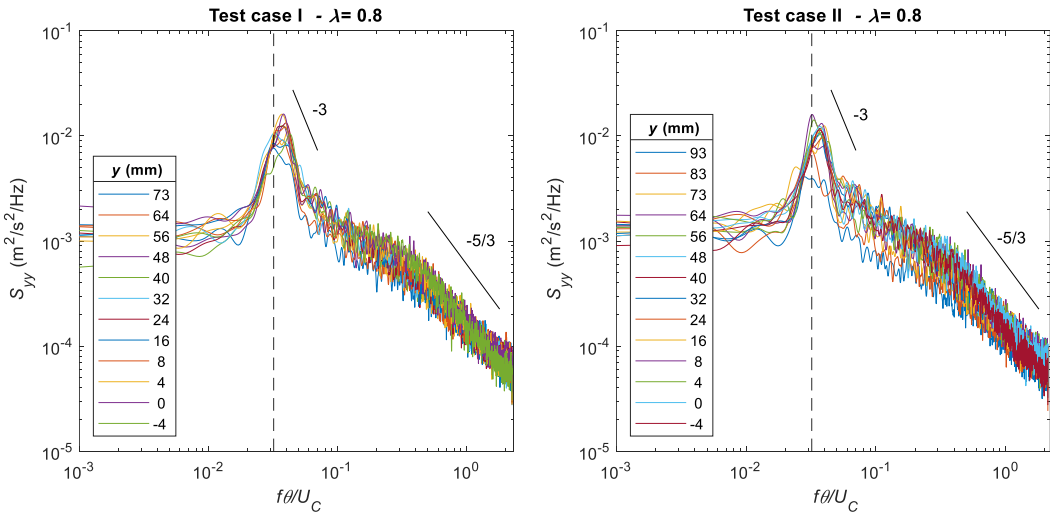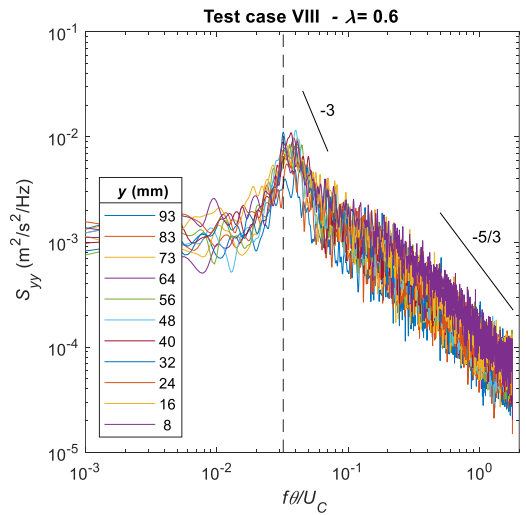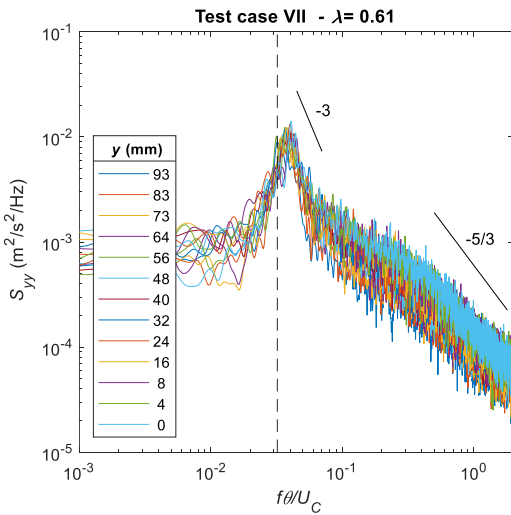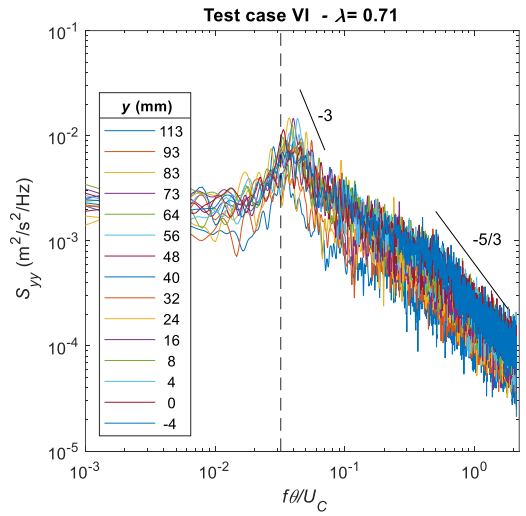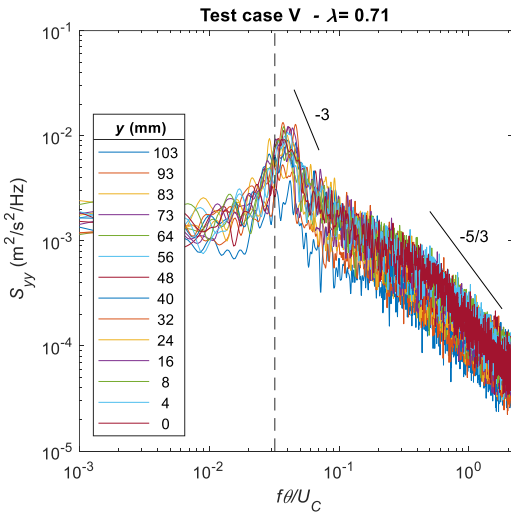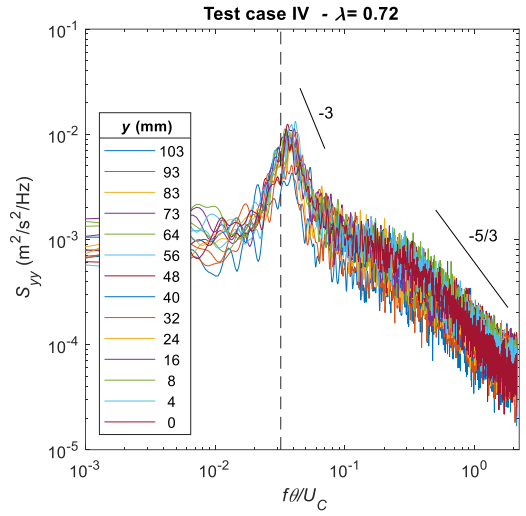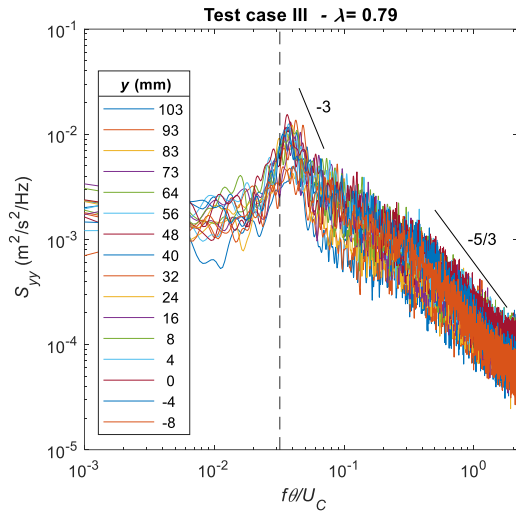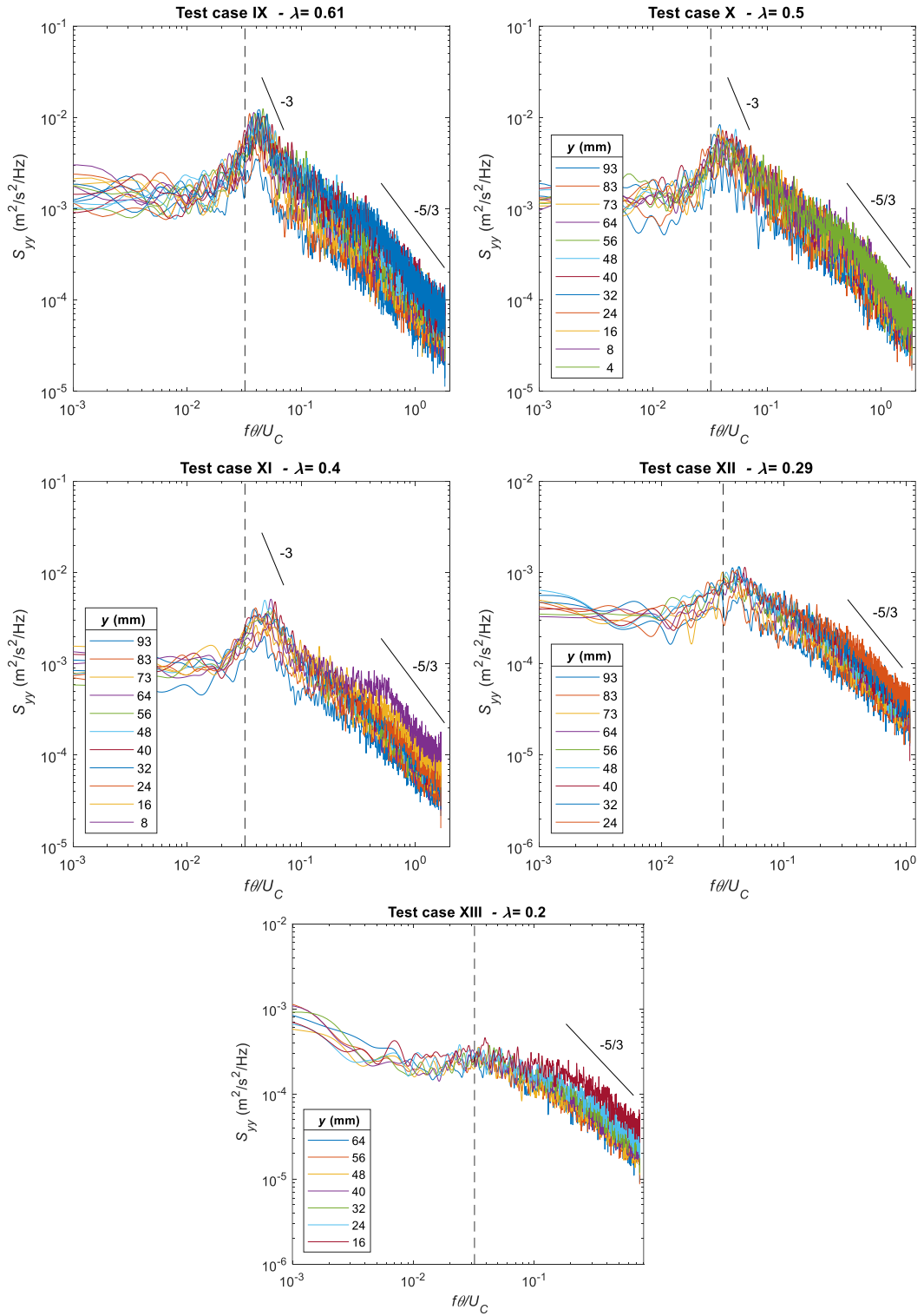
Figure 59 – Power spectral density of the lateral fluctuating velocity evaluated at the lateral positions where -r_{uv}>0.2 for all the test cases.

The spectra of Figure 59 suggest $\lambda \approx 0.3$ as a critical value for the onset of coherent vortices in partly vegetated channels, as also confirmed by the maximum value of -r_{uv} (Figure 57, b). In the current set of experiments, where a given system with a defined slope and cross-section was tested under different flow conditions and with different vegetation density, the velocity ratio was directly governed by the density. The density, by setting the velocity ratio, directly influenced the lateral transport of momentum by governing the onset of large-scale structures.

5.2.3   Anisotropy of turbulence

In Figure 60 the anisotropy invariant maps (Section 2.6) for test cases III, X and XIII, with velocity ratio equal to 0.8, 0.5 and 0.2, respectively, are shown as to illustrate the variability of turbulence anisotropy with density and velocity ratio.
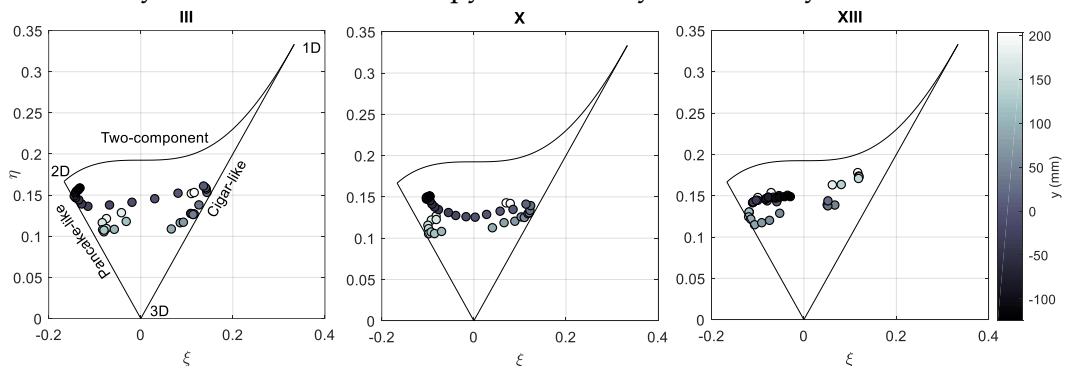
Figure 60 – Anisotropy invariant maps for test cases III, X and XIII, with λ equal to 0.8, 0.5 and 0.2, respectively.

A high degree of anisotropy within the array of cylinders was observed for all the investigated densities, but, for the densest array (with lateral spacing of 25 mm), an increased number of 2D structures was detected. In the main channel a trend almost independent from the density was detected, while, approaching the interface, different patterns were observed depending on the velocity ratio. Indeed, for test cases III and X, both presenting large-scale coherent structures, the points of the invariant map defined an analogous trend characterized by cigar-like structures at the interface., differently from test case XIII.

This different behavior related to the cylinder density and velocity ratio, was observed also in the lateral distribution of TKE, shown in Figure 61, for test cases III, X and XIII.
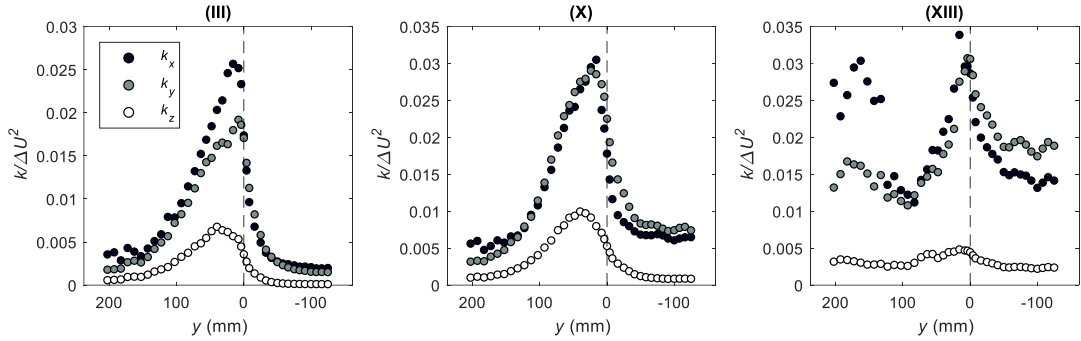
Figure 61 – Lateral distributions of TKE components for test cases III, X and XIII, with λ equal to 0.8, 0.5 and 0.2, respectively. Dashed line indicates the edge of the cylinder array.

5.3   Conclusions

The analysis of flow in partly vegetated channel with an array of rigid cylinders allowed exploring the effects of density and velocity ratio on the lateral momentum transport, as a result of the onset of large-coherent structures. Differently from previous analogous studies, where the effects of density have been studied only considering highly dense cylinder arrays with high velocity ratio (White and Nepf, 2008), in this study the density was varied keeping constant both the flume slope and cross-section, in order to achieve velocity ratio ranging in the interval 0.2-0.8. This allowed investigating the condition, in terms of vegetated shear layer velocity ratio, for the onset of KH type vortices. These large-scale structures play a key role in transporting mass and energy across the vegetated interface, as observed from the distribution of the lateral transport efficiency (Figure 57, a and b). Specifically, the analysis of velocity spectra and velocity statistics suggested $λ≈0.3$ as a critical value for the onset of large-scale interfacial vortices in partly vegetated channels. Even though the number of test is still limited (in the current data set only two cases were characterized by $λ<0.3$), the results are in agreement with analogous analysis performed on mixing layers in compound channels, where the critical value was found to be equal to 0.3 (Proust et al., 2017). In addition, the experiments performed with complex morphology vegetation, illustrated in Chapter 4, even covering a limited range of velocity ratios, are in agreement with this conclusion.

Differently from shear layers above submerged vegetation, where a criterion for the shape of the velocity profile (based on the presence of an inflection point and, hence, the presence of KH structures) is generally provided in terms of vegetation density (frontal area per canopy volume or, more generally, in terms of drag-density parameter), in the current analysis, the definition of a more general criterion for the prediction of the onset of large-scale structures in shear layers in partly vegetated channels is proposed.

References

Aberle, J., Järvelä, J., 2015. Hydrodynamics of Vegetated Channels, in: Rivers-Physical, Fluvial and Environmental Processess. pp. 255–277. doi:10.1007/978-3-319-17719-9

Ben Meftah, M., De Serio, F., Mossa, M., 2014. Hydrodynamic behavior in the outer shear layer of partly obstructed open channels. Phys. Fluids 26. doi:10.1063/1.4881425

Dupuis, V., Proust, S., Berni, C., Paquier, A., 2017. Mixing layer development in compound channel flows with submerged and emergent rigid vegetation over the floodplains. Exp. Fluids 58, 0. doi:10.1007/s00348-017-2319-9

Finnigan, J.J., 2000. Turbulence in plant canopies 519–571.

Ghisalberti, M., Nepf, H.M., 2004. The limited growth of vegetated shear layers. Water Resour. Res. 40, 1–12. doi:10.1029/2003WR002776

Ghisalberti, M., Nepf, H.M., 2002. Mixing layers and coherent structures in vegetated aquatic flows. J. Geophys. Res. 107, 1–11. doi:10.1029/2001JC000871

Ikeda, S., Kanazawa, M., 1996. Three-dimensional organizeed vortices above flexible water plants. J. Hydraul. Eng. 122, 634–640.

Jesson, M.A., Bridgeman, J., Sterling, M., 2015. Novel software developments for the automated post-processing of high volumes of velocity time-series. Adv. Eng. Softw. 89, 36–42. doi:10.1016/j.advengsoft.2015.06.007

Jesson, M.A., Sterling, M., Bridgeman, J., 2013. Despiking velocity time-series-Optimisation through the combination of spike detection and replacementmethods. Flow Meas. Instrum. 30, 45–51. doi:10.1016/j.flowmeasinst.2013.01.007

Nepf, H.M., 2012. Hydrodynamics of vegetated channels. J. Hydraul. Res. 50, 262–279. doi:10.1080/00221686.2012.696559

Nezu, I., Sanjou, M., 2008. Turburence structure and coherent motion in vegetated canopy open-channel flows. J. Hydro-Environment Res. 2, 62–90. doi:10.1016/j.jher.2008.05.003

Parsheh, M., Sotiropoulos, F., Porté-Agel, F., 2010. Estimation of Power Spectra of Acoustic-Doppler Velocimetry Data Contaminated with Intermittent Spikes. J. Hydraul. Eng. 136, 368–378. doi:10.1061/(ASCE)HY.1943-7900.0000202

Poggi, D., Porporato, A., Ridolfi, L., Albertson, J.D., Katul, G.G., 2004. The effect of vegetation density on canopy sub-layer turbulence. Boundary-Layer Meteorol. 111, 565–587. doi:10.1023/B:BOUN.0000016576.05621.73

Proust, S., Fernandes, J.N., Leal, J.B., Rivière, N., Peltier, Y., 2017. Mixing layer and coherent structures in compound channel flows: Effects of transverse flow, velocity ratio, and vertical confinement. Water Resour. Res. 53, 3387–3406. doi:10.1002/2016WR019873

Wahl, T.L., 2003. Discussion of '"Despiking Acoustic Doppler Velocimeter Data"' by Derek G. Goring and Vladimir I. Nikora January. J. Eng. Mech. 128, 2002–2003. doi:10.1061/(ASCE)0733-9372(2003)129

White, B.L., Nepf, H.M., 2008. A vortex-based model of velocity and shear stress in a partially vegetated shallow channel. Water Resour. Res. 44, 1–15. doi:10.1029/2006WR005651

White, B.L., Nepf, H.M., 2007. Shear instability and coherent structures in shallow flow adjacent to a porous layer. J. Fluid Mech. 593, 1–32. doi:10.1017/S0022112007008415

Zong, L., Nepf, H.M., 2012. Vortex development behind a finite porous obstruction in a channel. J. Fluid Mech. 691, 368–391. doi:10.1017/jfm.2011.479

6 Effects of vegetation morphology on shear layer structure in partly vegetated channels

Physical modelling of vegetation in laboratory analysis of flow-vegetation interaction represents a critical aspect. As observed for submerged tensile vegetation in current- (Ghisalberti and Nepf, 2006) and wave-dominated flows (Abdolahpour et al., 2018), embedding realism can provide a better understanding of flow and mixing in natural aquatic environments.

Abdolahpour et al. (2018) studied the effects of vegetation models in wave-dominated conditions by comparing the flow-vegetation interaction observed with rigid and natural-like vegetation, modelling marine seagrasses (tensile blade-shaped vegetation). Relative to the rigid cylinders, for the natural-like vegetation model, for which dynamic plant motion and reconfiguration were observed, significant difference in velocity attenuation within the canopy, and near-bed turbulence were registered. Considering flow over submerged vegetation, by comparing results on experiments carried out with rigid cylinders and dynamically scaled vegetation model for blade-shaped tensile vegetation, Ghisalberti and Nepf (2006) observed significant differences in flow structure, depending on deflection of plants and the presence of *monami* effect. Furthermore, lower momentum transport through the shear layer for flexible dynamically moving vegetation was observed. Comparing the flow-vegetation interaction for rigid and real-like canopies, the main differences in terms of hydrodynamic structures of the vegetated flow stem out from the vegetation reconfiguration and its motions.

When investigating flow-vegetation interaction in partly vegetated channels, the problem of plants representation is even more significant. The greater complexity connected to the simulation of riparian conditions is mainly due to the specific morphological features of the vegetation commonly found in these areas. As illustrated in Chapter 1, riparian vegetation is generally constituted by deciduous shrubs and bushes, presenting leaves, side branches, height-variable bio-mechanical properties, etc. The complex morphology of riparian vegetation, its reconfiguration (highly dependent on the presence of foliation, and in general on the leaf to stem area ratio) and dynamic motion alter the flow structure in channel-vegetated-bank systems, as illustrated in Chapter 4.

Thus, considering realistic riparian vegetation models, like the one considered in Chapter 4, it is expected to provide a better understanding of the flow and mixing in channel-vegetated-bank systems.

In previous studies with submerged vegetation, the comparison between rigid cylinders and real-like vegetation has been generally established by matching the maximum vegetation height and the frontal area of rigid and flexible canopy (Abdolahpour et al., 2018). Even for simple morphology vegetation (like aquatic seagrass), the direct comparison between a rigid canopy and a flexible one is a challenging task owing to the blade reconfiguration that, depending on the hydrodynamic forcing, alters the vegetation frontal area exposed to the flow and hence the drag. Therefore, the comparison is generally established referring to geometrical parameters evaluated on the undeformed vegetation configuration.

Dealing with complex morphology vegetation in partly vegetated channels, a direct comparison between a real-like vegetative obstruction and an array of rigid cylinders is even more difficult. Real vegetation drag is highly dependent on reconfiguration which is governed by flow features (hydrodynamic forcing), vegetation morphology (e.g. leaf to stem area ratio) and flexibility. In this study, the analogy between vegetated shear layers induced by a real-like vegetative obstruction and an array of rigid cylinders was established accurately defining geometric and kinematic similarities. Indeed, rather than pursuing the unfeasible task of creating a direct comparison between real-like plant stands and array of rigid cylinders, in this study the comparison is established on the basis of shear layer characteristics.

Considering realistic vegetation models adds complexity to modelling efforts, but can provide accurate understanding of the crucial processes in aquatic ecosystem. Nevertheless, the representativeness of the real-like vegetation model for the simulation of natural vegetation should be accurately quantified. With reference to studies with submerged tensile vegetation, the representativeness of vegetation has been generally achieved satisfying geometric and dynamic similarities between prototype vegetation and real vegetation (Abdolahpour et al., 2018; Ghisalberti and Nepf, 2006, 2002; Maltese et al., 2007). The dynamic similarity for prototype aquatic tensile submerged vegetation is generally obtained considering the forces acting on the submerged blade which affect its motion and reconfiguration: the drag force and the restoring forces due to rigidity and buoyancy. By matching the drag to rigidity force ratio (Cauchy number) and the buoyancy to rigidity force (buoyancy parameter), it is possible to obtain a dynamic similarity between canopy model and real aquatic meadows (Dijkstra and Uittenbogaard, 2010; Ghisalberti and Nepf, 2002; Nepf, 2012). Aquatic submerged meadows (like meadows of *Posidonia oceanica*) present high homogeneity in terms of geometry and mechanical properties within the canopy. In addition, the mutual interaction between the flow and the canopy motion approximately occurs in the same plane of the shear, recalling the plant flexural rigidity mainly in the direction of the mean flow.

When considering riparian conditions, shrubs and bushes, generally emerging from the water surface and occurring along river margins, interact with the flow with complex processes. Specifically, in partly vegetated channels, flexible foliated vegetation stands vertically in a flow characterized by a significant transversal shear and exhibits dynamic motions in response to the shedding process of KH vortices. Therefore, the motion of each stand, depending on the proximity to the shear dominated area of the flow, is governed by the torsional rigidity of the plant (recalled by the different mean hydrodynamic forces acting on the plant elements on each side of the stem), the flexural rigidity in the streamwise direction (recalled by the mean drag force), the flexural rigidity in the lateral and longitudinal directions (instantaneously recalled by the vortex shedding process). In addition, the motion of complex morphology vegetation is further regulated by the distribution of leaves and bio-mechanical properties along the elevation of the stands, that alters the distributions of forces and reactions on the plant stand, introducing additional forces. Finally, in riparian areas a high heterogeneity of intra- and inter-specific plant characteristics is generally observed.

In this study, the representativeness of the vegetation model was obtained by accurately matching the leaf to stem area ratio of the real like vegetation with common riparian species (see Section 4.1.2). In terms of dynamic representativeness, to a first approximation (due to the novelty of the considered experimental setup and the complexity of the problem), only a visual verification of the vegetation dynamics was considered, selecting the vegetation model with the most natural behavior, compared with the plant motions observed in real riparian settings. In the context of partly vegetated channels, the hydrodynamic impact of an oscillating vegetative obstruction remains relatively unexplored and, in the light of the results discussed in Chapter 4, is studied here by contrasting the turbulence structure of flows in partly vegetated channel with rigid (Chapter 5) and natural-like (Chapter 4) vegetative obstructions.

Specifically, in this Chapter, a comparison of the flow structure in a partly vegetated channel with rigid cylinders and in presence of a natural-like vegetative obstruction is established. The aim is to identify the main differences connected to the vegetation model in shear layers in riparian environments. Specifically, the results of the experimental series PN, discussed in Chapter 4, are compared with the results of the experimental series PR, illustrated in Chapter 5. Furthermore, a literature model for the prediction of the mean velocity was applied to the two considered configurations, giving the opportunity to discuss further differences due to the vegetation model. The goal of this Chapter is to explore the features of flow in natural riparian conditions in comparison with the results obtained simulating vegetation with rigid cylinders. This can help in assessing to which extent the rigid

cylinder model, extensively adopted in literature, is suitable for the interpretation of flow in natural settings.

6.1   Materials and methods

The comparison between the horizontal shear layers in partly vegetated channels was established considering the two sets of experiments discussed in Chapter 4, where a vegetative obstruction made by complex morphology plant stands was considered, and in Chapter 5, where vegetation was simulated using rigid cylinders. Owing to the difficult of establishing a direct comparison between natural-like reconfiguring plants and rigid cylinders, the similarity was achieved in terms of shear layer features and vegetation drag, as described by the drag-density parameter $C_D a$ (evaluated for both the conditions using Equation 4.1).

For the two sets of experiments, carried out in two different facilities, the percentage of the cross-section occupied by the vegetative obstruction was equal to 40%. The water depth to width ratio was kept approximately equal to 0.3 for both the experimental configurations.

The test runs with foliated plants stands F1, F2 and F3 (Table 7), for which a progressively increasing vegetation reconfiguration was observed (as described in Chapter 4), were compared with test runs III, X and XI (Table 11), characterized by three different cylinder densities and referred to as R1, R2 and R3, respectively. Specifically, the reconfiguration-induced vegetative drag reduction exhibited by the natural-like vegetation was simulated by reducing the cylinder density. This resulted in defining three pairings of similar shear layers, each characterized by analogous velocity ratio and drag-density parameter: (i) unreconfigured or slightly reconfigured foliated vegetation vs. dense array of rigid cylinders; (ii) moderately reconfigured foliated vegetation vs. sparse array of rigid cylinders; (iii) strongly reconfigured foliated vegetation vs. very sparse array of rigid cylinders.

For each pairing, the corresponding vegetated shear layer presented similar characteristic velocity and length (as described by λ and δ/θ), making the shear layers comparable. The details of the selected test cases and the shear layer characteristic parameters are reported in Table 13. The three pairings of test runs were characterized by decreasing velocity ratios λ (approximately equal to 0.8, 0.5 and 0.4, respectively) and drag-density parameter (approximately equal to 13, 1.5 and 1 m-1, respectively).

For all the selected runs the presence of large-scale coherent structures with characteristic Strouhal number equal to 0.032 was observed. Furthermore, the selected shear layers were characterized by a ratio between the shear layer width and momentum thickness approximately equal to 4.5.

The constancy of this ratio, interpretable as a shear layer shape factor, allowed the different cases to be comparable.

Table 13 – Test cases selected for comparison and characteristic shear layer features.

Test Run	Q (l/s)	h (mm)	h/B (-)	U_1 (m/s)	ΔU (m/s)	U_C (m/s)	λ (-)	δ (mm)	θ (mm)	δ/θ (mm)	$C_D a$ (m^{-1})	Re_θ (-)	Re_θ/Re_h (-)
Slightly reconfigured foliated vegetation vs. dense array of rigid cylinders													
F1	22.2	170	0.28	0.042	0.322	0.203	0.79	175	40	4.36	12.15	12912	0.209
R1 (III)	29.4	135	0.34	0.119	0.888	0.563	0.79	111	24	4.59	13.85	21468	0.158
Moderately reconfigured foliated vegetation vs. sparse array of rigid cylinders													
F2	50.0	170	0.28	0.216	0.571	0.502	0.57	170	37	4.58	1.43	21184	0.158
R2 (X)	31.7	133	0.33	0.311	0.623	0.622	0.50	106	23	4.59	2.03	14393	0.116
Strongly reconfigured vegetation vs. very sparse array of rigid cylinders													
F3	83.3	170	0.28	0.532	0.742	0.903	0.41	155	34	4.63	0.49	24857	0.115
R3 (XI)	31.7	122	0.31	0.397	0.524	0.659	0.40	104	22	4.72	1.24	11519	0.102

Comparing the three different pairings of shear layers, it should be taken into account that the process that induced the drag and velocity ratio reduction for the F and R cases was different. For the natural-like vegetative obstruction, the progressively increasing velocity within the vegetation induced increasing reconfiguration with corresponding drag reduction. For the R cases, the drag reduction was achieved by progressively reducing the cylinder density. Nevertheless, considering Equation 4.1 for the estimation of the drag-density parameter, the cylinder density reduction was the only technically feasible operation for reducing $C_D a$. A second fundamental difference between the two test cases was represented by the vegetation motion.

In the following, the comparison between the test cases of Table 13 is proposed in terms of normalized lateral distributions of velocity statistics. Comparing the lateral distributions of velocity statistics, it should be taken into account that for rigid cylinders the mean velocity within the vegetation was spatially averaged over the vegetation lateral spacing L_y, to remove plant-scale heterogeneity (see Section 6.1). Furthermore, for the R cases, the stem-scale spatial variability of flow features was not taken into account, while the for the F cases the velocity was averaged considering two different transects (see Section 4.1.3).

The normalization was achieved by adopting the velocity difference ΔU and the convection velocity U_C as scaling velocities, whereas the momentum thickness θ as characteristic scaling length. The lateral coordinate is normalized as $(y\text{-}y_i)/\theta$, where y_i is the position of the inflection point and θ the momentum thickness.

6.2 Results and discussion

6.2.1 Vegetation model: effects on the lateral distribution of velocity statistics

Considering the PN (Chapter 4) and PR (Chapter 5) test series, a common feature regarding the investigated vegetated shear layers was observed. Specifically, the ratio between the shear layer width and the momentum thickness δ/θ was found to remain approximately constant and ≈4.5 in the range of velocity ratio 0.4-0.8, independently from the vegetative obstruction features (Figure 62). In canonical plane mixing layer, $\delta/\theta=4\sqrt{\pi}\approx7.1$.
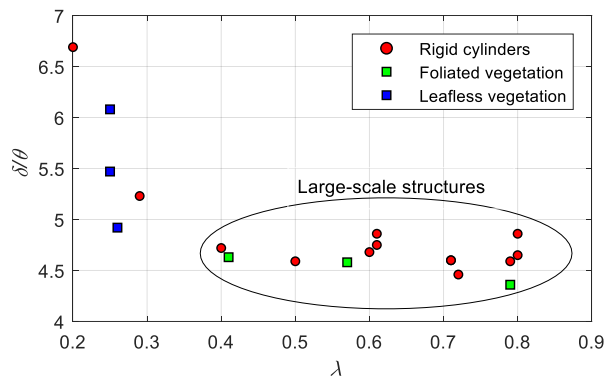

Figure 62 – Shear layer shape factor δ/θ plotted versus the velocity ratio λ. The test cases presenting large-scale structures are surrounded by an ellipse. The evaluation of length scales for leafless vegetation were affected by higher uncertainties.

The lateral distribution of longitudinal velocity, here synthetically described by the δ/θ ratio, was observed to be highly dependent on the presence of large-scale coherent structures and in turn on the velocity ratio. Indeed, the PR data set suggested $\lambda\approx0.3$ as a critical value for the KH vortex onset, and the test on foliated and leafless vegetation were in agreement with this conclusion.

To investigate the effects related to the vegetation features (morphologically complex reconfiguring vegetative obstruction vs. rigid cylinders), the comparison in terms of lateral distributions of dimensionless velocity and Reynolds stresses were performed for the test cases of Table 13, shown in Figure 63 and Figure 64.
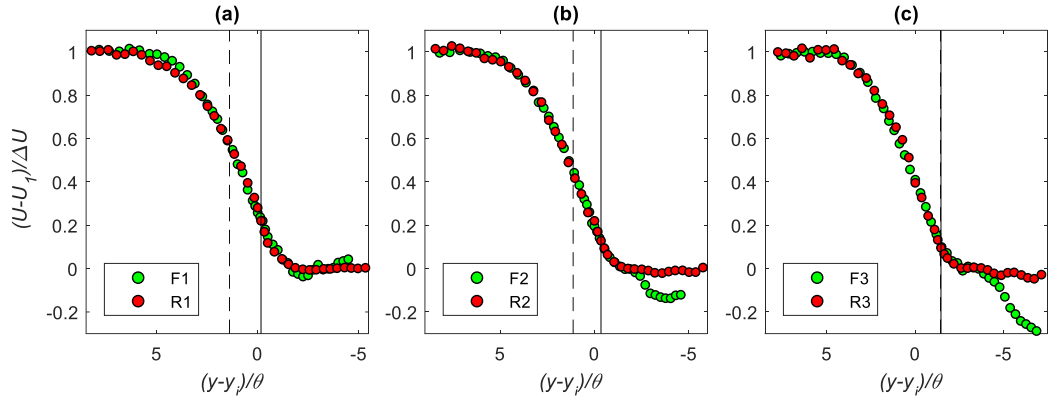
Figure 63 – Lateral distribution of normalized longitudinal velocity for F1-R1 (a), F2-R2 (b), F3-R3 (c) with λ equal to 0.8, 0.5 and 0.4, respectively. The dashed line indicates the position of the vegetated interface for morphologically complex plant stands (F case), whereas the solid line indicates the position of the rigid cylinders interface (R case).

The normalized velocity distributions for the F and R cases collapsed on the same curve, with greater differences observed within the vegetation with increasing plants reconfiguration.

As shown in Figure 64, the shear penetration within the vegetation was observed to strongly depend on the vegetation morphology and flexibility, and velocity ratio. The distance d_p between the vegetated interface and the lateral position where the Reynolds stress $-\overline{u'v'}$ decays to 10% of its maximum value are reported in Table 14, normalized with the shear layer width.

Table 14 – Maximum normalized Reynolds stress and shear penetration for the selected test cases.

Test Case	F1	R1	F2	R2	F3	R3
λ	0.79	0.79	0.57	0.50	0.41	0.40
$-\overline{u'v'}/\Delta U^2$	0.022	0.018	0.025	0.023	0.022	0.023
d_p/δ	0.75	0.21	0.65	0.13	0.24	0.05

The normalized lateral distributions of the Reynolds stress collapsed for the considered cases, even if greater asymmetry relatively to the peak was observed for rigid cylinders. For morphologically complex vegetation the lateral-longitudinal Reynolds stress peaked on the vegetated side of the mean position of the interface while, for cylinders, the Re stress peaked directly on the main channel side of the interface. The penetration of the shear is dependent on the strength and coherence of the large-scale structures, in turn strongly related to the velocity ratio. Indeed, in Figure 64 (a, b and c) the decreasing penetration related to the decreasing velocity ratio is also evident.
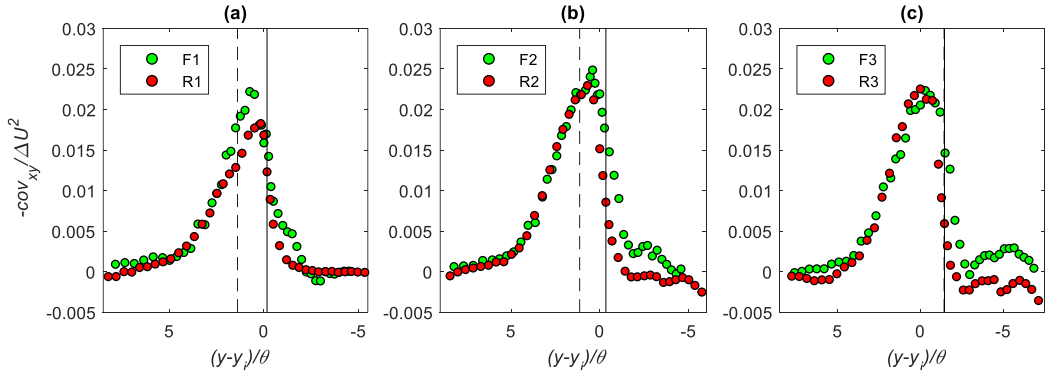
Figure 64 – Lateral distribution of lateral-longitudinal normalized Reynolds stress for F1-R1 (a), F2-R2 (b), F3-R3 (c) with λ equal to 0.8, 0.5 and 0.4 respectively. The dashed line indicates the position of the vegetated interface for morphologically complex plant stands (F case), whereas the solid line indicates the position of the rigid cylinders interface (R case).

The turbulence intensity of the lateral fluctuating velocity, shown in Figure 65, can provide information about the coherence of the interfacial large-scale structures. With decreasing velocity ratio, the turbulence intensity was observed to decrease, with rigid cylinders presenting always greater turbulence intensity than that related to the morphologically complex vegetation.
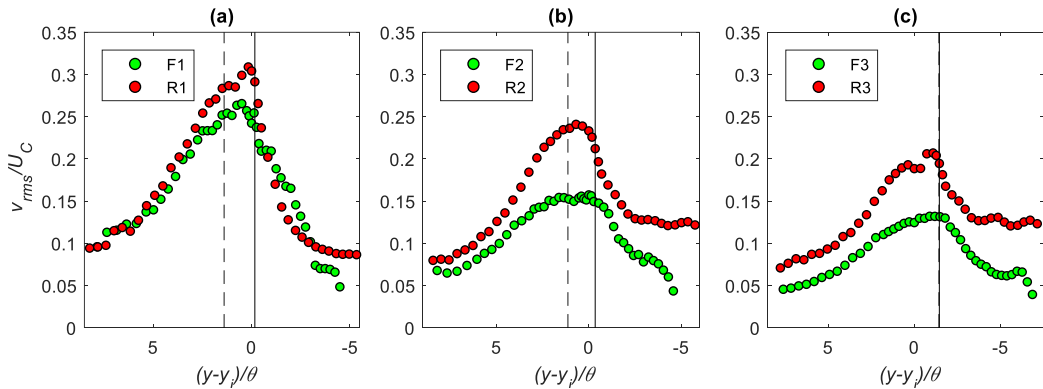

Figure 65 – Lateral distribution of the turbulence intensity for F1-R1 (a), F2-R2 (b), F3-R3 (c) with λ equal to 0.8, 0.5 and 0.4, respectively. The dashed line indicates the position of the vegetated interface for morphologically complex plant stands (F case), whereas the solid line indicates the position of the rigid cylinders interface (R case).

For the natural-like vegetative obstruction, more symmetric distributions of velocity statistics were observed. The effects of lateral motions of plants were visible at the interface, where smoother distributions were detected. Indeed, when vegetation lateral motion was limited (F1), the distribution exhibited a sharper peak (Figure 65, a), as for rigid cylinders. With increasing lateral motions (F2 and F3), the turbulence intensity reached a stable maximum value across the interface, differently from rigid cylinders, where a clear peak at the interface was always observable.

As shown in Figure 64 and Figure 65, with increasing vegetation reconfiguration, a greater similitude, in terms of asymmetry with the sparse array of rigid cylinders, is shown (F3-R3). On the other hand, in the comparison of lateral distributions for the not reconfigured vegetation with the dense array of rigid cylinders (F1-R1 and F2-R2), the major difference was related to the penetration of shear.

6.2.2 Efficiency of lateral transport

The greater differences emerging from the comparison of the two vegetation models stem out from the different vegetation morphology and the dynamic response exhibited by natural-like plant stands to the flow forcing. To further investigate the difference related to the vegetation morphology in terms of lateral transport of momentum, the lateral-longitudinal fluctuating velocity correlation coefficient was evaluated and plotted in Figure 66. This parameter quantifies the efficiency of the turbulent lateral transport of streamwise momentum and can provide information about location, size and strength of the interfacial vortices.
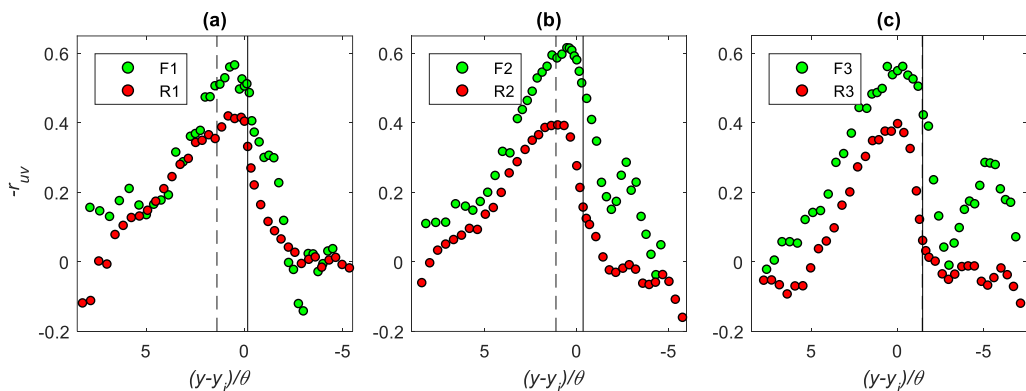

Figure 66 – Lateral distribution of correlation coefficient for F1-R1 (a), F2-R2 (b), F3-R3 (c) with λ equal to 0.8, 0.5 and 0.4, respectively. The dashed line indicates the position of the vegetated interface for morphologically complex plant stands (F case), whereas the solid line indicates the position of the rigid cylinders interface (R case).

The first striking difference between the investigated test cases, systematically observed across the different considered velocity ratios (Figure 66), concerned the degree of correlation between the longitudinal and lateral fluctuating velocity. For morphologically complex vegetation $|r_{uv}| \approx 0.6$, for rigid cylinders $|r_{uv}| \approx 0.4$. The different vegetated shear layers, induced by complex morphology vegetation and rigid cylinders, even presenting analogous features in terms of distributions of mean velocity and Reynolds stress, are characterized by notably different lateral transport efficiency. Specifically, characteristic values of $|r_{uv}|$ for canonical mixing layers are approximately 0.44, comparable to those observed for rigid vegetation (see Section 5.2.2).

The lateral transport efficiency was found to be dependent mainly on the preence of large-scale coherent vortices. Indeed, as shown in Figure 67, as long as the velocity ratio was sufficiently high to ensure the onset of vortical structures, $|r_{uv}|_{max}$ was found to reach an approximately constant maximum value, different for complex morphology vegetation and rigid cylinders.
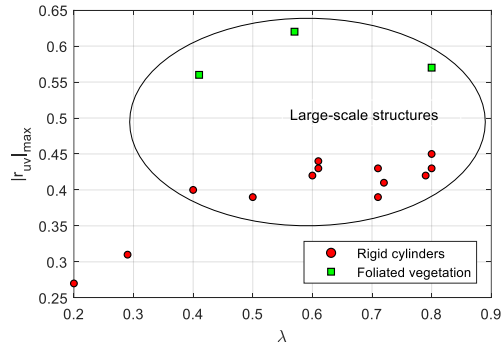

Figure 67 – Maximum correlation coefficient plotted versus the velocity ratio. The test cases presenting large-scale structures are surrounded by an ellipse.

The increased efficiency of lateral transport for the morphologically complex and dynamically moving natural-like vegetation can be reasonably associated with the lateral motion of plants that plays a key role in governing the interaction at the interface. Even though the lateral motion of the interface induces instantaneously variable interface drag conditions that can strain the vortex structure and induce a loss of coherence, the lateral motion of complex morphology vegetation can physically transfer patches of fluids across the interface, improving the lateral transport.

6.3 Vegetation models: effects on the vertical distribution of velocity statistics (F1-R1)

The vertical distribution of velocity statistics was investigated within the flow domain and here the comparison between the F1 and R1 cases is proposed as to investigate the effects of the vegetation features on the vertical variability of flow structure in partly vegetated channels. The vertical variability of the flow was investigated along five verticals (V1-V5) accurately located within the flow domain as to preserve the relative position of the verticals with respect to the inflection point, for both the vegetation models, as shown in Figure 68.
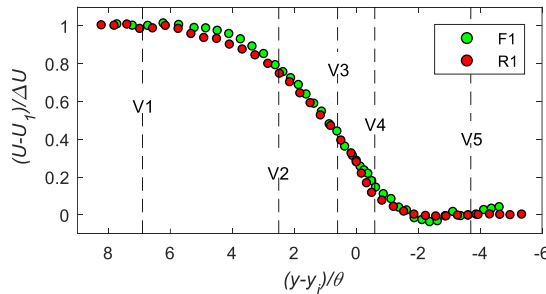

Figure 68 – Lateral position of inspected verticals within the vegetated shear layer.

Specifically, V1 (at $(y-y_i)/\theta \approx 7$) was located in the open main channel, in the region where velocity reached the constant ambient value U_2. V2 (at $(y-y_i)/\theta \approx 2.5$) was located in the outer layer, such as the region of the main channel interested by the shear layer. V3 and V4 (at $(y-y_i)/\theta \approx \pm 0.6$) were located symmetrically on both sides of the inflection point, in the high gradient part of the velocity profile. V5 (at $(y-y_i)/\theta \approx -3.7$) was located deeply within the vegetation, where velocity reached the constant ambient value U_1. Relatively to the vegetation interface, the V3 vertical for the F case was located in the area occupied by the moving interface. For both cases V4 and V5 were located within the vegetation.

While comparing the two cases, it should be taken into account that for natural-like conditions (F) the vegetative obstruction was made of foliated plant stands and grassy bed. The comparison is here performed only between not reconfiguring vegetation (F1) and rigid cylinders (R1).

Mean velocity and Reynolds stress
The vertical distributions of the longitudinal mean velocity are shown in Figure 69, where the velocity profiles for the F1 case are plotted together with the profiles of the R1 case. As reported in previous studies with rigid cylinders (White and Nepf, 2008), the velocity profiles in the open main channel presented a standard logarithmic profile (Figure 69).

Moving toward the vegetation through the shear layer, the profiles progressively showed higher uniformity along *z*.
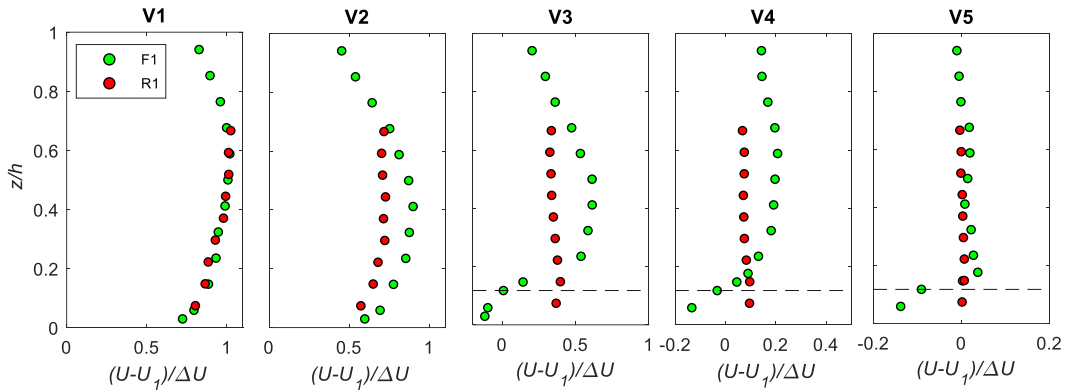

Figure 69 – Vertical distribution of the longitudinal velocity for the five inspected verticals, test cases F1-R1. The dashed line indicates the top of the grassy bed.

For natural conditions, where complex morphology vegetation stands above grassy bed, the transition to uniform velocity profiles is more slow and. only deep into the vegetation. the velocity exhibited a uniform vertical profile (besides the near-bed part of the profile where the effects of the bed roughness were more significant).

The percent difference between the mid-depth velocity and the depth averaged velocity, considering the five verticals, were ≈23% for the F1 case and ≈4% for the R1 case.

The effects of the vegetation morphology was also visible in the distribution of $-\overline{u'v'}$ and $-\overline{u'w'}$ (Figure 70 and Figure 71, respectively). For complex morphology vegetation, the presence of bed roughness and the vertical distribution of vegetative elements altered the vertical and lateral transport of momentum, while for the rigid cylinders the vertical distributions were observed to be approximately uniform.
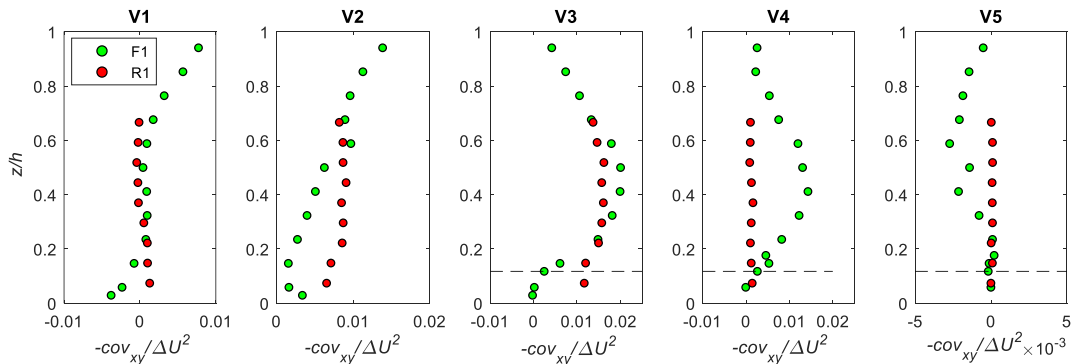

Figure 70 – Vertical distribution of the lateral-longitudinal Reynolds stress for the five inspected verticals, test cases F1-R1. The dashed line indicates the top of the grassy bed.
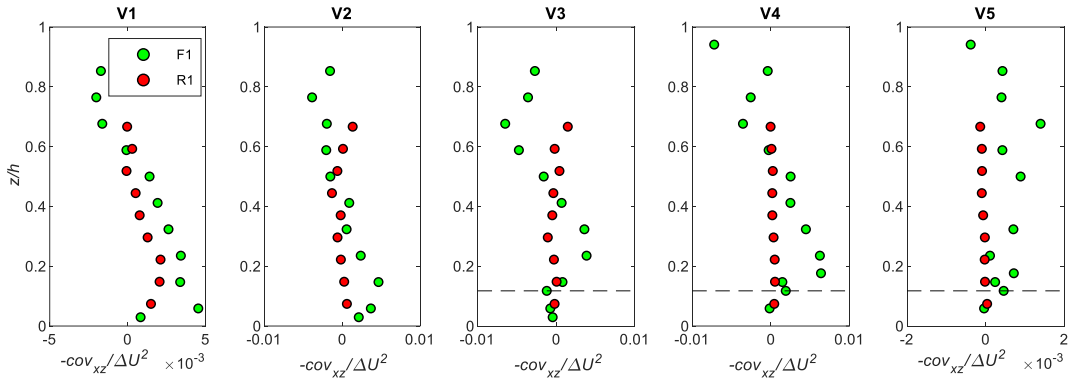
Figure 71 – Vertical distribution of the vertical-longitudinal Reynolds stress for the five inspected verticals, test cases F1-R1. The dashed line indicates the top of the grassy bed.

The proposed comparison, performed considering only F1 and R1 cases, did not take into account the effects of reconfiguration on vertical distributions of velocity statistics. In Figures 72, 73 and 74, the effects of plants reconfiguration on the vertical distribution of mean longitudinal velocity, lateral-longitudinal and vertical-longitudinal Reynolds stress are shown, considering test cases F1-F3. Greatest differences were observed for the within vegetation verticals (V5), where the effects of plant reconfiguration highly impacted the vertical distribution of flow features.

Figure 72 – Vertical distribution of the mean longitudinal velocity for the foliated test cases F1-F3, along the five inspected verticals. The dashed line indicates the top of the grassy bed.

Figure 73 – Vertical distribution of the lateral-longitudinal Reynolds stress the foliated test cases F1-F3, along the five inspected verticals. The dashed line indicates the top of the grassy bed.
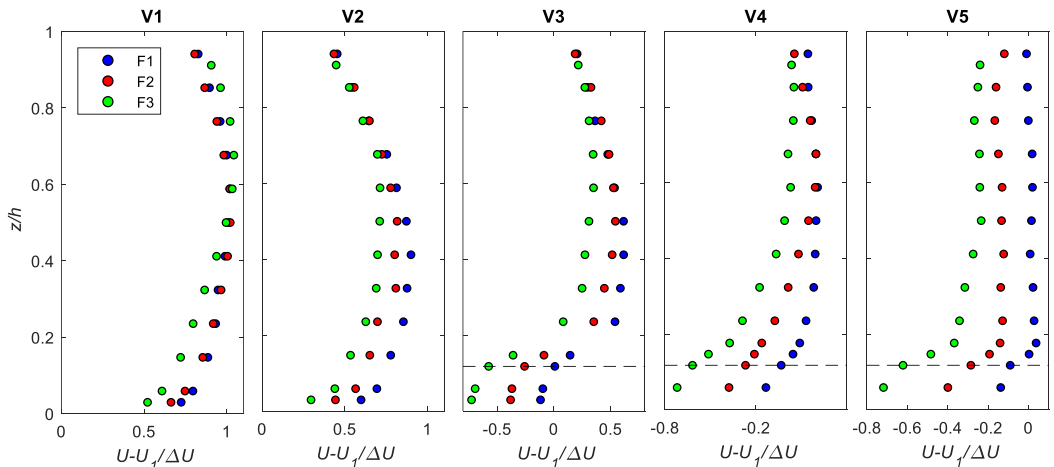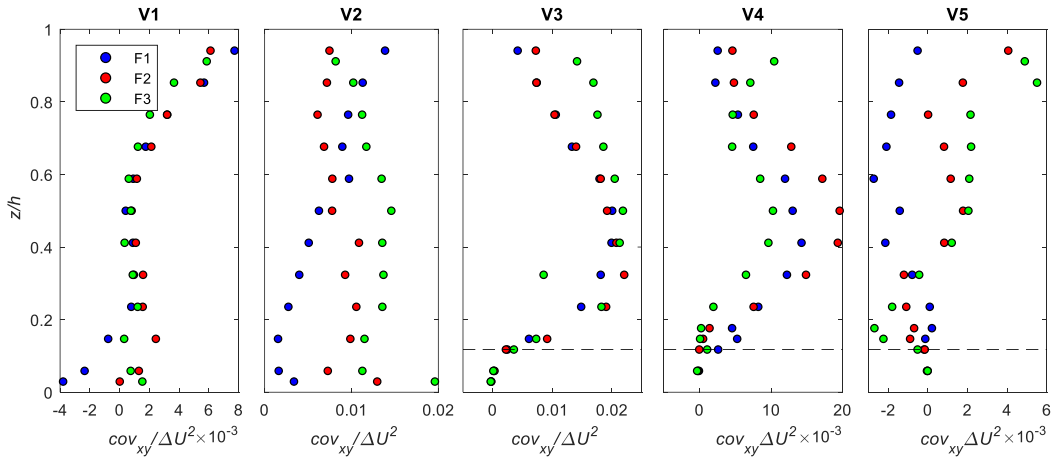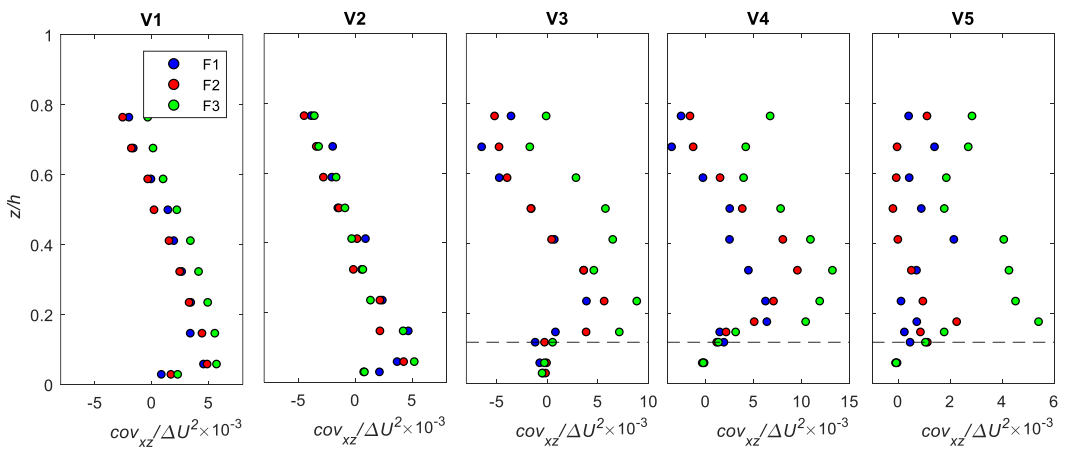

Figure 74 – Vertical distribution of the vertical-longitudinal Reynolds stress the foliated test cases F1-F3, along the five inspected verticals. The dashed line indicates the top of the grassy bed.

6.4   Mean Velocity prediction: the White & Nepf model

In this Section the White and Nepf (2008) model (WNM) for the prediction of the longitudinal mean velocity in a partly vegetated channel is tested with reference to the configurations of partly vegetated channel with rigid vegetation (PR test series) and natural-like reconfiguring vegetation (PN test series). In the following, the formulation for the lateral distribution of mean longitudinal velocity, as proposed by White and Nepf (2008), is briefly introduced. The WNM is a physically based model, deduced for a shallow partly vegetated channel (h/B<<1) with rigid emergent vegetation. Under the assumption of steady and fully developed mean velocity, the flow domain is divided into four zones, as schematized in Figure 75.
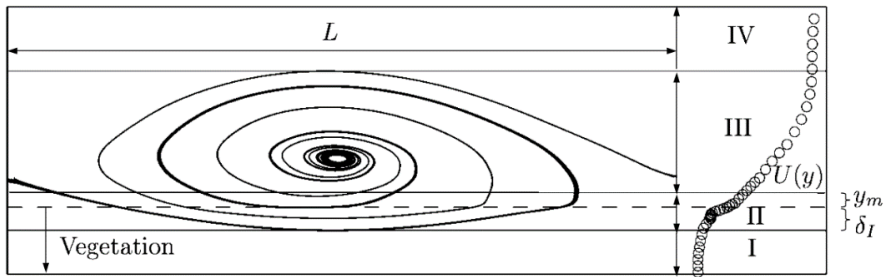
Figure 75 - Four zones velocity model: the vegetated layer (I), the inner layer, which penetrates of δ_I into the vegetation and extends of y_m outside the vegetation (II), the outer layer in the main channel (III), and the region of uniform flow in the main channel (IV). The streamlines for a typical vortex structure are also represented (White and Nepf, 2008).

Velocity in zones I and IV

The low speed stream velocity U_1 within the vegetated layer (zone I) is derived from a momentum balance, neglecting the effects of the bed friction (c_f/h<<$C_D a$ in this region) and is calculated using the following expression:

$$U_1 = \sqrt{\frac{2gS}{C_D a}},$$ (6.1)

where $S=-\partial h/\partial x$ is the free surface slope.

Analogously, in the main channel (zone IV), the high speed stream velocity U_2 can be evaluated as follows:

$$U_2 = \sqrt{\frac{2gh}{c_f}},$$ (6.2)

where c_f is the bed friction coefficient.

Velocity in zone II

In the inner region, i.e. zone II, the velocity $U_I(y)$ can be described by a hyperbolic tangent shear profile as:

$$U_I(y) = U_1 + U_S\left[1 + \tanh\left(\frac{y - y_i}{\delta_I}\right)\right],\tag{6.3}$$

where y_i is the lateral position of the inflection point exhibited by the velocity profile, U_S is the slip velocity and δ_I is the inner layer width. White and Nepf assumed the inflection point to coincide with the lateral interface position ($y=0$). Based on their experimental results, as also confirmed by White and Nepf (2007) and Poggi et al. (2004), the inner layer width was found to scale with $\delta_I \approx (C_D a)^{-1}$. In addition, they observed that, for large values of $C_D a$, with $(C_D a)^{-1}$ less than cylinder diameter d, the penetration length scale δ_I became independent of the drag-density parameter. Considering that the velocity transition cannot occur over a distance less than that first row of cylinders, they defined the following scaling for the inner layer width:

$$\delta_I \approx max\{0.5(C_D a)^{-1}, 1.8d\}.\tag{6.4}$$

The slip velocity U_S was semi-empirically evaluated as:

$$U_S = \frac{\delta_I}{\delta_O}\frac{U_2 - U_1}{(1 - \alpha^2)(1 + \alpha)\dfrac{\delta_I}{\delta_O}},\tag{6.5}$$

where δ_O is the outer layer width and α is a parameter evaluated as:

$$\alpha = tanh\left[1.89e^{(-4.03\delta_I/\delta_O)}\right].\tag{6.6}$$

Velocity in zone III

The velocity profile $U_O(y)$ in the outer layer (zone III), was deduced imposing the equilibrium between the pressure gradient, the shear stress gradient and the bed friction, neglecting the contribution of secondary currents. Specifically, a constant eddy viscosity ν_t was assumed across the outer layer. Based on their experimental results, the best prediction of the outer layer velocity profile was obtained by assuming:

$$\nu_t = \frac{0.7{u_*}^2\delta_O}{U_2 - U_{m'}},\tag{6.7}$$

where ${u_*}^2$ represents the lateral friction velocity (friction velocity evaluated at the interface position); $U_{m'}$ is the velocity at y_m, the lateral position where the outer layer velocity and its slope match the inner layer velocity and its slope.

The matching velocity $U_{m'}$ and the lateral position y_m can be evaluated using Equation 6.8 and 6.9, respectively:

$$U_{m'} = U_2 - \frac{U_2 - U_i}{1 + \dfrac{\delta_I/\delta_O}{1 - \alpha}}, \tag{6.8}$$

$$y_m = \delta_I \left[\tanh^{-1} \left(\frac{U_{m'} - U_i}{U_S} - 1 \right) \right] + y_i. \tag{6.9}$$

The resulting velocity profile is described by Equation 6.10:

$$U_O(y) = 3U_2 \tanh^2 \left[\sqrt{\frac{3}{4(U_{m'}/U_2 + 2)}} (y - y_m)/\delta_O + C \right] - 2U_2, \tag{6.10}$$

where

$$C = \tanh^{-1} \sqrt{1 + \frac{U_{m'}/U_2 - 1}{3}}. \tag{6.11}$$

For the outer layer width δ_O, White and Nepf (2008) proposed the following scaling:

$$\delta_O = \frac{3 \times 0.7}{2(U_{m'}/U_2 + 2)(1 - U_{m'}/U_2)} \frac{2h}{c_f} \frac{u_*^2}{U_2^2}. \tag{6.12}$$

The lateral friction velocity u_*^2 can be evaluated using Equation 6.13:

$$u_*^2 = 0.032 \beta \gamma \frac{\delta_O}{\theta} \frac{(U_1 + U_2)}{2} \Delta U, \tag{6.13}$$

where:

- β is a parameter that accounts for the efficiency of the mass (or momentum) exchange in zone III, the so-called exchange zone, assumed equal to 0.3;
- γ is the ratio of momentum to mass flux and was determined to be equal to 0.8;
- δ_O/θ is a shape factor of the shear layer, ratio between the outer layer width δ_O and the momentum thickness θ, assumed equal to 3.29.

Shear stress distribution
The authors proposed also a formulation for the lateral profile of depth averaged Reynolds stresses. Within the inner layer, assuming $\nu_t = u_*^2 \delta_I / U_S$, $\overline{u'v'}$ can be described using Equation 6.14:

$$\overline{u'v'} = \nu_t \frac{dU_I}{dy} = \frac{u_*^2 \delta_I}{U_S} \frac{dU_I}{dy}. \tag{6.14}$$

Within the main channel, in the outer layer (zone III), congruently with the assumption on the eddy viscosity (Eq. 4.7), Reynolds stresses can be described using the following expression:

$$\overline{u'v'} = v_t \frac{dU_O}{dy} = 0.7 u_*^2 \frac{U_2 + U(y)}{U_2 - U_{m'}} \sqrt{\frac{U + U_2}{U_{m'} + U_2}}. \tag{6.15}$$

6.4.1 Comparison between WNM predictions and experiments

The model proposed by White and Nepf (2008) is applied in this Section for testing its ability to predict the velocity profiles in vegetated shear layers generated by rigid cylinders (PR) and morphologically complex vegetation (PN). The significant differences in experimental setup and shear layer characteristics between the current experimental sets and the White and Nepf (2008) one, against which the model has been originally calibrated, are reported in Table 15.

Table 15 – Significant differences in experimental setup and shear layer characteristics between current data series and White and Nepf (2008) experiments.

Setup and shear layer characteristics	PR	PN	White and Nepf experiments
Vegetation model	Cylinders (aligned)	Foliated plant stands	Cylinders (staggered)
L_x, L_y (mm)	25 – 400, 25 – 50	-	20 – 44
d (mm)	4.5	-	6.5
ϕ	0.0008 – 0.0254	-	0.010 – 0.045
$C_D a$ (m^{-1})	0.46 – 21.9	0.5 – 12.2	9.2 – 274
h/B	0.2 – 0.3	0.3	<0.1
B_V/B	≈40%	≈40%	≈30%
U_1 (m/s)	0.095 – 0.655	0.042 – 0.532	0.002 – 0.022
ΔU (m/s)	0.33 – 0.75	0.32 – 0.74	0.04 – 0.29
λ	0.20 – 0.80	0.8 – 0.4	0.78 – 0.96
Re_θ / Re_h	0.05 – 0.22	0.11 – 0.21	0.17 – 4.22

Before discussing the performance of the WNM for the prediction of velocity, it should be taken into consideration that the model was calibrated and tested considering shallow flows and a vegetative obstruction made of an array of staggered cylinders, under specific the assumption of constant eddy viscosity across the main channel. Moreover, the model refers only to configurations where the cylinder density is sufficiently high as to have high velocity ratios and large-scale coherent structures. Indeed, in their work the authors calibrated and tested the model against experimental shear layers with velocity ratios >≈0.8.

In the current study, the model was applied to the entire data set of partly vegetated channels, for both the vegetation models. The model is not applicable to the cases in which no coherent structures were observed. Moreover, among the cases presenting large-scale coherent structures, it is expected to perform better for the test cases with the highest velocity ratios.

The WNM described in the previous Section was applied using as input parameters the two ambient velocities U_1 and U_2 and the lateral position of the inflection point y_i. In this regards, considering the PR tests, the inflection was always approximately located at the interface. For the lower cylinder density, the inflection resulted to be shifted toward the main channel.

The experimental velocity profiles are plotted with their corresponding predictions by the WNM in Figures 76-78. Information about the goodness of fit was deduced evaluating the root mean square error $RMSE$, using equation:

$$RMSE = \sqrt{\frac{\sum_{i=1}^{n}(U_i - U_{WN,i})^2}{n}}, \qquad (6.16)$$

where U_i and $U_{WN,i}$ are the measured and modeled mean velocity at the same location i, respectively, and n is the number of points per transect for which data were available. In Table 16 the root mean square error for each pairing of velocity profiles is reported for the considered test cases.

Table 16 – Root mean square error (RMSE) between experimental and predicted velocity.

Run	I	II	II	IV	V	VI	VII	VIII
ΔU (m/s)	0.747	0.811	0.888	0.728	0.751	0.828	0.624	0.639
λ (-)	0.80	0.80	0.79	0.72	0.71	0.71	0.61	0.60
$C_D a$ (m⁻¹)	21.88	19.20	13.85	9.68	8.43	6.89	5.14	4.45
$RMSE$ (m/s)	0.041	0.067	0.089	0.069	0.076	0.101	0.128	0.144
Run	IX	X	XI	XII	XIII	F1	F2	F3
ΔU (m/s)	0.737	0.623	0.524	0.423	0.333	0.322	0.571	0.748
λ (-)	0.61	0.50	0.40	0.29	0.20	0.79	0.57	0.41
$C_D a$ (m⁻¹)	3.46	2.03	1.24	0.73	0.46	12.15	1.43	0.49
$RMSE$ (m/s)	0.172	0.206	0.199	0.199	0.168	0.019	0.182	0.363

In Figure 76 are reported test cases I-III, referred to density D1, test cases IV-VI, referred to density D2x, and test cases VII-IX, referred to density D2y. For these cases, each density was tested with three different flow rates. The model correctly interpreted the lateral distribution of velocity for the density D1, performing better for the low flow rate case (I). For these cases, the velocity was better predicted within the inner layer. Greater differences were observed in the outer layer. With progressively decreasing density and velocity ratio, the root mean square error between experimental and predicted velocity was observed to increase, going from 0.041 m/s for λ=0.8 to 0.171 m/s for λ=0.6 (Table 16).

Test cases I-III were characterized by velocity ratio ≈0.8, whereas test cases IV-VI by λ≈0.7 and test cases VII-IX by λ≈0.6. For test cases with analogous velocity ratio and

decreasing drag-density parameter (I-III), the goodness of the prediction was observed to decrease (Table 16).

Figure 76 - Comparison between experimental velocity profiles (circles) and the predictions of the WNM (solid black curve) for the I-IX test cases (rigid cylinders). The plots of this panel are organized for density (lines) and flow rate (columns).

For the test cases with velocity ratios from 0.5 to 0.2, gathered in Figure 77, the WNM was not able to predict the velocity profile neither to provide information about the velocity gradients, even though test cases X and XI presented large-scale coherent structures. Indeed, for these cases the strength of coherent structures was notably lower and vortices did not enter the vegetation.

Figure 77 - Comparison between experimental velocity profiles (circles) and the predictions of the WNM (solid black curve) for the X-XIII test cases (rigid cylinders).

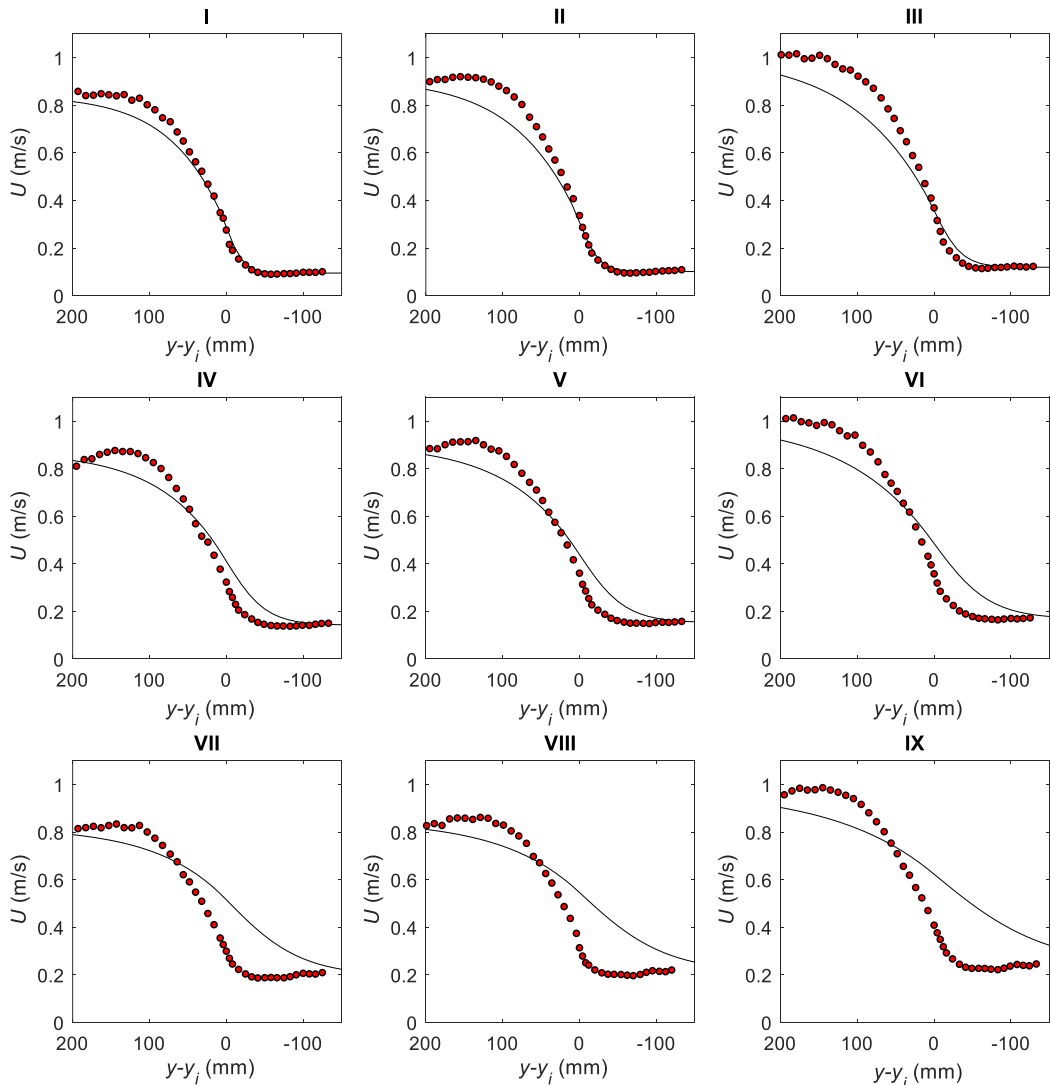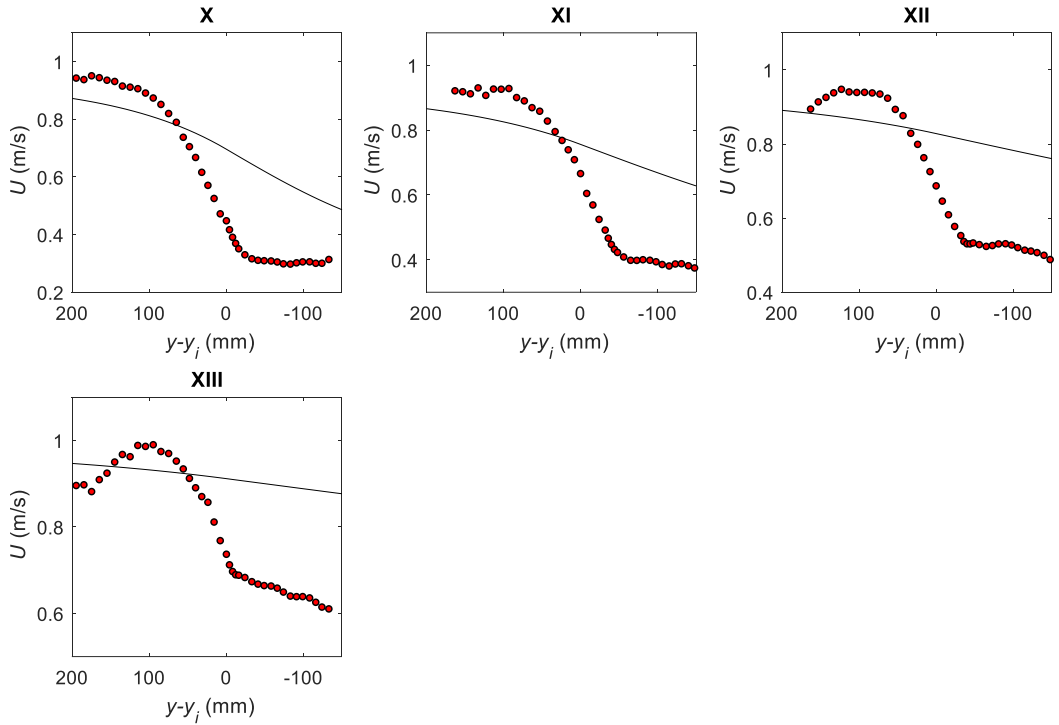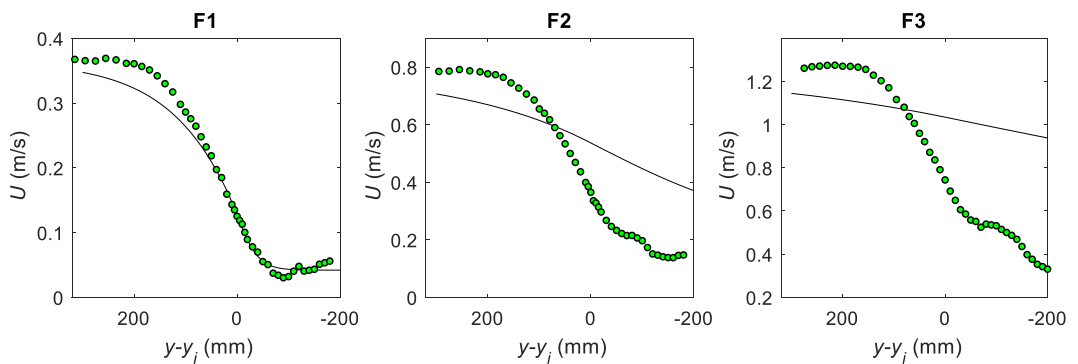*Figure 78 – Comparison between experimental velocity profiles (circles) and the predictions of the WNM (solid black curve) for the F1-F3 test cases (complex morphology vegetation).*

In Figure 78 the measured and predicted velocity profiles for natural-like reconfiguring plant stands are plotted together. The model correctly predicted only case F1 (with *RMSE*=0.019 m/s), where only slight plant reconfiguration and weak dynamic motion of vegetation were observed. With increasing reconfiguration (and decreasing drag and velocity ratio), the agreement with measured and predicted data progressively decreases. The model was found to provide not reliable predictions of velocity for reconfiguring vegetation (even though large-scale coherent structures were detected also for F2 and F3 case, but presenting velocity ratio lower than 0.8).

Considering the test cases I-III and F1, for which the model provided sufficiently good results, it should be noted that the drag-density parameter ranged between 21 and 12 m^{-1}, the shear layers of these runs were all characterized by velocity ratio approximately equal to 0.8. Moreover, for these cases, the model perfomed better for the within vegetation velocity prediction, suggesting that the $0.5C_D a^{-1}$, in this range of drag-density and velocity ratio, can be adopted as scaling length for the inner layer.

In the main channel the velocity was always higher than the WNM prediction. In this area the higher h/B ratios considered in the current study are expected to have more influence. Moreover, the assumption of constant eddy viscosity across the main channel was observed to be not realistic for the current series of experiments (Figure 79), presenting different distributions depending on the vegetation model.
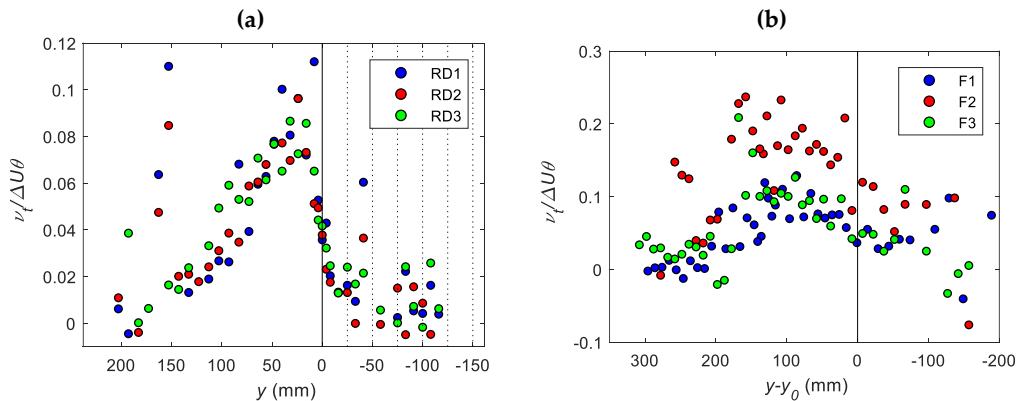

Figure 79 – Lateral distributions of normalized eddy viscosity for rigid cylinders (I-III) (a) and complex morphology vegetation (F1-F3) (b).

6.5 Conclusions

The features of vegetated shear layers induced by the presence of a morphologically complex and dynamically moving vegetative obstruction were compared with similar shear layers induced by an array of rigid cylinders. The comparison of the two sets of experiments, carried out in two different facilities, was based on the similarity between the shear layer characteristic velocity and shape factor, as described by the velocity ratio and the width to momentum thickness ratio, respectively. Moreover, the channel width to depth ratio and the total obstruction provided by vegetation relatively to the channel width were kept comparable between the two sets of experiments.

Therefore, the hydraulic similarity among the two sets of vegetated shear layers was achieved by matching both geometric and kinematic properties and the comparison performed with reference to the normalized lateral distributions of velocity statistics. The reconfiguration-induced vegetative drag reduction exhibited by the natural-like vegetation was simulated by reducing the cylinder density. This resulted in defining three pairings of similar shear layers, each characterized by analogous velocity ratio and drag-density parameter: (i) unreconfigured or slightly reconfigured foliated vegetation vs. dense array of cylinders; (ii) moderately reconfigured foliated vegetation vs. sparse array of cylinders; (iii) strongly reconfigured foliated vegetation vs. very sparse array of cylinders.

The results showed that the normalized lateral distributions of velocity and Reynolds stress were approximately independent on the vegetation features, presenting a strong dependence on the velocity ratio, which governed the presence of large-scale structures and the shape of the velocity and Reynolds stress profiles. Even presenting comparable distributions of flow characteristics, the penetration of the shear within the vegetation was strongly dependent on vegetation morphology and flexibility. Indeed, for natural-like vegetation, the shear penetrated up to the 75% of the shear layer width into the vegetation, presenting a decreasing trend with decreasing velocity ratio (induced by vegetation reconfiguration). For rigid cylinders, on the other hand, the penetration of shear was limited to 25% of the shear layer width, with analogous decreasing trend with decreasing velocity ratio.

The lateral motion of the vegetated interface (observed for test cases F1-F3) induced limited shear layer turbulence, averaging the turbulence intensity across the interface. For rigid cylinders, a clear peak in turbulence intensity was always observed at the interface, with asymmetric lateral distributions.

For the three pairings of shear layers, the presence of coherent large-scale structures with a Strouhal number of 0.032 was detected. Nevertheless, the efficiency of the lateral transport of momentum was observed to be considerably and systematically

higher for morphologically complex and dynamically moving vegetation, with respect to rigid cylinders. For the rigid cylinders the efficiency was comparable to that of canonical mixing layers.

The investigated vegetated shear layers presented some universal characteristics independent of the vegetation features, mainly governed by the drag-density parameter and the resulting velocity ratio. However, the flexibility-induced mechanisms of natural vegetation were found to significantly affect the turbulent flow structure, markedly modifying the lateral exchanges across the interface.

A comparison between the vertical distributions of normalized mean velocity and Reynolds stress was performed. The considered vertical profiles were measured at five lateral positions located at the same relative location with respect to the inflection point of the transversal velocity profile. Considering a natural-like vegetative obstruction led to non-uniform distributions along the vertical, owing to the presence of a grassy bed and the non-uniform distribution of plant elements. For rigid vegetation, the vertical distributions resulted to be highly uniform. Thus, assuming negligible the vertical variability in natural riparian conditions cannot be always realistic.

Finally, a comparison between a literature model for mean velocity prediction in partly vegetated channel was applied to the current data set. The model predicted the shape of the velocity profile with sufficient accuracy only for shear layers presenting high velocity ratio (0.8) and drag-density parameter (in the range 21-12 m-1) (Table 16). The model, originally built and tested considering rigid cylinders, was applied also to the natural-like vegetation test cases. In this condition the model predicted the shape of the velocity profile only for not or just slightly reconfigured vegetation (F1, see Figure 78, a). For moderately and strongly reconfigured vegetation (with shear layers with velocity ratios equal to ≈0.6 and ≈0.4 and drag-density parameter equal to 1.43 and 0.49 m-1, respectively), the model did not predict correctly the velocity distribution and its characteristic inflection (Figure 78, b and c).

References

Abdolahpour, M., Ghisalberti, M., Mcmahon, K., Lavery, P.S., 2018. The impact of flexibility on flow , turbulence , and vertical mixing in coastal canopies. doi:10.1002/lno.11008

Dijkstra, J.T., Uittenbogaard, R.E., 2010. Modeling the interaction between flow and highly flexible aquatic vegetation. Water Resour. Res. 46, 1–14. doi:10.1029/2010WR009246

Ghisalberti, M., Nepf, H.M., 2006. The structure of the shear layer in flows over rigid and flexible canopies. Environ. Fluid Mech. 6, 277–301. doi:10.1007/s10652-006-0002-4

Ghisalberti, M., Nepf, H.M., 2002. Mixing layers and coherent structures in vegetated aquatic flows. J. Geophys. Res. 107, 1–11. doi:10.1029/2001JC000871

Maltese, A., Cox, E., Folkard, A.M., Ciraolo, G., La Loggia, G., Lombardo, G., 2007. Laboratory measurements of flow and turbulence in discontinuous distributions of Ligulate seagrass. J. Hydraul. Eng. 133, 750–760.

Nepf, H.M., 2012. Hydrodynamics of vegetated channels. J. Hydraul. Res. 50, 262–279. doi:10.1080/00221686.2012.696559

Poggi, D., Porporato, A., Ridolfi, L., Albertson, J.D., Katul, G.G., 2004. The effect of vegetation density on canopy sub-layer turbulence. Boundary-Layer Meteorol. 111, 565–587. doi:10.1023/B:BOUN.0000016576.05621.73

White, B.L., Nepf, H.M., 2008. A vortex-based model of velocity and shear stress in a partially vegetated shallow channel. Water Resour. Res. 44, 1–15. doi:10.1029/2006WR005651

White, B.L., Nepf, H.M., 2007. Shear instability and coherent structures in shallow flow adjacent to a porous layer. J. Fluid Mech. 593, 1–32. doi:10.1017/S0022112007008415

7 Synthesis and conclusions

In the framework of this thesis, the features of different vegetated shear layers were experimentally investigated as to provide a contribution in the understanding of the flow-vegetation interaction in partly vegetated channels. In this Chapter a brief synthesis of the contents of the thesis is provided.

The first series of experiments focused on the hydrodynamic structure of the flow over submerged rigid vegetation, described in Chapter 3. The analysis of this configuration, allowed transferring to the context of vegetated flows the methods of the anisotropy invariant maps for the interpretation of the turbulence anisotropy. Starting from the consideration that in natural conditions vegetation generally occurs in lateral zone approximately parallel to the flow, the research interest was focused on partly vegetated channels. Indeed, as emerged from the literature review, important gaps exist in the knowledge of the hydrodynamic processes related to the presence of riparian vegetation in natural ecosystems and its modelling in experimental studies.

To deepen the understanding of the flow-vegetation interactions in partly vegetated channels, two experimental campaigns were designed and carried out as to provide a data set for the investigation of the hydrodynamic structure of the flow in channel-vegetated-bank systems.

In Chapter 4, the results of the experimental analysis of flow in a partly vegetated channel with complex morphology plant stands are discussed. The objective of the study was to investigate how vegetation reconfiguration and dynamic motions affect the transport of mass and momentum. To this aim, a novel experimental arrangement was designed as to mimic natural riparian conditions. Specifically, plant stands presenting lateral branches and leaves were accurately selected to obtain a combination of plant properties and vegetation density analogous to those of natural conditions. The results highlighted that foliated vegetation reconfigured by adapting its morphology to the increased hydrodynamic forcing, reinforcing that complex shrub-like vegetation undergoes drag reduction caused by both the seasonal shedding of leaves and the reconfiguration. This marked drag reduction was associated with decreasing shear layer velocity ratio, leading to weaker and coherent interfacial shear layer-scale flow structures, resulting in notably lower lateral transport of longitudinal momentum for the leafless than for the foliated cases. The dominant frequency of the large coherent structures matched the lateral dynamic motions of the plants. These frequencies were consistent with the canonical ML scaling (with the applicability of the classical Strouhal number

St≈0.032), indicating that they can be predicted from the basic flow characteristics for dynamically moving natural-like shrubs and bushes. Overall, the presence of leaves directly induced and enhanced mixing mechanisms at the cross-section scale, in contrast with the local scale effects induced by the leafless plants.

The large-scale coherent structures were found to play a key role in the interfacial processes between vegetation and the main channel, governing the lateral transport of mass and momentum. Moreover, the reduction of vegetation drag due to reconfiguration was found to have direct implications on the onset and coherence of these vortices, by altering the velocity ratio.

Driven by the interest in investigating the effects of density and velocity ratio on large-scale structures, a second experimental campaign was carried out considering a vegetative obstruction made of rigid cylinders, described in detail in Chapter 5. Six different packing densities of cylinders were considered providing, by changing also the flow rate, a wide range of vegetated shear layers, characterized by velocity ratios ranging from 0.8 down to 0.2. The velocity ratio of the shear layers was found to depend mainly on the cylinder density and spatial distribution and only slightly on the flow rate. The results suggested λ≈0.3 as a critical velocity ratio for the onset of large-scale structures, consistently with analogous investigations on flows in compound channels.

The experiments with rigid cylinders were also carried out in order to benchmark the tests with complex morphology vegetation and to spot the effects of vegetation morphology and motions, as described in Chapter 6. Dealing with the challenge of comparing a complex morphology vegetative obstruction (presenting foliation, branches, reconfiguration behavior and dynamic motion) with an array of rigid cylinders, a similarity in terms of shear layer features was established. Indeed, the comparability of the different shear layers was achieved by considering equal velocity ratio and analogous drag-density parameter between the complex morphology vegetation and the rigid cylinders. A shape factor (δ/θ) approximately equal to 4.5 was observed for all the vegetated shear layers presenting large-scale coherent structures, independently from the vegetative obstruction feature. The results showed that the lateral distribution of velocity and Reynolds stress were approximately independent on the vegetation features, presenting a strong dependence on the velocity ratio, which governed the presence of large-scale structures and hence the distributions velocity and Reynolds along the cross-section. Even presenting comparable distributions of flow characteristics and drag-density parameter, the penetration of the shear within the vegetation was strongly dependent on the vegetation features. Indeed, for complex morphology vegetation, the Reynolds stress penetrated up to the 75% of the shear layer width into the vegetation, presenting a decreasing trend with decreasing velocity ratio (induced

by vegetation reconfiguration). For rigid cylinders, on the other hand, the penetration of shear, with velocity ratio comparable to that of the F corresponding cases, was limited to 25% of the shear layer width, with analogous decreasing trend with decreasing velocity ratio. Greater differences in penetration were observed for high drag not reconfigured vegetation relative to dense rigid cylinders. For reconfigured vegetation the analogy with sparse array of rigid cylinders was stronger. For all the selected cases the presence of coherent large-scale structures was observed. Nevertheless, the efficiency of the lateral transport of momentum was observed to be considerably higher for morphologically complex and dynamically moving vegetation, with respect to rigid cylinders. For the rigid cylinders the efficiency was comparable to that of canonical MLs.

Finally, the suitability of a literature model for the prediction of flow velocity in partly vegetated channels was assessed with reference to the current experimental data sets. The model showed to be able to predict velocity only for the test cases with the highest velocity ratio and drag-density parameter. For real-like vegetation, the quick drop in drag-density parameter due to reconfiguration made the model unable to predict the velocity. Analogous results were observed for medium and sparse cylinder densities.

7.1 Future directions

The results gathered in this thesis provided a contribution in the understanding of the hydrodynamic processes in natural watercourses. The investigated laboratory configurations represent an approximation of natural riparian conditions, where complex cross-section geometries are coupled with heterogeneous vegetation covers. In this context, the significance of the results of this research stems out from the consideration that the knowledge of hydrodynamic processes in partly vegetated channels is currently based on even stronger approximations about the vegetation morphology and bio-mechanics (rigid cylinders).

In order to get deeper in the characterization of turbulence in natural contexts, further laboratory analyses should deal with the dynamic characterization of prototype riparian vegetation in horizontal shear dominated flows. This calls for the drag characterization of single plant stands within the vegetated shear layer and, therefore, drag force measurements (coupled with flow velocity measurements) are needed.

Furthermore, the partly vegetated channel configurations considered in this thesis are referred to channels with a rectangular cross-section partially obstructed by vegetation. In natural contexts, rivers generally present a compound cross-section. Thus, the different drag conditions governing the shear layer dynamics are

expected to depend on both the vegetative drag and the relative flow depth between the main channel and the floodplain.

Finally, field measurements at the vegetation organism and sub-organism scale could provide the ground truth for the understanding of the hydrodynamic processes involving vegetation in natural riverine systems. Owing to the high costs of such measurements, examples are still rare.

Sufficiently accurate tools for the simulation of vegetated flows and prediction of velocity in vegetated flows are needed. To this purpose, the characterization of hydrodynamic behavior of vegetation and its parametrization, in shear dominated flows, is needed.

Appendix A: Acoustic Doppler Velocimetry, instruments and data processing

The investigations of the mean and turbulent flow structure within the experimental vegetated channels described in this thesis were performed using acoustic Doppler velocimetry technique. In this Appendix the principles of operation of the ADV probe are briefly introduced. Successively, the strategies adopted for the ADV data acquisition and processing are illustrated. The need to carefully define proper and systematic acquisition and data processing strategies was driven by the wide variety of approaches adopted in analogous literature investigations.

During the present study, three different ADVs were used. The main features of the instruments and the application case are reported in Table 17.

Table 17 – Used ADV probes main features; f_{max} is the maximum sampling rate of the instrument.

Test series	ADV	Manufacturer	f_{max} (Hz)
UR - Rigid submerged (uniformly vegetated channel) Chapter 3	Micro ADV 16 MHz	SonTek	50
PN - Natural-like emergent (partially vegetated channel) Chapter 4	Vectrino+	Nortek	200
PR - Rigid emergent (partially vegetated channel) Chapter 6	Vectrino II	Nortek	100

A.1 ADV principle of operation

The detailed description of the velocimeter operation can be found in McLelland and Nicholas (2000) and García et al. (2005). Instrument specific characteristics can be found in the operation manuals, from which part of the following information is deduced. An ADV measures three-dimensional flow velocities using the Doppler shift principle. The instrument consists of a sound emitter, three to four sound receivers, and a signal conditioning electronic module. The sound emitter generates an acoustic signal at a given frequency F_s that is reflected back by sound-scattering particles present in the water, which are assumed to move at the same velocity as that of the water. The scattered sound signal is detected by the receivers and used to compute the Doppler phase shift F_D, from which the flow velocity in the radial

or beam directions is calculated, as schematically depicted in Figure 80. The relation between the flow velocity and the Doppler shift is:

$$F_D = -F_S \frac{V}{C}$$

(A.1)

where V represents the velocity of the source relative to the receiver and C the speed of sound (dependent on water temperature and salinity).
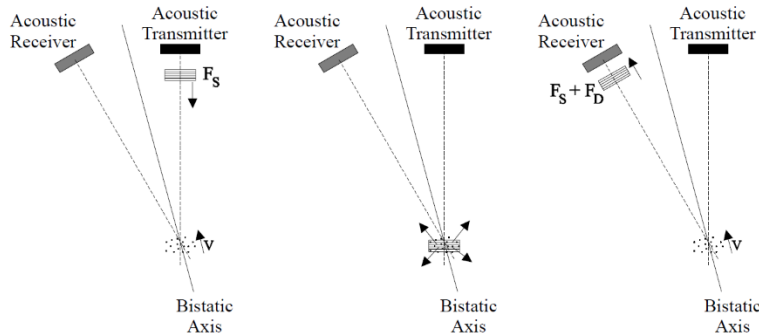

Figure 80 – Basic operation of a bistatic Doppler current meter (from ADV Field Manual, SonTek)

Figure 80 shows the operation of a bistatic Doppler current meter, such as the ADV. The term bistatic refers to the fact that the ADV uses separate acoustic transducers to transmit and to receive. The transmitter generates sound with the majority of the energy concentrated in a narrow cone, while the receiver is most sensitive to sound coming from a very narrow angular range. The transducers are mounted such that their beams intersect at a volume of water located some distance away. This beam intersection determines the location of the sampling volume (the volume of water in which measurements are made). The transmitter generates a short pulse of sound at a known frequency, which propagates through the water along the axis of its beam. As the pulse passes through the sampling volume, the acoustic energy is reflected in all directions by particulate matter (sediment, small organisms, bubbles, etc.). Some portion of the reflected energy travels back along the receiver axis, where it is sampled by the ADV and the processing electronics measures the change in frequency. The Doppler shift measured by one receiver is proportional to the velocity of the particles along the bistatic axis of the receiver and transmitter. The bistatic axis is located halfway between the axes of the transmitted and received beams.

A.1.1 Probe geometry and 3D velocity measurements

A single transmit-receive pair measures the projection of the water velocity onto its bistatic axis. The ADV uses one transmitter and two or three-four acoustic receivers (for 2D or 3D probes, respectively). The receivers are aligned to intersect with the

transmit beam pattern at a common sampling volume. The ADV combines velocity measurements from each receiver, knowing the relative orientation of the three bistatic axes, to calculate the 3D water velocity at the sampling volume.

The velocity measured by each receiver is referred to as the bistatic velocity, and is the projection of the 3D velocity vector onto the bistatic axis of the acoustic receiver. Bistatic velocities are output directly by the ADV only in specialized applications; normally they are converted to Cartesian velocities using probe geometry. This coordinate system transformation is operated with a transformation matrix, dependent on the geometry of the probe. Cartesian velocities give the 3D velocity field relative to the orientation of the ADV probe. The orientation of the probe represents a critical aspect. Indeed, the misorientation of the probe can lead to errors in the estimation of mean velocity and Reynolds stresses (Peltier et al., 2013).

A.1.2 Pulse-coherent processing and sampling rate selection

The ADV uses a dual pulse-pair scheme with different pulse repetition rates separated by a lag time (McLelland and Nicholas, 2000). The longer pair of pulses is used for higher precision velocity estimates, while the shorter pulse is used for ambiguity resolution, assuming that the real velocity goes beyond the limit resolvable by the longer time lag. These process defines the instrument sampling rate f_{SR}. After the digital velocity signal is obtained with frequency f_{SR}, the instrument performs an average of N values to produce a digital signal with frequency $f_R = f_{SR}/N$, which is the ADV user-set frequency with which velocity data are recorded (García et al., 2005). As illustrated by García et al. (2005), two main conclusions can be drawn from the considerations above. First, energy in the signal with a frequency higher than f_{SR} is filtered out, i.e. acquisition process acts as a low-pass filter. Second, aliasing of the signal occurs since the velocity signal is sampled at a frequency f_{SR}, and the highest frequency that can be resolved by the instrument is $f_{SR}/2$ (Nyquist theorem, see Bendat and Piersol (1966)). This indicates that energy in the frequency range of $f_{SR}/2 < f < f_{SR}$ is folded back into the range $0 < f < f_{SR}/2$, which may or may not be of importance depending on the flow characteristics. Flows with a large convective velocity, U_C, will have a considerable portion of the energy in the range of wave-lengths: $f_{SR}/2U_C < f/U_C < f_{SR}/U_C$ while flows with a low convective velocity will have no energy in this range and, therefore, aliasing will not be of relevance.

Thus, the definition of the sampling rate should be done according the flow characteristics. In addition, the choice of the sampling rate for ADV measurements depends on the aims of the analysis. If on the one hand it can be considered of lower importance for the mean flow analysis, on the other hand it is crucial for the realistic estimation of turbulence descriptors, including higher order moments, spectra and integral scales. Even though the noise effect on ADV measurements can be reduced

using lower sampling rates, the highest instrument frequency of acquisition should be adopted for turbulence investigation. A useful indication for assessing the capability of the instrument in processing the turbulence can be obtained comparing the characteristic frequency of the large coherent structures and the acquisition frequency with the dimensionless parameter $F_C=f_R/(U_C L)$ as defined by García et al. (2005). The ratio between user-set ADV frequency (f_R) and large eddies characteristic frequency ($U_C L$) should be greater than 20 or, according to Nezu and Nakagawa (1993), greater than 16.67, with reference to open-channel flows. For vegetated flows, the problem is generally complicated by the presence of a variety of different scales.

In the framework of this thesis, for turbulent flow structure analysis, the highest available acquisition frequency was considered, verifying with the spectral analysis that the instrument was capable to process a good portion of the inertial subrange. Figure 81 and Figure 82 show power density spectra evaluated in different points of the vegetated flow domain for various frequencies.
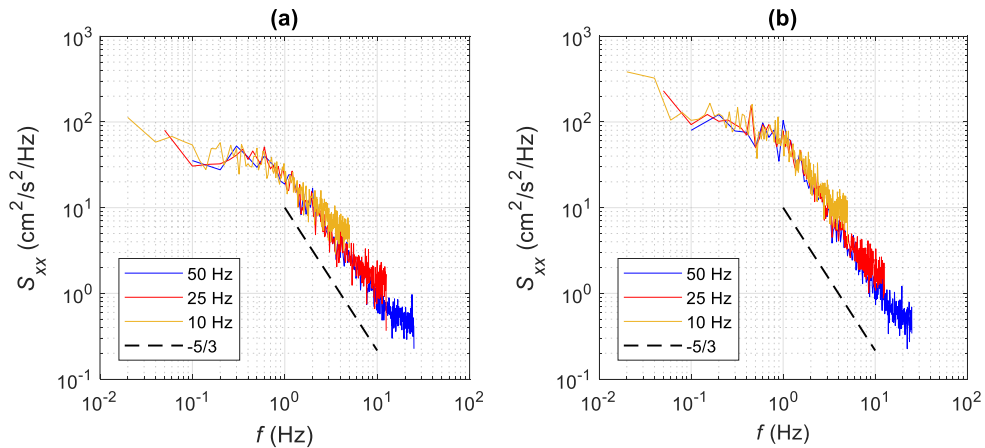

Figure 81 – Power spectral density evaluated for three different sampling rates: 10, 25 and 50 Hz. Submerged rigid vegetation case (SonTek MicroADV), 12000 sample size. Within the cylinder array, z=25 mm (a); above the cylinders array, z=65 mm (b). The dashed line indicates the -5/3 slope.
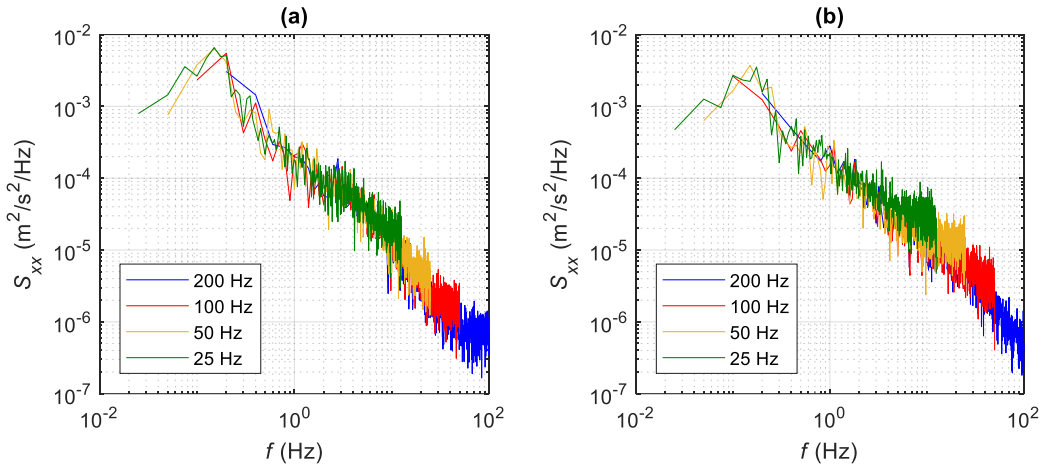
Figure 82 – Power spectral density evaluated for four different sampling rates: 25, 50, 100 and 200 Hz. Emergent real-like vegetation case (Nortek, Vectrino+), 12115 sample size. In the main channel, y=220 mm (a), within the foliated vegetation, y=180 mm (b).

The lower frequency acquisitions neglected a considerable portion of the energy of the signal. For the current analysis, considering the need to characterize the turbulent flow structure, the highest available acquisition frequency was adopted, verifying with spectral analysis that the instrument was capable to process a good portion of the spectrum.

A.1.3 Sample size

In order to characterize the mean and the turbulent flow, the sample size of the ADV single data point acquisition should be carefully defined in order to achieve sufficiently stable velocity statistics estimations. A great variety of sampling durations is used by researchers, in laboratory and field studies, without systematic validation. Only few literature studies focused on the effects of sample size on turbulent and mean flow analysis (Chanson, 2008; Chanson et al., 2005a). In this study the length of the acquisition was carefully defined as to have well converging turbulence statistics.

In Figure 83 and Figure 84 different velocity statistics (mean, covariance, square, skewness and kurtosis) normalized with the value at the end of the acquisition are plotted against the sample size n. The plots are referred to the position of highest turbulence intensity for the different analyzed cases.
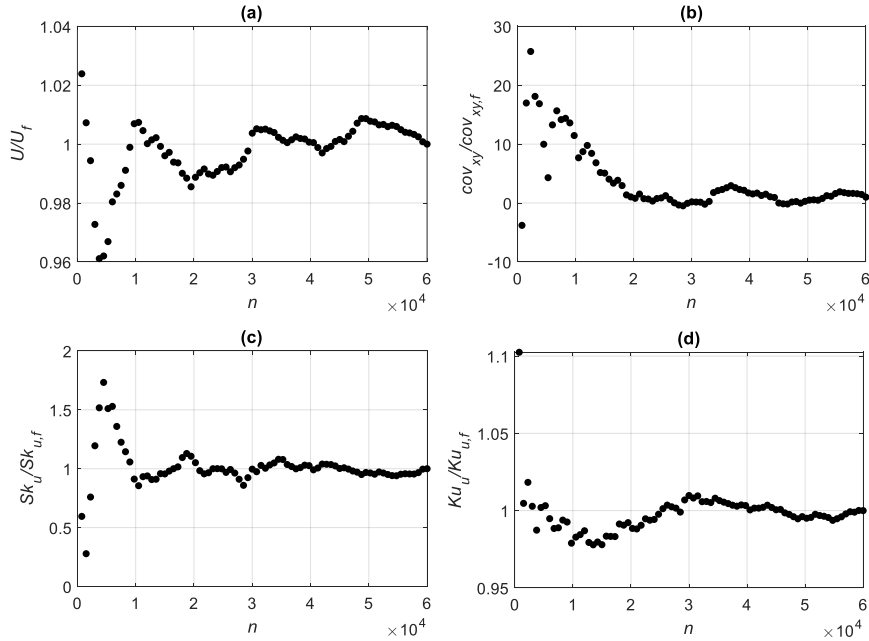
Figure 83 – Velocity statistics evaluated for different sample size n up to 60 000 (20 minutes at 50 Hz), mean longitudinal velocity (a), lateral-longitudinal Reynolds stress (b), skewness (c) and kurtosis (d). Values are normalized with respect to the statistics at the end of the 20 minutes long acquisition (subscript f). Submerged rigid vegetation case (SonTek, MicroADV), measurement location z=65 mm (region of high turbulence intensity).

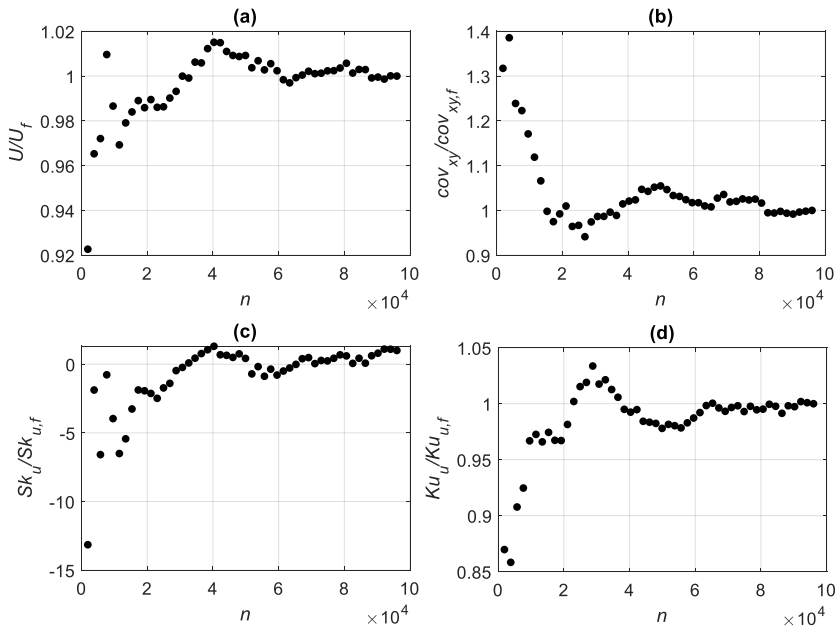*Figure 84 – Velocity statistics evaluated for different sample size n up to 10 000, mean longitudinal velocity (a), lateral-longitudinal Reynolds stress (b), skewness (c) and kurtosis (d). Values are normalized with respect to the statistics at the end of the 8 min long acquisition. Emergent natural-like vegetation case (Nortek, Vectrino+), measurement location y=0 (region of high turbulence intensity).*

Analogous analyses were performed considering the Nortek Vectrino II probe. As pointed out by Chanson et al. (2005b) basic turbulence studies need large sample size (60000-90000 samples), also considering that the higher order statistics need large n to reach stability. As shown in Figure 83 and Figure 84, a sample size of 20000 was found to be adequate to obtain well converging turbulence statistics. The details of the sampling rate and the sample size adopted for each series of experiments are reported in Table 18.

Table 18 – Specification of sampling rate and sample size adopted for the different instruments and test series.

Test series	ADV	f_R (Hz)	n (-)	Duration (s)
UR	MicroADV	50	60000	1200
PN	Vectrino+	200	24000	120
PR	Vectrino II	100	24000	240

A.1.4 ADV measurements quality, accuracy and pre-filtering

Several aspects of the ADV operations affect the quality of velocity data. The most important of these is the velocity range (VR) setting. This determines the maximum velocity that can be measured. In general, the lowest VR, compatible with the velocity and the turbulence intensity of the flow, was adopted. The instrument-generated noise in velocity data is proportional to the VR setting; higher VRs have higher noise levels. When operating in highly turbulent flows, the ADV showed low correlation values indicating increased noise in velocity measurements. For turbulent flow, the noise level may be reduced by increasing the VR.

The ADV is designed to measure velocity as rapidly as possible. A single estimate of the 3D velocity field is referred to as a ping. The ADV pings several times per second, with a frequency equal to f_{SR} (depending on the instrument type and on the velocity range). As the noise in a single ping is too high for practical use, the ADV averages a number of pings to reduce the noise level in each output velocity sample. The number of pings averaged is set to meet the user-specified sampling rate f_R. An important result of the ADV sampling scheme is that reducing the sampling rate decreases the noise in each sample (by increasing the number of pings averaged per sample). The instrument generated noise, also referred to as Doppler noise, is random; averaging multiple points will converge toward the true value without introducing bias. The noise level decreases with the square root of the number of samples averaged; thus, data output at 1 Hz has about one-fifth the noise of data output at 25 Hz. In the present study, considering the need to analyze the turbulent flow structure, the highest sampling rate was adopted.

Accuracy for ADV velocity data refers to the presence of a bias in mean velocity measurements after removing instrument-generated noise. Two main factors influence the accuracy of ADV velocity measurements: sound speed and probe geometry. For all the adopted instruments the accuracy was ±1% of the measured value.

A.1.4.1 ADV Data quality indicators and pre-filtering
The ADV records for each velocity measurement two quality indicators: the signal to noise ratio (SNR) and the signal correlation score (CORR). The SNR provides information about the signal strength, by measuring the intensity of the reflected acoustic signal and is measured in dB. Without sufficient signal strength, the ADV is unable to make accurate velocity measurements. As SNR decreases, the noise in ADV velocity measurements increases. The strength of the return signal is a function of the amount and type of particulate matter in the water and therefore in all the experiments water was adequately seeded using additional particulate matter.

The correlation score is a data quality parameter that is a direct output of the Doppler velocity calculations. It is strictly related to the pulse-coherent process. The ADV computes a correlation value for each acoustic receiver, with each velocity sample. Correlation is expressed as a percentage: perfect correlation of 100% indicates reliable, low noise velocity measurements; 0% correlation indicates the output velocity value is dominated by noise (no coherent signal). Correlation can be used to monitor data quality during collection and to edit data in post-processing.

In the present study all the ADV measurements were pre-filtered, discarding measurements with SNR lower than 15-30 dB and CORR lower than 70%.

A.2 ADV data post-processing
ADV outputs cannot be considered real velocity measurements and need to be accurately processed (Chanson, 2008; Goring and Nikora, 2002; Jesson et al., 2013) to filter out the combined effects of Doppler noise, signal aliasing and other disturbances. Indeed, the aliasing of the Doppler signal generates spikes in the record that have to be detected and replaced. In this Section the methods adopted for ADV data despiking are illustrated. An extensive description of the different literature methods can be found in Goring and Nikora (2002), Jesson et al. (2013) and Parsheh et al. (2010).

The despiking process adopted for ADV data analysis involves (two mutual dependent) stages: (1) the actual spike detection and (2) the spike replacement.

Depending on the adopted ADV probe, two different methods were used for spike detection:

1. for the SonTek probe data, the phase-space thresholding (PST) method was adopted (Goring and Nikora, 2002; Wahl, 2003), using the WinADV software (Wahl, 2000);
2. for the Nortek probe data, the modified phase-space thresholding (mPST) method (Parsheh et al., 2010), using the Velocity Signal Analyser (VSA) software (Jesson et al., 2015).

The PST method is widely adopted in literature (e.g. Dupuis et al., 2017; Hamidifar and Omid, 2013; Mera et al., 2015; Zeng and Li, 2014) and therefore was selected for the SonTek data analysis. For the Nortek data, analyzed using the VSA software, the mPST method was adopted as done in a recent work of Vettori and Nikora (2017). The mPST was found to perform better also for severely contaminated time series, being able to accurately recover the power spectra up to the frequency corresponding to the half the mean sampling rate of the valid data points (Parsheh et al., 2010). The selection of the characteristic scalar (CS) for the application of the mPST (Parsheh et al., 2010) was done testing the usage of the standard deviation (STDEV) and the median absolute value (MAD). The two scalars performed equally well and the STDEV was adopted for all the analyses.

While the WinADV software does not allow replacing detected spikes (which are simply removed from the time series), the VSA software allows selecting among different replacement methods (Jesson et al., 2013):

*   last good value (LGV);
*   linear interpolation (LI);
*   12-point polynomial (12PP).

Since for the PST and the mPST the spikes are detected assuming a threshold evaluated considering also the replaced spikes, the methods are iterative and, therefore, spike replacement can affect spike detection in the subsequent iterations (Goring and Nikora, 2002).

For the Nortek probes data, the selection of the replacement method to use coupled with the mPST despiking method was made testing the different available alternatives (LGV, LI, 12PPI). Useful indications can be found in Jesson et al. (2013).

With reference to the analyzed data, the different replacement methods had negligible influence on the velocity statistics, the invariants of the anisotropic stress tensor, and the percentage of good data. On the contrary, the choice of the replacement method notably affected the energy spectra, the autocorrelation functions and, in turn, the resulting integral scales.

As an example, in Figure 85, the spectra of the fluctuating longitudinal and lateral velocity components evaluated at a significant location within the flow domain are reported for the unfiltered signal and for the mPST filtered signals using the three different replacement methods. As shown in Figure 85, the 12PP method altered the spectra, while the unfiltered signal, the LGV and LI signals led to comparable results.
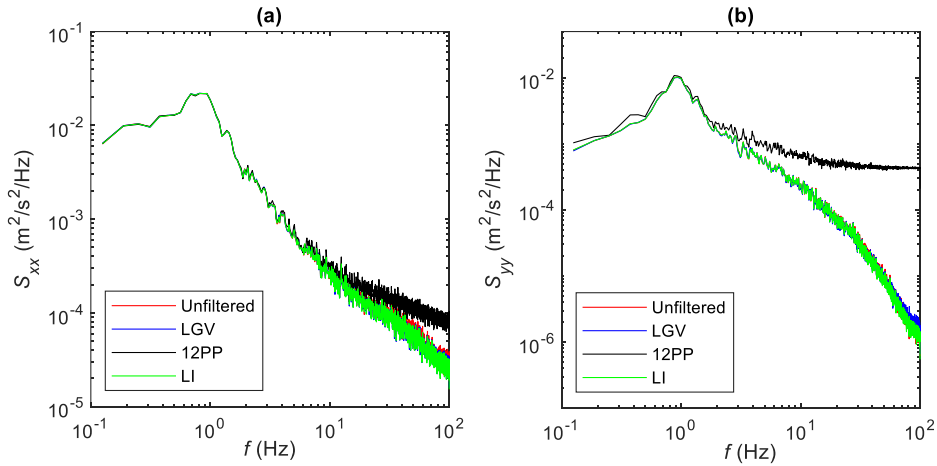

Figure 85 – Energy spectra for the longitudinal (a) and lateral (b) fluctuating velocities evaluated for the unfiltered signal and for the filtered time series using three different replacement method. Measurements are referred to the PN series, F3 case at y=0 mm.

In Figure 86 the autocorrelation functions evaluated for the unfiltered and the mPST filtered data series are shown for a significant measurement location. Also in this case the LGV and LI methods led to analogous results, while the 12PP method altered the shape of the autocorrelation function.
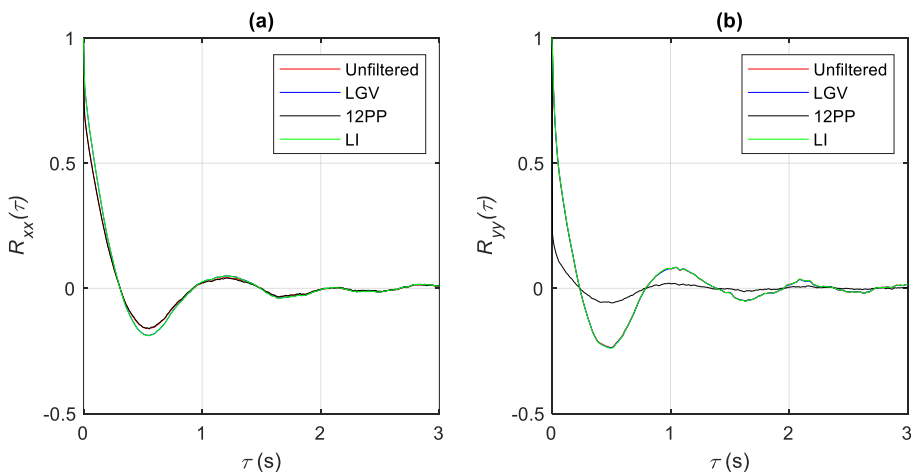

Figure 86 – Autocorrelation functions for the longitudinal (a) and lateral (b) fluctuating velocities evaluated for the unfiltered signal and for the filtered time series using three different replacement method. Measurements are referred to the PN series, F3 case at y=0 mm.

The observed percentage difference in the integral time scale evaluated from the autocorrelation functions of Figure 86 was approximately equal to 75% between the LGV and the 12PP, 13% between the unfiltered and the LGV, and 0.3% between the LGV and the LI. Different flow conditions and location within the flow domain were tested leading to analogous results. Therefore, considering that LGV and LI produced comparable results and the greater simplicity of the LGV method, the mPST was coupled with the LGV replacement method. These results are consistent with the conclusions of Jesson et al. (2013).

In summation, the post-processing methods and software adopted for each experimental series are reported in Table 19.

Table 19 – Specification of post-processing software, and de-spiking and replacement methods for each experimental series.

Test series	ADV	Software	De-spiking	CS	Replacement
UR	SonTek	WinADV	PST	STDEV	-
PN, PR	Nortek	VSA	mPST	STDEV	LGV

References

Bendat, J., Piersol, A., 1966. Measurements and Analysis of Random Data. Int. J. Control 3, 395. doi:10.1080/00207176608921391

Chanson, H., 2008. Acoustic Doppler Velocimetry (Adv) in the Field and in Laboratory : Practical Experiences. Int. Meet. Meas. Hydraul. Sewers 49–66.

Chanson, H., Trevethan, M., Koch, C., 2005a. Discussion of "Turbulence Measurements with Acoustic Doppler Velocimeter" by Carlos M. García, Mariano I. Cantero, Yarko Niño, and Marcelo H. García. J. Hydraul. Eng. 131, 1062–1073. doi:10.1061/(ASCE)0733-9429(2005)131:12(1062)

Chanson, H., Trevethan, M., Koch, C., 2005b. Discussion of "Turbulence Measurements with Acoustic Doppler Velocimeters" by Carlos M. Garcia, Mariano I. Cantero, Yarko Nino, and Marcelo H. Garcia. J. Hydraul. Eng. 131, 1062–1073. doi:10.1061/(ASCE)0733-9429(2005)131:12(1062)

Dupuis, V., Proust, S., Berni, C., Paquier, A., 2017. Mixing layer development in compound channel flows with submerged and emergent rigid vegetation over the floodplains. Exp. Fluids 58, 0. doi:10.1007/s00348-017-2319-9

García, M.C., Cantero, I.M., Niño, Y., García, H.M., 2005. Turbulence Measurements with Acoustic Doppler Velocimeters. J. Hydraul. Eng. 1062–1073. doi:10.1061/(ASCE)0733-9429(2005)131:12(1062)

Goring, D.G., Nikora, V.I., 2002. Despiking Acoustic Doppler Velocimeter Data. J. Hydraul. Eng. 128, 117–126. doi:10.1061/(ASCE)0733-9429(2002)128:1(117)

Hamidifar, H., Omid, M.H., 2013. Floodplain Vegetation Contribution to Velocity Distribution in Compound Channels. J. Civ. Eng. Urban. 3, 357–361.

Jesson, M.A., Bridgeman, J., Sterling, M., 2015. Novel software developments for the automated post-processing of high volumes of velocity time-series. Adv. Eng. Softw. 89, 36–42. doi:10.1016/j.advengsoft.2015.06.007

Jesson, M.A., Sterling, M., Bridgeman, J., 2013. Despiking velocity time-series-Optimisation through the combination of spike detection and replacementmethods. Flow Meas. Instrum. 30, 45–51. doi:10.1016/j.flowmeasinst.2013.01.007

McLelland, S.J., Nicholas, A.P., 2000. A new method for evaluating errors in high-frequency ADV measurements. Hydrol. Process. 14, 351–366. doi:10.1002/(SICI)1099-1085(20000215)14:2<351::AID-HYP963>3.0.CO;2-K

Mera, I., Franca, M.J., Anta, J., Peña, E., 2015. Turbulence anisotropy in a compound meandering channel with different submergence conditions. Adv. Water Resour. 81, 142–151. doi:10.1016/j.advwatres.2014.10.012

Nezu, I., Nakagawa, H., 1993. Turbulence in Open-Channel Flows. A.A. Balkema, RO. Box 1675,3000 BR Rotterdam, Netherlands.

Parsheh, M., Sotiropoulos, F., Porté-Agel, F., 2010. Estimation of Power Spectra of Acoustic-Doppler Velocimetry Data Contaminated with Intermittent Spikes. J. Hydraul. Eng. 136, 368–378. doi:10.1061/(ASCE)HY.1943-7900.0000202

Peltier, Y., Rivière, N., Proust, S., Mignot, E., Paquier, A., Shiono, K., 2013. Estimation of the error on the mean velocity and on the Reynolds stress due to a misoriented ADV probe in the horizontal plane: Case of experiments in a compound open-channel. Flow Meas. Instrum. 34, 34–41. doi:10.1016/j.flowmeasinst.2013.08.002

Vettori, D., Nikora, V.I., 2017. Flow–seaweed interactions: a laboratory study using blade models. Environ. Fluid Mech. 1–26. doi:10.1007/s10652-017-9556-6

Wahl, T.L., 2003. Discussion of '"Despiking Acoustic Doppler Velocimeter Data"' by Derek G. Goring and Vladimir I. Nikora January. J. Eng. Mech. 128, 2002–2003. doi:10.1061/(ASCE)0733-9372(2003)129

Wahl, T.L., 2000. Analyzing ADV Data Using WinADV. Build. Partnerships 1–10. doi:10.1061/40517(2000)300

Zeng, C., Li, C.W., 2014. Measurements and modeling of open-channel flows with finite semi-rigid vegetation patches. Environ. Fluid Mech. 14, 113–134. doi:10.1007/s10652-013-9298-z

Notation

a_{ij}	Anisotropic stress tensor component
a_L	Frontal projected area of leaves per canopy volume
a_S	Frontal projected area of stems per canopy volume
B	Channel width
B_V	Width of vegetated area
b_{ij}	Normalized anisotropic stress tensor component
C	Speed of sound
C_D	Drag coefficient
$C_D a$	Drag-density parameter
c_f	Friction factor
cov_{ij}	Covariance of fluctuating velocity components
d	Plant stems characteristic diameter, cylinder diameter
d_p	Penetration of shear from the vegetated interface
F	Drag force
Fr	Froude number
F_C	Dimensionless frequency parameter
F_D	Doppler phase shift
F_s	Frequency of ADV acoustic signal
f	Frequency; observed frequency of KH vortices
f_{ML}	Characteristic mixing layer frequency of large-scale vortices
f_S	Frequency of large-scale coherent structures (Sukhodolov and Sukhodolova, 2012)
f_{SR}	ADV sampling rate
f_R	User-set ADV sampling rate
f_V	Observed frequency of plant motion
g	Gravitational acceleration
$g(\omega), f(t)$	Fourier transform pair functions
H	Size of hyperbolic region for quadrant analysis
h	Water depth
i	Flume slope
K_i	Turbulent kinetic component in the ith direction
Ku_i	Kurtosis of fluctuating velocity component
k	Cylinder height
k_s	Wave number
L	Object characteristic length
LAI	Leaf area index
L	Characteristic length

L_i	Integral length scale of the ith fluctuating velocity component
L_x, L_y	Spacing between cylinders
m	Moment of the PDF
P	Probability density function
P_w	Rate of TKE per unit mass production by wakes
P_s	Rate of TKE per unit mass production by shear
Q	Flow rate
R_{ii}	Autocorrelation function of the ith fluctuating velocity component
Re	Reynolds number
Re_d	Vegetation characteristic diameter based Reynolds number
Re_h	Water depth based Reynolds number
Re_k	Cylinder height based Reynolds number
Re_x	Boundary layer abscissa based Reynolds number
Re_θ	Momentum thickness based Reynolds number
$RMSE$	Root mean square error
r_{uv}	Pearson correlation coefficient
S_i	Total contribution of the ith quadrant to the Reynolds stress
$S_{i,H}$	Contribution of extreme events of the ith quadrant to the Reynolds stress
S_{ii}	Power density spectrum of the ith fluctuating velocity component
S_{ij}	Power density cross-spectrum of the ith and j^{th} fluctuating velocity components
St	Strouhal number
S_x, S_y	Spacing between natural-like plant stands
Sk_u, Sk_v, Sk_w	Skewness of fluctuating velocity components
T_i	Integral length scale of the ith fluctuating velocity component
t	Time
U, V, W	Mean velocity components
U^*	Friction velocity at the canopy top
U_1	Mean longitudinal velocity within the vegetated area
U_2	Mean longitudinal velocity within the main channel
U_c	Vegetated shear layer convection velocity
U_I	Mean longitudinal velocity in the inner layer
U_k	Mean velocity at the canopy top
U_m	Cross-sectional mean velocity

$U_{m'}$	Velocity at y_m
U_O	Mean longitudinal velocity in the outer layer
U_S	Slip velocity
U_{WN}	Velocity predicted with WNM
u, v, w	Instantaneous velocity components
u_{b*}	Friction velocity on the blade
u_*	Lateral friction velocity
u', v', w'	Instantaneous fluctuating velocity components
$u_{rms}, v_{rms}, w_{rms}$	Root mean square of fluctuating velocity components
x, y, z	Spatial coordinates
x_D	Flow deflection length scale
y_0	Lateral position of the vegetated interface
$y_{0.1}, y_{0.9}$	Lateral positions for ML width definition
y_i	Lateral position of the inflection point

Greek symbols

α	WNM parameter
β	Efficiency of the mass exchange in zone III (WNM)
γ	Ratio of momentum to mass flux (WNM)
ΔU	Velocity difference or differential velocity
δ	Vegetated shear layer width
$\delta(x)$	Boundary layer thickness
δ_e	Vortex penetration length scale
δ_I	Inner layer width
δ_O	Outer layer width
δ_S	Viscous sub-layer thickness
δ_V	Penetration of canopy-scale vortices for horizontal shear layer
ε	Turbulent kinetic energy dissipation rate
λ	Velocity ratio or normalized velocity difference
$\lambda_1, \lambda_2, \lambda_3$	Eigenvalues of the anisotropic stress tensor
λ_V	Density roughness
θ	Momentum thickness
ν	Kinematic viscosity of water
ν_t	Eddy viscosity
ξ, η	Coordinates of invariant maps
ρ	Water density

$\sigma_i{}^2$	Variance of the ith fluctuating velocity component
σ_f	Standard deviation of frequency at spectral peak along the transect
σ_{fv}	Standard deviation of observed frequency of plant motions
τ	Time lag
τ_0	Time lag at the first zero crossing
τ_c	Turbulent shear stress at the mixing layer centerline
τ_e	Time lag corresponding to $R(\tau_e)=1/e$
τ_{min}	Time lag corresponding to $R(\tau_{min})= R_{min}$
ϕ	Solid volume fraction of vegetation
χ	Vogel exponent
ω	Angular frequency